UNIVERSITÀ DEGLI STUDI DI PADOVA

Facoltà di Ingegneria

PLASMA BOUNDARY RECONSTRUCTION AND SHAPE CONTROL OF TOKAMAK DISCHARGES IN RFX-MOD

Tesi di Laurea Magistrale in Ingegneria dell'Automazione

Laureando:
Pierangelo Merlo

Relatore: Chiar.mo Prof. Angelo Cenedese
Correlatore: Dott. Ing. Giuseppe Marchiori

III Periodo
Anno Accademico 2010/2011

Contents

Abstract **7**

1 Fusion energy and plasma modelling **9**
1.1 Introduction: Energy issues and nuclear reactions 9
1.2 The Lawson criterion 11
1.3 Plasma, the fourth state of matter 13
1.4 MHD Equations 14
1.5 The Tokamak and RFP configurations 15

2 The RFX-mod experiment **19**
2.1 Specifications and structure 19
2.2 RFX-mod diagnostics 22
2.3 RFX-mod magnetic field coils 24

3 The nonlinear model and simulator **29**
3.1 The Grad-Shafranov equation 29
3.2 The free boundary problem 30
3.3 Maxfea, a free boundary solver for the GSE 31
3.4 Validation against experimental data 33
3.5 Estimation of vertical instability growth rate 40

4 Plasma boundary reconstruction **43**
4.1 Radial expansion method for gap estimation 44
4.2 Integral flux map and boundary reconstruction 48
4.3 Plasma centroid: the current moment method 58

5 Derivation of a linear state-space model **63**
5.1 Calculation of the modified inductance matrix 64

5.2 Calculation of the resistance matrix 67
5.3 Reconnection of the electromagnetic model 68
5.4 Plasma displacement instabilities 75
5.5 Validation of the linear model 80

6 Plasma position and shape control **87**
6.1 Stabilization of the plasma current centroid 87
6.2 Model order reduction for gap control 97
6.3 Kalman filter design 101
6.4 LQR controller design 106
6.5 Regulator benchmark: Tokamak perturbations 111
6.6 LQG regulation: power consumption 129
6.7 Circular-DN transition with LQG control 132

Conclusions **135**

A Linear model and LQG control: Simulink scheme **137**

B Plasma boundary reconstruction: Matlab code **139**

C Controller implementation: FORTRAN77 code **151**

List of tables **163**

List of figures **165**

Bibliography **169**

Ringraziamenti

Giunto a questo punto del mio percorso, ritengo di dover ringraziare le persone che più mi sono state vicine e più mi hanno aiutato in questi anni Universitari, e in particolar modo in quest'ultimo periodo, nel corso della stesura di questa Tesi.

Desidero innanzitutto ringraziare il Prof. Angelo Cenedese e l'Ing. Giuseppe Marchiori per la dedizione con cui mi hanno guidato nel lavoro di Tesi, coinvolgendomi e stimolandomi nell'interesse per la Ricerca, dedicandomi molto del loro prezioso tempo e non facendomi mai mancare il loro incoraggiamento. Nondimeno, voglio ringraziare gli altri Professori del Dipartimento di Ingegneria dell'Informazione per le lezioni appassionanti e per aver saputo avvalorare l'impegno mio e dei miei compagni di corso come studenti.

Voglio poi esprimere la mia gratitudine ai miei genitori. A mia madre, che vorrei potesse oggi partecipare alla mia gioia per questo risultato, e che ha infuso in me l'amore per lo studio. A mio padre, che è stato sempre presente in questi anni, sapendo sopportare i miei momenti peggiori, e che mi ha trasmesso il senso pratico che deve caratterizzare un Ingegnere.

Infine, ma non per ultimi, voglio ringraziare tutti i miei amici, che mi hanno spesso riportato "con i piedi per terra" dopo le lunghe giornate di studio. Un grazie particolare a Fabio, che non solo mi ha aiutato con l'inglese rileggendo con me le bozze di questa Tesi: senza di lui, questi ultimi anni di Università sarebbero stati meno ricchi di gioia e di colore.

Abstract

This work focuses on plasma shape reconstruction and control problems with reference to the configuration of the *RFX-mod* device, a large RFP experimental machine built for plasma physics studies and operating in Padua, Italy. Nuclear fusion experiments require a strong engineering effort to provide the conditions where particular plasma configurations can be reproduced. The critical aspects of plasma geometry diagnosis and of active plasma shape control will be analyzed in depth, referring when possible to considerations emerging from experimental results.

The thesis is organized as follows. The first chapter provides an introduction to plasma physics, and reviews the basic energetic issues that underlie the development of devices with increasing complexity and with performances that are approaching the conditions where net power generation from nuclear fusion reactions is possible.

The second chapter lists the main features of the RFX-mod experiment, and resumes the key aspects of its use as a Tokamak, producing a plasma configuration that differs from the nominal use of the machine as a RFP device.

The third chapter focuses on the use of a simulator that allows the study of equilibrium plasma configurations and that will be used to evaluate dynamic properties as well. Particular attention will be put on critical aspects of plasma parametrization to obtain results that are consistent with experimental data. The simulator already implements a modelization of the RFX-mod machine, and some modifications to the existing mesh representing the design of the device will be implemented in the following of this work.

The fourth chapter defines the plasma shape reconstruction problem, reviews the available methods for geometry parameters reconstruction currently used on the experiment, and proposes original contributions to adapt the existing methods to the plasma configuration considered hereby.

The fifth chapter deals with the derivation of a linear model, required to use linear control techniques commonly implemented in automation engineering. The validity of the model will be assessed, and its limitations will be accurately reviewed.

Finally, the sixth chapter defines the shape control problem, presents the main guidelines that were adopted to design the controller, and proposes extensive tests that should assess the possibility to apply the control scheme to the experimental framework.

Chapter 1

Fusion energy and plasma modelling

1.1 Introduction: Energy issues and nuclear reactions

Energy is the most primary resource that our society requires for its own support and development. The economic system on which modern countries are based on is strongly influenced by energy price and availability, and international balances heavily depend on energy trade. While the most relevant part of energy production comes today from fossil fuels, a prospective decrease in availability of these resources, together with a growing sensibility towards environmental issues among the population, is demanding structural changes in energy production and distribution schemes.

There is growing interest towards renewable energy sources. While hydroelectric power still contributes predominantly to production of electricity from renewable sources, a small but growing percentage comes from solar and wind energy. However, it is debatable whether these sources will be able to significantly lessen the dependence on non renewable sources in the long term. An alternative possibility comes from nuclear energy, that exploits nuclear mass reactions to release energy from the involved reagents. The total mass of protons and neutrons composing an atom nucleus is higher than the mass of the nucleus as a whole. The mass difference, Δm, is related to a variation in binding energy by the relation

$$\Delta E = \Delta m \, c^2.$$

Binding energy per nucleon (figure 1.1), that is the ratio between the amount of energy needed to break the atomic nucleus and its mass number, has its maximum value around mass number 50. This means that it's possible to free energy by breaking heavier elements in lighter ones, which is a fission reaction, or by merging together light elements, which is a fusion reaction.

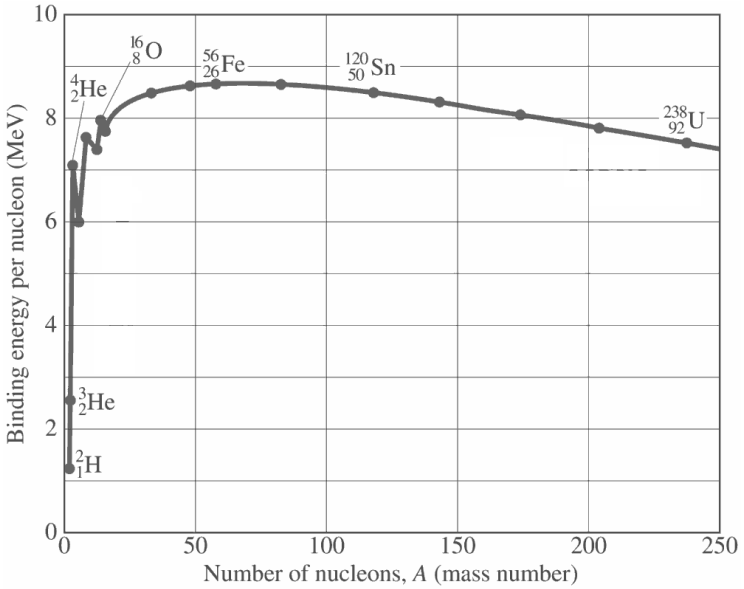

Figure 1.1: Binding energy per nucleon

Nuclear fission has been used for quite a long time now as a source of thermal energy for electricity production, exploiting the process of breaking heavy uranium-235 nuclei by absorption of a slow-moving neutron. However, nuclear fission technology has some unsolved issues that make it less attractive; nuclear fusion could overcome some of these problems, but fusion reactors are still at an experimental stage and may be commercially available only in several decades. We can compare the two approaches in terms of the major issues concerning nuclear energy safety and sustainability. In the following, when talking about nuclear fusion, we refer to the magnetic fusion approach, that tries to keep a gas of hydrogen isotopes hot and dense enough to favor fusion reactions by confining it with intense magnetic fields; inertial confinement will not be considered in this work.

- Fission reactors contain the amount of fuel needed for several days of operation. If control on the reaction is lost, there is enough energy to produce an explosion, and even when the reaction is stopped, thermal power production will not stop immediately, but will exponentially decrease instead because of a process called *decay heat*. This means that cooling systems must be operational even after an emergency stop. On the other hand, fusion reactors would contain reagents in the form of very rarefied gases, and the conditions where the reaction may occur are so difficult to obtain that if control on the reaction is lost there would be immediately no net power output.

- Some fission products are unstable elements with a very long half-life, ranging up to the scale of million years. It is almost impossible to assure that radioactive waste will remain isolated from the environment for the time needed to make long-lived fission products unharmful to the biosphere, since the time scale to deal with is several degrees of magnitude the time scale of human life. On the other hand, fusion reactions would produce no long-lived radioactive products, although the inner layer of the reactor may be activated by neutron bombardment. First wall materials must be accurately chosen to minimize activation.

- Uranium is a finite resource, although its availability depends on the price one is willing to spend to extract it, and breeder reactors can use uranium-238 that is much more common in nature than uranium-235. Considering this, there could be enough resources for a very long time from now, so availability is not a major issue. Fusion uses deuterium, which can be found in parts of $1/10000$ in sea water, and tritium, that can be obtained as a short-lived fission product of lithium. Again, lithium is a finite resource but its availability does not seem to pose a problem. Moreover, at a second stage, when fusion technology will be mature, one can expect to sustain a deuterium-deuterium reaction, that does not require tritium.

- A very critical aspect that has an impact on international balances is the risk of nuclear proliferation. Nuclear fission fuel mostly consists in enriched uranium, that is uranium with a higher percentage of uranium-235 with respect to the natural ratio between uranium-235 and uranium-238, (around 0.72%). To produce nuclear fuel for common fission reactors, the ratio must be increased to $3\% - 5\%$, but if high-enrichment levels are reached ($> 20\%$), it could be used to build atomic weapons. The enrichment ratio to produce an atomic bomb is commonly around 80%. Conversely, magnetic fusion does not rely on processes that could be directly exploited to produce weapons.

1.2 The Lawson criterion

As mentioned before, fusion research studies the conditions where hydrogen isotopes fusion reactions may occur. The deuterium-tritium reaction is particularly of interest:

$$ {}^2_1H + {}^3_1H \rightarrow {}^4_2He + n + (W_{DT}), \qquad W_{DT} = 17.58MeV. $$

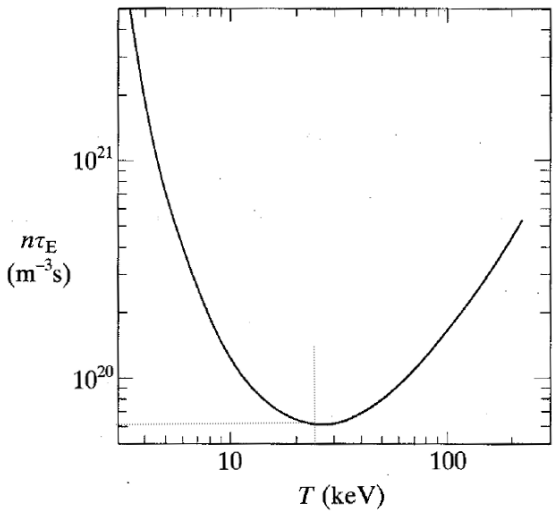

Figure 1.2: The Lawson criterion

The reaction is clearly exergonic, but when evaluating the power balance of a prospective fusion reactor, one must consider the power balance of macroscopic energy exchanges, and seek for the working point where power input to the reactor equals power output. The most common formulation of power balance equations for a fusion reactor comes from the Lawson criterion. Power input consists of a term, P_{ext}, representing power from external sources and P_N, representing nuclear power. The latter depends on the deuterium-tritium reaction cross-section and on temperature, that translates in kinetic speed of the reagents. This dependence can be expressed by the term $\langle \sigma v \rangle$:

$$P_{in} = P_N + P_{ext}, \qquad P_N = \frac{n^2}{4} \langle \sigma v \rangle W_{DT}.$$

In the hypothesis of the Lawson criterion, all the nuclear power is also output to the system, assuming that reagents that have incurred in a fusion reaction could not be confined. Power output is then composed of transport power, P_T, that depends on the energy confinement time τ_E, and of bremsstrahlung power P_B, that is due to the irradiation generated by continuous accelerations of charged particles:

$$P_{out} = P_N + P_T + P_B, \qquad P_T = \frac{3nkT}{\tau_E}, \qquad P_B = bn^2\sqrt{T}.$$

The Lawson criterion then assumes that $P_{ext} = \eta P_{out}$, where η is the efficiency of energy conversions. This defines the conditions where reactor temperature can be maintained, without providing power to external appliances. The power balance equation can

be solved with respect to the term $n\tau_E$, leading to

$$n\tau_E = \frac{3kT}{\frac{1}{4}\left(\frac{\eta}{1-\eta}\right)\langle\sigma v\rangle W_{DT} - b\sqrt{T}}.$$

This relation is graphed in figure 1.2 as a function of temperature. Since it is extremely critical to obtain high values for the product $n\tau_E$, an optimal working point for T is found where the function reaches its minimum value; other considerations lead to the individual target values for n and τ_E:

$$T \approx 20keV, \quad n \approx 10^{20}m^{-3}, \quad \tau_E \approx 1s.$$

We should now focus on the physical properties of the reagents, initially a rarefied gas of deuterium and tritium, when approaching these extreme conditions.

1.3 Plasma, the fourth state of matter

As seen in the previous section, it is necessary to heat a gas of hydrogen isotopes to an extremely high temperature, and to keep it confined long enough to reach the conditions specified by the Lawson criterion. In these conditions, the gas is fully ionized, this means that electrons and ions are not bound to each other but are free to move almost independently. An ionized gas can be called a plasma in the sense of fusion physics when its charged particles are not affected by the electric field generated by spatial charge separation between electrons and ions. This concept can be formalized defining the Debye length, λ_D, as a limit for charge separation. Calling n the number density of ions/electrons in the volume, T the temperature, and being k the Boltzmann constant and e the electron charge, we have:

$$\lambda_D = \sqrt{\frac{kT\varepsilon_0}{ne^2}}.$$

Plasma is then a fully ionized gas where particles are shielded from fields due to charge separation. There must then be a large enough number of particles in a Debye sphere, that is a sphere of radius λ_D. One must have that

$$n\frac{4}{3}\pi\lambda_D^3 \gg 1.$$

Another common assumption is that $\lambda_D \ll L$, where L is a measure of the scale of the system considered. Plasma has two important properties that make it very different from a non ionized gas, and these properties are so unique that sometimes plasma is

referred to as the fourth state of matter. Being composed by charged particles, it is a good electricity conductor, and its dynamics are influenced by external electric and magnetic fields; in the same way, current flowing through a plasma can generate its own magnetic field. Secondly, the Debye length limit on charge separation implies that plasma particles show a collective behavior. Plasma modelling should then reflect in an accurate way these properties. Different approaches are possible:

- One can study the dynamics of the single particles composing a plasma as if they were influenced only by the effect of external fields, neglecting interaction with other particles, but this approach would not lead to a self-consistent model.

- The previous approach can be reformulated conforming to the kinetic theory of gases, by considering the dynamics of electrons or of ions as a whole, and considering quantities such as particle density and flow instead of single particle mass and speed. Interaction between electrons and ions is then taken into account with an impact term in the force balance. This leads to a more accurate model, but it's not totally self-consistent yet, because the external fields effect on particle dynamics is taken into account, but the reciprocal effect of particle motion on the existing fields is not modelled.

- Magnetohydrodynamics (MHD) leads to a simpler yet self-consistent model. The existence of different species (electrons and ions) is neglected, and plasma is treated as a single conducting fluid. Maxwell equations give reason of the interaction with external fields, and Navier-Stokes equation models fluid dynamics.

1.4 MHD Equations

In fusion engineering, MHD is the approach of interest for plasma modelling, because equilibrium and stabilization aspects require self-consistency. Simpler models rely on ideal MHD, in which plasma is modelled as ideally conductive. However, for the sake of generality, resistive MHD equations are reported, where a conductivity coefficient σ is defined. It is also assumed that no net charge unbalance is possible inside the plasma: this approximation is acceptable when the conditions on λ_D are satisfied. The quantities involved are the electric field $\mathbf{E}$; magnetic field $\mathbf{B}$; current density $\mathbf{J}$; fluid velocity $\mathbf{v}$; pressure p; mass density ρ. $\mathbf{E}_i$ is the impressed field, a term defined to model external

forces per unit charge. The resulting equations are:

$$\nabla \times \mathbf{E} = -\frac{\partial \mathbf{B}}{\partial t} \quad (1.1)$$

$$\nabla \times \mathbf{B} = \mu_0 \mathbf{J} \quad (1.2)$$

$$\nabla \cdot \mathbf{E} = 0 \quad (1.3)$$

$$\nabla \cdot \mathbf{B} = 0 \quad (1.4)$$

$$\mathbf{J} = \sigma(\mathbf{E} + \mathbf{v} \times \mathbf{B} + \mathbf{E}_i) \quad (1.5)$$

$$\rho(\frac{\partial \mathbf{v}}{\partial t} + \mathbf{v} \cdot \nabla \mathbf{v}) = \mathbf{J} \times \mathbf{B} - \nabla p \quad (1.6)$$

1.5 The Tokamak and RFP configurations

Nowadays, experimental devices built to develop knowledge on magnetic fusion physics and engineering are toroidal geometry machines: deuterium and tritium are injected into a doughnut-shaped vacuum chamber, and plasma conditions are created inside this chamber. The first experiments on magnetic confinement were carried out on linear geometry discharge tubes. The principle that leads to close the geometry in a torus is to allow a current J_ϕ to flow in the plasma, and to avoid losing the charged particles at the edges of the configuration. In toroidal geometry it is common to refer to the set of cylindrical coordinates (R, ϕ, Z), the Z axis corresponding to the axis of symmetry of the torus. However, for some considerations it is useful to refer to another set of coordinates, (θ, r, ϕ) (fig. 1.3).

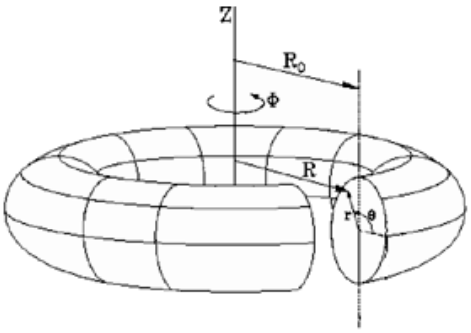

Figure 1.3: Toroidal and cylindrical coordinates

Studying plasma equilibrium means to produce equations that take configuration geometry into account and that are verified when velocity and $\frac{\partial \cdot}{\partial t}$ terms are equal to zero.

The momentum balance equation (eq. 1.6) becomes:

$$\mathbf{J} \times \mathbf{B} = \nabla p. \tag{1.7}$$

Assuming that current is mostly flowing in the $\hat{i}_\phi$ toroidal direction (J_ϕ), confinement is possible when there is a component of $\mathbf{B}$ in the $\hat{i}_\theta$ direction (B_θ), generating pressure gradient in the $\hat{i}_r$ direction ($\partial p/\partial r$). However, the Tokamak configuration is characterized by a prevalence of the B_ϕ component over the B_θ component, to obtain a stable configuration. In this respect, the safety factor $q(r)$ is defined as

$$q(r) = \frac{r}{R}\frac{B_\phi(r)}{B_\theta(r)}.$$

This parameter defines a property of magnetic field lines: it is equal to the number of turns in the toroidal direction corresponding to a complete turn in the poloidal direction. Charged particles tend to orbit around magnetic field lines, and a consequence of ideal MHD (Alfvén theorem) states that plasma flows conserving magnetic flux locally. It is then possible that plasma assumes a helical configuration when magnetic field lines close in a toroidal turn. There could be a perturbation in plasma displacement, $\bar{\xi}$, that is resonant with the configuration of magnetic field lines. This happens whenever

$$\bar{\xi} = \bar{\xi}_0 cos(m\theta - n\phi), \qquad \frac{m}{n} = q(r). \tag{1.8}$$

It could be shown that such a perturbation would lead to an instability, destroying the toroidal equilibrium configuration. If the B_ϕ component is not null, then all perturbations characterized by $m = 0$ will be stabilized, because the condition of resonance (eq. 1.8) between plasma displacement and magnetic field lines can never be verified. Sometimes these instabilities are referred to as *sausage* instabilities, because they consist in a deformation of plasma shape that is a function of the ϕ coordinate only. However, one also commonly wants to stabilize *kink* instabilities, that are also dependent from θ. The minimal requirements to have a macroscopically stable Tokamak configuration are defined by the following conditions [2], that impose to stabilize all internal kink instabilities with $m = 1$ (Kruskal-Shafranov limit) and all those with $m \leq 3$ through the limit of the first wall (r_a):

$$\begin{aligned} q(0) &\geq 1 \\ q(r_a) &\geq 3 \end{aligned}$$

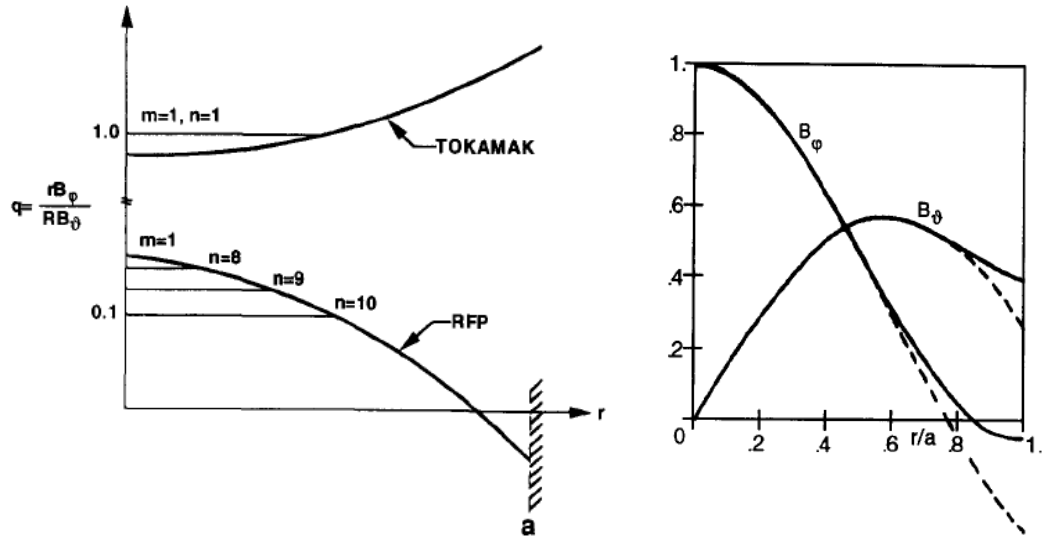

(a) Safety factor profiles in Tokamak and RFP (b) Magnetic field profile in RFP

Figure 1.4: Radial profiles for equilibrium configurations

These conditions have a consequence on the ratio between B_ϕ and B_θ at the first wall limit: in fact, the following relation should be verified:

$$B_\phi(r_a) \geq 3\frac{R}{r_a}B_\theta(r_a). \tag{1.9}$$

The Tokamak configuration is then characterized by a prevalence of the B_ϕ component over the B_θ component, to provide stability to the configuration. Instead, the RFP configuration obtains plasma stability with an alternative approach [3]. As mentioned before, the safety factor $q(r)$ shows whether there are resonant field surfaces at a given radius. It is important that $q(r)$ always has a non null derivative: in fact, if $q(r)$ is rational for a given r, a resonant surface exists and an instability could grow from it. However, if $q(r)$ varies, there will not be a resonant surface at a higher radius, and the instability is stopped. This property is called *shear*. In the RFP configuration, shear is obtained with a monotonically decreasing profile for $B_\phi(r)$, that changes sign when approaching the edge of the configuration (fig. 1.4).

The British physicist J. B. Taylor [4] has shown that both Tokamak and RFP configurations are states of minimal plasma energy with the constraint of magnetic helicity conservation. Thus the RFP configuration naturally obtains the reversal of the B_ϕ component, without forcing it with the external coils. The F and Θ parameters are used to

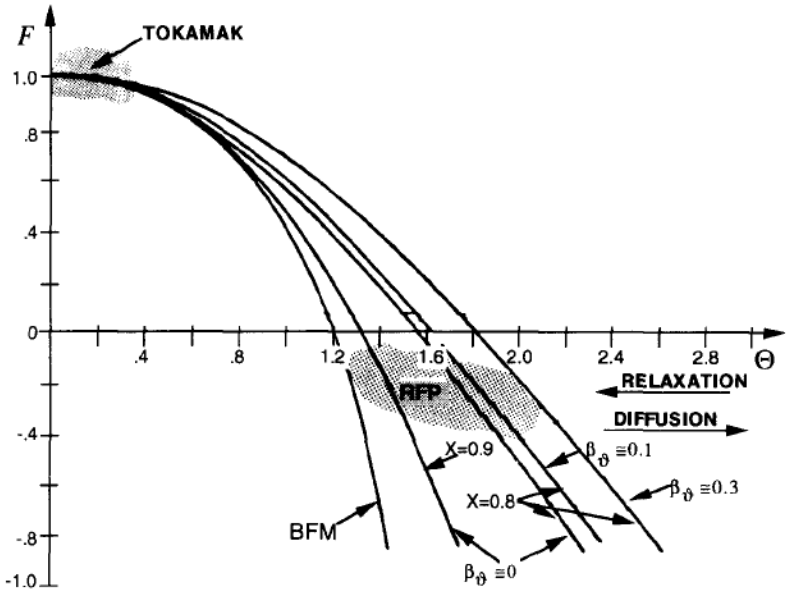

Figure 1.5: F-Θ graph: Taylor equilibrium states

graph Taylor states, and are defined as follows:

$$F = \frac{B_\phi(r_a)}{\langle B_\phi \rangle}, \qquad \Theta = \frac{B_\theta(r_a)}{\langle B_\phi \rangle}$$

The $\langle\ \rangle$ brackets indicate average values. With these definitions, the F-Θ graph (fig. 1.5) represents the possible equilibrium configurations in helicity conservation, and shows the typical evolution of a RFP discharge, that starts as a Tokamak discharge and then evolves with growing values of Θ over time.

Chapter 2

The RFX-mod experiment

2.1 Specifications and structure

RFX-mod is an experimental device built to study RFP operation at high plasma current (up to $2MA$). In table 2.1 are reported the main specifications of the machine. The plasma is formed in a toroidal vacuum chamber internally covered with graphite tiles. The vacuum vessel is closely surrounded by a thin copper shell, meant to stabilize fast-growing unstable MHD modes. These structures are important when developing an axisymmetric model of the machine, and will be now analyzed in more detail; a sectional view of the main layers composing the machine is presented in figure 2.1.

Major radius (structure)	$2\ m$			
Major radius (vessel)	$1.995\ m$			
Max. inductive energy	$72.5\ MJ$			
Max. toroidal field	$0.6\ T$			
Max. plasma current	$2\ MA$	(RFP)	$200\ kA$	(Tok.)
Current rise time	$15 - 50\ ms$	(RFP)	$200\ ms$	(Tok.)
Flat-top time	$250\ ms$	(RFP)	$\sim 1\ s$	(Tok.)
Discharge time	$350\ ms$	(RFP)	$\sim 1.2\ s$	(Tok.)

Table 2.1: RFX-mod specifications

Graphite first-wall The first layer facing the plasma consists in 2016 trapezoidal graphite tiles. Graphite (carbon) as first-wall material was chosen for the properties of low activation, good resistance to high energy fluxes, and low mass number: in fact, when sputtering of first wall material occurs, some atoms of first wall material contaminate the

plasma, and high mass number elements would cause high energy losses for irradiation. The first-wall layer is only $16\ mm$ thick, to keep the plasma edge as near as possible to the stabilizing shell.

Vacuum vessel The material chosen for the vacuum vessel is INCONEL 625, a special paramagnetic type of steel. The vessel comprises 72 wedge-shaped elements, each of which consists of a sandwich structure, with a $2\ mm$ thick inner wall and a $1\ mm$ thick outer wall connected by a $0.5\ mm$ corrugated sheet and two poloidal stiffening end rings, providing the necessary resistance to support the ultra high vacuum regime.

Thin copper shell Before the machine modifications that were carried out in years 2000-2003 [5], RFX was equipped with a $65\ mm$ thick aluminium shell with a time constant of $450ms$, that was meant to stabilize MHD modes on a time scale comparable with the duration of the discharge. The machine has then been modified to include a flexible active control system made up by 192 saddle coils that can be controlled independently and that can react on the time scale of $50ms$: this is the characteristic time for magnetic field penetration of the thin copper shell, that has the purpose of stabilizing fast-growing MHD modes with time constants lower than $50ms$. The shell is characterized by the presence of an equatorial gap and a poloidal gap, that allow transformer action from external fields to induce loop voltage on the plasma. The presence of the poloidal gap imposes that the total toroidal current flowing in the shell must be zero; this fact will be accurately taken into account when developing mathematical models of the device.

Supporting structure The supporting structure is made of AISI 304 stainless steel, and it sustains the vessel, shell, saddle coils and toroidal field coils. Like the shell, it presents

Graphite first-wall	$0.459\ m$
Vessel, inner face	$0.475\ m$
Vessel, outer face	$0.505\ m$
Shell, inner face	$0.5115\ m$
Shell, outer face	$0.5145\ m$
Structure, inner face	$0.553\ m$
Structure, outer face	$0.600\ m$

Table 2.2: Radius of assembly layers

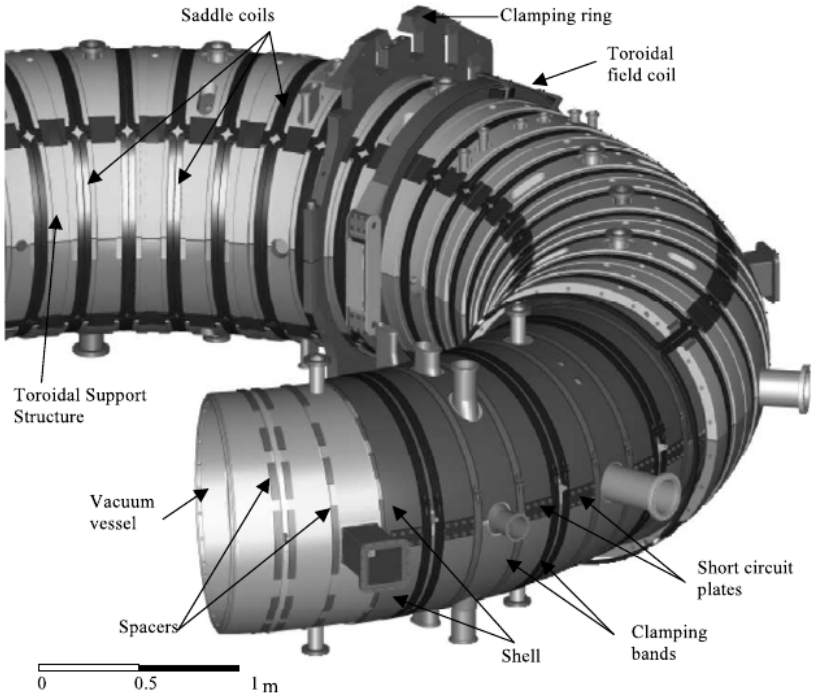

Figure 2.1: Sectional view of RFX-mod toroidal assembly

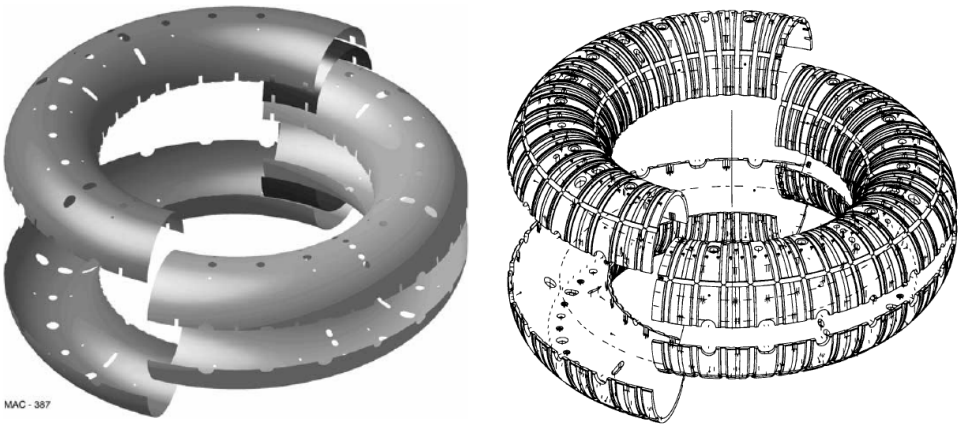

Figure 2.2: RFX-mod shell and structure, exploded view

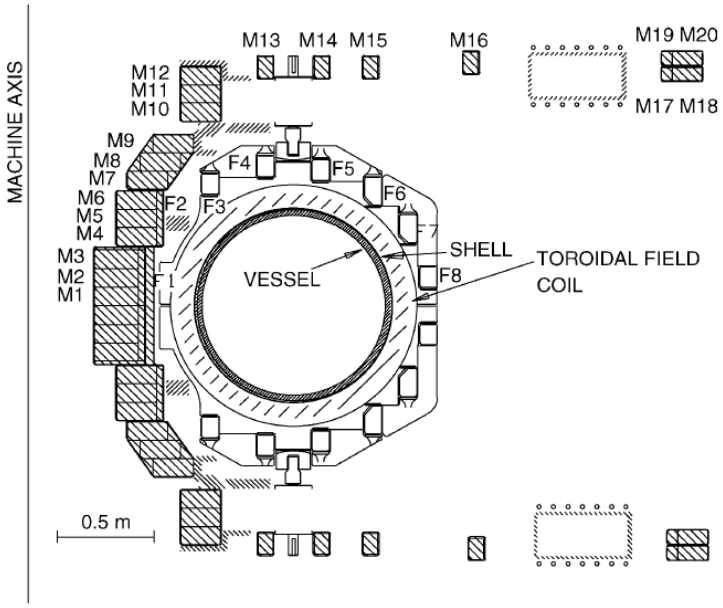

Figure 2.3: RFX-mod section

toroidal and poloidal gaps, but the inner toroidal gap is short-circuited. Exploded views of the shell and structure are reported in figure 2.2, while table 2.2 lists the radius of the various layers of the toroidal assembly.

2.2 RFX-mod diagnostics

Many diagnostics operate on the experiment: density and temperature probes, but also x-ray tomography, interferometry and Thomson scattering diagnostics, to mention some. A top view of RFX-mod with the position of the main diagnostics is reported in figure 2.5. However, the real time control system for plasma position control is based uniquely on magnetic diagnostics, so only these will be considered in the rest of this work.

Magnetic probe arrays RFX-mod is equipped with several probe arrays that provide measurements of magnetic field, loop voltage, and magnetic flux. Together, these probes form the magnetic diagnostic system. We will consider inner magnetic probe arrays, that are positioned on the outer face of the vessel. Other magnetic probe arrays are present at outer surfaces, but inner probes are less influenced from the effect of passive structures

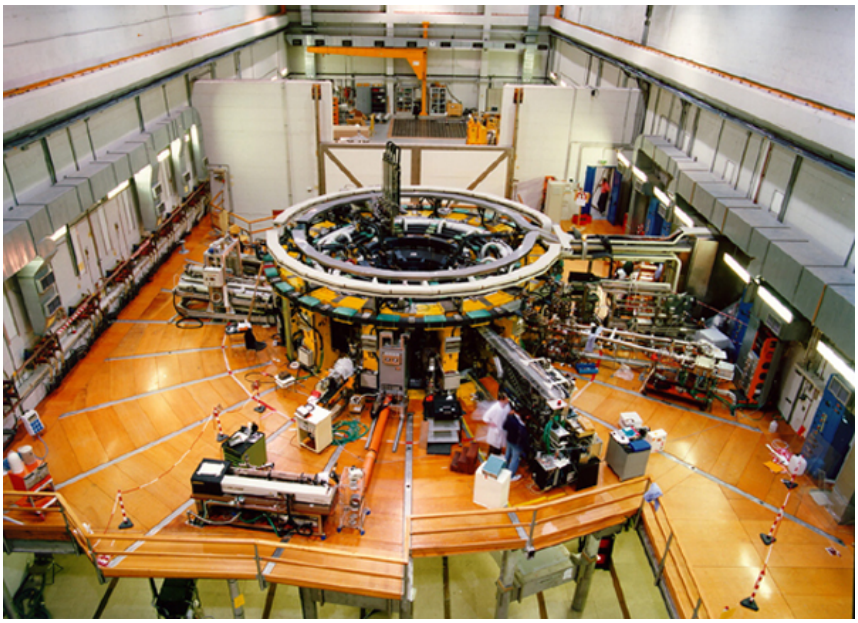

Figure 2.4: Machine room of RFX-mod

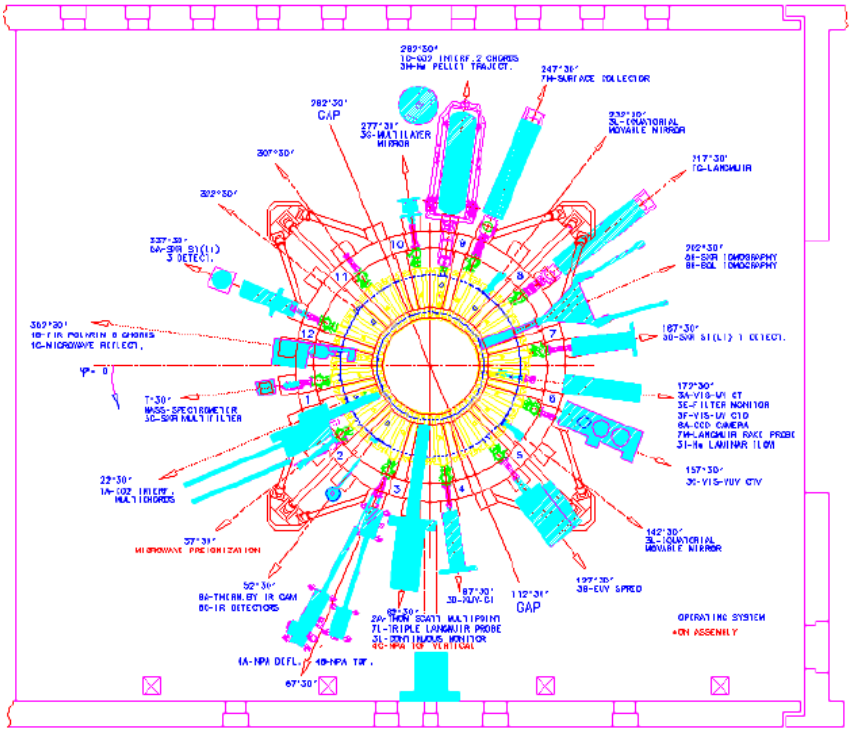

Figure 2.5: Top view of RFX-mod main diagnostics

and provide the most informative measurements to diagnose plasma characteristics. Table 2.3 lists the magnetic probes of interest and their position around the torus.

Sensor / position	$r\ [m]$	$\theta\ [^\circ]$	Pol. #	$\phi\ [^\circ]$	Tor. #
Pol. and tor. B field	0.508	$72 + k \cdot 90$	4	$l \cdot 7.5$	48
Pol. and tor. B field (dense array)	0.508	$27 + k \cdot 45$	8	$30,\ 142.5,$ $210,\ 322.5$	4
Radial B field	0.507	$0 + k \cdot 90$	4	$l \cdot 7.5$	48
Tor. loop voltage	0.507	$22.5 + k \cdot 45$	8	-	1
Poloidal flux ψ	0.507	$22.5 + k \cdot 45$	8	-	1

Table 2.3: RFX-mod inner magnetic probes ($k, l \in \mathbb{Z}$)

2.3 RFX-mod magnetic field coils

Poloidal field circuit The poloidal field coil system is composed by a magnetizing circuit (M coils) that is used to provide transformer action on the plasma and induce plasma current without generating field in the plasma region, and a field shaping circuit (F coils) that is used to control plasma shape and does not provide transformer action. The position of these coils is visible in a section of the machine (fig. 2.3). Since the system is perfectly top-down symmetric, no net horizontal field can be generated on the equatorial plane of the machine. The magnetizing circuit is coupled with the field shaping circuit because of the particular circuit layout [6], visible in figure 2.6. In the rest of this work, M coils will be referred to with the number of the the S sector they belong in the poloidal circuit. In fact, in RFX-mod the M coils are actually numbered as in fig. 2.3, and are interconnected in series interleaving them to maximize inductive balance (table 2.4).

S sector	M coils in series				
1	1	5	9	14	17
2	2	6	10	15	19
3	3	7	11	16	18
4	4	8	12	13	20

Table 2.4: RFX-mod PF circuit sectors with M coils interconnection

In RFP operation, typically the M coils are pre-charged to the maximum (positive) current value using the PMAT converter ($1350\ V/50\ kA$). In this phase PMSS is open and PT is closed; then the discharge is started by closing PMSS and opening PT: the current in the M coils will decrease with the time constant of the resulting LR circuit, providing transformer action on the plasma; PCAT converters ($1350\ V/12.5\ kA$) are used to control the current decay rate, while F coil current is controlled by PVAT converters ($1350\ V/6.25\ kA$). Machine operation in a Tokamak discharge is quite different, and will be summarized in the next paragraph. It is important to point out that all the power supply units connected to the poloidal circuit can operate only in one quadrant (positive voltage, positive current).

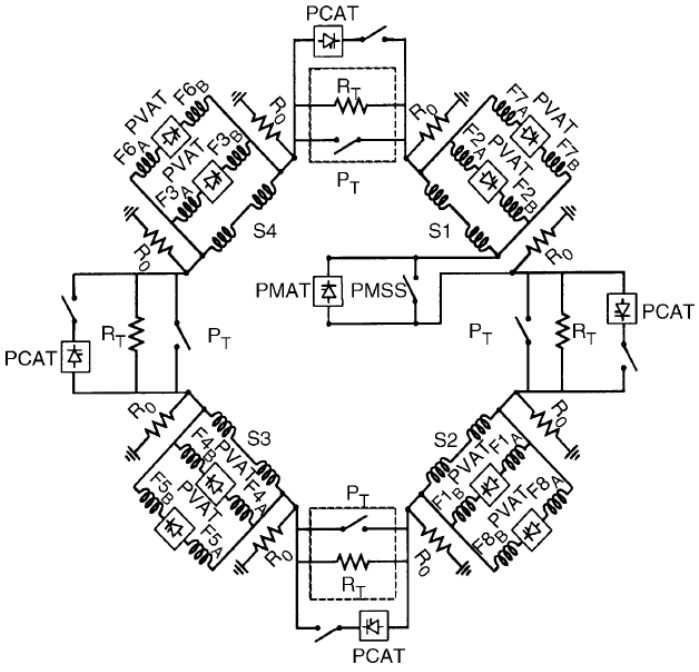

Figure 2.6: RFX poloidal field circuit

RFX-mod as a Tokamak RFX-mod is a very flexible machine, that can operate also in Tokamak configuration since the $F - \Theta$ diagram (fig. 1.5) suggests that a RFP discharge starts as a Tokamak discharge. As mentioned before, in Tokamak operation the poloidal field circuit follows a different sequence to initiate the discharge. It is not necessary to pre-charge the M coils, since the machine will operate at much lower plasma current ($\sim 100\ kA$ for the Tokamak, $2\ MA$ max. for RFP); transformer action is provided by gen-

erating a growing (negative in sign) current in the M coils with the PCAT converters. The limit on plasma current in Tokamak configuration descends from the fact that B_θ should be limited to comply with eq. (1.9). The prevalence of the B_ϕ component over the B_θ component also has a consequence on the magnetic diagnostic system, since B_θ pickup coils will be affected by a relevant offset due to spurious pickup of the B_ϕ component because of small angular errors in pickup coil positioning. These errors will have to be accurately taken into account in the following.

Regarding F coils, in double-null Tokamak configuration $F3$ and $F8$ must carry a positive current to produce null points and to horizontally elongate the plasma, resulting in a highly triangular shape. All the other F coils carry negative current. To obtain this configuration, PVATs feeding $F3$ and $F8$ must be physically inverted before the discharge. Sign constraints of the converters must be accurately taken into account when designing the shape controller, that ultimately regulates voltage applied to the F coils.

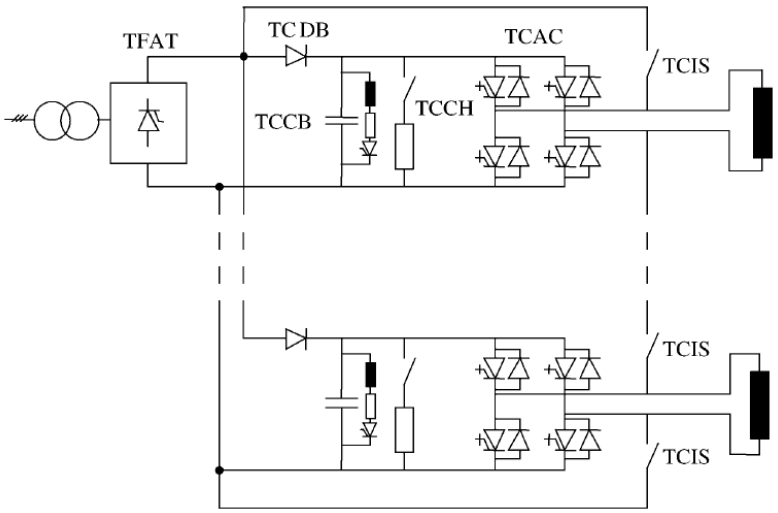

Figure 2.7: RFX toroidal field circuit

Toroidal field circuit Toroidal field coils are used to provide stability to the plasma in the first phase of a RFP pulse and are critical in Tokamak discharges, since as seen in section 1.5 the toroidal field must be prevalent over the poloidal field. The toroidal circuit is composed of two identical groups, each feeding 6 of the 12 toroidal winding sectors [7]. The electric scheme of the circuit feeding one of the groups is reported in figure 2.7. The circuit is composed of ac/dc converters (TFAT - $3\ kV/16\ kA$), blocking diodes (TCDB - $4\ kV/5.5\ kA$), capacitor banks (TCCB - $4\ kV/16\ mF$), chopper groups (TCCH

- 3 $kV/4.6\ kA$), inverters (TCAC - 3 $kV/6\ kA$) and static breakers (TCIS - 4 $kV/16\ kA$, 128 MA^2s). The circuit is designed to allow field reversal during RFP discharges, and a maximum toroidal field of $0.67\ T$ can be produced. In Tokamak discharges, the toroidal field is ideally constant over time so this circuit does not require dynamic modelling for the purpose of this work.

Saddle coils The 48×4 saddle coils (SC) for active MHD control (figure 2.8) are independently fed by 192 AC/DC switching converters ($400\ A/650\ V$) that are not bound to sign constraints that affect the poloidal field circuit converters, and have very quick dynamics: they can produce $40\ mT$ DC field and $1\ mT$ at $100\ Hz$. In RFP discharges, saddle coils are operated out of axisymmetry, aiming at controlling specific $m \neq 0$ MHD modes. In axisymmetry, the SC are important because they can provide a horizontal field component on the equatorial plane that other coils cannot provide because of top/down symmetry. These will be introduced in the model (sect. 5.4) to stabilize plasma position in double null Tokamak configuration.

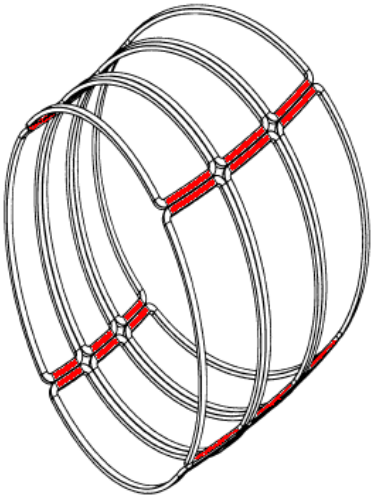

Figure 2.8: A subset of 12 saddle coils
In red, the conductors that will be included in the axisymmetric model

Chapter 3

The nonlinear model and simulator

3.1 The Grad-Shafranov equation

A common assumption in order to carry out calculations in toroidal geometry is axisymmetry: physical quantities of interest are assumed to be invariant with respect to the toroidal angle ϕ. This assumption is well verified in the Tokamak configuration because its ideal equilibrium does not show a dependence of plasma displacement and shape on the toroidal angle. Under the hypothesis of axisymmetry, the plasma equilibrium problem can be reformulated on the 2D space of a section of the torus located at an arbitrary angle ϕ, thus simplifying the original 3D equilibrium problem. The possibility to model non-axisymmetric instabilities ($n > 0$) is lost, but in Tokamak configuration this is acceptable if one assumes to have high enough values for $q(r)$, so that these instabilities would be characterized by a high poloidal number m, and their impact would be less important. It is still possible to analyze plasma displacement stability in terms of the position of its axis on the poloidal plane, and it is possible to study the shape of the plasma section as well.

Under these assumptions, **B** and **J** can be expressed in terms of two scalar functions, namely, the poloidal flux function $\psi(R, Z)$ and the poloidal current function $f(R, Z)$. $\psi(R, Z)$ is the magnetic flux linked with the circumference obtained by revolving the point (R, Z) around the z axis. The Grad-Shafranov equation is usually expressed in terms of poloidal flux scaled by a factor 2π: $\tilde{\psi} = \psi/2\pi$ is the poloidal flux *per radian*. $f(R, Z)$ is the total current linked with the same circumference, scaled by a factor $\mu_0/2\pi$.

The following relations can be derived from MHD equations [8]:

$$\begin{aligned}\mathbf{B} &= \frac{1}{R}\nabla\tilde{\psi}\times\hat{i}_\phi + \frac{f}{R}\hat{i}_\phi \\ \mathbf{J} &= \frac{1}{R}\nabla\left(\frac{f}{\mu_0}\right)\times\hat{i}_\phi - \frac{1}{\mu_0 R}\Delta^*\tilde{\psi}\,\hat{i}_\phi.\end{aligned}$$

In the previous equation, $\Delta^*\tilde{\psi}$ is the differential operator defined by

$$\Delta^*\tilde{\psi} = R\frac{\partial}{\partial R}\left(\frac{1}{R}\frac{\partial\tilde{\psi}}{\partial R}\right) + \frac{\partial^2\tilde{\psi}}{\partial Z^2}.$$

Substituting the expressions for $\mathbf{B}$ and $\mathbf{J}$ in the equilibrium momentum balance equation (1.7) , we have the Grad-Shafranov equation (GSE):

$$\Delta^*\tilde{\psi} = -f\frac{df}{d\tilde{\psi}} - \mu_0 R^2\frac{dp}{d\tilde{\psi}}. \tag{3.1}$$

3.2 The free boundary problem

The Grad-Shafranov equation is a nonlinear elliptic partial differential equation linking the poloidal flux function to pressure and toroidal current profiles in the plasma; it is usually convenient to refer to the normalized flux function $\bar{\psi}$, defined with respect to the flux value at the magnetic axis ψ_{ax} and at the plasma boundary, ψ_b:

$$\bar{\psi} = \frac{\psi_{ax} - \psi}{\psi_{ax} - \psi_b}.$$

The plasma boundary is the last closed magnetic flux surface inside the discharge chamber. There are two possibilities in a Tokamak: this surface could be tangent to the first wall, in which case the plasma is in a *limiter* configuration, or it could be a line that passes through a saddle point of the flux function, that is called an *x-point*, in which case the plasma is in a *diverted* configuration and the magnetic line that represents the plasma boundary is a *separatrix* (figure 3.1). The diverted configuration is important in a Tokamak because it allows better energy confinement time; the points were the separatrix intersects with the first wall are the points with the highest energy flux and thermal load, and their position can be accurately controlled by monitoring the position of the x-point. In the divertor region there is also the possibility to extract heavier ionized particles that would contaminate the plasma.

In an experimental context, the plasma boundary is a well-defined entity. However, we are now interested in how the GSE could be implemented in a simulator that provides

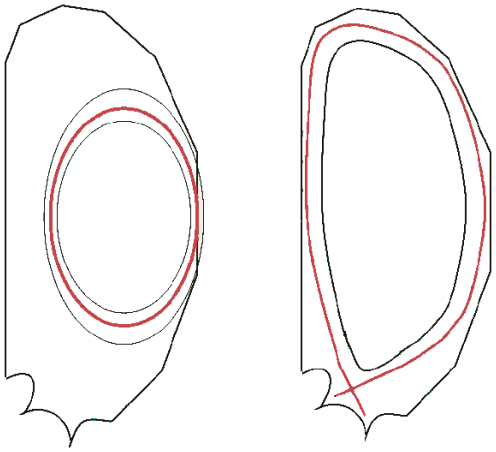

Figure 3.1: Limiter and diverted configuration for a generic Tokamak

detailed information on plasma equilibrium calculating the profile of the main physical quantities of interest and a map of the flux function on the poloidal cross section. Obviously, the location of the plasma boundary is part of the unknown; for this reason, the simulator must solve a *free boundary* problem.

3.3 Maxfea, a free boundary solver for the GSE

Maxfea is a free boundary GSE solver, written in FORTRAN77 in the early 1990s. It processes the following data:

- A parametrization for the toroidal plasma current density $J_\phi(\bar{\psi})$
- The position of the magnetic axis of the configuration
- The current flowing in the external poloidal field coils
- The total plasma current
- Geometric design of the machine section over a 2D mesh of first-order elements (triangles)
- Magnetic and electric properties of the materials composing the machine

The toroidal plasma current density profile depends on two parameters - α and β - and has the following form, where R_{ax} is the horizontal position of the magnetic axis:

$$J_\phi(\bar{\psi}) = \lambda \left[\frac{R}{R_{ax}}\beta + \frac{R_{ax}}{R}(1-\beta) \right] (1-\bar{\psi}^\alpha)$$

The parameters α and β are chosen consistently with expected experimental conditions, as will be shown in the following. The parameter λ is used to impose the value of the total plasma current. The profile adopted for $J_\phi(\bar{\psi})$ is consistent with the GSE (eq. 3.1) and with the chosen parametrization for the f and p functions [9]:

$$\begin{aligned} p(\bar{\psi}) &= p_{ax}\left[-\frac{\alpha+1}{\alpha}\bar{\psi}+\frac{1}{\alpha}\bar{\psi}^{\alpha+1}+1\right] \\ f(\bar{\psi}) &= f_{ax}\sqrt{\left(1+\frac{1}{\alpha}\right)\left[\frac{\alpha}{\alpha+1}-\bar{\psi}+\frac{\bar{\psi}^{\alpha+1}}{\alpha+1}\right]}. \end{aligned}$$

Maxfea requires an additional degree of freedom so that currents in some of the poloidal field coils can be altered from the predetermined value, to converge to the required magnetic axis position. The code uses an iteration scheme based on the Picard algorithm to converge to a reconstruction of the flux map $\psi(R, Z)$ on the whole domain of the poloidal section.

After the program has converged to an initial plasma configuration, a time transient evolution can be performed to evaluate stability of the initial equilibrium or to simulate an experimental scenario. The time transient simulation can be performed imposing the current flowing in the control circuits, or the applied voltage. In the latter case, the program evolves the current in the poloidal field coils accordingly to self and mutual inductances and resistances, and to inductive coupling with the plasma and with passive structures. At every step of the simulation, the program computes the new magnetic axis of the configuration, and finds the location of the plasma boundary according to the resulting flux map. The user is prompted to choose whether the simulation should conserve the poloidal flux at the magnetic axis, or the plasma current. In plasma current conservation mode, the program can follow a predetermined evolution for plasma current values, consistent with experimental data. In flux conservation mode, it is relevant to point out that Maxfea does not account for dissipative phenomena in the plasma, so plasma current would grow at higher values than those achieved in experimental conditions with the same evolution for external coil currents. However, one can easily implement in the routine reserved for user-defined control an equation to simulate a decay in the poloidal flux over time due to plasma resistivity, so simulations can be made self-consistent in the case of resistive plasma. In flux conservation mode, the program applies the following law:

$$\psi_{ax}(t) = \psi_{ref}(t) = \psi_{ref}(0) \quad \forall t \geq 0;$$

however, the value $\psi_{ref}(t)$ is accessible, so the following law can be implemented[1] to produce the effect of a constant plasma resistance R_{pla}

$$\frac{\partial \psi_{ref}}{\partial t}(t) = -R_{pla} I_{pla}(t). \tag{3.2}$$

3.4 Validation against experimental data

As mentioned before, Maxfea can provide virtual measurements from sensors placed at user defined points. We can compare the data provided by virtual measurements with experimental measurements from RFX-mod when trying to emulate the experimental conditions on the simulator. The current in poloidal field coils is imposed to be the same as in the experiment, and plasma parameters will be tuned to achieve the best matching. In particular, we will consider the poloidal beta parameter β_θ

$$\beta_\theta = \frac{\langle p \rangle}{\frac{B_\theta^2(r_a)}{2\mu_0}}$$

and the normalized plasma inductance l_i

$$l_i = \frac{\displaystyle\int_0^{r_a} \left(\frac{B_\theta^2(r)}{2\mu_0} \right) 2\pi r dr}{\left(\frac{B_\theta^2(r_a)}{2\mu_0} \right) \pi r_a^2}.$$

Limiter (circular) Tokamak discharge We will consider the circular Tokamak discharge obtained in shot $\#29648$. In the simulations involving plasma with circular cross section, the parameters of current and pressure profiles in the simulator were set as follows

$$\alpha = 3, \quad \beta = 0.25$$

leading to the following plasma parameters:

$$l_i = 0.76, \quad \beta_\theta = 0.26.$$

The first evaluation that will be proposed concerns the validity of formula 3.2 to simulate the dynamics of resistive plasma. RFX plasma is characterized by high resistivity

[1] In Maxfea, this is achieved applying discrete variations on ψ_{ref} at every k-th simulation step Δt: $\psi_{ref}((k+1)\Delta t) = \psi_{ref}(k\Delta t) - R_{pla} I_{pla}(k\Delta t)$. ψ_{ax} and ψ_{ref} are stored in user-accessible variables as normalized values of flux per radian e.g. `psa`$= \psi_{ax}/2\pi$, `psaref`$= \psi_{ref}/2\pi$.

when compared to big tokamaks. We will be assuming an equivalent resistance for the plasma with value

$$R_{pla} = 12.9\ \mu\Omega.$$

This value has been obtained by considering the ratio between average loop voltage and plasma current in equilibrium regime. In figure 3.2 is reported the evolution of plasma current in the experimental case and the resulting plasma current with resistive plasma when operating the simulator in flux conservation mode, imposing the experimental values of active circuits current. The resulting model provides an acceptable approximation of resistive plasma, since the resulting values of plasma current are comparable with experimental values. However, in the following, we will consider the comparison with experimental data forcing the simulator to impose the experimental values of both active circuits current and plasma current. Eventually, the resistive model can be used to benchmark a controller that regulates transformer action to sustain plasma current. For the purposes of this work, we will consider the design of a controller that regulates plasma position and shape assuming that plasma current remains constant, thus assuming that the control loop for plasma current regulation is external and independent from the shape controller. The use of the resistive model can be seen as a possible extension of this work.

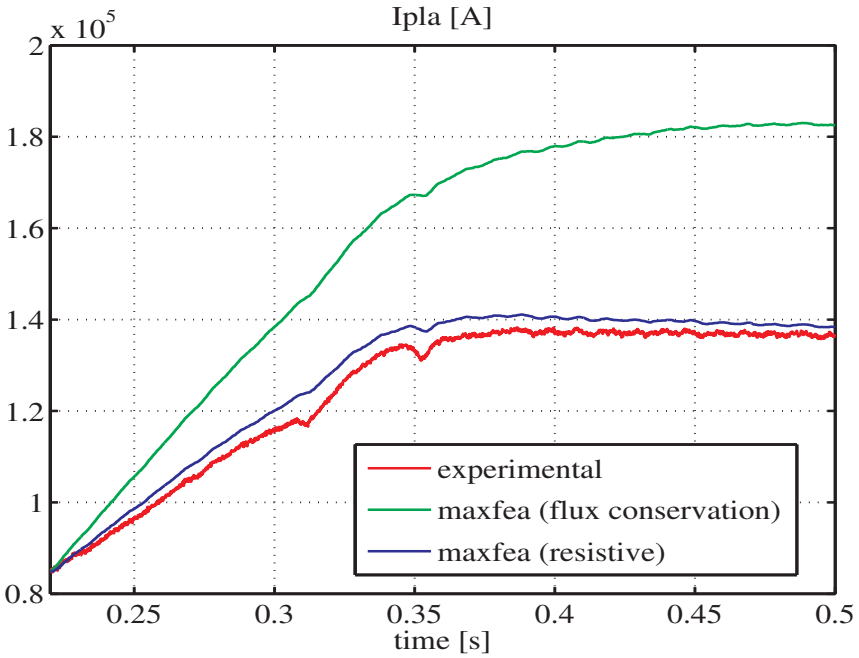

Figure 3.2: Shot #29648, plasma current

We will now consider the comparison of virtual measures provided by Maxfea with experimental measures. The choice of the parameters α, β used in simulation is critical: the vertical equilibrium field $B_{v,eq}$ required to counteract plasma radial expansion depends on the Λ parameter

$$\Lambda = \beta_\theta + \frac{l_i}{2} - 1 \tag{3.3}$$

and in the case of a circular plasma of major radius R_0 and minor radius r_a, it is expressed as follows [16]:

$$B_{v,eq} = -\frac{\mu_0 I_{pla}}{4\pi R_0}\left(ln\frac{8R_0}{r_a} + \Lambda - \frac{1}{2}\right).$$

If plasma parameters are not well matched to experimental values, the equilibrium field generated by F coils current, valid for the experimental conditions, will not match the equilibrium field required for the chosen parametrization. This would produce simulations affected by a horizontal displacement of the plasma column when imposing active circuits current. For this reason, comparison with experimental data shows overall good agreement but some discrepancies are to be addressed to plasma parametrization and plasma centroid displacement.

To check the correctness of these parameters, we can compare two estimates of Λ that can be obtained from magnetic measures. Actually, we have a measure of poloidal field $B_\theta(r, \theta_i)$ at $r = r_b$ and at 8 different angles, $\theta_i \in \Theta_b$. Calculating the terms of the harmonic expansion of $B_\theta(r, \theta)$ so that

$$B_{\theta,0}(r_b) = \frac{1}{8}\sum_{i=1}^{8} B_\theta(r_b, \theta_i), \quad B_{\theta,c}(r_b) = \frac{1}{4}\sum_{i=1}^{8} B_\theta(r_b, \theta_i)cos(\theta_i)$$

we can calculate the following value, that is an equivalent of Λ at the measurement radius:

$$\Lambda^* = \frac{B_{\theta,c}(r_b)}{B_{\theta,0}(r_b)}\frac{R_0}{r_b}.$$

The actual value of Λ at $r = r_a$ can be derived with the following correction, accounting for toroidal geometry:

$$\Lambda = 2\left(1 + \frac{r_a^2}{r_b^2}\right)^{-1}\left(\Lambda^* + \frac{1}{4}\left(1 - \frac{r_a^2}{r_b^2}\right) - \frac{1}{2}ln\frac{r_b}{r_a}\right).$$

In RFX, however, it is important to take into account the effect of eddy currents in the vacuum vessel, that would make a difference in the resulting field at the inner graphite radius. Actually, the experimental routine for plasma parameters estimations (sect. 4.1) has been used to produce figure 3.3, where the resulting estimates of Λ in Maxfea and in

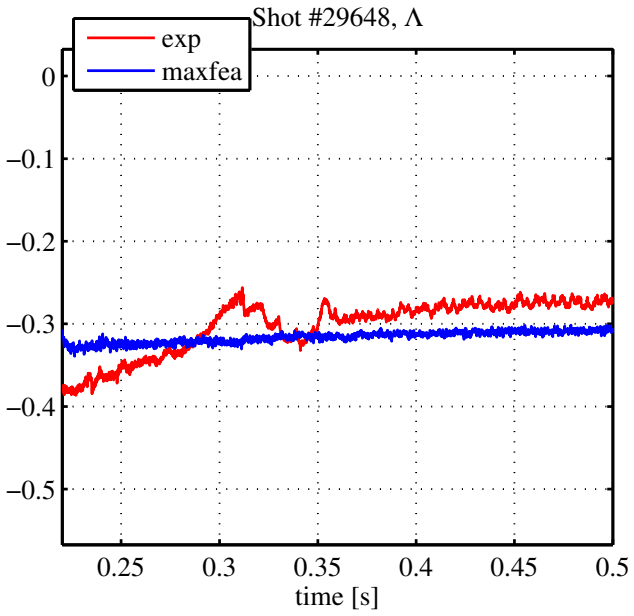

Figure 3.3: Shot #29648, Λ estimates from magnetic data

experimental conditions are compared, showing an overall good agreement on average values.

In figure 3.4 are reported the measures of poloidal field and of flux difference with respect to the flux loop probe at $\theta = -112.5°$. These measures are available with higher precision in the experiment than the absolute value of the poloidal flux, and will be used in radial expansion methods to reconstruct some estimates of plasma-first wall distances (gaps).

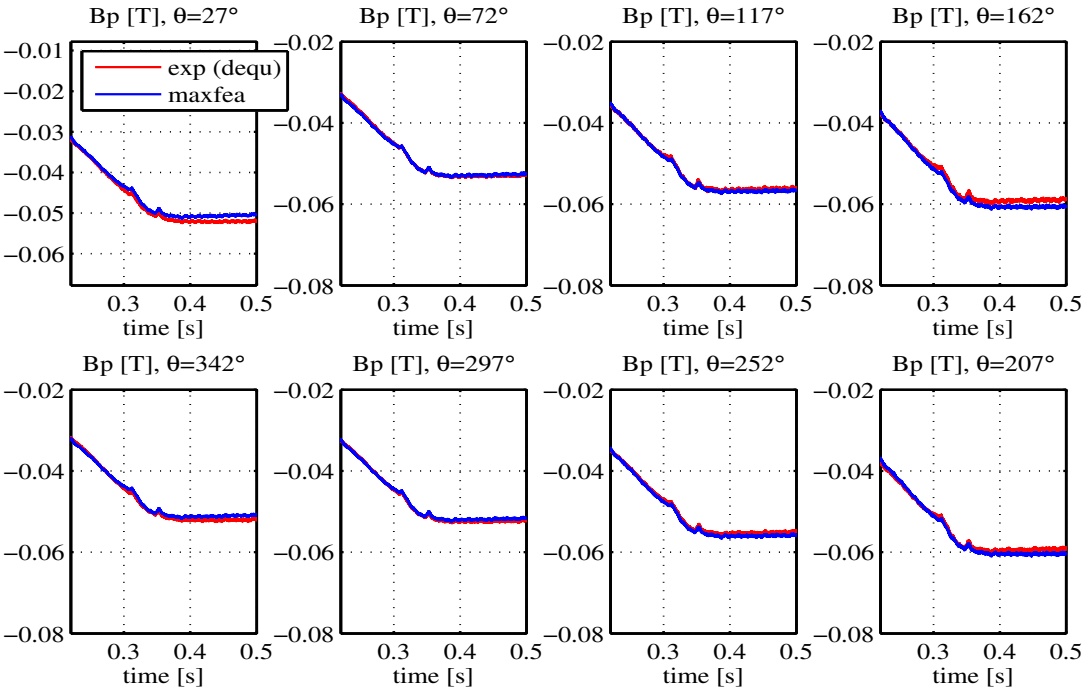

(a) Poloidal field

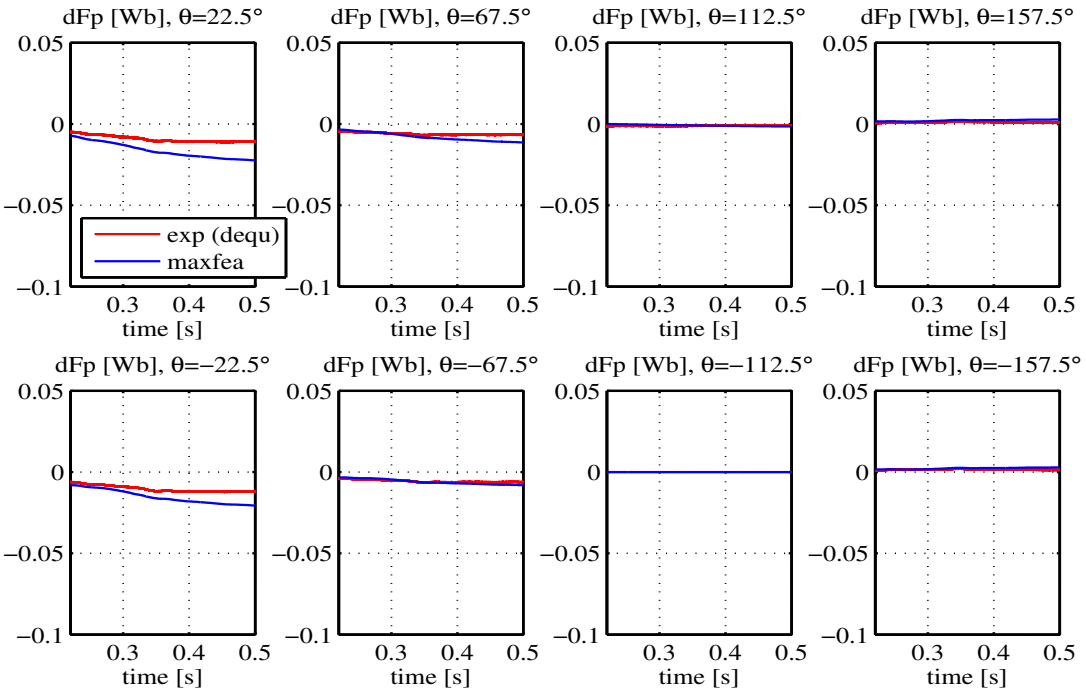

(b) Flux differences

Figure 3.4: Shot #29648, experimental and simulated magnetic data

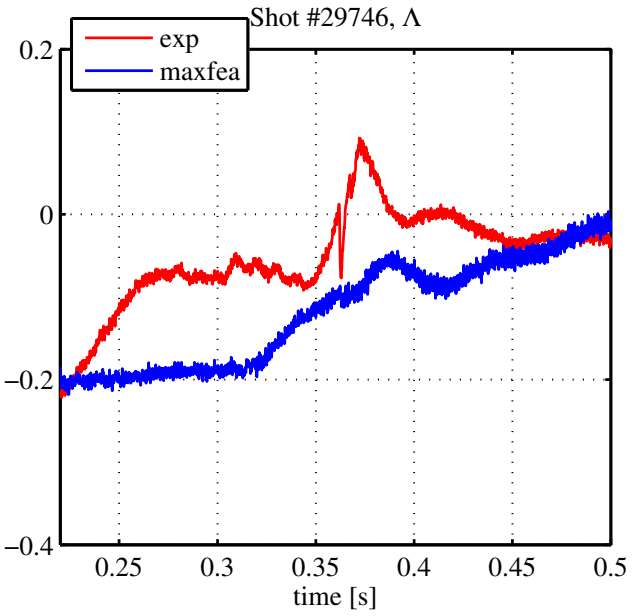

Figure 3.5: Shot #29746, Λ estimates from magnetic data

Double-null Tokamak discharge To compare the simulation with impressed current to the experimental data in a double-null Tokamak configuration, the parametrization has been adjusted as follows

$$\alpha = 1, \quad \beta = 0.25$$

leading to the following values for plasma parameters:

$$li = 1.00 \text{ (circular)}, \quad li = 0.95 \text{ (double null)}$$

$$\beta_p = 0.26 \text{ (circular)}, \quad \beta_p = 0.29 \text{ (double null)}$$

The chosen parametrization has an overall good average agreement in terms of resulting estimates for Λ (fig. 3.5), and there is good agreement between experimental data and reconstructed magnetic data (fig. 3.6). The parametrization chosen is acceptable, and the virtual measures can be used to assess the performance of plasma boundary reconstruction methods that will be considered in the next chapter, comparing the results with the boundary reconstruction provided by the simulator itself.

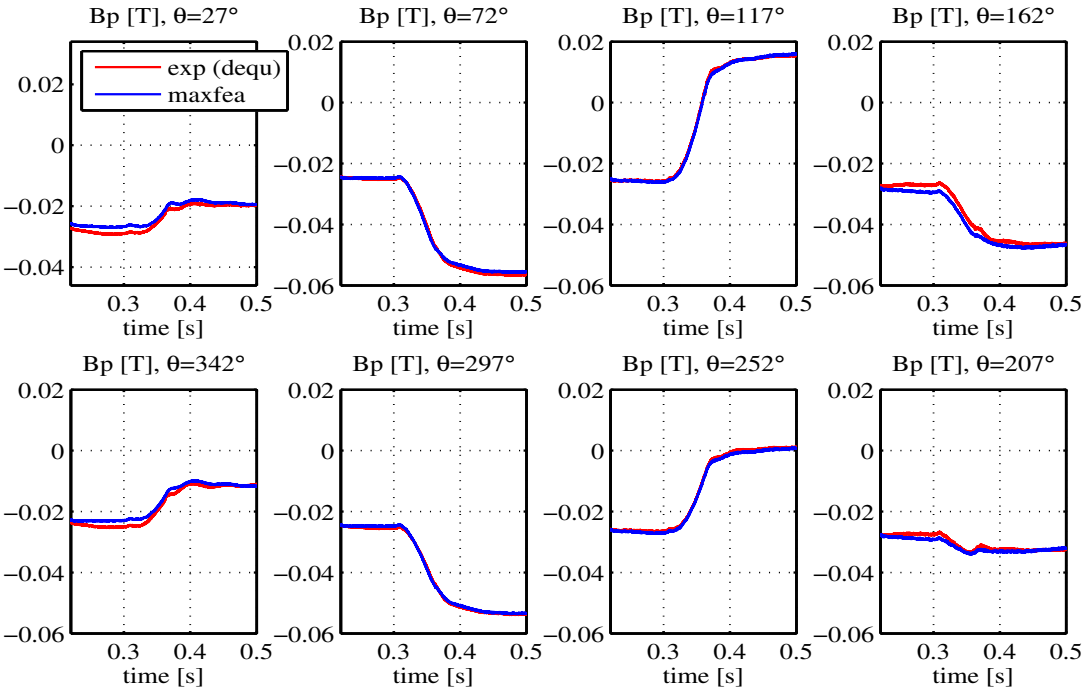

(a) Poloidal field

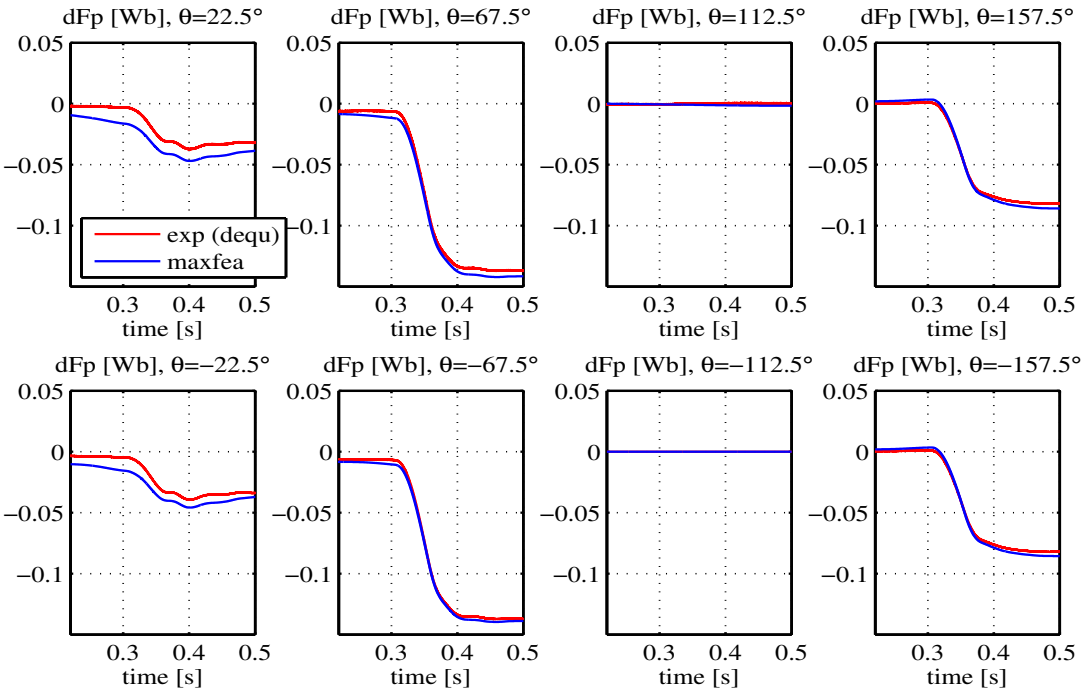

(b) Flux differences

Figure 3.6: Shot #29746, experimental and simulated magnetic data

3.5 Estimation of vertical instability growth rate

Before the experimental sessions where double-null Tokamak discharges were actually obtained, the nonlinear simulator has been used to analyze the prospected plasma configuration (table 3.1) for what concerns stability. It was expected that a vertical displacement instability would exist, due to the shape of the equilibrium field and to the fact that $F3$ coils would exert an attractive force on the plasma.

Coil	$F1$	$F2$	$F3$	$F4$	$F5$	$F6$	$F7$	$F8$
I[A]	-2746	-889	2349	0	-1692	-1157	-233	426

Table 3.1: *dnfat38* double-null configuration, field shaping coils current

Field shaping coils have been assumed to be ideally conductive, and a voltage pulse ($\Delta V = 5000\ V,\ \Delta t = 0.3ms$) has been applied to the $F4$ coil, leading to a peak current of $+230A$ on $F4$, and perturbing the other coils as well because of inductive coupling. This type of perturbation cannot be produced on the real machine, since $F4$ can carry only negative current and the maximum voltage pulse amplitude is limited by PVAT voltage saturation; voltage sign constraints could be respected applying a positive voltage perturbation on $F3$ coils, but $F4$ coils have been chosen instead because they are horizontally more central, and have a greater impact on vertical stability. In fact, the purpose of this analysis was to actually explore the existence of the vertical unstable mode, and to study the sensitivity of the simulator to the initial position of the magnetic axis. Combinations of $F4$ and $F5$ coils have also been tried, but results were not much different. The current centroid of the plasma has been considered to estimate growth rates; the resulting time constants for the vertical instability have been obtained by considering the derivative of Z_j over time, and performing a polynomial fit of the logarithm of the curve.

Initial conditions				Time constant
R_{ax} $[\pm 0.002\ m]$	Z_{ax} $[\pm 0.002\ m]$	R_j $[m]$	Z_j $[m]$	τ_{vert} $[ms]$
2.030	0.000	2.0141	0.0000	65.4
2.010	0.000	1.9927	0.0000	64.5
2.050	0.000	2.0374	0.0000	61.8
2.030	0.005	2.0148	0.0070	117.5
2.030	-0.005	2.0148	-0.0071	109.3

Table 3.2: Estimates of vertical instability growth rate

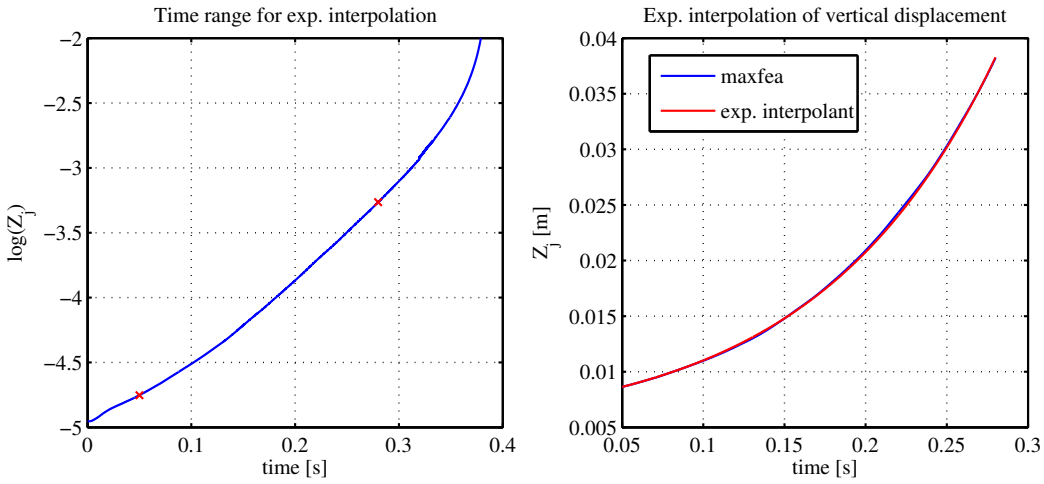

(a) $log(Z_j(t))$ (b) $Z_j(t)$ and exponential fit

Figure 3.7: Exponential fit of plasma vertical displacement
Initial conditions: $R_{ax} = 2.03$, $Z_{ax} = 0.005$

This analysis has been useful since it suggested that it was necessary to use a finer mesh in the simulator to lessen the dependence on the initial position of the magnetic axis. With the older mesh, small perturbations in the position of the magnetic axis led to large differences in resulting time constants. The simulator can only place the magnetic axis in the center of a triangle of the mesh, and the previous mesh had an average precision of $\pm 1\ cm$ in magnetic axis placement. The finer mesh allowed higher precision ($\pm 0.2cm$), and led to consistent growth rate estimates in the case of $\sim 1\ cm$ changes of the magnetic axis in the horizontal direction. Strong variations emerged instead perturbing the initial conditions with displacements of the magnetic axis in the vertical direction, but this is consistent with the fact that in this case the simulator would converge to an initial equilibrium with non top-down symmetric values of current in $F7, u$ and $F7, d$. In table 3.2 are reported the resulting time constants estimates for the vertical instability, and in figure 3.7 is reported an example of curve fitting with the exponential law associated with the calculated time constant.

Chapter 4

Plasma boundary reconstruction

Using the finite element code Maxfea presented in the previous section, one can obtain a reconstruction of the plasma boundary that should agree with particular experimental conditions. To be more precise, Maxfea produces a reconstruction of the boundary and a simulated value of all the magnetic measurements (magnetic field and flux), given its reconstruction of the equilibrium on the basis of general plasma parameters and known values of current flowing in the active coils. However, the reconstruction is strongly influenced by the chosen parametrization, and Maxfea uses iterative procedures that do not assure a finite time of convergence. The complexity of the code itself makes it unsuitable for real-time use. For these reasons, the simulator can be used as a diagnostic tool over experimental data to reconstruct equilibrium configurations and time evolutions, and it is a valuable tool to perform closed loop simulations and to benchmark the performance of controllers in a simulated environment. However, when implementing the same controllers in the experimental environment, one must be able to reconstruct the variables of interest (e.g. plasma centroid position or plasma boundary to first-wall distance) from sensor measurements, in real-time. For this reason, the following chapter will deal with the validation of some equations and algorithms that should provide an estimate of these variables complying with real-time constraints. Magnetic measurements and eventually active circuits current will be used as input variables for reconstruction, without requiring additional information on plasma parametrization. The algorithms will be tested using virtual magnetic data produced by Maxfea, to compare the estimated variables to their "real" value, that is directly accessible in simulations.

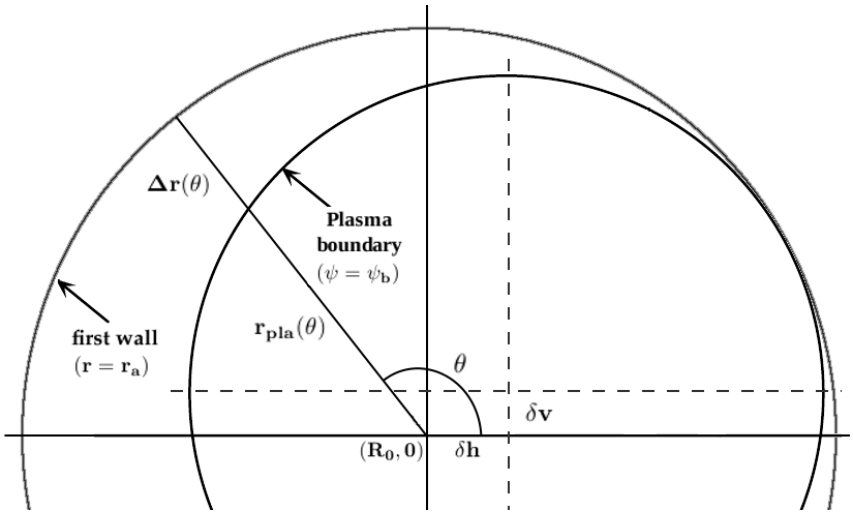

Figure 4.1: Definition of plasma geometric measures

4.1 Radial expansion method for gap estimation

The relation between the poloidal flux $\psi(r,\theta)$ and the the poloidal field $B_\theta(r,\theta)$

$$B_\theta(r,\theta) = \frac{1}{2\pi(R_0 + r\cos(\theta))}\frac{\partial\psi}{\partial r}(r,\theta) \tag{4.1}$$

suggests that, knowing an estimate of ψ_b, the value of the poloidal flux at the boundary, one can reconstruct the plasma-first wall gap $\Delta r(\theta) = r_a - r_{pla}(\theta)$ using a linear expansion between the measurement point (r_0,θ) and the plasma boundary with a first order approximation:

$$\Delta r(\theta) \approx r_a - r_0 + \frac{\psi(r_0,\theta) - \psi_b}{2\pi B_\theta(r_0,\theta)(R_0 + r_0\cos\theta)}.$$

Actually, this approximation is too rough for several reasons. First of all, in RFX-mod the pick-up probes providing a measurement of B_θ and flux loop probes are located at different radius/angle (see table 2.3). Secondly, in RFX-mod both kind of measures are affected by a spurious component, due to eddy currents in the vessel. It is then convenient to reconstruct the measures at the first wall radius r_a, removing the effect of eddy currents in the vessel. The program *eqflu* [10] implemented in the real-time control system of RFX-mod actually adopts this strategy, using several approximations to correct the measures and reconstruct the distance between the first wall and the plasma boundary. In the version of the program that was used to diagnose RFX-mod shots before the double-null Tokamak campaign, it was assumed that $B_\theta(r,\theta)$ satisfies the following relation:

$$B_\theta(r,\theta) \approx \frac{A}{r} + B(\theta) + \mu_0 J(\theta)\frac{r_L}{r}, \tag{4.2}$$

$J(\theta)$ represents the toroidal current flowing in the vessel, that is assumed to be proportional to the measured loop voltage at angle θ; A and $B(\theta)$ group the terms of the Fourier expansion of $B_\theta(r,\theta)$, that can be computed at the poloidal field measurement radius r_b:

$$A = \frac{r_b}{n}\sum_{i=1}^{n} B_\theta(r_b,\theta_i), \quad B(\theta) = \sum_{k=1}^{m}\left[B_{k,c}\cos(\theta) + B_{k,s}\sin(\theta)\right], \text{ where}$$

$$B_{k,c} = \frac{2}{n}\sum_{i=1}^{n}\cos(k\theta_i)B_\theta(r_b,\theta_i), \quad B_{k,s} = \frac{2}{n}\sum_{i=1}^{n}\sin(k\theta_i)B_\theta(r_b,\theta_i), \quad k = 1...m \leq \frac{n}{2}.$$

The previous version of the program used only 4 measures of B_θ ($n = 4$) and computed only the first harmonic ($m = 1$), while it has recently been updated to use 8 measures of B_θ ($n = 8$), taking an average value on dense arrays, and to use the first 3 harmonics ($m = 3$). Actually, in the case of double null Tokamak discharges, there is a higher variability of $B_\theta(r,\theta)$ with respect to the angle, and it is more difficult to reconstruct the poloidal field with a simple harmonic expansion.

A measure of $\psi(r_{fl},\theta_i)$ is available at flux-loops measurement points ($r = r_{fl}, \theta_i \in \Theta_{fl}$). Integrating eq. (4.1) one can extrapolate the flux $\psi(r_a,\theta_i)$:

$$\psi(r_a,\theta_i) = \psi(r_{fl},\theta_i) + 2\pi\int_{r_{fl}}^{r_a}(R_0 + r\cos(\theta_i))B_\theta(r,\theta_i)\,dr, \quad \theta_i \in \Theta_{fl}. \tag{4.3}$$

This integral can be expressed in explicit form given the approximations of eq. (4.2). For a limiter configuration, to actually compute the plasma-first wall distance, an estimate of ψ_b is obtained computing the interpolating spline $f(\theta)$ for the flux function at the first wall radius r_a:

$$f(\theta): \quad f(\theta_i) = \psi(r_a,\theta_i), \quad \theta_i \in \Theta_{fl},$$

and the maximum value of the flux at the first wall is extrapolated as follows:

$$\psi_b = \max_\theta f(\theta). \tag{4.4}$$

Equation (4.3) can be rewritten to link ψ_b and $\psi(r_a,\theta)$, and it should be solved with respect to $\Delta r(\theta)$. However, the resulting equation does not have a closed-form solution. In the previous version of the routine an explicit solution for $\Delta r(\theta)$ was obtained by assuming that $(R_0 + r\cos(\theta)) \approx (R_0 + r_a\cos(\theta))$. In this case, the solution would be

$$\Delta r(\theta) = r_a\left[1 - \exp\left(-\left|\frac{\psi(r_a,\theta) - \psi_b}{2\pi r_a\, B(r_a,\theta)\,(R_0 + r_a cos(\theta))}\right|\right)\right].$$

This approximation has been removed in the new version of the program *eqflu*, and the value of $\Delta r(\theta)$ is now computed numerically [11]. Moreover, the approximation expressed in (4.2) has also been changed to take into account the fact that the $m > 0$ harmonics of $B(\theta, r)$ depend on r as well. Actually, these approximations gave accurate results in the case of circular plasma, when $\Delta r(\theta)$ is small, but have a stronger impact in the case of double null plasma, when the resulting distance from the first wall is higher. Experimental session as well as application of the old routine to Maxfea data in the case of double null shots gave inaccurate results and often showed that the estimated value for $\Delta r(\theta)$ diverged. The program has been updated and now exploits the approximation of cylindrical geometry, where the magnetic scalar potential Φ, such that $\mathbf{B} = \nabla\Phi$, can be expressed as

$$\Phi(r,\theta) = \Phi_0 + \sum_{k=1}^{m} \left[\left(A_{k,c} r^k + B_{k,c} r^{-k} \right) \cos(k\theta) + \left(A_{k,s} r^k + B_{k,s} r^{-k} \right) \sin(k\theta) \right].$$

The coefficients of the series up to $m = 3$ can be computed from the measurements exploiting the relations

$$B_\theta(r,\theta) = \frac{1}{r}\frac{\partial\Phi}{\partial\theta}(r,\theta), \qquad \frac{\partial\psi}{\partial\theta}(r,\theta) = -2\pi r R_0 \frac{\partial\Phi}{\partial r}(r,\theta).$$

The first relation can then be used in eq. (4.3) to extrapolate the flux at the first wall, and then to numerically find the value of $\Delta r(\theta)$ with a procedure that iterates on different values of r, computing at every step the value of $\psi(r,\theta)$. The updated routine has been tested on both the cases of circular plasma and double null shots simulations, applying the *eqflu* program to Maxfea data (fig. 4.2, plot: *radial exp.*). In the circular plasma case, results are accurate. In the double null case, the estimates of $\Delta r(\theta)$ don't diverge anymore but top/down asymmetries emerge in some cases (e.g. gaps at $\pm 112.5°$ and $\pm 157.5°$ in fig. 4.2.b).

These asymmetries could be related to the fact that B_θ measurements are actually taken at non top/down symmetric points. Moreover, the routine still relies on the hypothesis of limiter plasma, searching for the maximum as in eq. (4.4) to estimate the flux at the boundary. Actually, in double null shots the boundary is a separatrix, and the flux at the boundary should be computed estimating its value at the null points of the configuration. To overcome these limitations, a different approach is proposed in next section, where magnetic data is used together with information on external coils current, trying to reconstruct the complete flux map of the configuration.

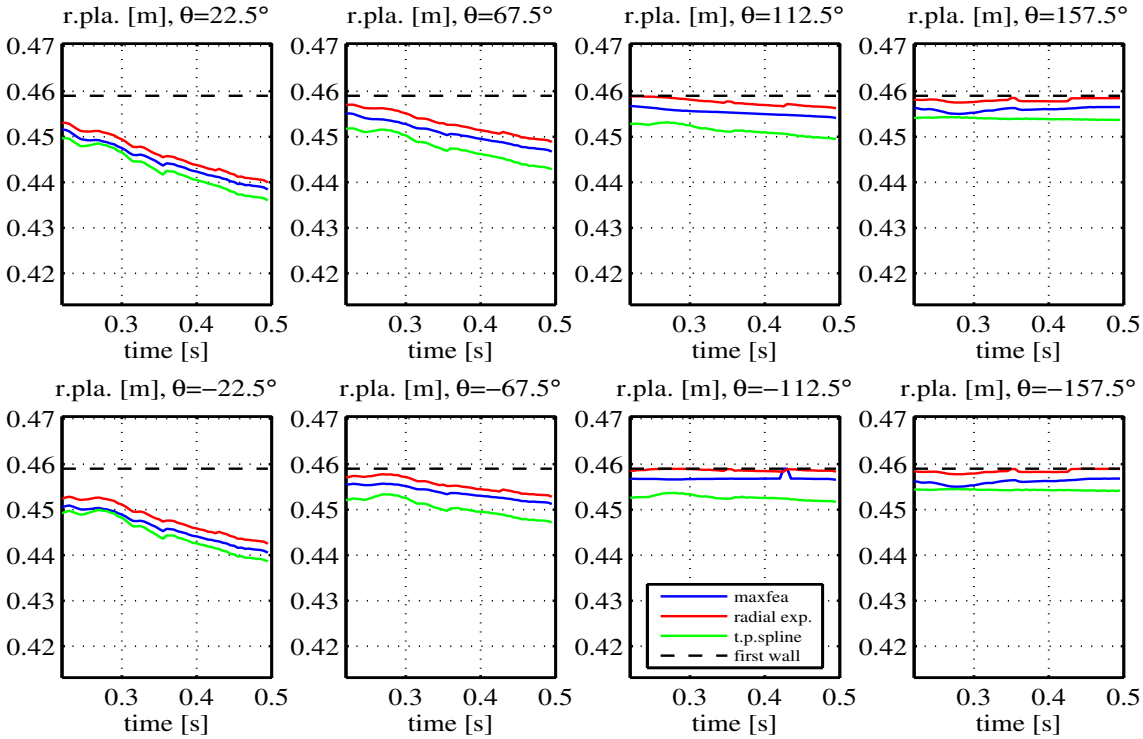

(a) Shot #29648

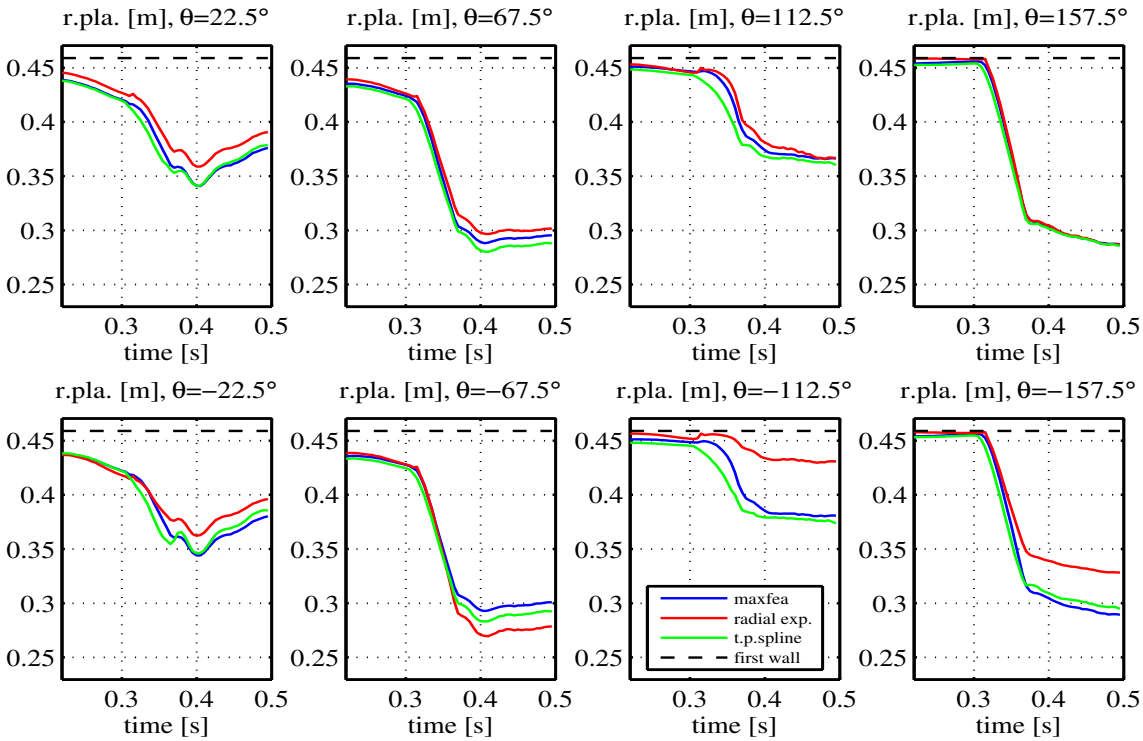

(b) Shot #29746

Figure 4.2: Application of gap estimation methods to Maxfea virtual measures

maxfea: plasma boundary intersection with radius at given angle

radial exp: updated experimental routine *eqflu* that will be in use on RFX-mod

t.p.spline: flux map reconstruction from virtual measures + gap postprocessing

4.2 Integral flux map and boundary reconstruction

Most real-time boundary reconstruction codes (e.g. XLOC on JET) [12] [13] reconstruct the flux map $\psi(R, Z)$ on the whole cross-section of the torus, using an appropriate set of base functions $\mathcal{F}_m = \{\psi_i(R, Z),\ i = 1 \ldots m\}$ such that

$$\psi(R, Z) = \sum_{i=1}^{m} a_i \psi_i(R, Z).$$

In the case of XLOC, the set of base functions is a polynomial base, e.g. assuming $\xi = \left(R^2 - R_0^2\right)$,

$$\mathcal{F}_{27} = \left\{1,\ \xi,\ \xi^2,\ \ldots \xi^7,\ Z,\ Z\xi,\ Z\xi^2,\ \ldots Z\xi^6,\ \ldots Z^7\right\}.$$

The choice of a polynomial base is particularly suited for computing derivatives with respect to R or Z, and this is useful to express equivalent measures of magnetic field at given measurement points from the reconstructed flux map, and to impose the Grad-Shafranov equation in vacuum: $\Delta^*\psi = 0$. The problem can be finally led to a least squares problem, trying to minimize the quadratic error at measurement points. This approach however has also some drawbacks, since a simple polynomial is not suited to match the flux map on the whole cross-section. The region has to be split in different areas with different polynomials, and continuity constraints (soft-tie points and hard-tie points, fig. 4.3) must be introduced. Moreover, it is necessary to take into account explicitly the effect of divertor coils in the x-point region, subtracting their effect from measures, and superimposing their impact on the flux map using Green's functions.

Trying to adapt the XLOC code to the configuration of RFX-mod would be out of range for this work. However, it is interesting to evaluate whether some of the ideas that underlie the XLOC code could be exploited in a simpler, tentative method for flux map reconstruction. The *eqflu* code described in the previous section provides an estimated value of $\psi(r, \theta)$ at the 8 angles corresponding to flux-loop probes, and at $r \leq r_a$. XLOC integrates flux measures and field measures by defining opportunely the least squares problem. In RFX-mod, instead, the program *eqflu* already uses field measures to correct flux measures, exploiting radial expansion methods. It is possible to use the reconstructed value of $\psi(r, \theta)$ and to interpolate it using standard surface interpolation routines. In this case, the information available from flux and field measures is integrated by *eqflu*, and it is possible to use a set of base functions $\mathcal{F}$ that is not affect to the limitations of the polynomial base, reconstructing the flux map on the whole cross section. The

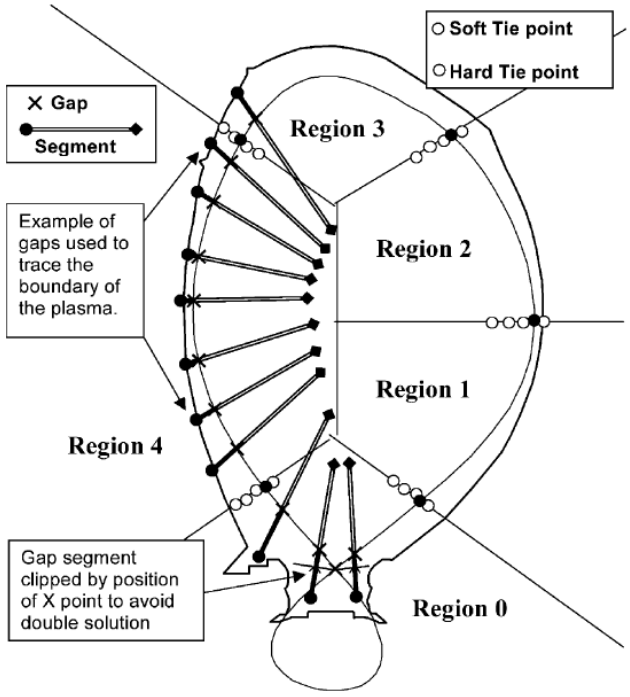

Figure 4.3: XLOC approach to plasma boundary reconstruction

Grad-Shafranov equation is no longer imposed. The capability to model the exact physical properties of the flux map in the vacuum region, expressed by $\Delta^*\psi = 0$, is lost, but it is possible to reconstruct a continuous map even inside the plasma region, where the vacuum GS equation is no longer valid, and it is not necessary to divide the cross section in different regions. Actually, the hypothesis that underlie the *eqflu* program imply that the reconstructed value of flux is reliable only *outside* the plasma boundary line, since a relation of inverse proportionality between magnetic field and radius r is assumed; this is valid only outside the region where plasma current flows. However, the reconstruction could be reliable enough in the case of strongly peaked plasma current profile (high internal inductance), and we are interested in evaluating how reliably the plasma boundary is located by the program, more than in how well the actual value of the flux function is matched. Finally, for what concerns the use of an interpolant of the flux function, it can be noted that the *eqflu* program already uses a spline interpolation to find the value of ψ_b in limiter configuration, as in eq. (4.4). The use of an interpolating surface can be seen as a 2D extension of the original idea.

The interpolating surface of choice is the *thin-plate spline* [14]. This is a standard 2D

interpolating method for scattered data, readily available on scientific codes like Matlab, and has the interesting property that the interpolating surface is found as the solution of a linear problem, without iterative procedures, thus making it suitable for real-time applications. We will use this method to interpolate $m = 24$ points of the flux function, of whom 8 are measurement points and 16 are reconstructed points. The thin-plate spline interpolates the data

$$Y = [F_1(R_{c,1}, Z_{c,1}) \ \cdots \ F_m(R_{c,m}, Z_{c,m})]'$$

using a set of basic functions that are centered in the points above, and that depend on the distances

$$\rho_i^2(R, Z) = (R - R_{c,i})^2 + (Z - Z_{c,i})^2, \quad i = 1 \ldots m;$$

the resulting set of basis functions is

$$\mathcal{F}_{m+3} = \left\{ \phi\left(\rho_1^2(R, Z)\right) \ \ldots \phi\left(\rho_m^2(R, Z)\right), \ R, Z, 1 \right\}$$

where the function $\phi(\cdot)$ is defined as

$$\phi(\rho^2) = \rho^2 \log(\rho^2).$$

Actually, the thin-plate spline also has the advantage that once the interpolating surface coefficients have been computed, it is possible to compute partial derivatives, for example with respect to R, that can be expressed on the following basis:

$$\mathcal{F}'_{m+1} = \left\{ \phi'\left(\rho_1^2(R, Z)\right) \ \ldots \phi'\left(\rho_m^2(R, Z)\right), \ 1 \right\}$$

where

$$\phi'(\rho^2(R, Z)) = \left(\log(\rho^2(R, Z)) + 1\right) \frac{\partial \rho^2(R, Z)}{\partial R}.$$

Exploiting this fact, it should be possible to use the thin-plate spline as a method to integrate flux and field measures, as it's done in XLOC. By now, we will use the thin-plate spline as an interpolant of the flux function only, and not of its partial derivatives that could express the magnetic field.

The thin-plate spline $f_A(R, Z)$ is a linear combination of the basis function with coefficients

$$A_1 = [a_1 \ \ldots \ a_m]', \quad A_2 = [a_{m+1} \ \ldots \ a_{m+3}]', \quad A = \begin{bmatrix} A_1 \\ A_2 \end{bmatrix}$$

and is often used as a smoothed approximating surface, where the smoothness parameter ν appears as a weight to a term expressing the roughness of the surface in the total energy function:

$$W(f_A) = (1-\nu)\sum_{i=1}^{m} |F_i - f_A(R_{c,i}, Z_{c,i})|^2 + \nu \int_{\mathbb{R}^2} \left(\frac{\partial^2 f_A}{\partial R^2}\right)^2 + 2\left(\frac{\partial^2 f_A}{\partial R \partial Z}\right)^2 + \left(\frac{\partial^2 f_A}{\partial Z^2}\right)^2 dRdZ.$$

It could be shown that the integral on the right is well defined. Actually, the resulting surface is asymptotically flat. In this context, we will set $\nu = 0$ when elaborating Maxfea data, since we want to find the surface that exactly passes through the given (measured or reconstructed) values of flux at predefined points. The solution will be characterized by coefficients A such that $W(f_A) = 0$. Setting $\nu > 0$ (typically $\nu = 0.04$) has shown to be useful when processing experimental data, since it lessens the effect of measurement noise. The solution of the minimization problem

$$\min_A W(f_A)$$

is obtained by considering the representation of the data points in homogeneous coordinates,

$$X = \begin{bmatrix} R_{c,1} & Z_{c,1} & 1 \\ \vdots & \vdots & \vdots \\ R_{c,m} & Z_{c,m} & 1 \end{bmatrix},$$

and applying a $Q - R$ decomposition

$$X = \begin{bmatrix} Q_1 & Q_2 \end{bmatrix} \begin{bmatrix} R_1 \\ 0 \end{bmatrix};$$

the value of the basis functions is computed in the data points and collected in Φ

$$\Phi = \begin{bmatrix} \phi\left(\rho_1^2(R_{c,1}, Z_{c,1})\right) & \dots & \phi\left(\rho_m^2(R_{c,1}, Z_{c,1})\right) \\ \vdots & & \vdots \\ \phi\left(\rho_m^2(R_{c,1}, Z_{c,1})\right) & \dots & \phi\left(\rho_m^2(R_{c,m}, Z_{c,m})\right) \end{bmatrix},$$

and the solution is finally found as

$$\begin{aligned} A_1 &= Q_2 \left(Q_2' \Phi Q_2 + \frac{\nu}{1-\nu} I_{m-3}\right) Q_2' Y \\ A_2 &= R_1^{-1} Q_1' (Y - \Phi A_1). \end{aligned}$$

The solution of the minimization problem has thus the same complexity of a least squares problem of size m. The data points are now defined as the 8 flux measurement

points ($r = r_{fl},\ \theta \in \Theta_{fl}$), plus 16 reconstructed points, where the value of the flux is extrapolated with the *eqflu* program. The procedure can be applied to experimental data or to Maxfea virtual measures. The reconstructed points are found at the same angle of the measurement points, and on two inner circumferences, for a total of 24 points:

$$r \in \left\{ r_{fl},\ \frac{3}{4} r_{fl},\ \frac{1}{2} r_{fl} \right\}, \quad \theta \in \Theta_{fl}.$$

The interpolating surface is an approximation of the flux function on the poloidal cross section. Applying the procedure described above to Maxfea virtual magnetic data, the resulting flux map reconstruction showed good agreement with the flux map provided by the simulator in the case of circular plasma, but the structure of the set of basis functions made it difficult to reconstruct the flux map of a double null plasma, since this configuration is strongly shaped by the field generated by external coils.

To obtain better results in the case of double null plasma, the same approach used by XLOC to better reconstruct the flux map in the divertor region was adopted: the effect of F coils was subtracted from measures; *eqflu* has been used to reconstruct the flux at the inner circumferences, and the interpolating thin-plate spline relative to these points has been obtained as $f_{tp}(r, \theta)$. This is equivalent to reconstructing the flux map due to plasma current distribution and to current in passive elements. Actually, the thin-plate spline is defined in (R, Z) coordinates, but from now on we will be referring more conveniently to (r, θ) coordinates. Finally, the effect of F coils on the whole flux map has been added back. The effect of the external coils on the flux map can be reconstructed using Green's function; it would be very simple to reconstruct a correct flux map in the hypothesis of circular coil cross section, using only one filament of current per coil. Since in RFX-mod F coils have a rectangular cross section, the reconstruction gave better results using the flux maps $\psi_{F,i}(r, \theta),\ i = 1 \ldots 8$, obtained from Maxfea when imposing a current only in one of the F coils at a time, without plasma. Maxfea actually computes this flux map modeling an uniform current distribution in active coils, using a filament of current per mesh triangle. When reconstructing the resulting flux map given the current $I_{F,i}$ in every i-th coil circuit, the flux maps were then linearly combined, proportionally to the current flowing in these coils. With these considerations, an approximation of the flux function is found as

$$\psi_{tp}(r, \theta) = f_{tp}(r, \theta) + \sum_{i=1}^{8} I_{F,i} \psi_{F,i}(r, \theta).$$

The next step of the algorithm consists in the calculation of the estimated value of ψ_b. The algorithm handles correctly the transition between limiter and double null plasma

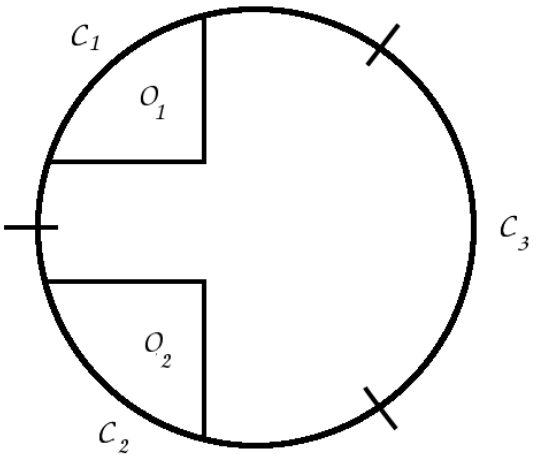

Figure 4.4: Regions for the calculation of ψ_b

by dividing the circumference at $r = r_a$ in three regions:

$$\begin{aligned}
\mathcal{C}_1 = &\quad \left\{r = r_a,\ \tfrac{\pi}{3} \leq \theta < \ \pi\right\} \\
\mathcal{C}_2 = &\quad \left\{r = r_a,\ \pi \leq \theta < \tfrac{5}{3}\pi\right\} \\
\mathcal{C}_3 = &\ \left\{r = r_a,\ -\tfrac{1}{3}\pi \leq \theta < \tfrac{1}{3}\pi\right\}.
\end{aligned}$$

On the three sectors of circumference, the maximum value of the reconstructed flux function is found as

$$\psi_{b,i} = \max_{(r,\theta)\in\mathcal{C}_i} \psi_{tp}(r,\theta), \quad i = 1 \ldots 3.$$

Next, the gradient of ψ_{tp} is computed in regions $\mathcal{O}_1$ and $\mathcal{O}_2$ (fig. 4.4), where the formation of the null points of the configuration is expected, and if a null point is found in these regions within a certain tolerance υ, then $\psi_{b,1}$ and $\psi_{b,2}$ are overridden by the value at the null point:

$$\begin{aligned}
\psi_{b,1} = \psi_{tp}(r_{o,1},\theta_{o,1}) \quad &\text{if} \quad (r_{o,1},\theta_{o,1}) \in \mathcal{O}_1,\ |\nabla\psi_{tp}(r_{o,1},\theta_{o,1})| < \upsilon \\
\psi_{b,2} = \psi_{tp}(r_{o,2},\theta_{o,2}) \quad &\text{if} \quad (r_{o,2},\theta_{o,2}) \in \mathcal{O}_2,\ |\nabla\psi_{tp}(r_{o,2},\theta_{o,2})| < \upsilon
\end{aligned}$$

Finally, the value of the flux at the boundary is obtained as

$$\psi_b = \max_i \psi_{b,i}.$$

The final stage of the algorithm is the application of a contour routine to trace the line of the boundary, searching for the points

$$(r,\theta): \quad \psi_{tp}(r,\theta) = \psi_b. \tag{4.5}$$

While the interpolation routine is efficient and suitable for real time use, since the size of the problem is fixed, the contour routine should be studied *ad-hoc* to eventually comply with real time constraints. However, often it is not required to compute the full reconstruction of the plasma boundary in real time. Most commonly, shape controllers need the reconstruction of plasma-first wall distance only at gaps. In this work, we will consider the design of a shape controller that uses 8 gap measures: $\Delta r(\theta),\ \theta \in \Theta_{fl}$. To obtain the estimates of these measures, the value of the interpolating surface could be computed only on the circumference at $r = r_a$ and in the $\mathcal{O}$ regions to estimate ψ_b, and finally at some points along the radius at selected angles only to estimate gaps. A simple linear interpolation between values along the radius should provide a good localization of points satisfying eq. (4.5), with little computational load. In the present implementation, the estimation of gap measures is obtained through postprocessing of the reconstructed contour line, returning the estimates proposed in fig. 4.2 (plot: *t.p.spline*).

Application to Maxfea data In figure 4.5.a is reported the application of the algorithm to Maxfea data in the case of circular Tokamak equilibrium (shot #29648, $t = 0.4s$), and in figure 4.5.b is the case of DN tokamak equilibrium (shot #29746, $t = 0.4s$). These are equilibrium simulations, obtained referencing the simulator with current values at $t = 0.4s$. The data points for the thin-plate spline are represented as pink crosses, while the black crosses are the reconstruction of plasma-first wall distance obtained with the *eqflu* routine. Red crosses are the reconstructed position of null points. In these figures it is possible to compare the reconstructed boundary line (red) with the boundary line traced by the simulator (blue), showing good agreement.

Application to experimental data In figure 4.6 is the application of the boundary reconstruction algorithm to experimental data, at the time instants corresponding to Maxfea figures. The thin-plate spline flux interpolation returns a contour that is consistent with the expected plasma shape obtained in simulation. This is a supporting evidence that the double-null configuration has actually been obtained in experimental sessions, although the reconstructed flux map suggests that the configuration degraded to a limiter configuration at successive time instants (fig. 4.7). This undesired behavior could be corrected with the feedback action of a shape controller, that was absent in the experimental configuration when shot #29746 was performed.

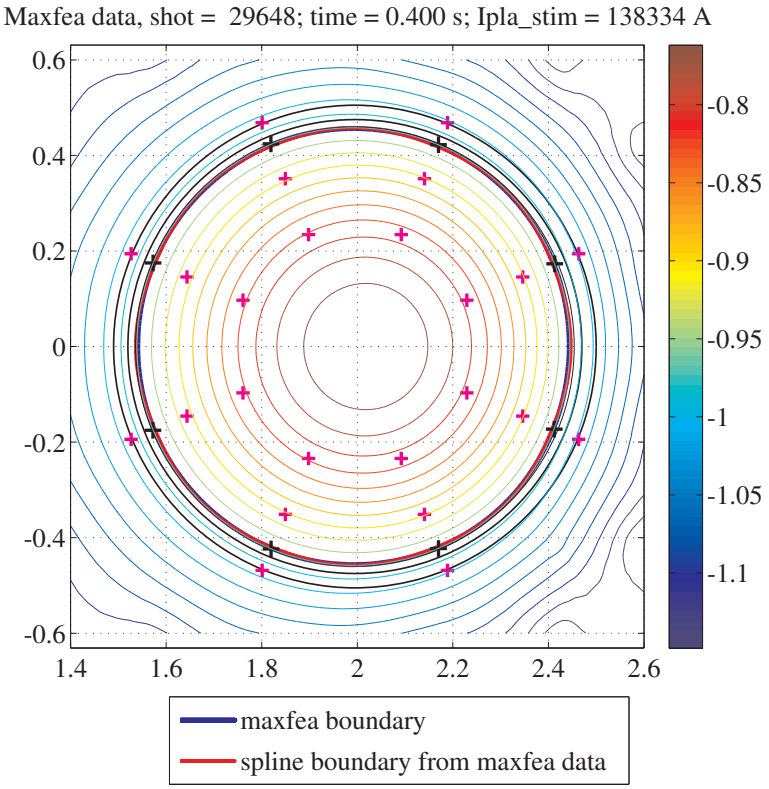

(a) Shot #29648

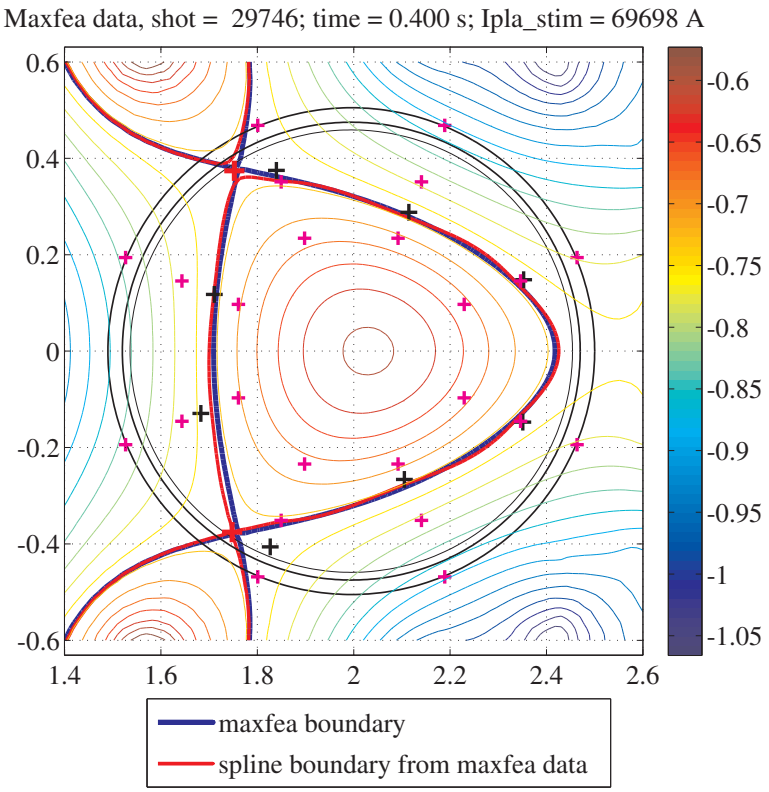

(b) Shot #29746

Figure 4.5: Application of thin-plate spline reconstruction to Maxfea virtual measures
Magenta crosses: interpolation points of reconstructed *eqflu* flux.
Black crosses: *eqflu* gap estimation. Red crosses: estimated null points.

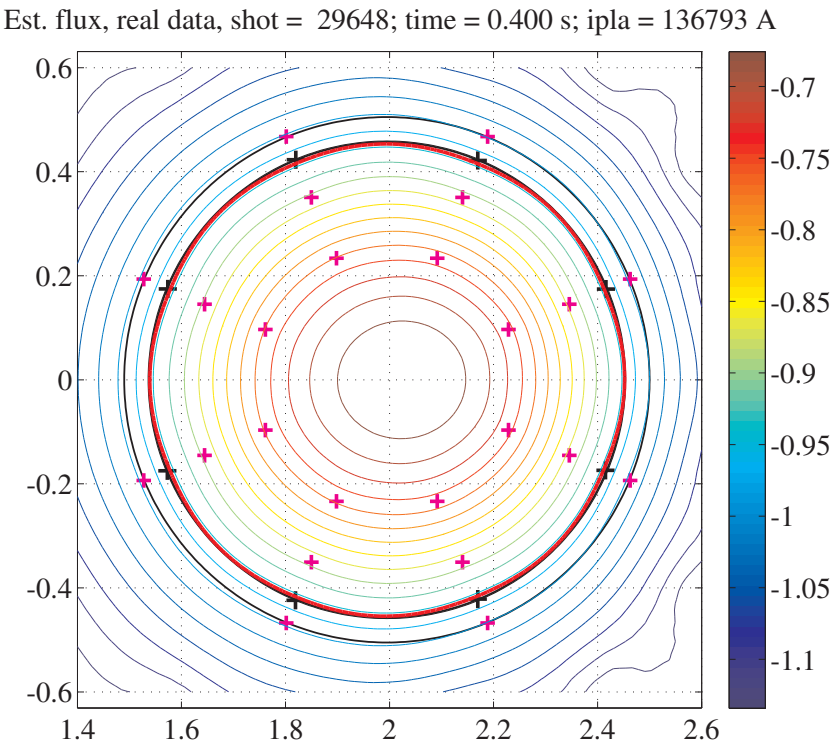

(a) Shot #29648

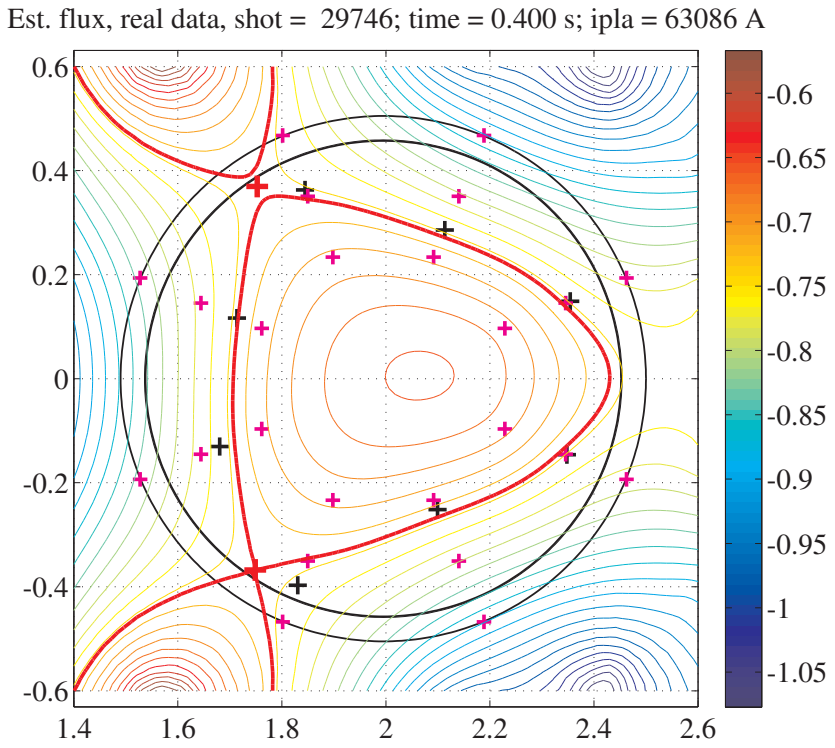

(b) Shot #29746

Figure 4.6: Thin-plate spline flux map reconstruction, experimental data
Red line: boundary reconstruction, thin-plate spline contour.
Magenta crosses: interpolation points of reconstructed *eqflu* flux.
Black crosses: *eqflu* gap estimation. Red crosses: estimated null points.

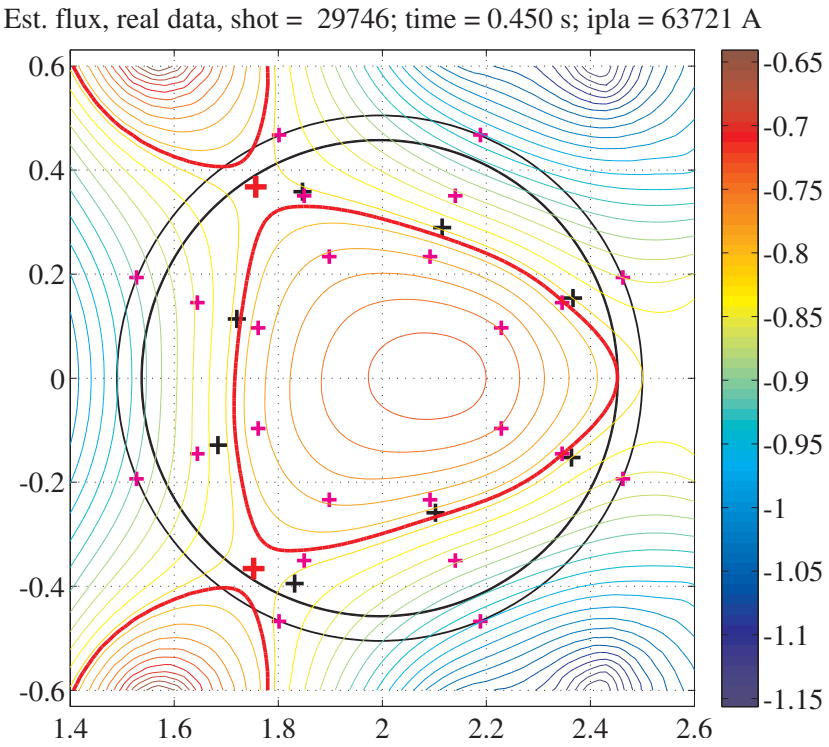

Figure 4.7: Reconstructed evolution of the experimental discharge
Red line: boundary reconstruction, thin-plate spline contour.
Magenta crosses: interpolation points of reconstructed *eqflu* flux.
Black crosses: *eqflu* gap estimation. Red crosses: estimated null points.

4.3 Plasma centroid: the current moment method

An estimate of plasma geometric centroid can be obtained once the plasma radius has been estimated at various angles with the methods presented in previous sections, considering the harmonic expansion of the function $r_{pla}(\theta)$ and evaluating the first order terms $r_{1,c}$ and $r_{1,s}$, such that

$$r_{pla}(\theta) = r_{pla,0} + \sum_{k=1}^{+\infty} r_{k,c}\cos(k\theta) + r_{k,s}\sin(k\theta)$$

to obtain an estimate of horizontal and vertical displacement as $\delta h = r_{1,c}$, $\delta v = r_{1,s}$. However, often plasma displacement is controlled by estimating the location of the current centroid, using this as the controlled variable. The current centroid is defined as an average over the axisymmetric surface Ω that includes the plasma region, weighted by toroidal plasma current density $J_\phi = \mathbf{J}\cdot\hat{i}_\phi$:

$$I_{pla} = \int_\Omega J_\phi(R,Z)d\Omega \tag{4.6}$$

$$R_j = \frac{1}{I_{pla}}\int_\Omega R J_\phi(R,Z)d\Omega \tag{4.7}$$

$$Z_j = \frac{1}{I_{pla}}\int_\Omega Z J_\phi(R,Z)d\Omega \tag{4.8}$$

It will be evident that to produce an estimate of R_j and Z_j, it's necessary to have a measure of field and flux at the same radius/angle. Since in RFX-mod field and flux measures are available at slightly different locations, we will be considering the reconstructed first-wall value of field and flux computed by the *eqflu* routine at $r = r_a,\ \theta_i \in \Theta_{fl}$, that also removes the effect of eddy currents in the vessel from measures. We will thus be assuming that $\partial\Omega = \{(r,\theta):\ r = r_a,\ \theta\in[0,2\pi]\}$, and we will refer to the set of coordinates (R,ϕ,Z) to derive the equations of interest. The plasma current can be estimated considering that

$$I_{pla} = \frac{1}{\mu_0}\oint_{\partial\Omega}\mathbf{B}\cdot\mathbf{dl} \approx -\frac{1}{\mu_0}\sum_{i=1}^{8} B_\theta(r_a,\theta_i)\Delta l, \quad \Delta l = \frac{2\pi r_a}{8}. \tag{4.9}$$

The vertical centroid Z_j can be calculated with the following relations:

$$\begin{aligned}
\mu_0 Z_j I_{pla} &= \int_\Omega \mu_0 Z\mathbf{J}\cdot\hat{i}_\phi d\Omega = \int_\Omega Z\nabla\times\mathbf{B}\cdot\hat{i}_\phi d\Omega = \\
&= \int_\Omega \nabla\times(Z\mathbf{B})\cdot\hat{i}_\phi d\Omega - \int_\Omega \nabla Z\times\mathbf{B}\cdot\hat{i}_\phi d\Omega = \\
&= \oint_{\partial\Omega} Z\mathbf{B}\cdot\mathbf{dl} - \int_\Omega \mathbf{B}\cdot\hat{i}_R d\Omega;
\end{aligned}$$

the first term can be estimated with the following formula

$$\oint_{\partial\Omega} Z\mathbf{B}\cdot\mathbf{dl} \approx -\sum_{i=1}^{8} Z_i B_\theta(r_a,\theta_i)\Delta l;$$

the second term instead can be expressed in terms of the poloidal flux ($\tilde{\psi}=\psi/2\pi$) as

$$-\int_\Omega \mathbf{B}\cdot\hat{i}_R d\Omega = -\int_\Omega \frac{\nabla\tilde{\psi}\times\hat{i}_\phi}{R}\cdot\hat{i}_R d\Omega = \int_\Omega (\nabla\tilde{\psi}\times\nabla\ln R)\cdot\hat{i}_\phi d\Omega =$$

$$-\int_\Omega \nabla\times(\ln R\nabla\tilde{\psi})\cdot\hat{i}_\phi d\Omega = -\oint_{\partial\Omega}\ln R\nabla\tilde{\psi}\cdot\mathbf{dl} \approx +\sum_{i=1}^{8}\ln R_i(\nabla\tilde{\psi})_i\Delta l.$$

To estimate the horizontal centroid R_j, an explicit relation with field and flux measurements can be obtained considering the integral expressing the second order moment instead of the first order moment written in eq. (4.7):

$$\begin{aligned}\mu_0 R_j^2 I_{pla} &= \int_\Omega \mu_0 R^2\mathbf{J}\cdot\hat{i}_\phi d\Omega = \int_\Omega R^2\nabla\times\mathbf{B}\cdot\hat{i}_\phi d\Omega = \\ &= \int_\Omega \nabla\times(R^2\mathbf{B})\cdot\hat{i}_\phi d\Omega - \int_\Omega \nabla R^2\times\mathbf{B}\cdot\hat{i}_\phi d\Omega = \\ &= \oint_{\partial\Omega} R^2\mathbf{B}\cdot\mathbf{dl} + 2\int_\Omega R\mathbf{B}\cdot\hat{i}_Z d\Omega; \end{aligned} \tag{4.10}$$

the first term is readily expressed as

$$\oint_{\partial\Omega} R^2\mathbf{B}\cdot\mathbf{dl} \approx -\sum_{i=1}^{8} R_i^2 B_\theta(r_a,\theta_i)\Delta l$$

while the second results

$$2\int_\Omega R\mathbf{B}\cdot\hat{i}_Z d\Omega = 2\int_\Omega R\frac{\nabla\tilde{\psi}\times\hat{i}_\phi}{R}\cdot\hat{i}_Z d\Omega = -2\int_\Omega(\nabla\tilde{\psi}\times\nabla Z)\cdot\hat{i}_\phi d\Omega =$$

$$2\int_\Omega \nabla\times(Z\nabla\tilde{\psi})\cdot\hat{i}_\phi d\Omega = 2\oint_{\partial\Omega} Z\nabla\tilde{\psi}\cdot\mathbf{dl} \approx -2\sum_{i=1}^{8} Z_i(\nabla\tilde{\psi})_i\Delta l.$$

In the previous formulas, the gradient $\nabla\tilde{\psi}$ can be computed considering the harmonic expansion of the flux function

$$\psi(r_a,\theta) = \psi_0(r_a) + \sum_{m=1}^{4}\left[\psi_{s,m}(r_a)\sin(m\theta) + \psi_{c,m}(r_a)\cos(m\theta)\right]$$

and deriving the right hand side term to obtain

$$\frac{\partial\psi}{\partial\theta}(r_a,\theta) = \sum_{m=1}^{4}\left[m\psi_{s,m}(r_a)\cos(m\theta) - m\psi_{c,m}(r_a)\sin(m\theta)\right];$$

the gradient appearing in previous formulas is finally expressed as

$$(\nabla\tilde{\psi})_i = \frac{1}{2\pi r_a}\frac{\partial\psi}{\partial\theta}(r_a, \theta_i).$$

The resulting estimates of R_j and Z_j are reported in figure 4.8: there's a certain offset ($\sim 1\ cm$) from the value computed by the simulator numerically evaluating integrals of eq. (4.7) and eq. (4.8). In the case of the estimate of R_j, the offset is due to the fact that the simulator computes the first order moment (eq. 4.7), while we estimate the second order moment (eq. 4.10). The offset on the estimate of the vertical centroid in DN configuration is more suspect. It is present also using the data at the measurement radius, without applying *eqflu*. It was argued that the spatial resolution of magnetic probes over the circumference was too low in RFX-mod to allow a good determination of these quantities; however, the reconstruction of these estimates using 16 virtual measures (fig. 4.9) shows little improvements. Nonetheless, applying the algorithm to experimental data (fig. 4.10) shows an overall agreement between displacement of the current centroid and estimates of δh and δv as defined at the beginning of this section. Since the problem of horizontal and vertical displacement seems not to be very relevant in the experiment, the position of the current centroid will be used to actually set up a controller for plasma position, to address the problem of plasma displacement instability in the simulator and in the linear model derived in the next chapter. In simulations, we will be assuming to use ideal estimates of R_j and Z_j as first order moments. Controlling the current centroid allows better decoupling between the position control problem and the shape control problem, the latter being the key topic of this work.

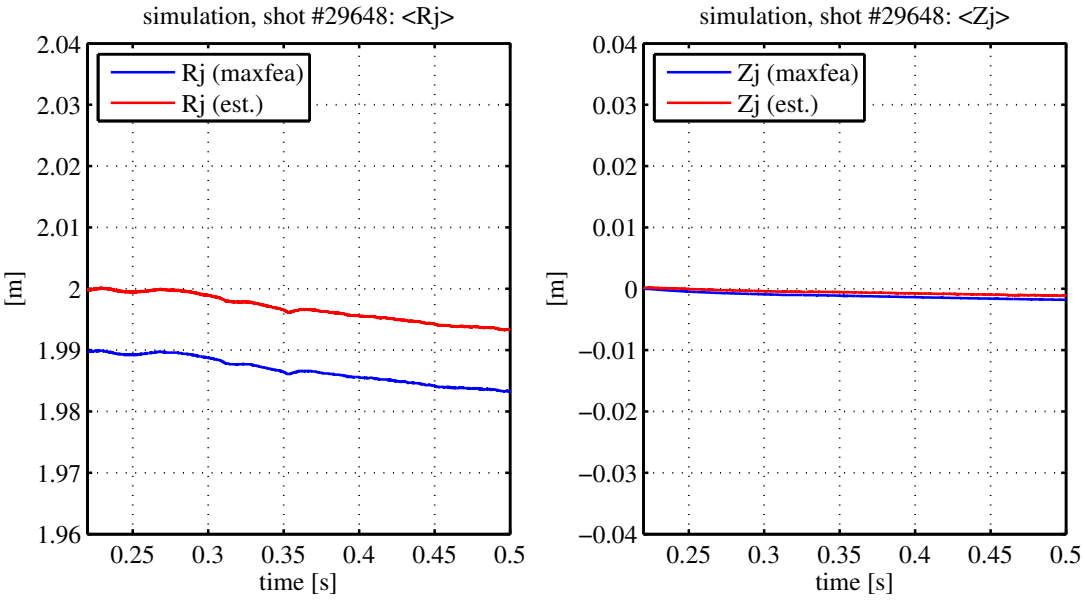

(a) Shot #29648

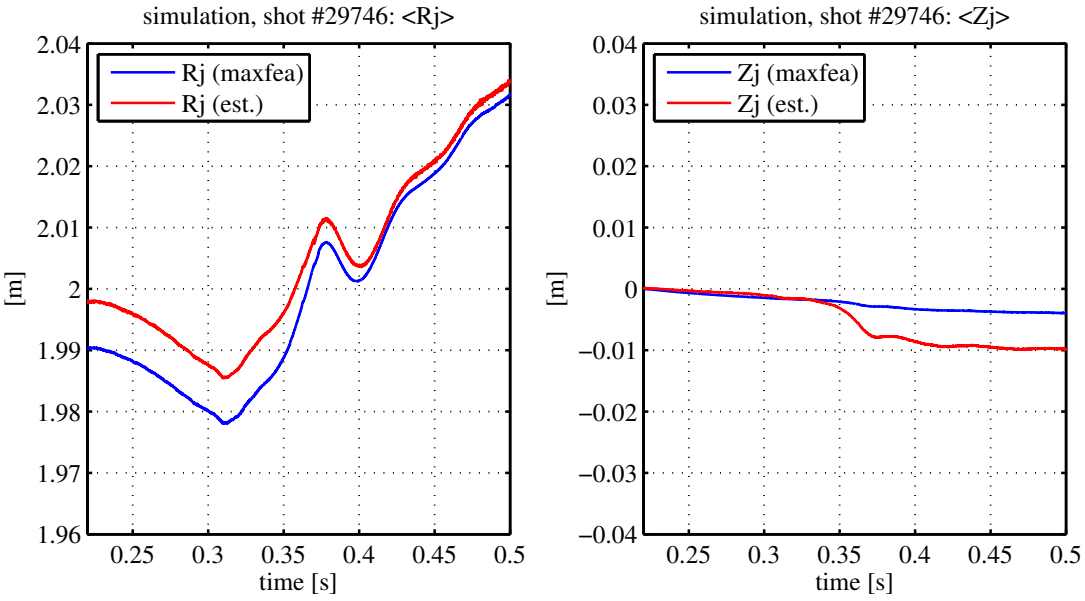

(b) Shot #29746

Figure 4.8: Shot #29746, current centroid reconstruction, simulated data
Measures are reconstructed at $r = r_a$ with *eqflu*

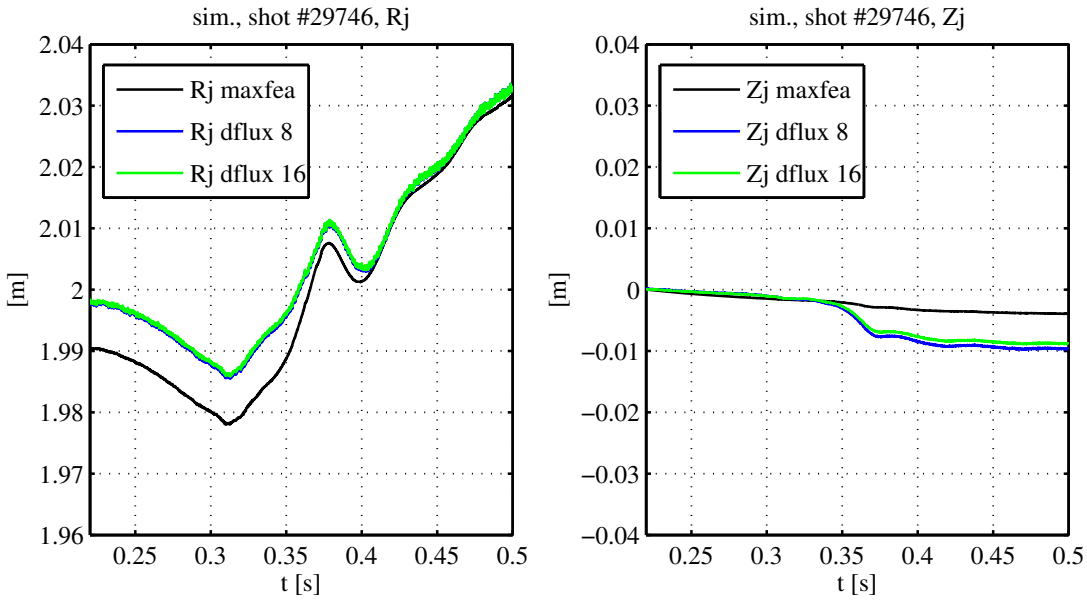

Figure 4.9: Shot #29746, current centroid reconstruction, higher probe resolution
Measures are taken at $r = r_b$ without applying *eqflu*

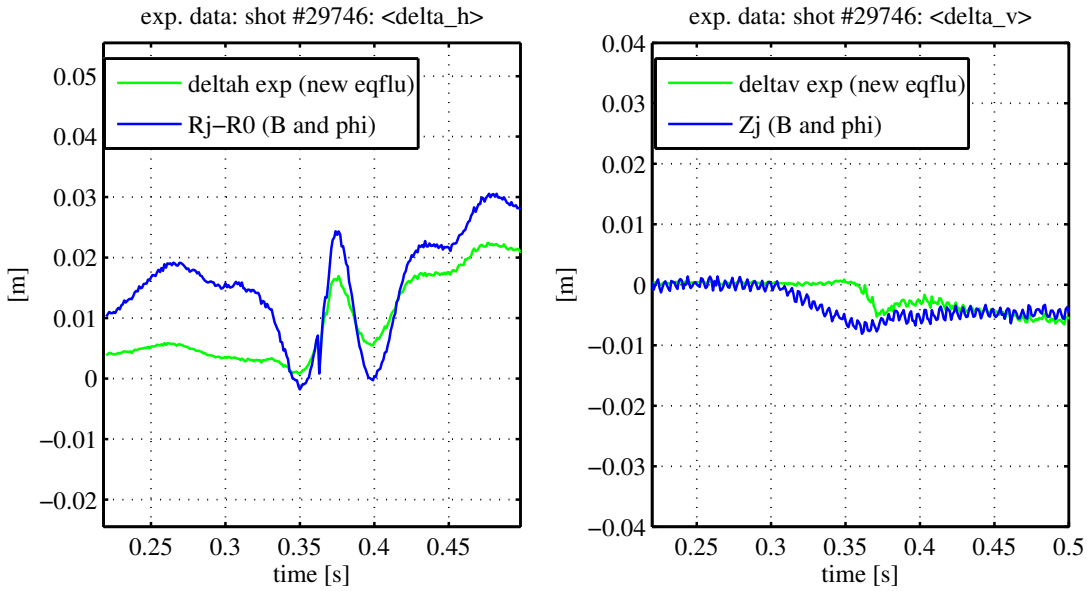

Figure 4.10: Shot #29746, application to experimental data

Chapter 5

Derivation of a linear state-space model

Our purpose is to control the shape of the plasma boundary in a double-null Tokamak configuration, using standard feedback control techniques for linear state-space systems; it is then necessary to calculate a linearized plasma response model. A way to achieve this result is to apply a discretization of the vessel, shell and mechanical structure in axisymmetric elements, and to consider toroidal currents flowing in these elements as state space variables. The presence of plasma has to be taken into account when deriving the linear model. The initial equilibrium configuration is obtained from experimental data of shot $\#29746$, taking average values in the time interval between $0.395\ s$ and $0.415\ s$. The resulting equilibrium point is characterized by plasma parameters reported in table 5.1, and by external coils current reported in table 5.2.

Plasma current [A]	62567
Plasma inductance l_i	0.96
Poloidal β	0.30
Current centroid R_j [m]	2.016
Current centroid Z_j [m]	0
Gap [cm], $\theta = \pm 22.5°$	8.95
Gap [cm], $\theta = \pm 67.5°$	15.49
Gap [cm], $\theta = \pm 112.5°$	6.73
Gap [cm], $\theta = \pm 157.5°$	15.58

Table 5.1: Plasma parameters in shot #29746, $t \approx 0.4s$

Coil	$M1$	$M2$	$M3$	$M4$
I[A]	-2253	-1119	-1705	-4812

Coil	$F1$	$F2$	$F3$	$F4$	$F5$	$F6$	$F7$	$F8$
I[A]	-2531	-910	2580	-24	-1514	-1035	-96	390

Table 5.2: Coil currents in shot #29746, $t \approx 0.4\ s$
These are the equilibrium currents when double-null configuration is obtained

5.1 Calculation of the modified inductance matrix

The linearized model will substantially consist in an electric network inductively coupled. Without plasma, network dynamics are regulated by vacuum resistance and inductance matrices:

$$V = L_0\dot{I} + RI, \quad \Psi = L_0 I.$$

The presence of the plasma is taken into account by substituting the L_0 matrix with the modified inductance matrix L^*, numerically obtained with a flux perturbation method, as described in [15]. The method relies on the use of a free-boundary equilibrium solver, so a special mesh was used in Maxfea where the vessel and shell are both divided into 60 elements, and the structure is divided in two layers of 60 elements (figure 5.1). Firstly, the simulator must be initialized with the equilibrium external coil current and plasma current. The resistivity of all passive elements is set to zero, since the procedure aims at identifying the inductive part of the model only. Other methods that aim at identifying the modified inductance matrix prescribe to apply current perturbations to all the elements included in the model: this is known as the current perturbation approach. However, the flux perturbation approach has the advantage that it is sufficient to perturb magnetic flux linked to plasma facing elements only, to obtain a model that accounts for the dynamics of the whole system; moreover, the flux perturbation approach guarantees that plasma will evolve through stable equilibrium points when applying the linearizing procedure, since flux conservation and the presence of ideal conductors surrounding the plasma assure plasma stability during the simulation. Eventually, unstable dynamics will emerge when introducing material resistivity by means of the matrix R. The system can be partitioned as follows:

$$I = [\ \underbrace{I'_v}_{n_v}\ \ \underbrace{I'_{sh}}_{n_{sh}}\ \ \underbrace{I'_{st}}_{n_{st}}\ \ \underbrace{I'_a}_{n_a}\ ]'.$$

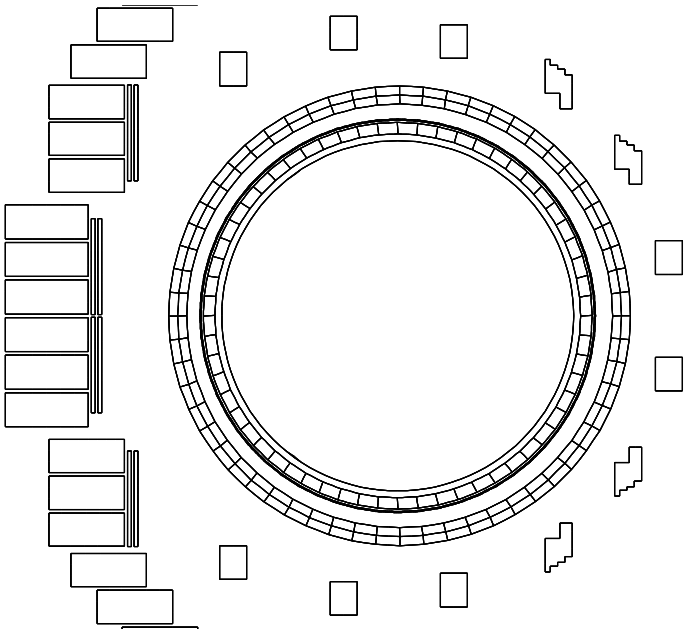

Figure 5.1: Discretized mesh used to derive the linear model

I_v are the currents in vessel elements, I_{sh} in shell elements, I_{st} in structure elements and I_a in active coils. The same partitioning is done on the flux vector:

$$\Psi = [\ \underbrace{\Psi'_v}_{n_v}\ \ \underbrace{\Psi'_{sh}}_{n_{sh}}\ \ \underbrace{\Psi'_{st}}_{n_{st}}\ \ \underbrace{\Psi'_a}_{n_a}\ ]'.$$

If we group in I_z currents not related to vessel elements, $I_z = [\ I'_{sh}\ I'_{st}\ I'_a\ ]'$, and in the same way $\Psi_z = [\ \Psi'_{sh}\ \Psi'_{st}\ \Psi'_a\ ]'$, we obtain

$$\begin{bmatrix}\Psi_v\\ \Psi_z\end{bmatrix} = L^* \begin{bmatrix}I_v\\ I_z\end{bmatrix}, \quad L^* = \begin{bmatrix}L^*_v L^*_{vz}\\ L^*_{vz} L^*_z\end{bmatrix}, \quad K^* = (L^*)^{-1} = \begin{bmatrix}K^*_v K^*_{vz}\\ K^*_{vz} K^*_z\end{bmatrix};$$

n_v flux perturbations are imposed on vessel elements:

$$\Psi_v \rightarrow \Psi_v + \delta\Psi_{v,i},$$

each one of these perturbations is imposed in the simulator by applying for a time interval Δt a voltage proportional through the constant $\kappa/\Delta t$ to a column of $L_{0,v}$, the part of the vacuum inductance matrix relative to vessel elements, leading to

$$\delta\Psi_{v,i} = \int_t^{t+\Delta t} \frac{\kappa}{\Delta t}\ \mathrm{col}_i L_{0,v}\ dt = \kappa\ \mathrm{col}_i L_{0,v}.$$

Since all the other circuits are assumed to be ideally conductive, they will have no variation in linked flux. The resulting current perturbations in vessel elements δI_v can be grouped in $\Delta I_v = [\delta I_{v,1} \cdots \delta I_{v,n_v}]$. The following relation can be used to calculate the part of the inverse modified inductance matrix relative to vessel elements, K_v^*:

$$\Delta I_v = \kappa \, K_v^* L_{0,v}.$$

The rest of the K^* matrix is unchanged from the vacuum matrix $K_0 = (L_0)^{-1}$:

$$K_0 = \begin{bmatrix} K_{0,v} K_{0,vz} \\ K_{0,vz} K_{0,z} \end{bmatrix}, \quad K_{vz}^* = K_{0,vz}, \quad K_z^* = K_{0,z}.$$

The full modified inductance matrix is finally obtained as $L^* = (K^*)^{-1}$. It is now easy to reintroduce circuit resistance and to obtain a state space dynamic model

$$\begin{aligned} \dot{x} &= Ax + Bu \\ y &= Cx \end{aligned}$$

where the state space variables are currents in the discretized circuits, $x = I$, and the input is applied voltage to the active coils:

$$A = -(L^*)^{-1} R \tag{5.1}$$

$$B = \text{col}_a (L^*)^{-1}; \tag{5.2}$$

col_a indicates the operation of extracting the columns of $(L^*)^{-1}$ relative to active coils.

The flux perturbation method is also very effective to identify the matrix C that will produce a set of outputs y including plasma-first wall distance, plasma centroid displacements, and other plasma-related measurements. Actually, a variation of these quantities can be ascribed to flux perturbations in a closed line surrounding the plasma. Firstly, a proportionality relation between flux perturbations in vessel elements and plasma-related quantities y is identified by grouping the resulting perturbations of output quantities in a rectangular matrix $\delta Y = [\delta y_1 \cdots \delta y_{n_v}]$. The perturbations are columns of $L_{0,v}$, so the matrix $C_{\psi,v}$ linking flux perturbations in vessel elements and outputs is computed as follows:

$$y = C_{\psi,v} \Psi_v, \quad C_{\psi,v} = \delta Y (L_{0,v})^{-1}. \tag{5.3}$$

There is no direct dependence of plasma-related measurements from flux perturbations in the other circuits (eventually, the dependence from external circuit dynamics is accounted by inductive coupling), so

$$y = C_\psi \Psi, \quad C_\psi = [C_{\psi,v} | \, 0 \,].$$

It is easy to derive the final C matrix linking circuit currents and outputs, since flux perturbations in vessel elements in the presence of plasma are derived from the whole current distribution by considering the modified inductance matrix:

$$C = C_\psi L^*. \tag{5.4}$$

5.2 Calculation of the resistance matrix

To take into account conductor resistivity in the linear model, the R matrix must be derived. The matrix is assumed to be diagonal. Active coil circuits are assumed to be not resistively coupled: actually, resistive coupling exists between F and M coils, but it will be considered at a successive stage. Discretized conductors are assumed to be not resistively coupled since the most relevant coupling effect is provided by the inductive term; resistive coupling will eventually be considered at a successive stage as well, when passing from side current equations to mesh current equations (sect 5.3).

The intrinsic resistance of the active coils is known, and is reported in table 5.3. It is notable that in double null Tokamak configuration, some resistances are connected in series to F coils, to increase system controllability.

Coil	$M1$	$M2$	$M3$	$M4$
$\mathbf{R}[\mathbf{m\Omega}]$	3.618	3.820	3.626	3.930

$\mathbf{R_a}[\mathbf{m\Omega}]$
600

Coil	$F1$	$F2$	$F3$	$F4$	$F5$	$F6$	$F7$	$F8$
$\mathbf{R}[\mathbf{m\Omega}]$	34.64	37.34+R_a	50.34	59.59+R_a	68.77	77.54	83.35+R_a	86.73

Table 5.3: Intrinsic M and F coil resistance
R_a is connected in series in DN Tokamak discharges

Resistance of passive elements is calculated by the simulator on the basis of toroidal geometry and material conductivity, that is set as follows for vessel, shell and structure elements:

$$\sigma_v = 0.112 \cdot 10^6[\Omega^{-1}m^{-1}], \quad \sigma_{sh} = 0.556 \cdot 10^8[\Omega^{-1}m^{-1}], \quad \sigma_{st} = 0.9259 \cdot 10^6[\Omega^{-1}m^{-1}].$$

These values of conductivity are scaled values that take into account, for instance, the fact that the vessel has a corrugated structure and thus has a higher resistance than that of a full torus. Maxfea calculates the total resistance of the material with a numerical integration that is in good agreement with the analytical solution for a toroidal conductor

with thickness δ, average radius r and axis R_0:

$$R_{tor} = \left(\frac{\sigma \, \delta \, r}{\sqrt{R_0^2 - r^2}} \right)^{-1} .$$

The resulting total toroidal resistance of vessel, shell and structure the non discretized mesh used for model validation is also equal, considering roundoff errors, to the value obtained considering the three circuits formed respectively by the parallel connection of the elements composing vessel, shell and structure in the discretized mesh with material resistivity. This version of the 2D mesh has actually been used to compute the resistance of elements $R_{v,i}$, $R_{sh,i}$, $R_{st,i}$ composing the linear model, so the total toroidal resistance of the three passive conductors can be computed as follows

$$R_v = \left(\sum_{i=1}^{n_v} \frac{1}{R_{v,i}} \right)^{-1}, \quad R_{sh} = \left(\sum_{i=1}^{n_s h} \frac{1}{R_{sh,i}} \right)^{-1}, \quad R_{st} = \left(\sum_{i=1}^{n_s t} \frac{1}{R_{st,i}} \right)^{-1}$$

and, as stated before, these values are in good agreement with the resistance of passive toroidal elements in the non discretized resistive mesh. Values of total resistance for passive structures are reported in table 5.4.

$R_v[\Omega]$	$1.178 \cdot 10^{-3}$
$R_{sh}[\Omega]$	$2.261 \cdot 10^{-5}$
$R_{st}[\Omega]$	$7.758 \cdot 10^{-5}$

Table 5.4: Total resistance for toroidal structures

5.3 Reconnection of the electromagnetic model

Passive conductors Circuit equations for the electric network representing the electromagnetic model must be manipulated to impose some of the constraints that exist on the real system. One of these constraints is the condition of zero total toroidal current in the shell and structure, due to the presence of poloidal gaps (visible in fig. 2.2) that break electric continuity.

This condition can be imposed by reconnecting the elements composing discontinuous structures, passing from side currents representation (i_k variables in fig. 5.2, left) to mesh currents representation ($\tilde{i}_k$ variables in fig. 5.2, right). This is a transformation

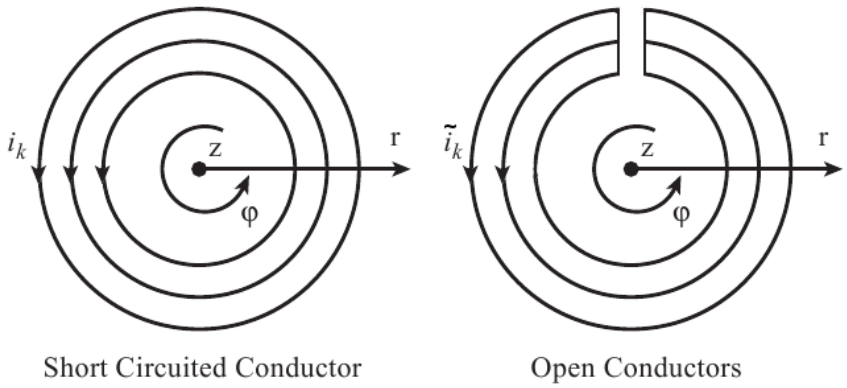

Figure 5.2: Side currents and mesh currents representations

that removes one degree of freedom so it is not invertible. The transformation is defined considering T matrices that allow to obtain linked flux with reconnected model elements starting from linked flux in the non reconnected model. In the case of shell and structure elements involved in the reconnection, this can be expressed as

$$\Psi_{sh} = \begin{bmatrix} \psi_1 \\ \psi_2 \\ \vdots \\ \psi_{n,sh} \end{bmatrix} \xrightarrow{T_{sh}} \tilde{\Psi}_{sh} = \begin{bmatrix} \tilde{\psi}_1 \\ \tilde{\psi}_2 \\ \vdots \\ \tilde{\psi}_{n,sh-1} \end{bmatrix}$$

$$\Psi_{st} = \begin{bmatrix} \psi_1 \\ \psi_2 \\ \vdots \\ \psi_{n,st} \end{bmatrix} \xrightarrow{T_{st}} \tilde{\Psi}_{st} = \begin{bmatrix} \tilde{\psi}_1 \\ \tilde{\psi}_2 \\ \vdots \\ \tilde{\psi}_{n,st-1} \end{bmatrix}.$$

Once mesh currents $\tilde{I}_{sh}$ and $\tilde{I}_{st}$ are computed considering the dynamics of the reconnected model, it is possible to obtain the resulting side currents as

$$\tilde{I}_{sh} = \begin{bmatrix} \tilde{i}_1 \\ \tilde{i}_2 \\ \vdots \\ \tilde{i}_{n,sh-1} \end{bmatrix} \xrightarrow{T'_{sh}} I_{sh} = \begin{bmatrix} i_1 \\ i_2 \\ \vdots \\ i_{n,sh} \end{bmatrix}$$

$$\tilde{I}_{st} = \begin{bmatrix} \tilde{i}_1 \\ \tilde{i}_2 \\ \vdots \\ \tilde{i}_{n,st-1} \end{bmatrix} \xrightarrow{T'_{st}} I_{st} = \begin{bmatrix} i_1 \\ i_2 \\ \vdots \\ i_{n,st} \end{bmatrix}.$$

When considering the sum of side currents obtained from the reconnected mesh current model, the condition of zero total toroidal current will be satisfied. It is important to stress that we are performing a reconnection of the electromagnetic model instead of defining a linear transformation between two equivalent linear models, or a projection to a linear subspace. Shell and structure elements are reconnected by imposing

$$T_{sh} = \begin{bmatrix} 1 & -1 & 0 & \cdots & 0 \\ 0 & 1 & -1 & \cdots & 0 \\ & & \ddots & \ddots & \\ 0 & \cdots & 0 & 1 & -1 \end{bmatrix} \in \mathbb{Z}^{(n,sh-1)\times n,sh}$$

$$T_{st} = \begin{bmatrix} 1 & -1 & 0 & \cdots & 0 \\ 0 & 1 & -1 & \cdots & 0 \\ & & \ddots & \ddots & \\ 0 & \cdots & 0 & 1 & -1 \end{bmatrix} \in \mathbb{Z}^{(n,st-1)\times n,st};$$

these matrices define the following transformations that are used to obtain the reconnected model:

$$\tilde{\Psi}_{sh} = T_{sh}\Psi_{sh} \tag{5.5}$$

$$\tilde{\Psi}_{st} = T_{st}\Psi_{st} \tag{5.6}$$

$$I_{sh} = T'_{sh}\tilde{I}_{sh} \tag{5.7}$$

$$I_{st} = T'_{st}\tilde{I}_{st}. \tag{5.8}$$

If I_{sh} and I_{st} are obtained through transformation (5.7) and (5.8), the conditions

$$\sum_{k=1}^{n,sh} i_{sh,k} = 0, \qquad \sum_{k=1}^{n,st} i_{st,k} = 0$$

will hold. These transformation can be applied to the submatrices of L^* and R relative to shell and structure elements to define equivalent inductance and resistance submatrices for the reconnected model:

$$\tilde{L}^*_{sh} = T_{sh}L^*_{sh}T'_{sh} \quad \tilde{L}^*_{st} = T_{st}L^*_{st}T'_{st}$$
$$\tilde{R}_{sh} = T_{sh}R_{sh}T'_{sh} \quad \tilde{R}_{st} = T_{st}R_{st}T'_{st}.$$

However, mutual inductances with other elements must also be transformed. T_{sh} and T_{st} can be completed by the identity matrix in positions relative to other elements to define a transformation on the whole L^* and R matrices. This task will be formalized at the end of this section.

Active conductors We will now perform electromagnetic reconnection of active conductors. The first operation that must be done is the reconnection of $F7$ coils since, as mentioned in sect. 3.3, the simulator needs to alter current distribution in active coils to converge to an equilibrium with the magnetic axis imposed by the user. The perfect top/down symmetry of RFX-mod has to be broken, and while all the other coil circuits are already defined complying with series interconnections in the real machine, $F7$ is divided in its upper $F7,u$ and lower $F7,d$ elements in the linearizing procedure. However, the reconnection of these elements is straightforward defined, considering that

$$\psi_{F7} = \begin{bmatrix} 1 & 1 \end{bmatrix} \begin{bmatrix} \psi_{F7,u} \\ \psi_{F7,d} \end{bmatrix}, \quad \begin{bmatrix} I_{F7,u} \\ I_{F7,d} \end{bmatrix} = \begin{bmatrix} 1 \\ 1 \end{bmatrix} I_{F7}.$$

The first manipulation is thus trivial, and can be obtained by summing the two adjacent rows and columns relative to the $F7$ coil in the L^* and R matrices. We will not formalize this technical passage, assuming that L^* and R are already reduced so that the separation between $F7,u$ and $F7,d$ is not present.

It is convenient to focus on circuit reconnection equations that must be applied to model more realistically the poloidal circuit of RFX-mod (2.3), that is characterized by the presence of sector interconnections that introduce resistive coupling between M and F coils. We consider a condition of perfect balance between sectors: the resistance R_0 in figure 2.6 is assumed to be infinite, and all sectors are subject to zero total current, so coupling between different sectors can be neglected:

$$\begin{cases} I_{S1} = I_{M1} + I_{F2} + I_{F7} = 0 \\ I_{S2} = I_{M2} + I_{F1} + I_{F8} = 0 \\ I_{S3} = I_{M3} + I_{F4} + I_{F5} = 0 \\ I_{S4} = I_{M4} + I_{F3} + I_{F6} = 0 \end{cases} \tag{5.9}$$

These assumption are valid since we do not need to model PCAT converters. Current in the F coils is controlled by PVAT converters, so a variation in total sectors current is substantially a variation in M coils current, required to provide transformer action and sustain plasma current; in validation, however, we will set the simulator to conserve plasma current, and plasma resistivity will not be modelled. We will simply assume that it is possible to study the equivalent equilibrium point with I_M rescaled to comply with the condition of zero total sector current. This hypothesis simplifies the nonlinear model of the poloidal circuit used in simulations (appendix C), and is not restrictive for what concerns controller design: M coils are arranged to generate no net magnetic field in the plasma region, so it will be still possible to apply the shape controller in the case of nonzero total sector current without modification. The equilibrium point defined by table 5.2, obtained from experimental data, is characterized by the I_S currents reported in table 5.5.

Sector	S1	S2	S3	S4
I$[$**A**$]$	-3259	-3259	-3243	-3266

Table 5.5: Sector currents in shot #29746, $t \approx 0.4s$

We will thus consider the rescaled equilibrium currents reported in tab. 5.6, where I_M are changed to comply with the constraints imposed by eq. (5.9).

Coil	$M1$	$M2$	$M3$	$M4$
I[A]	1006	2140	1538	-1545

Coil	$F1$	$F2$	$F3$	$F4$	$F5$	$F6$	$F7$	$F8$
I[A]	-2531	-910	2580	-24	-1514	-1035	-96	390

Table 5.6: Rescaled coil currents, complying with $I_{S,i} = 0,\ i = 1 \dots 4$

Before reconnection, circuit equations model the situation that is represented in fig. 5.3.a (sector S1 only): there are 3 independent currents per sector. Imposing eq. (5.9) allows to express I_M currents in function of I_F currents, reducing the model to 2 independent currents per sector. The resulting model (fig. 5.3.b) is obtained applying the

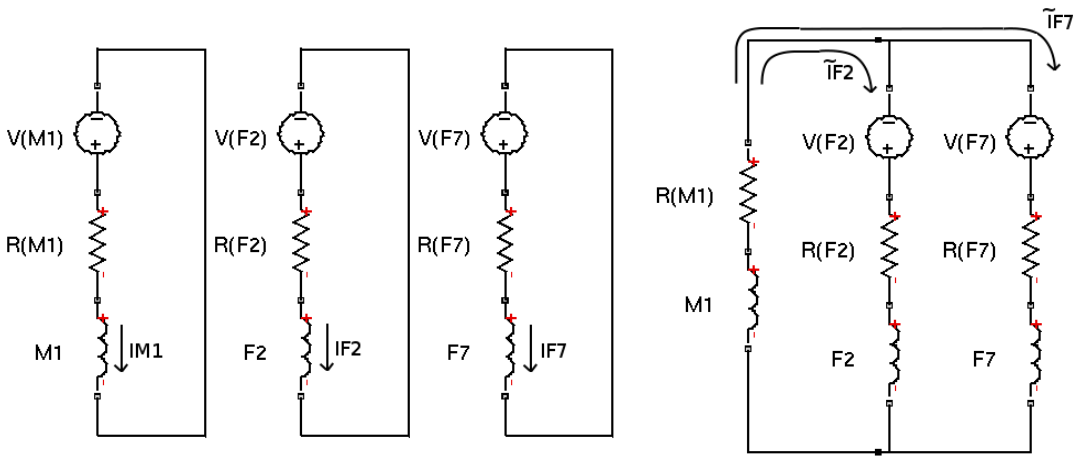

(a) Sector S1 before reconnection (b) Sector S1 after reconnection

Figure 5.3: Poloidal circuit sector representations in the linear model

following reconnection matrix

$$T_a = \left[\begin{array}{cccc|c} 0 & -1 & 0 & 0 & \\ -1 & 0 & 0 & 0 & \\ 0 & 0 & 0 & -1 & \\ 0 & 0 & -1 & 0 & \\ 0 & 0 & -1 & 0 & I_{8\times 8} \\ 0 & 0 & 0 & -1 & \\ -1 & 0 & 0 & 0 & \\ 0 & -1 & 0 & 0 & \end{array}\right]$$

that allows to obtain I_M and I_F currents separately once $\tilde{I}_F$ currents are computed for the reconnected network. Clearly, $I_F = \tilde{I}_F$ while I_M is computed as the opposite of the sum of the two F coils currents in the same sector. The resulting relations for linked flux and currents are expressed as

$$\tilde{\Psi}_F = T_a \begin{bmatrix} \Psi_M \\ \Psi_F \end{bmatrix}, \quad \begin{bmatrix} I_M \\ I_F \end{bmatrix} = T_a' \tilde{I}_F.$$

Complete reconnection matrix The definition of reconnection matrices that allow to obtain a complete reconnected electromagnetic model can be resumed by the following scheme: T matrices allow to obtain linked flux to circuit elements in the reconnected

model from linked flux in the non reconnected model :

$$\begin{aligned} \Psi_{sh} &\xrightarrow{T_{sh}} \tilde{\Psi}_{sh} \\ \Psi_{st} &\xrightarrow{T_{st}} \tilde{\Psi}_{st} \\ \Psi_{a} &\xrightarrow{T_{a}} \tilde{\Psi}_{a}. \end{aligned}$$

In the same way, after currents in the reconnected model have been computed according to reconnected model dynamics, the resulting side currents can be computed considering T' matrices:

$$\begin{aligned} \tilde{I}_{sh} &\xrightarrow{T'_{sh}} I_{sh} \\ \tilde{I}_{st} &\xrightarrow{T'_{st}} I_{st} \\ \tilde{I}_{a} &\xrightarrow{T'_{a}} I_{a}. \end{aligned}$$

The linear model of the reconnected network can be finally obtained applying a reconnection matrix T to the inductance matrix L^* and resistance matrix R, so that

$$\tilde{L}^* = TL^*T', \quad \tilde{R} = TRT'. \tag{5.10}$$

The T matrix takes the form

$$T = \begin{bmatrix} I_{n_v \times n_v} & 0 & 0 & 0 \\ 0 & T_{sh} & 0 & 0 \\ 0 & 0 & T_{st} & 0 \\ 0 & 0 & 0 & T_a \end{bmatrix}. \tag{5.11}$$

We can now apply eq. (5.10) to obtain matrices $\tilde{L}^*$ and $\tilde{R}$; state space matrices are finally obtained as follows:

$$\begin{aligned} \tilde{A} &= -(\tilde{L}^*)^{-1}\tilde{R} \\ \tilde{B} &= \mathrm{col}_a(\tilde{L}^*)^{-1} \\ \tilde{C} &= [C_{\psi,v}\ 0]\tilde{L}^*. \end{aligned} \tag{5.12}$$

Resistive compensation It is useful to calculate input voltage required to sustain the equilibrium configuration reported in tab. 5.6. At equilibrium, $V_{PVAT,ref} = \tilde{R} I_{F,ref}$, where $\tilde{R}$ is not diagonal, accounting of resistive coupling in the poloidal circuit. The resulting PVAT equilibrium voltages are reported in tab 5.7. Here and in the following, we will express PVAT applied voltage with the sign convention of the actuators, that can produce only positive voltage in the range

$$V_{PVAT,i}[V] \in [0,\ 1350], \quad i = 1 \ldots 8.$$

It is important to note that PVATs 3 and 8 are inverted with respect to standard machine operation to produce the double-null configuration.

PVAT	1	2	3	4	5	6	7	8
[V]	95.8	583.6	135.9	21.4	109.7	74.2	69.2	25.6

Table 5.7: PVAT voltages for resistive compensation

5.4 Plasma displacement instabilities

The linear system defined by eq. (5.12) contains two unstable eigenvectors, whose components over state space variables relative to vessel elements are graphed in figure 5.4. These eigenvectors are relative to horizontal and vertical plasma displacement instabilities, since they denote a distribution of currents in vessel, shell and structure elements that compensates for plasma displacement. If passive structures were ideally conductive, the effect of induced currents would be that of generating magnetic field producing a stabilizing force on the plasma. Passive structures resistivity leads to a dissipation of the stabilizing current distribution, so the horizontal/vertical instabilities will grow. The presence of a vertical unstable mode was actually expected and some estimates of its time constant have been already calculated in the case of ideally conductive coils (cfr. sect. 3.5). Actually, in the resistive model the horizontal unstable mode is dominant over the vertical mode, since time constants of the two modes (before the introduction of saddle

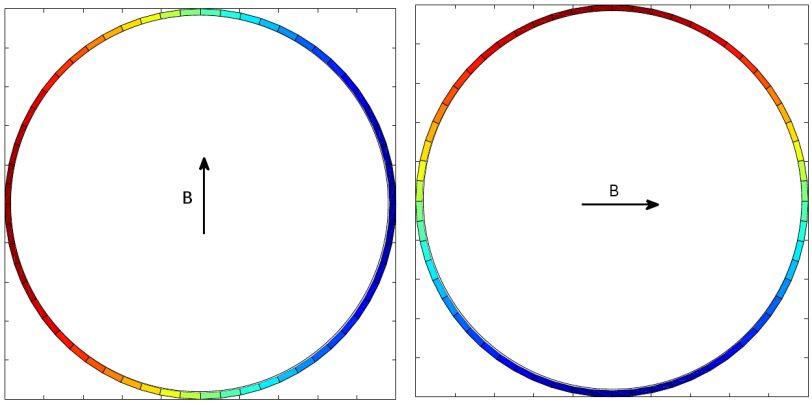

(a) Horizontal instability (b) Vertical instability

Figure 5.4: Components of unstable eigenvectors (vessel), and resulting field

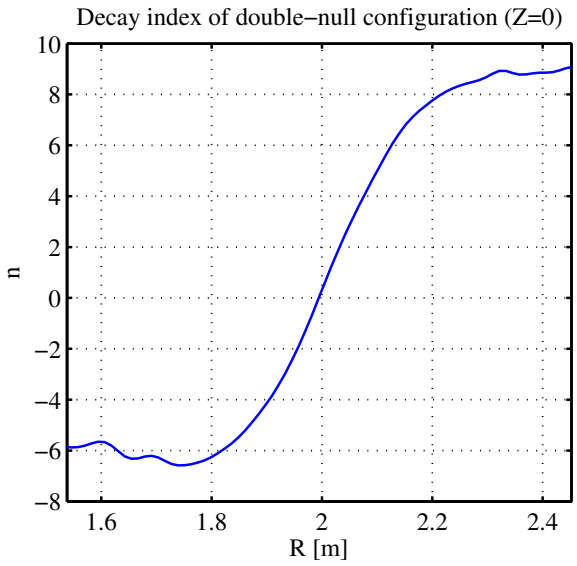

Figure 5.5: Decay index of the field generated by external coils

coils circuits) are:

$$\tau_{horz} = 51.12\ ms \qquad \tau_{vert} = 60.72\ ms.$$

The presence of the horizontal instability can be explained considering that $F8$ coils carry a positive current that exerts an attractive force on the plasma; the role of $F8$ coils in this configuration is actually to increase plasma volume and triangularity, elongating the plasma outwards. More formally, the presence of the instability is consistent with values of the decay index n [16] for this configuration:

$$n = -\frac{R}{B_Z}\frac{\partial B_Z}{\partial R}.$$

In the case of a circular plasma, the condition for vertical stability is $n > 0$, while for horizontal stability $n < \frac{3}{2}$ is required. The decay index for the double null configuration of interest has been computed from the external equilibrium field produced by active coils on the equatorial plane of the machine (Z=0), and is plotted in figure 5.5. Both the conditions stated above are violated.

Introduction of saddle coils circuits The two unstable modes have to be stabilized before setting up the shape control problem. In fact, F coils cannot be used to stabilize the vertical mode, since they cannot generate radial field on the equatorial plane. It is necessary to introduce in the model some conductors representing the saddle coils system of

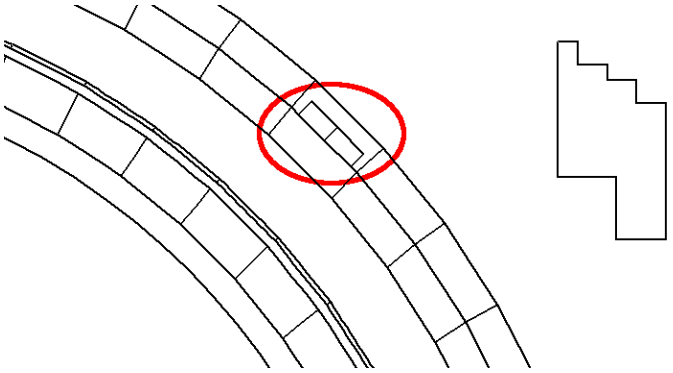

Figure 5.6: Mesh modifications to include saddle coils circuits, detail

RFX-mod, that can actually generate radial field in the real machine. 4 state space variables have been added, representing the axisymmetri current flowing in the saddle coils on the external side, on the upper side, on the internal side and on the bottom side of the machine. If these coils are all controlled with the same current, the effect of currents flowing along the $\hat{i}_\theta$ direction cancels between adjacent coils, so in axisymmetry it is only necessary to represent conductors that are parallel to the $\hat{i}_\phi$ direction (fig. 2.8). The mesh used in Maxfea has been modified to include these circuits (fig. 5.6), and the linearizing procedure has been repeated.

The introduction of ideally conductive saddle coils led to a model where the two unstable modes were still present, even if characterized by a longer time constant. Since it is necessary to feedback control saddle coils circuits to stabilize the system, it has been considered useful to model saddle coils circuits as resistive. As a matter of fact, the presence of ideal conductors in a voltage controlled system introduces poles in $s = 0$, making the system more difficult to control, and less realistic. To produce an equivalent value of resistance for the axisymmetric circuit, the section of the copper wire actually used in saddle coils windings has been calculated as $h_c \cdot w_c$; values of equivalent resistance of each saddle coil circuit have been computed considering the total length $l_{c,i}$ of the two conductors composing every circuit in toroidal geometry, and total number of turns per winding:

$$h_c = 1.3\ mm, \quad w_c = 2.8\ mm, \quad R_{sc,i} = 60\frac{\rho\, l_{c,i}}{h_c w_c}$$

leading to the following values of resistance:

$$R_{sc,ext} = 8.74\Omega, \quad R_{sc,up} = R_{sc,down} = 7.25\Omega, \quad R_{sc,int} = 5.76\Omega.$$

The initial R matrix has been extended including these values of resistance, and the

modified inductance matrix has been computed again considering the mesh with saddle coils conductors. The reconnection matrix T_a relative to active circuits has also been extended properly with the identity matrix in positions relative to saddle coils circuits. The vector of active coils currents including saddle coils, $\bar{I}_a$, is now defined as

$$\bar{I}_a = \begin{bmatrix} I_a \\ I_{SC} \end{bmatrix}, \quad I_{SC} = [\, I_{SC,ext},\, I_{SC,up},\, I_{SC,int},\, I_{SC,down}\,]'\,.$$

We denote with $\bar{L}^*$, $\bar{R}$, $\bar{T}$ the modified inductance and resistance matrices and the reconnection matrix relative to the model including saddle coil circuits. The inductance and resistance matrices of the reconnected model including saddle coils circuits are defined as

$$L_C^* = \bar{T}\bar{L}^*\bar{T}', \quad R_C = \bar{T}\bar{R}\bar{T}', \tag{5.13}$$

and the resulting linear model is defined as

$$\begin{aligned} A_C &= -(L_C^*)^{-1}R_C \\ B_C &= \mathrm{col}_a(L_C^*)^{-1} \\ C_C &= [C_{\psi,v}\ 0]L_C^*. \end{aligned} \tag{5.14}$$

The components of the two unstable eigenvectors, after introduction of resistive saddle coil circuits, are reported in figure 5.7. Time constants of the two unstable modes are slightly longer

$$\tau_{horz} = 54.29\ ms \qquad \tau_{vert} = 65.30\ ms$$

and in the case of the vertical instability, the inductive effect of plasma vertical displacement over external and internal saddle coils (#13 and #15) is clearly visible.

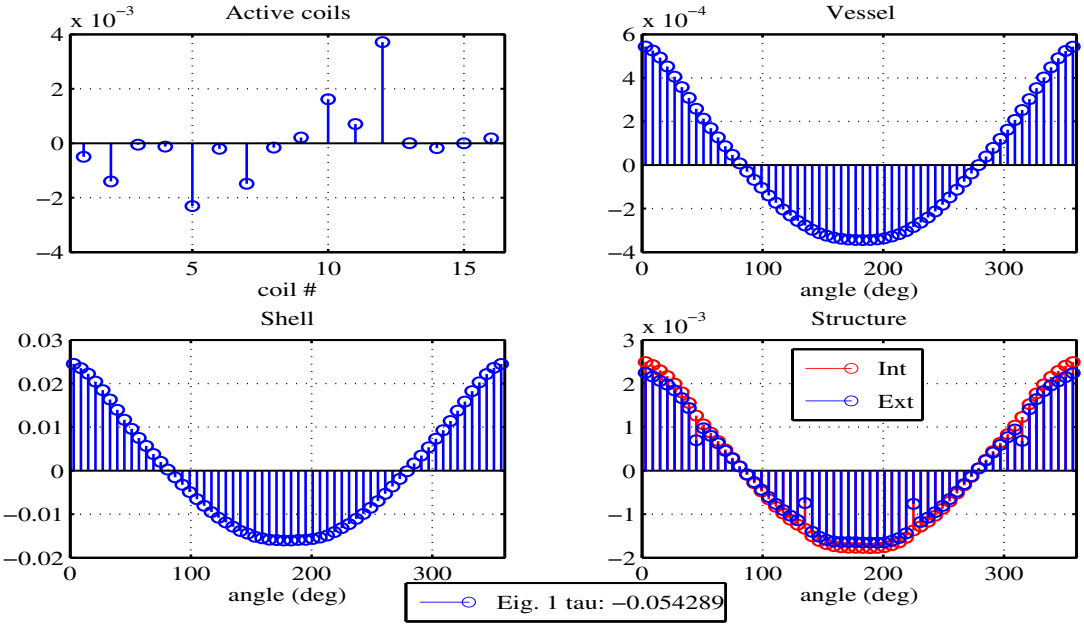

(a) Horizontal instability

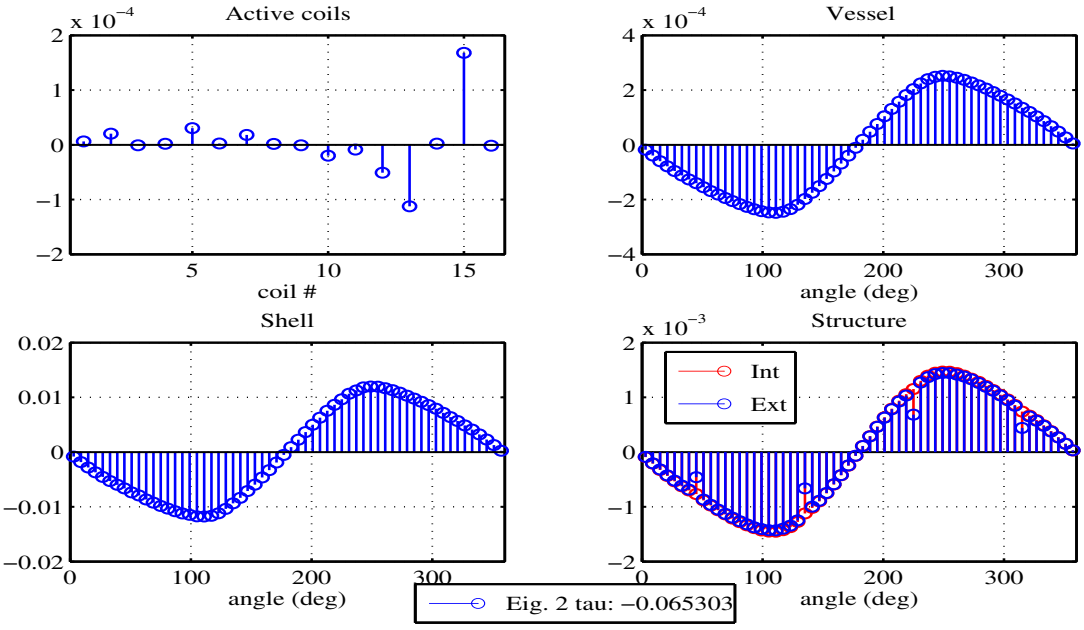

(b) Vertical instability

Figure 5.7: Unstable eigenvectors after introduction of saddle coils circuits
Coils $\#1-4$ are M coils, $\#5-12$ are F coils and $\#13-16$ are saddle coils

Pert. #	Coil currents	t_{start} [ms]	t_{end} [ms]	ΔV [V]
1	$I_{F,1}(-)$, $I_{F,2}(-)$, $I_{F,5}(-)$, $I_{F,6}(-)$	1.0	1.4	3000
2	$I_{F,3}(+)$	1.0	1.4	5000
3	$I_{F,8}(+)$	1.0	1.4	3000
4	$I_{SC,ext}(+)$, $I_{SC,int}(-)$	1.0	3.0	208×48

Table 5.8: Voltage perturbations for linear model validation

5.5 Validation of the linear model

To evaluate the correctness of the linear model that has been derived, some voltage pulses have been applied to the active circuits, comparing the response of the linear and nonlinear model. Table 5.8 lists the properties of the perturbations applied. In validation simulations, sign constraints of the PVAT converters are taken into account in terms of applied voltage sign and current sign, while voltage saturation limits are not imposed when applying voltage perturbations; voltage limits however will be applied to feedback control action in the next chapter.

By now, we will consider the effect of perturbations #1 and #2 applied to F coils. Perturbation #3 strongly impacts on the horizontal unstable mode both in the linear and nonlinear model, so it will be used to test the position stabilizing controller, together with perturbation #4 that affects the vertical mode. The application of the first two perturbations (figures 5.9, 5.10) shows that linear model shows good tendency agreement with the nonlinear model, but the presence of the horizontal unstable mode, whose impact is slightly overestimated in the linear model (figure 5.8), makes the agreement worst on longer time scales. The vertical unstable mode does not appear explicitly in the nonlinear model.

In section 3.5, the time constant of the vertical mode had been estimated for a similar double-null configuration, in the case of ideally conductive coils; the effect of a voltage perturbation would in that case produce a current variation in active coils that would remain over time, perturbing the equilibrium field on longer time scales, and the divergence of the vertical position was actually observed. In the case of resistive coils, the perturbation of the equilibrium field is restored, since current in the F coils tends to return to the equilibrium value supported by applied voltage for resistive compensation. For this reason, voltage perturbations on F coils are not very effective to produce the vertical instability; a destabilizing radial field produced by saddle coils (pert. #4) has a more

direct impact on vertical displacement; the effect of this perturbation will be analyzed in next chapter, where validation tests will be repeated after the inclusion of feedback action for plasma position stabilizing control. Overall agreement suggests however that the linear model that has been obtained represents a good starting point for controller design.

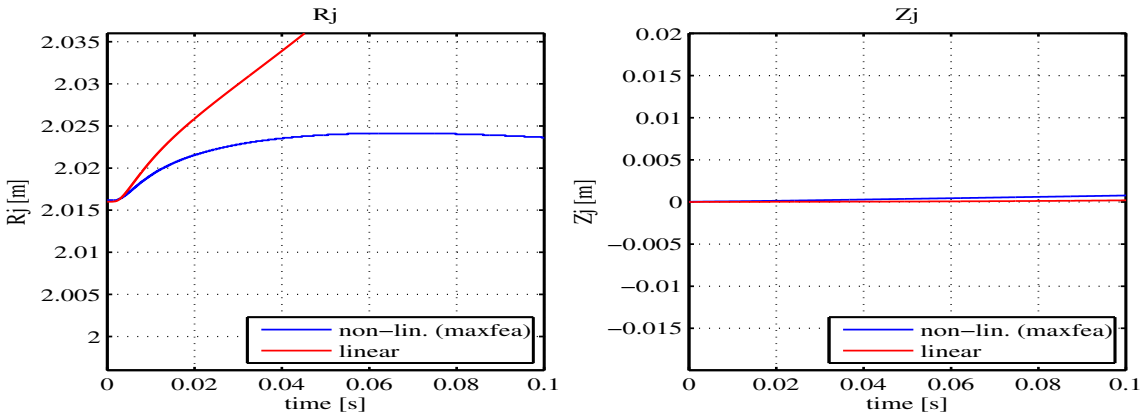

(a) Pert. #1

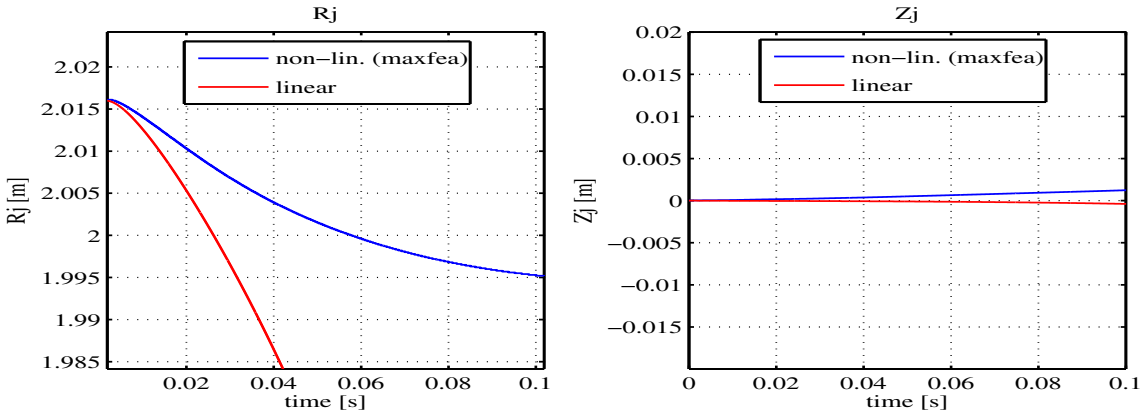

(b) Pert. #2

Figure 5.8: Perturbations #1 and #2, open loop. Current centroid

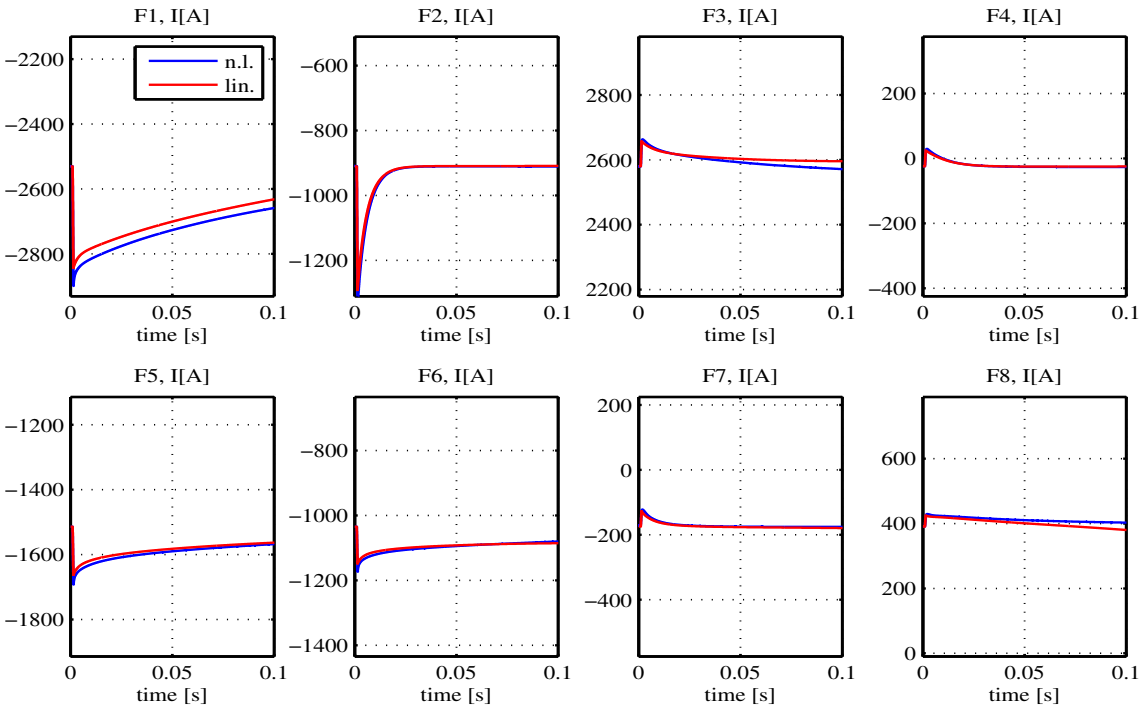

(a) F coils current

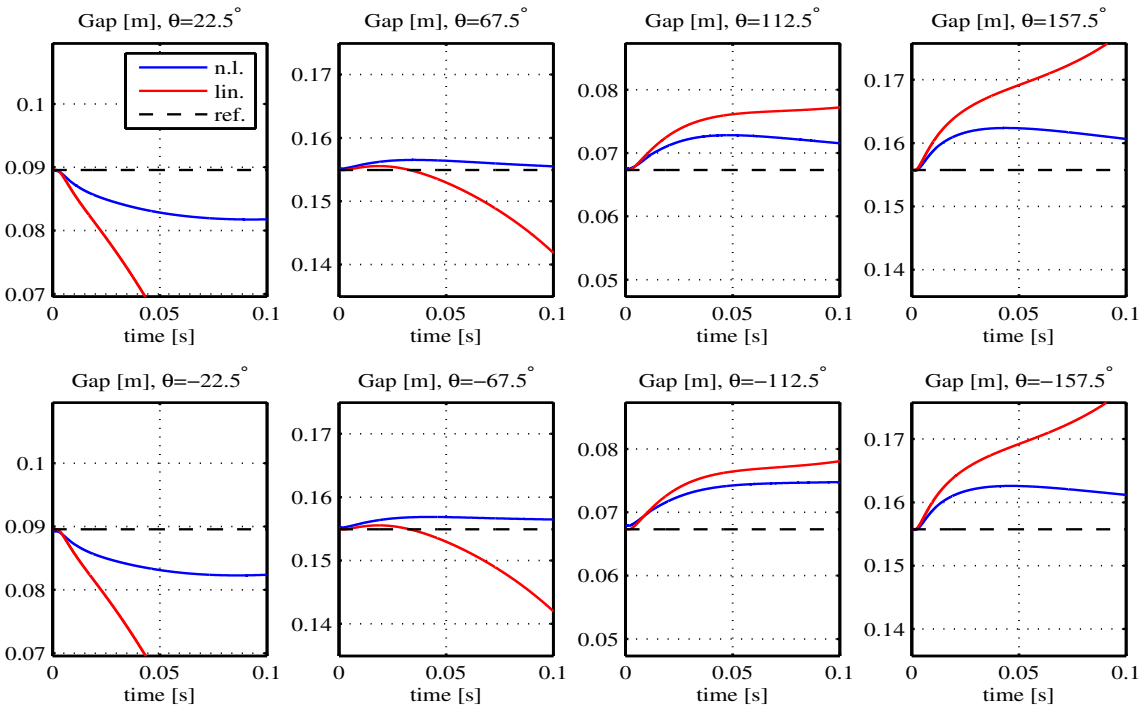

(b) Plasma-first wall gaps

Figure 5.9: Perturbation #1, open loop. F coils currents and gaps

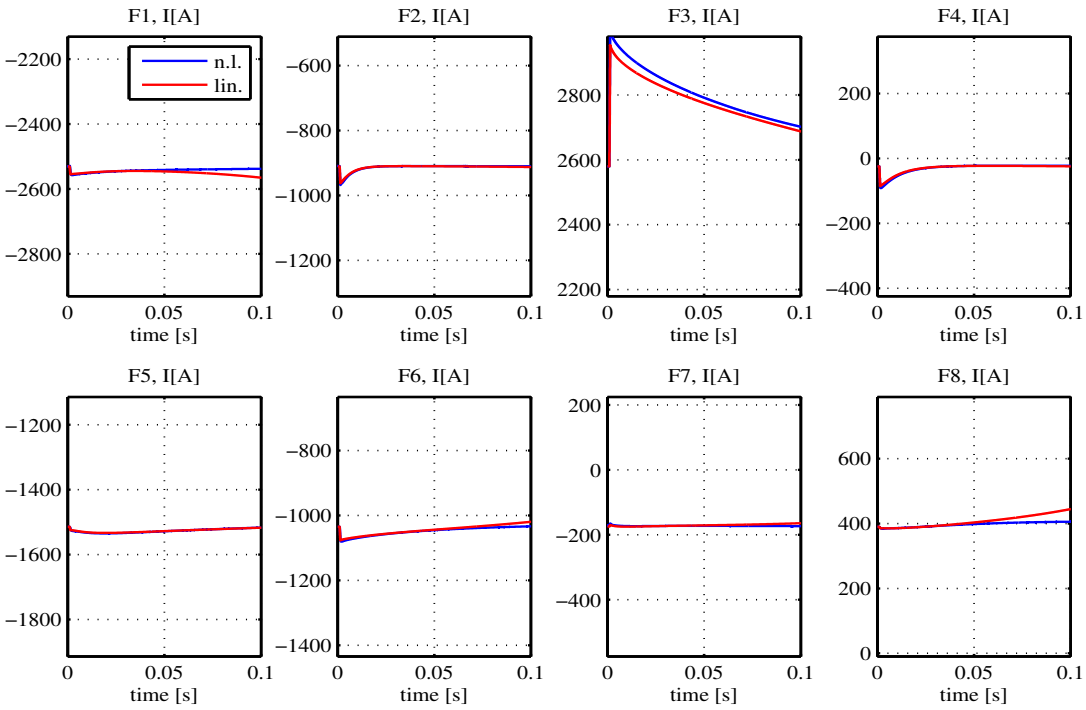

(a) F coils current

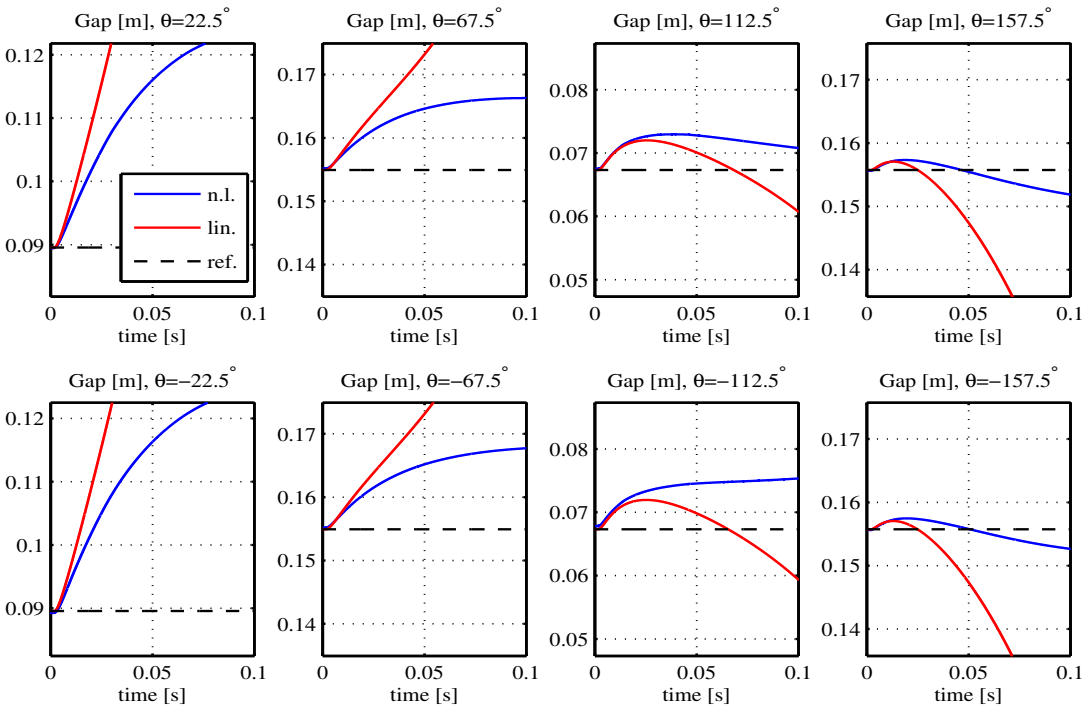

(b) Plasma-first wall gaps

Figure 5.10: Perturbation #2, open loop. Currents and gaps

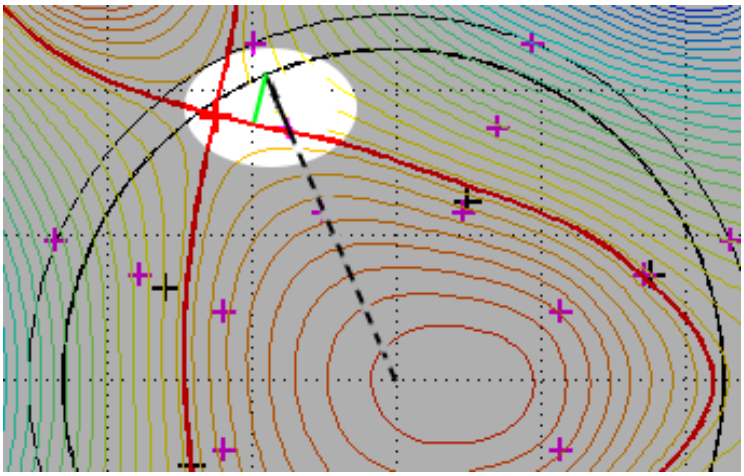

Figure 5.11: Definition of plasma-first wall distance measures
Green: geometric distance. Black: distance along r.

Gap measures in Maxfea An important improvement in the identification of the output relation between state space variables and gaps has been obtained by implementing in the nonlinear simulator a function that calculates plasma-first wall distance along the radius linking the machine axis to the first wall at the angle relative to flux-loop probes. In fact, Maxfea would normally compute first wall distance from user-defined points as a geometric distance, intersecting plasma boundary orthogonally (fig. 5.11, green solid line). The measure of interest is instead the evaluation of plasma-first wall distance along a line passing through the machine axis (fig. 5.11, black solid line). This measure is coherent with radial expansion methods described in section 4.1 suggesting that, in first approximation, a linear relation exists between flux perturbations in plasma facing elements and gaps along the radius. The difference between the two measures of distance are evident in gaps at $\theta = \pm 112.5°$, that are very close to the null point of the configuration. In fig. 5.12.a is reported the comparison between the output of the linear model derived considering the geometric distance computed by Maxfea and the same measure in nonlinear simulations (perturbation # 1); in figure 5.12.b is the same comparison when considering the distance along the radius both in the derivation of the linear model and in nonlinear simulations. The gap along the radius is actually the measure that has been used to produce validation plots reported in figures 5.9,5.10, and that will be used for controller design, since it leads to better adherence of the gap variations predicted by the linear model to the corresponding nonlinear simulation output.

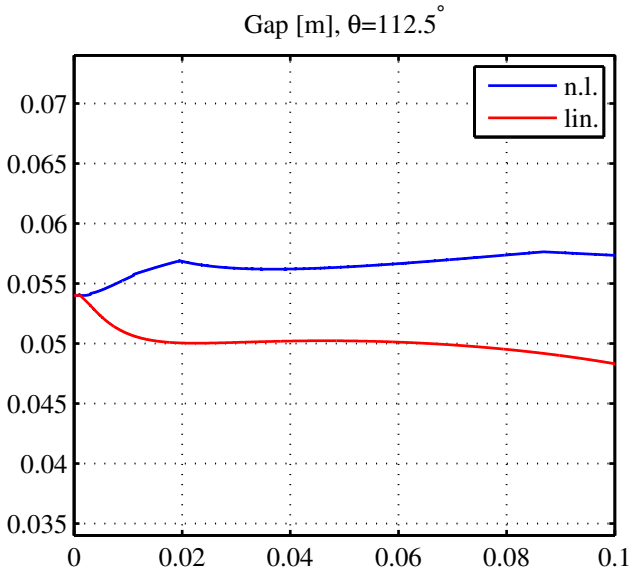

(a) Geometric distance

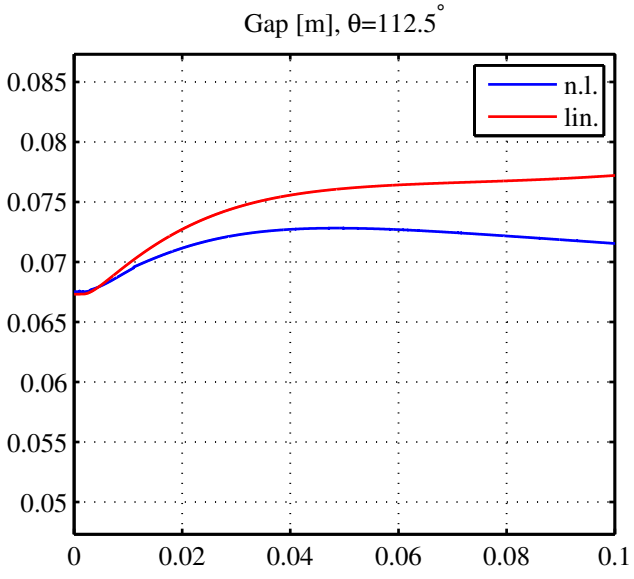

(b) Distance along r

Figure 5.12: Perturbation #1, different plasma-first wall distance measures

Chapter 6

Plasma position and shape control

6.1 Stabilization of the plasma current centroid

As seen in the previous chapter, the presence of unstable plasma displacement modes degrades the matching between the linear and nonlinear model, and poses a problem since the vertical unstable mode cannot be stabilized using F coils. The first task to be executed to successfully design the shape controller is to stabilize the vertical and horizontal displacement modes appearing in the linear model. A position stabilizing controller will be designed and applied to both the linear and the nonlinear model, to allow closed loop time domain response comparison.

Saddle coils power supply systems have no voltage sign constraints, and these coils have quicker dynamics than field shaping coils (sect. 2.3), thus the set can be used to suppress the unstable modes with timely action, leaving field shaping coils for shape control only. Therefore, the best way to achieve position stabilization is to use the set of saddle coils introduced in RFX-mod. Using these coils as actuators, the control action required to stabilize the two unstable modes can be decoupled: internal/external (cosine) saddle coils can generate radial field to stabilize the vertical unstable mode; top/down (sine) coils can generate vertical field to stabilize the horizontal mode.

We will be referring to the linear model 5.14; the controlled output variable for plasma position stabilization will be the current centroid position. The reason of this choice is that this measure can be estimated on the experiment from magnetic data with simple formulas (sect. 4.3), leading to a more robust control action. Plasma centroid coordinates have been included among the output variables in the derivation of the linear model: in the state-output matrix C_C, we will denote with $\mathrm{row}_R(C_C)$ and $\mathrm{row}_Z(C_C)$ the rows respectively relative to R_j and Z_j. The input of the linear model is the voltage applied to

active circuits; we will now consider the input matrices that take the form

$$B_R = B_C \begin{bmatrix} 0 & \cdots & 0 & 0 & -1 & 0 & 1 \end{bmatrix}', \qquad B_Z = B_C \begin{bmatrix} 0 & \cdots & 0 & 1 & 0 & -1 & 0 \end{bmatrix}';$$

these are the matrices required to obtain two single-input models, where inputs are respectively voltage applied to saddle coils circuits to generate vertical field (horizontal force on the plasma) and radial field (vertical force). The PBH test proves that the horizontal unstable mode is observable and reachable in the SISO model of the horizontal displacement, defined by the set of state-space matrices $(A_C, B_R, \text{row}_R(C_C), 0)$, with transfer function $G_{0,R}(s)$. The same holds for the vertical mode, in the model defined by $(A_C, B_Z, \text{row}_Z(C_C), 0)$ with transfer function $G_{0,Z}(s)$. Actually, the following matrices

$$\begin{bmatrix} A_C - \lambda_{horz} I & B_R \end{bmatrix} \qquad \begin{bmatrix} A_C - \lambda_{vert} I & B_Z \end{bmatrix}$$

$$\begin{bmatrix} A_C - \lambda_{horz} I \\ \text{row}_R(C_C) \end{bmatrix} \qquad \begin{bmatrix} A_C - \lambda_{vert} I \\ \text{row}_Z(C_C) \end{bmatrix}$$

have all full rank. It will now be shown that the application of two proportional feedback controllers, designed to stabilize the horizontal and vertical mode separately in the two SISO models, will actually stabilize the system as a whole.

When designing SISO controllers for the models defined hereby, the application of model reduction methods is mandatory, since classic SISO controller design techniques (e.g. root locus) would be unusable given the high number of poles and zeros. However, the open-loop bode diagram of the systems (fig 6.1.a and 6.2.a) shows a rather simple low-pass dynamic for both models, suggesting that the model can be approximated by a simpler one in terms of frequency response using PEM identification techniques. In fact, PEM identification leads to the minimization in the space of parameter vector ξ of a L_2 norm between $G_0(s)$, that in this case represents the full-state transfer function, and $G_\xi(s)$, the one obtained with PEM:

$$\min_\theta \int_{\omega_1}^{\omega_2} ||G_0(j\omega) - G_\xi(j\omega)||^2 d\omega.$$

In this case, $\omega_1 = 1\ rad/s$, $\omega_2 = 10^4\ rad/s$ provide a good approximation in the band of interest. A notable result is that PEM transfer functions reduce the order of the SISO models to 4, showing only one unstable pole. Actually, also model reduction techniques based on Hankel norm minimization have been tried, giving good approximation in terms of frequency response with 5 poles, but Hankel model reduction is based

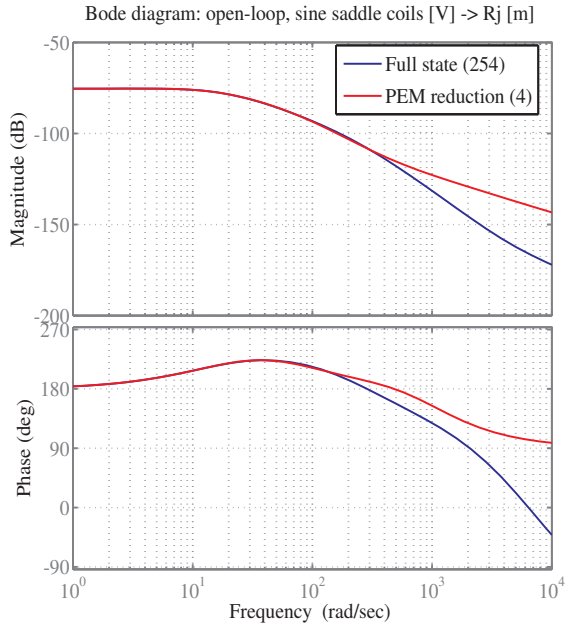

(a) $G_{0,R}(s)$ (full state) and $G_{\xi,R}(s)$ (PEM)

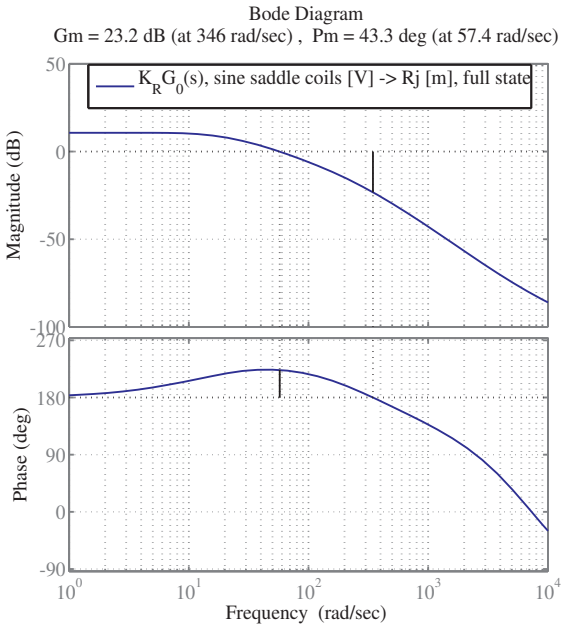

(b) $K_R \cdot G_{0,R}(s)$ (loop gain with controller)

Figure 6.1: Bode diagrams for horizontal position stabilization

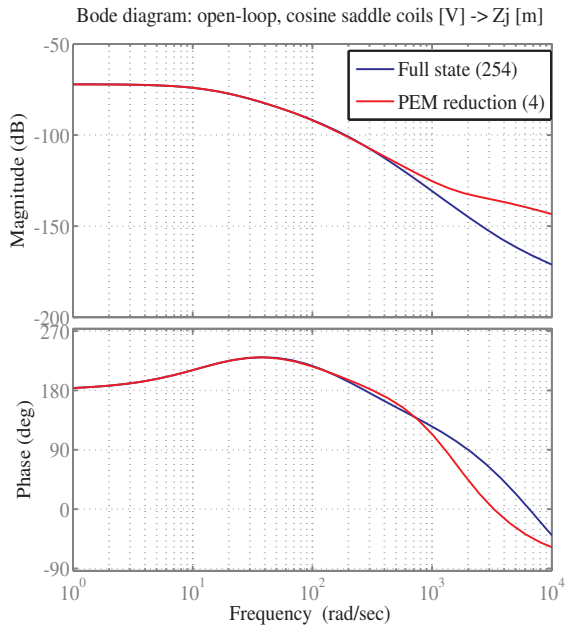

(a) $G_{0,Z}(s)$ (full state) and $G_{\xi,Z}(s)$ (PEM)

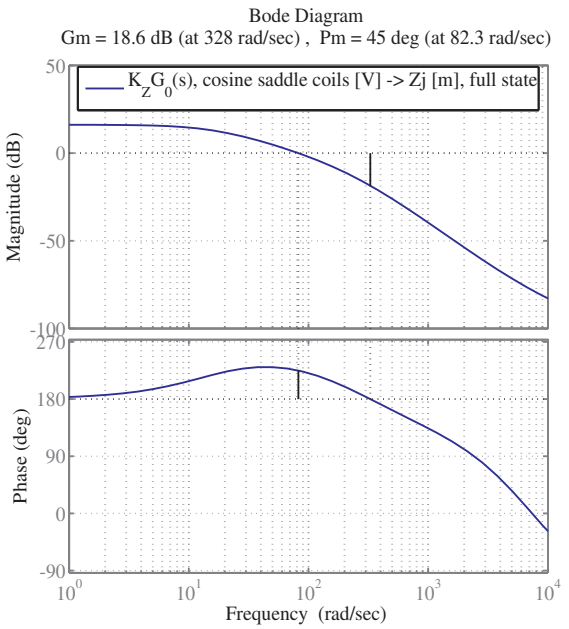

(b) $K_Z \cdot G_{0,Z}(s)$ (loop gain with controller)

Figure 6.2: Bode diagrams for vertical position stabilization

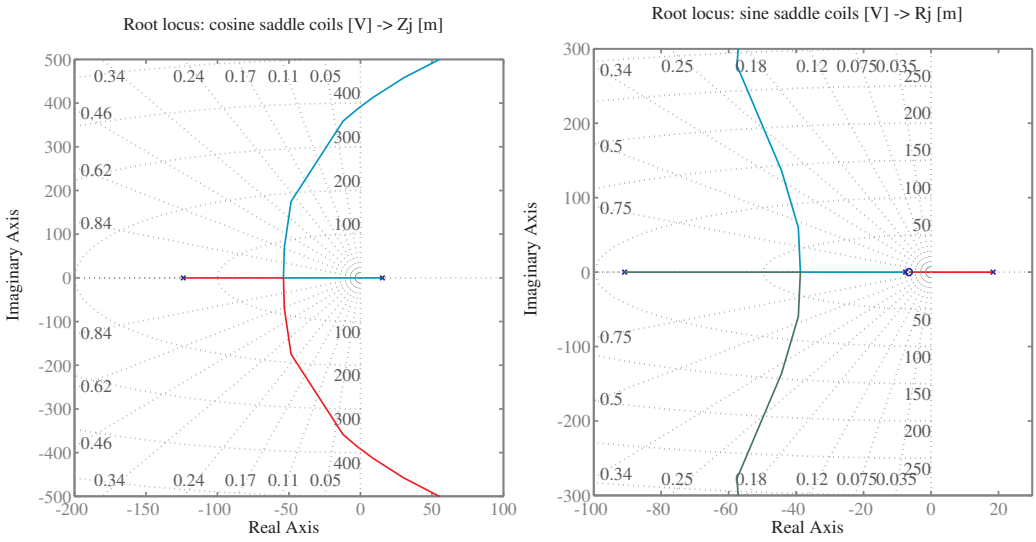

(a) Vertical displacement (b) Horizontal displacement

Figure 6.3: Root locus of reduced order (PEM) transfer functions, detail

on the hypothesis that the original system is stable, since the Hankel norm of a system $\mathcal{S} = (A, B, C, D)$ is defined as

$$||\mathcal{S}||_H^2 = \sup_{u \in L_2(-\infty,0]} \frac{\int_0^{+\infty} y(t)^2 dt}{\int_{-\infty}^{0} u(t)^2 dt} \tag{6.1}$$

where $y(t)$ is obtained from $u(t)$ through the reachability gramian. Hankel model reduction would operate only on the stable part of the system, maintaining the two unstable poles, and the root locus of the resulting transfer functions would show that the unstable pole relative to the horizontal instability is not controllable in the vertical displacement transfer function, and vice-versa (quasi-cancellation of unstable pole and zero). However, Hankel norm model reduction techniques will be considered to reduce the order of the stabilized system (sect. 6.2). Calling $G_{\xi,R}(s)$ the PEM TF between sine saddle coils voltage and horizontal displacement, and $G_{\xi,Z}(s)$ the PEM TF between cosine saddle coils voltage and vertical displacement, we have

$$\begin{aligned} G_{\xi,R}(s) &= \frac{-0.0006796(s-870.8)(s+418.7)(s+6.291)}{(s+903.9)(s+84.86)(s-16.75)(s+7.116)} \\ G_{\xi,Z}(s) &= \frac{0.00070302(s+470.1)(s^2-2356s+2.29\cdot 10^6)}{(s+3035)(s+649)(s+113.8)(s-13.6)}. \end{aligned}$$

The root locus (fig 6.3) suggests that a proportional controller will stabilize the reduced order transfer functions. Feedback gains were chosen to maximize closed-loop

bandwidth maintaining a phase margin of approx. $45°$:

$$K_R = 2.0 \cdot 10^4 \; [V/m] \qquad K_Z = 2.6 \cdot 10^4 \; [V/m]$$

The resulting loop gain frequency response of the two SISO systems has been evaluated on the original full-state model (fig 6.1.b and 6.2.b), showing good stability margins. It is also confirmed that the application of the decoupled feedback action to the state space system provides stabilization, in fact considering the closed loop system

$$\mathcal{S}_0 = (A_S, B_C, C_C, 0): \quad A_S = A_C - B_R K_R \text{row}_R(C_C) - B_Z K_Z \text{row}_Z(C_C), \tag{6.2}$$

the dominant eigenvalue and the relative time constant τ_S results

$$\max_i Re[\lambda_i(A_S)] = -4.7765, \quad \tau_S = 209 \; ms.$$

Simulations have been performed on both the linear and nonlinear model to test the controller, and the stabilization is effective (fig. 6.4 and 6.5). Validation tests are performed applying PVAT resistive compensation voltages, as reported in table 5.7, and altering the equilibrium with some of the voltage perturbations reported in table 5.8.

The destabilizing input for the horizontal displacement is a $+3000 \; V, \; 0.4 \; ms$ impulse on the $F8$ coils (perturbation #3). To rise the vertical instability, the F coils are not very effective, since they will not generate net radial field on the equatorial plane, and an impulse on cosine saddle coils is used instead. An impulse of $10000 \; V (48 \times 208.33 \; V), \; 2 \; ms$ (perturbation #4, tab. 5.8) is applied to the axisymmetric circuit, leading to a peak current over the $400A$ saturation limit of the real system. This represents a strong perturbation in terms of radial field; however, the nonlinear simulation does not show divergence on the vertical displacement of the plasma column in open loop (fig. 6.5.a): if the currents in the F coils are not altered, the plasma moves to another equilibrium point, with a vertical offset with respect to the original position; this could explain why on the experimental sessions the vertical instability was not clearly observed.

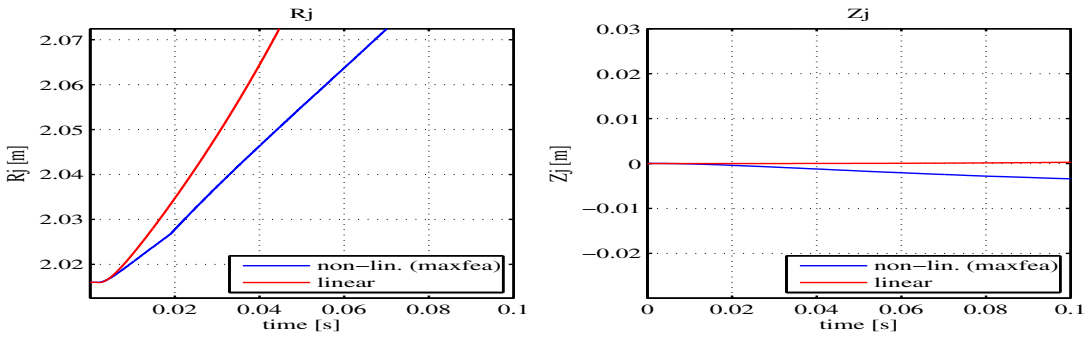

(a) Open loop response to voltage impulse

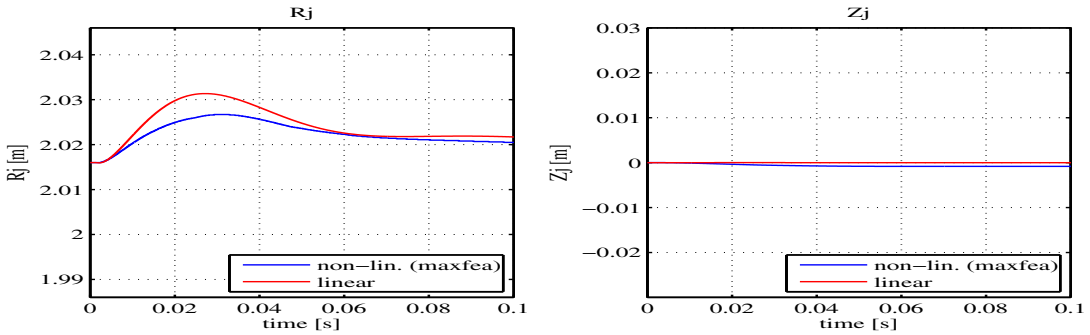

(b) Closed loop response to voltage impulse

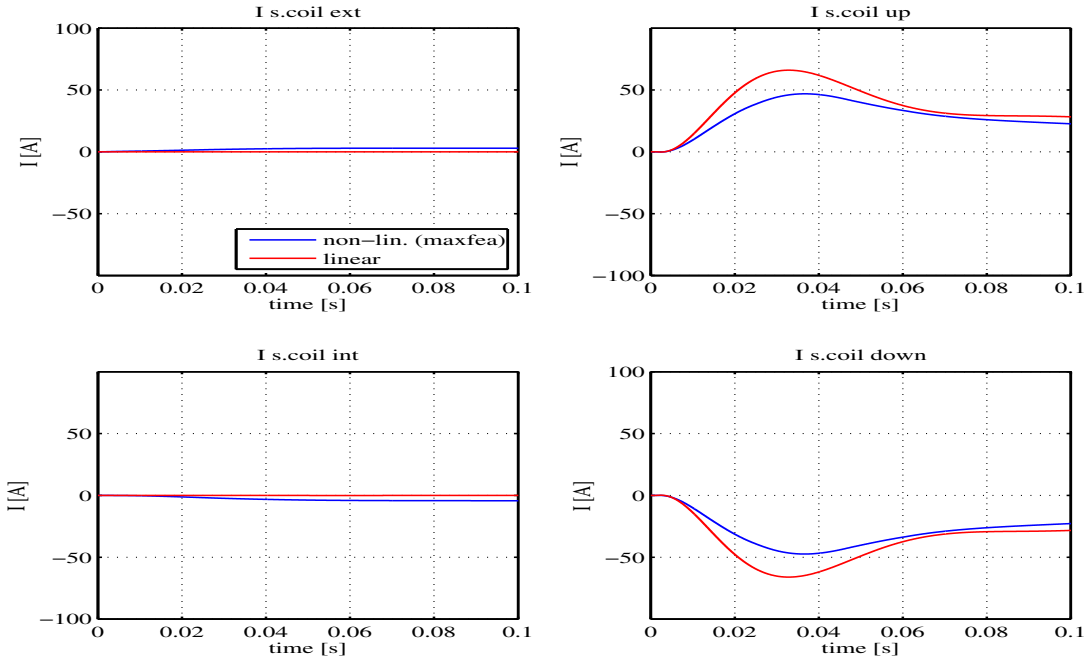

(c) Saddle coils currents in closed loop

Figure 6.4: Volt. perturbation #3, radial position controller test

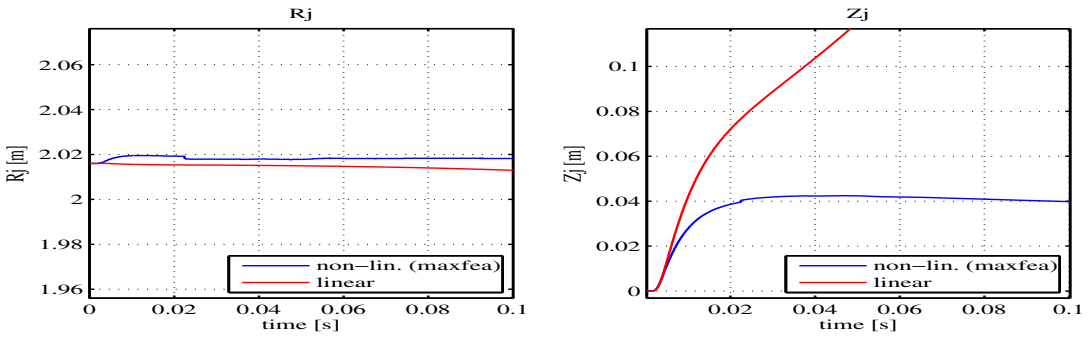

(a) Open loop response to disturbance

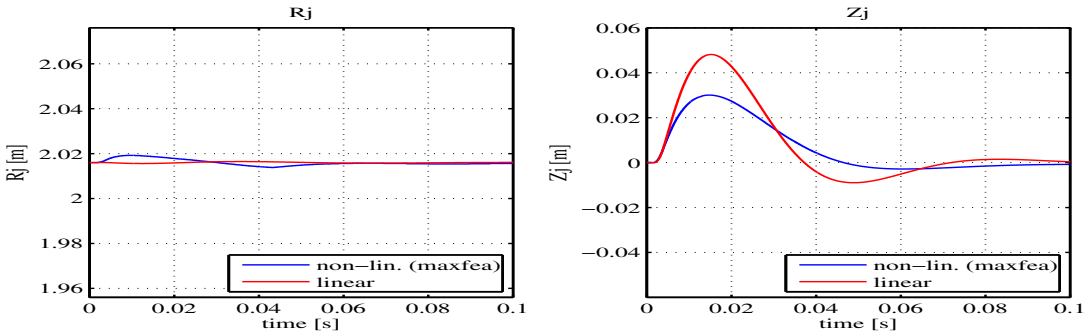

(b) Closed loop response to disturbance

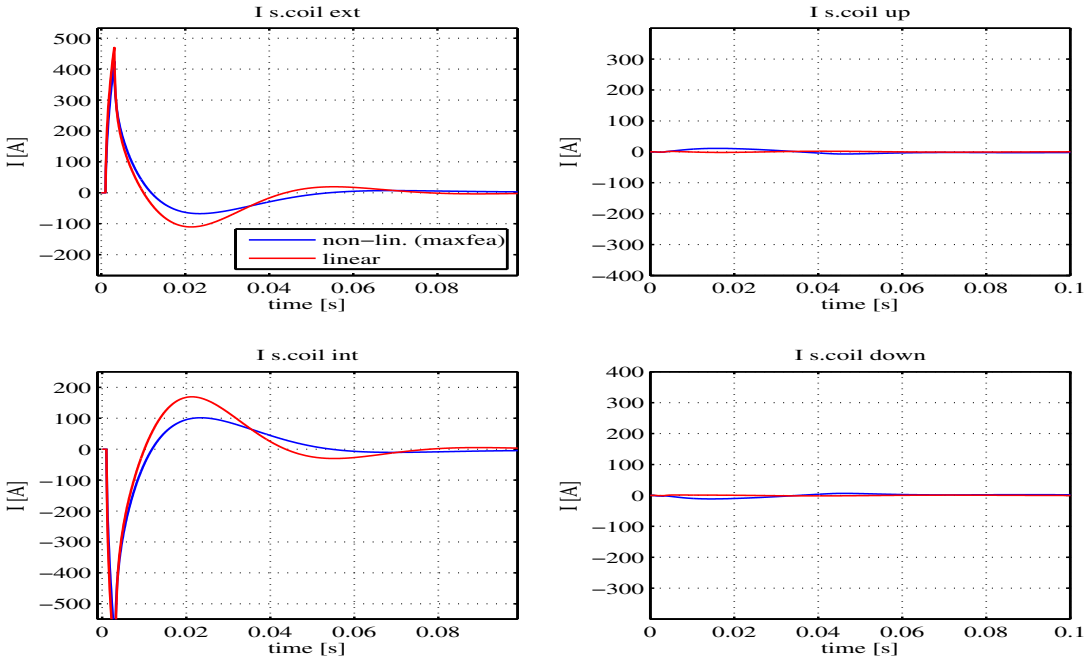

(c) Saddle coils currents in closed loop

Figure 6.5: Volt. perturbation #4, vertical position controller test

Validation of the stabilized model In the following graphs, voltage perturbations that have been applied in the previous chapter (#1 and #2, figures 5.9, 5.10) to validate the linear model will be considered again, comparing the response of the stabilized linear and nonlinear model. The stabilization is effective (figure 6.6 compared with figure 5.8), and it is confirmed that the stabilized linear model has good agreement in terms of voltage pulse response with the nonlinear model with applied feedback (figures 6.7, 6.8).

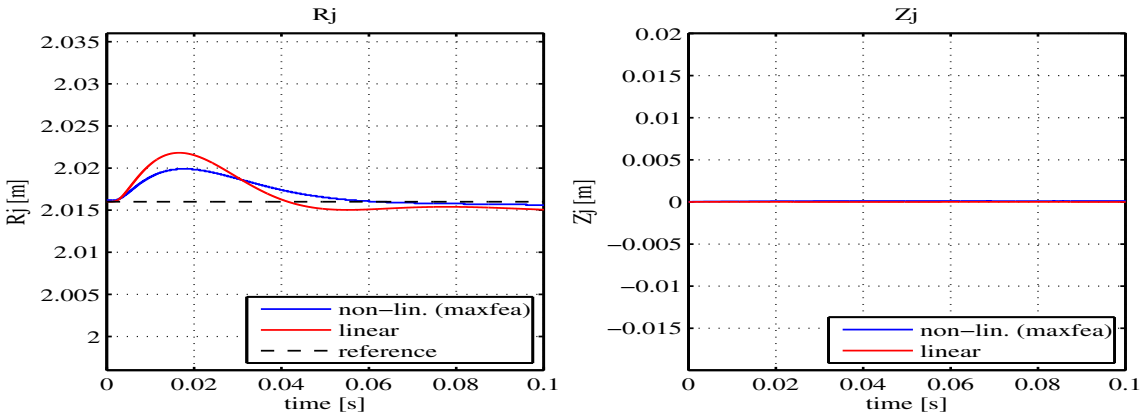

(a) Pert. #1

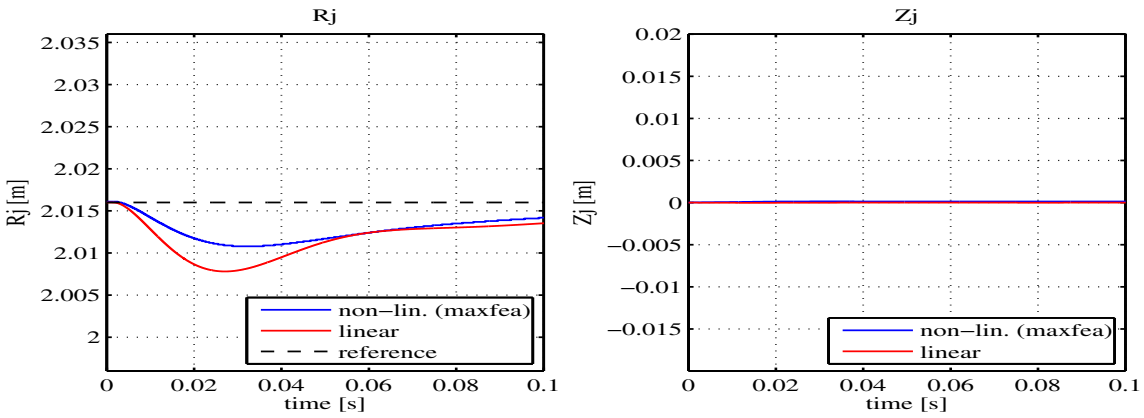

(b) Pert. #2

Figure 6.6: Volt. perturbations #1, #2, closed loop on R_j and Z_j. Controlled variables

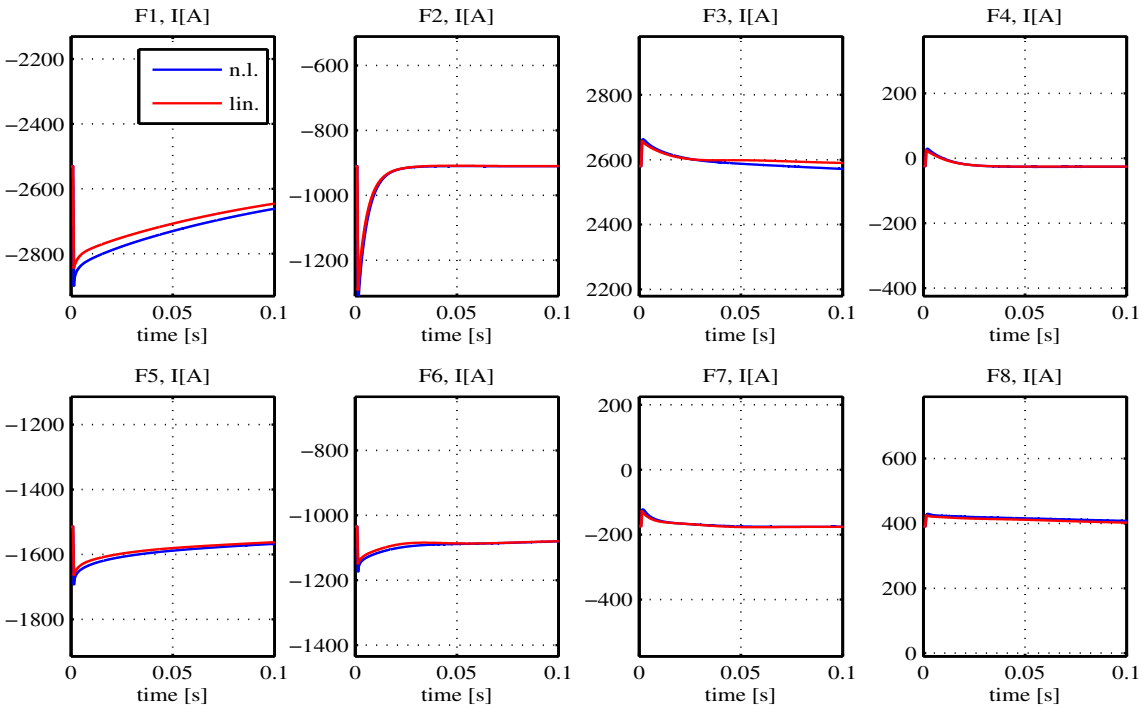

(a) F coils current

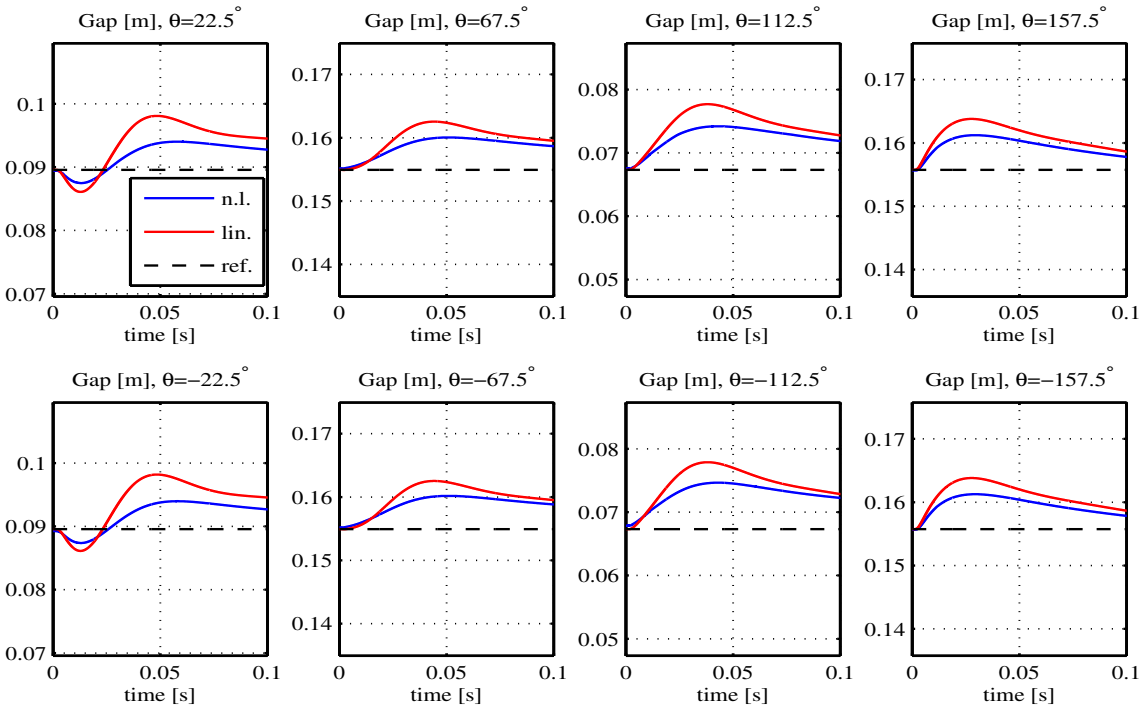

(b) Plasma-first wall gaps

Figure 6.7: Volt. perturbation #1, closed loop on R_j and Z_j. F coils current, and gaps

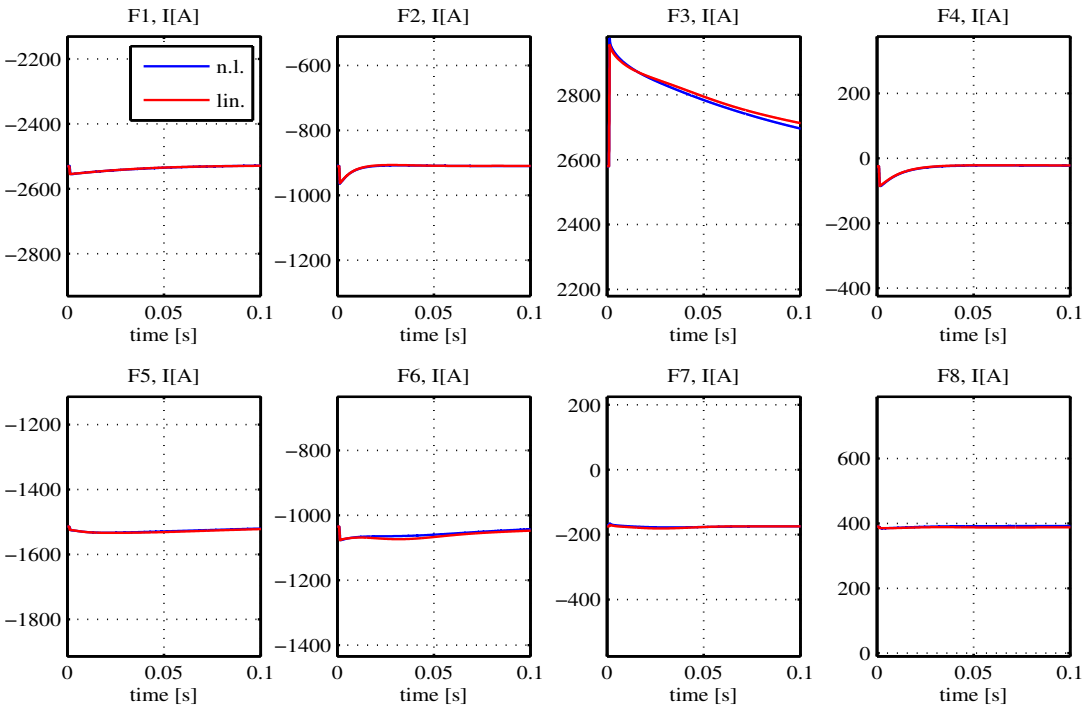

(a) F coils current

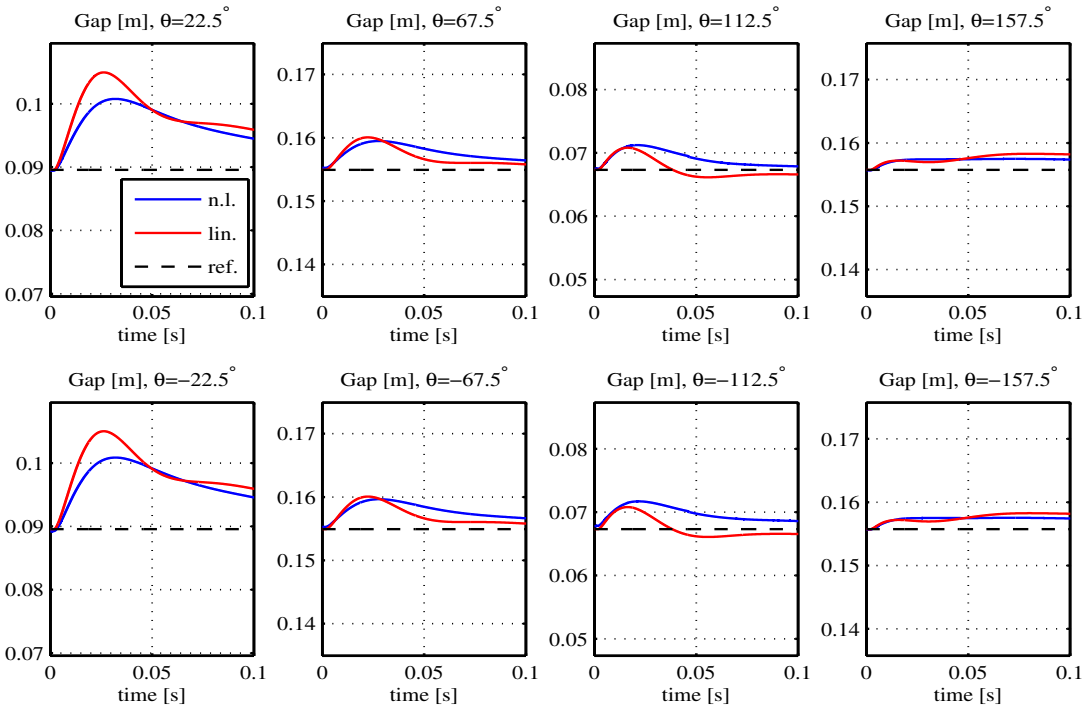

(b) Plasma-first wall gaps

Figure 6.8: Volt. perturbation #2, closed loop on R_j and Z_j. F coils current, and gaps

6.2 Model order reduction for gap control

The high-dimensionality of the linear model obtained hereby could pose some problems in terms of numerical reliability and computational load when designing a regulator for real-time shape control. Moreover, the Kalman filter based on a model where state space dimensions are much higher than input/output dimensions would lead to high variance in state space estimates. For these reasons, it is convenient to apply model reduction techniques to obtain a model with lower dimensionality. It will be shown that a model with state-space dimension one order of magnitude lower will suffice to provide good adherence to time domain response of the full-state model. As mentioned before, Hankel model reduction routines will be used to perform this task. The Hankel norm of a linear system $\mathcal{S} = (A, B, C, D)$ of size n, defined in eq. (6.1), is equivalent to the following:

$$||\mathcal{S}||_H^2 = \sigma_1^2, \quad \sigma_1 \geq \sigma_2 \geq \ ... \ \sigma_n$$

where σ_i are Hankel singular values, obtained considering the Gramians $\mathcal{P}$ and $\mathcal{Q}$ of $\mathcal{S}$:

$$\sigma_i = \sqrt{\lambda_i(\mathcal{P}\mathcal{Q})} \tag{6.3}$$

$$\mathcal{P} = \lim_{t\to\infty} \int_0^t e^{A\tau} B B' e^{A'\tau} d\tau \tag{6.4}$$

$$\mathcal{Q} = \lim_{t\to\infty} \int_0^t e^{A'\tau} C' C e^{A\tau} d\tau. \tag{6.5}$$

In this case, we want to find the *Minimum Degree Approximation* (MDA) of the stabilized full-state system $\mathcal{S}_0$ (eq. 6.2) of size $n = 250$, whose transfer function matrix is $S_0(s)$, with a reduced order model $\mathcal{S}_R$ of size $k < n$ with transfer function matrix $S_R(s)$, defined by the following set of matrices:

$$\mathcal{S}_R = (\tilde{A}, \tilde{B}, \tilde{C}, 0). \tag{6.6}$$

It can be shown that using Hankel model reduction techniques, based on the calculation of the original model singular values and the truncation of these to the k-th order, a H_∞ bound on the response of the error model is satisfied [17]:

$$||S_0(\omega) - S_R(\omega)||_\infty \leq 2 \sum_{i=k+1}^{n} \sigma_i.$$

Figure 6.9 reports $\log \sigma_i$ for the system $\mathcal{S}_0$. The plot of singular values shows a steep descent when passing from order 5 to 6 and from order 11 to 12, but truncating the model to $k = 5$ or $k = 11$ would show poor consistence with $\mathcal{S}_0$ in terms of frequency response;

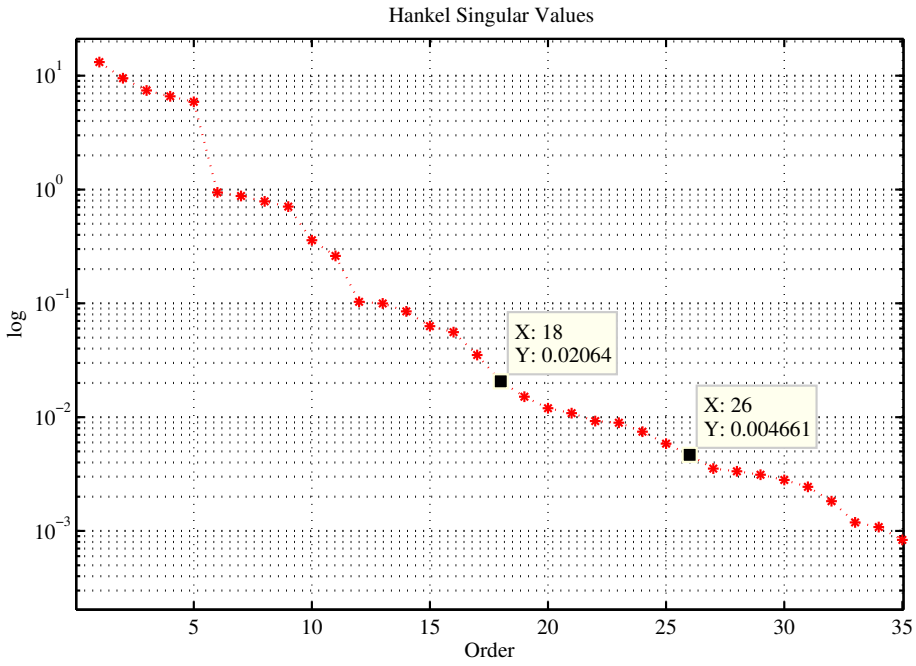

Figure 6.9: Singular values (*log*) plot, system $\mathcal{S}_0$

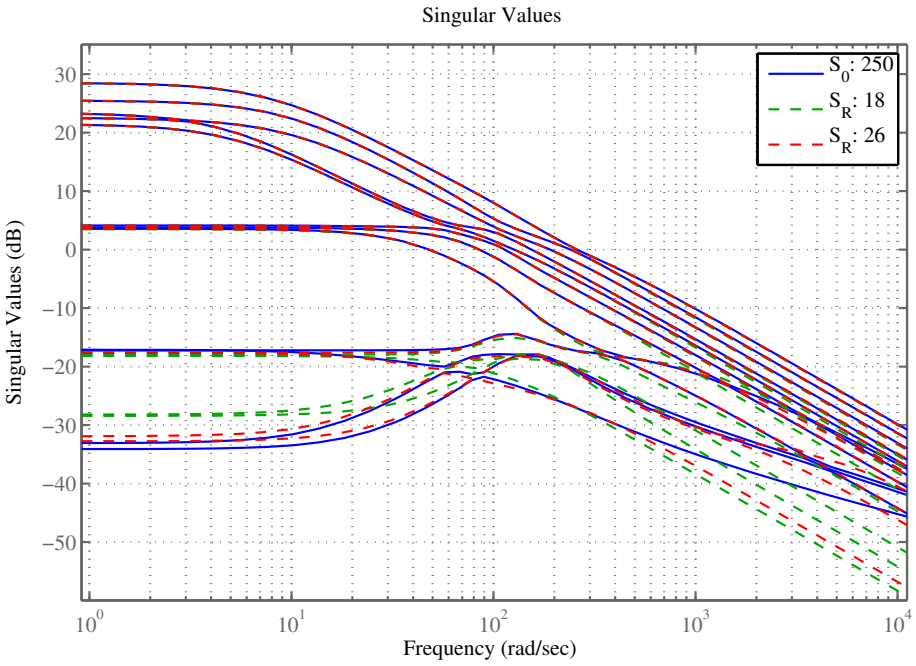

Figure 6.10: Bode plot, transfer function singular values

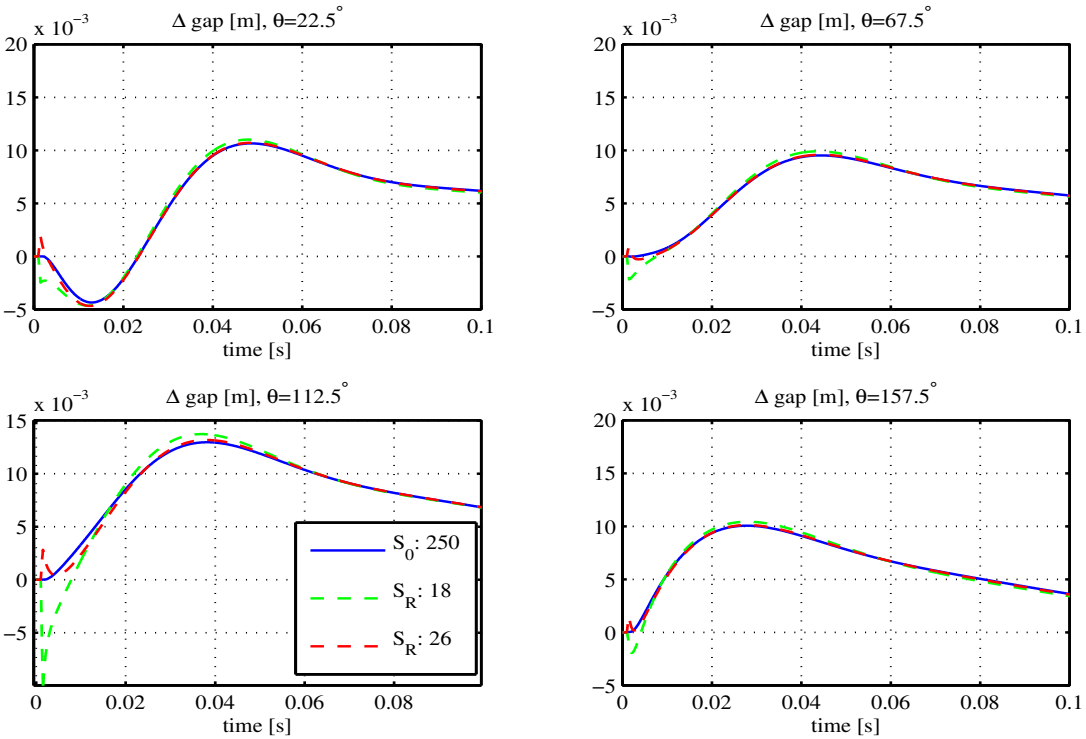

(a) Pert. # 1

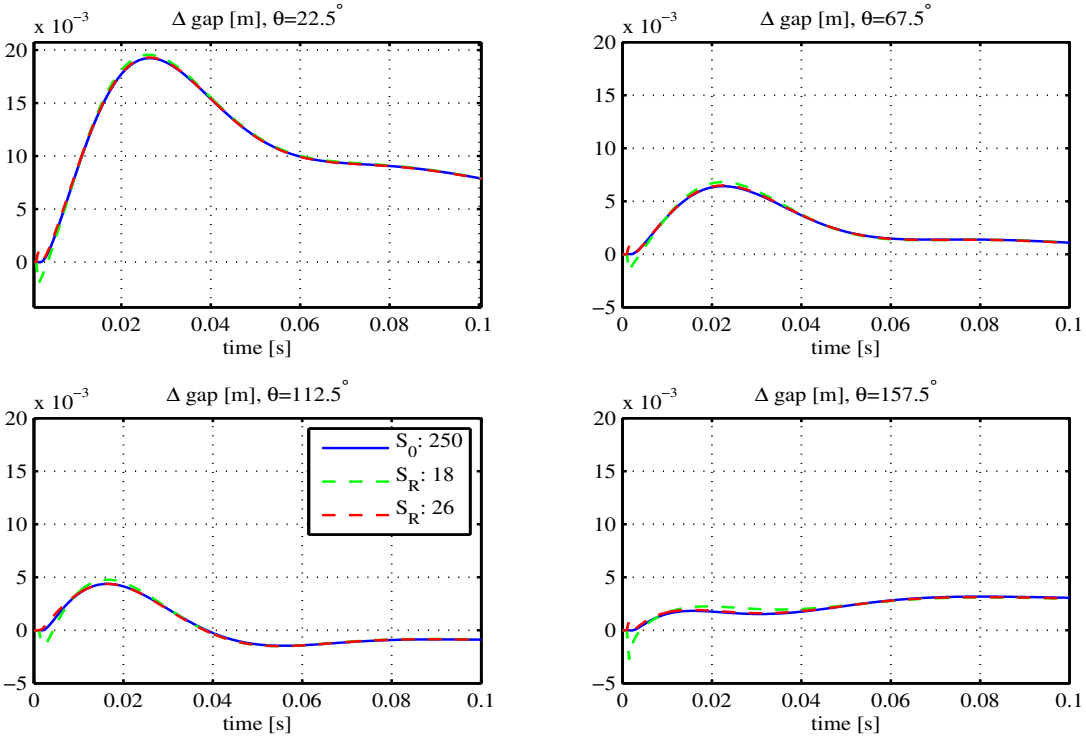

(b) Pert. # 2

Figure 6.11: Gaps response to voltage perturbations, reduced order models
Only 4 of 8 gaps are reported, considering top-down symmetry

the plot is otherwise quite flat at higher orders. The choice of k is thus based on evaluation of the response of two selected models in the band of interest: the models obtained with $k = 18$ and $k = 26$ are considered instead. These are firstly compared in terms of singular values of their frequency response matrices (fig 6.10), showing that it is convenient to choose $k = 26$ to have a good adherence of the first 12 singular values of the frequency response in terms of system gain at $\omega = 0$ and in the range $\omega \in 10^2 \div 10^3\ rad/s$.

Next, the two models are compared in terms of time-domain response to voltage pulses #1 and #2 of table 5.8 and considering the resulting variations in gaps (fig 6.11). There is very good adherence with the full-state model in the case $k = 26$, with small discrepancies due to not perfect matching with the original model at high frequencies; these discrepancies are heavier in the case $k = 18$, so in the following we will consider the model obtained with $k = 26$.

To set up the LQG control scheme for feedback regulation of plasma-first wall distance, it is important to choose input and output variables of interest. Output variables provide information to the Kalman filter to produce state estimates; input variables also provide information to the Kalman filter, and will be used by the LQ regulator to apply the linear feedback. Since we want to maximize the information available to the Kalman filter, all output variables (including saddle coils currents) will be kept. Instead, since we operate on the stabilized model, and we don't want to use saddle coils circuits as actuators for the shape control regulator, voltage input variables relative to saddle coils circuits will be removed. Finally, in the model obtained hereby, plasma current is one of the output variables, but when deriving the linearized model, and when performing validation

#	**Input variables**
$1 \div 8$	$V_{PVAT,i},\ i = 1 \ldots 8\ [V]$

#	**Output variables**
1	$I_{pla}\ [A]$ (trivial)
2	$R_j\ [m]$
3	$Z_j\ [m]$
$4 \div 11$	Gaps $[m]$
$12 \div 19$	$I_{F,i},\ i = 1 \ldots 8\ [A]$
$20 \div 23$	$I_{SC,i},\ i = 1 \ldots 4\ [A]$

Table 6.1: Input/output variables for LQG control

simulations, Maxfea was always set to operate at constant plasma current. So, the corresponding row of C_C is trivial (row of zeros), and in validation there are no plasma current variations so this variable provides no information to produce state estimates. Nevertheless, to maintain a more general representation of the control scheme, the variable is kept in the set of outputs, in the case the model should be extended with a control loop on plasma current. Table 6.1 resumes the input/output variables in the reduced model used for LQG control. We will substantially refer to the reduced order model $\mathcal{S}_R$ with $k = 26$, and remove the input variables relative to saddle coils circuits.

Controllability and observability Since the singular values kept by the Hankel reduction routine are all positive, the resulting reachability and observability gramians must be both full rank in the reduced order model $\mathcal{S}_R$ (consider eq. 6.3), that consequently is both reachable and observable. Removing the inputs relative to saddle coils circuits means that we are referring to the model $\mathcal{S}_L$ obtained from $\mathcal{S}_R$ (eq. 6.6) by the following positions:

$$\mathcal{S}_L = (A_L, B_L, C_L, 0),$$
$$A_L = \tilde{A}, \quad B_L = \tilde{B} \begin{bmatrix} I_{8\times 8} \\ 0_{4\times 8} \end{bmatrix}, \quad C_L = \tilde{C}.$$

Controllability is preserved, since the matrix $\mathcal{R}(A_L, B_L)$ has full row rank; the tolerance of the `rank()` routine in Matlab must be manually set to a value lower than the smaller singular value of $\mathcal{S}_R$ ($\sigma_{26} = 0.0031$) to obtain reliable results when performing the numeric test[1].

6.3 Kalman filter design

In the hypothesis that $\mathcal{S}_L$ describes the dynamics of the process to be controlled, a state estimator can be obtained as a linear observer, characterized by the following dynamics:

$$\dot{\hat{x}}(t) = (A_L - LC_L)\hat{x}(t) + B_L u(t) + Ly(t). \tag{6.7}$$

The general criterion to choose observer pole allocation is to have quicker observer dynamics than closed loop process dynamics. However, the choice of the L matrix is

[1] It is also possible to remove unused inputs for LQG control on the original stabilized full state model $\mathcal{S}_0$, *before* applying the Hankel reduction routine. In this case, reachability and observability of the reduced order model would be assured and no numeric test would be needed.

more conveniently obtained expressing the problem as an optimal estimation problem, assuming one wants to find the estimator in the class defined by eq. (6.7) that minimizes the asymptotic variance P of the estimation error $e(t) = x(t) - \hat{x}(t)$

$$P = \lim_{t\to\infty} \mathrm{E}[e(t)e(t)'],$$

given that measurements are affected by additive white gaussian noise $v(t)$ and model state dynamics are affected by additive white gaussian noise $w(t)$, whose variance matrices are

$$\mathrm{E}[w(t)w(t)'] = Q, \quad \mathrm{E}[v(t)v(t)'] = R.$$

The effect of additive noise on $\mathcal{S}_L$ is expressed by the following equations:

$$\begin{aligned} \dot{x}(t) &= A_L x(t) + B_L u(t) + w(t) \\ y(t) &= C_L x(t) + v(t). \end{aligned}$$

Under these hypothesis, the estimator minimizing P exists in the class (6.7), and it is the Kalman filter, characterized by

$$L = PC_L' R^{-1}$$

where P is the positive definite solution of the associated continuous-time algebraic Riccati equation:

$$A_L' P + P A_L - P C_L' R^{-1} C_L P + Q = 0.$$

We choose to design R as a diagonal matrix (uncorrelated measurement errors); the diagonal terms can be chosen on the basis of experimental measurement variances. We will consider the application to experimental data from shot $\#29746$ of plasma current estimation formula (4.9), of current centroid estimation formulas derived in section 4.3, of thin-plate spline based gap reconstruction of section 4.2 (considering a top/down symmetric average) and finally an average of variances for measured F coils currents; saddle coil circuits current variance is assumed to be the same as F coils. The time range considered for variance estimation is $t \in [0.43, 0.45]s$. The resulting measurement variances are reported in table 6.2.

State noise variance Q should be tuned accordingly to how reliable is model $\mathcal{S}_L$ in predicting state dynamics. The choice of state noise variance is complicated by the fact that state space variables do not have any physical meaning in $\mathcal{S}_L$, since they cannot be expressed as a linear combination of state space variables of $\mathcal{S}_0$. We must also remember

Measure	Variance ($[\cdot]^2$)
$I_{pla}\ [A]$	$2.45 \cdot 10^4$
$R_j[m]$	$9.1 \cdot 10^{-8}$
$Z_j[m]$	$5.2 \cdot 10^{-7}$
gaps $[m]$, $\theta = \pm 22.5°$	$1.17 \cdot 10^{-7}$
gaps $[m]$, $\theta = \pm 67.5°$	$2.73 \cdot 10^{-7}$
gaps $[m]$, $\theta = \pm 112.5°$	$6.26 \cdot 10^{-7}$
gaps $[m]$, $\theta = \pm 157.5°$	$2.38 \cdot 10^{-7}$
$I_F,\ I_{SC}\ [A]$	135

Table 6.2: Output variances from experimental data

that the estimator should finally process data generated by the nonlinear simulator, that could be forced to operate in conditions where plasma parametrization itself differs from the one used to derive the linear model (section 6.5); we should thus adopt a conservative approach, assuming that $\mathcal{S}_L$ is not reliable to perform open-loop prediction; to obtain frequency separation between the state estimator and the process, we will choose Q to be diagonal and to take the form

$$Q = q^2 I_{26\times 26}.$$

The parameter q is chosen so that resulting observer poles, eigenvalues of $(A_L - LC_L)$, are characterized by a fast enough time constant, considering the expected time constant of the closed-loop shape controller. The resulting choice of q and the resulting Kalman filter dominant time constant τ_F is as follows:

$$q = 800, \quad \tau_F = 3.80\ ms.$$

In figure 6.12 is reported the application of the Kalman filter to data from simulations on the full-state linear model (perturbation # 1 with current centroid position control, without shape control, cfr. fig. 6.7). Measures are altered with the addition of measurement noise of variance as in tab. 6.2, and the performance of the Kalman filter in lessening measurement noise is assessed. In figure 6.13 is reported the application of the Kalman filter to Maxfea data. The filtered measures accurately track the measures generated by the nonlinear model, thanks to the choice of high enough model variance.

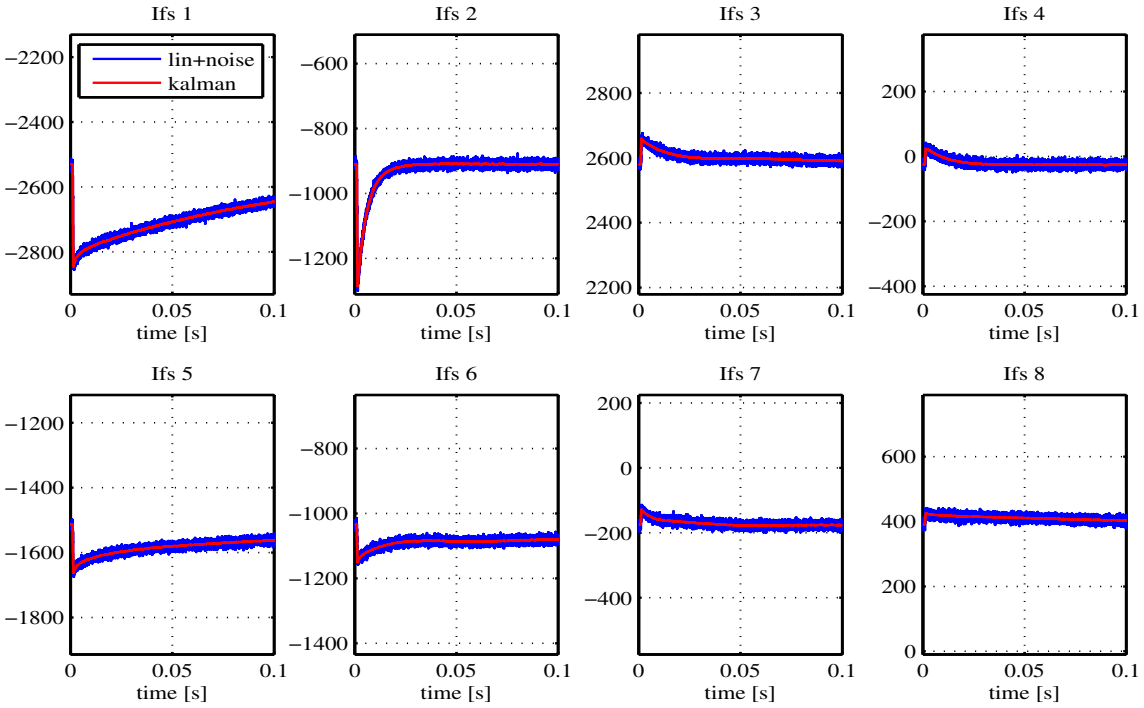

(a) F coils current

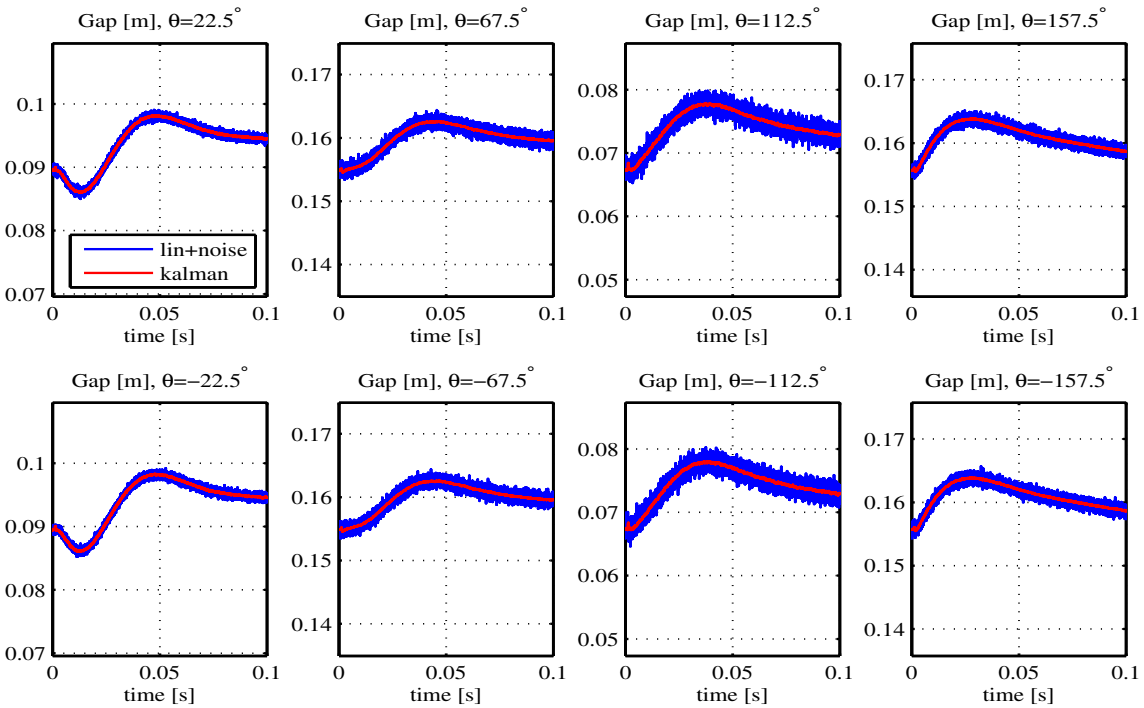

(b) Plasma-first wall gaps

Figure 6.12: Pert. #1, linear sim. + meas. noise, and Kalman (reduced order) filtering

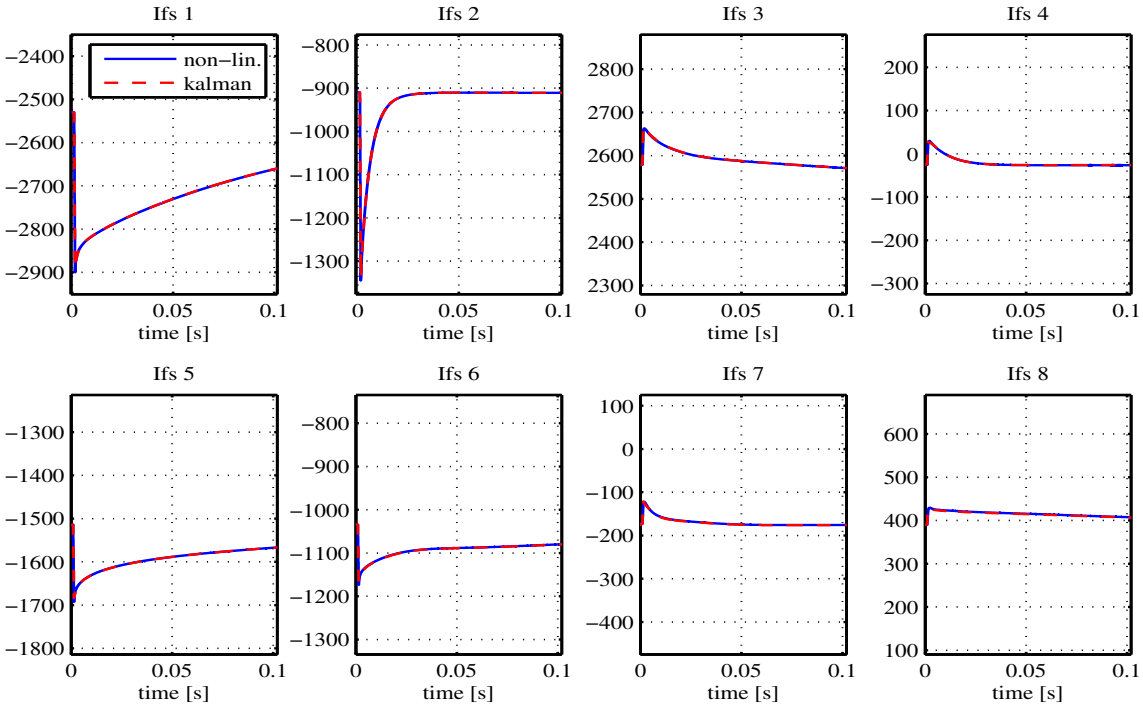

(a) F coils current

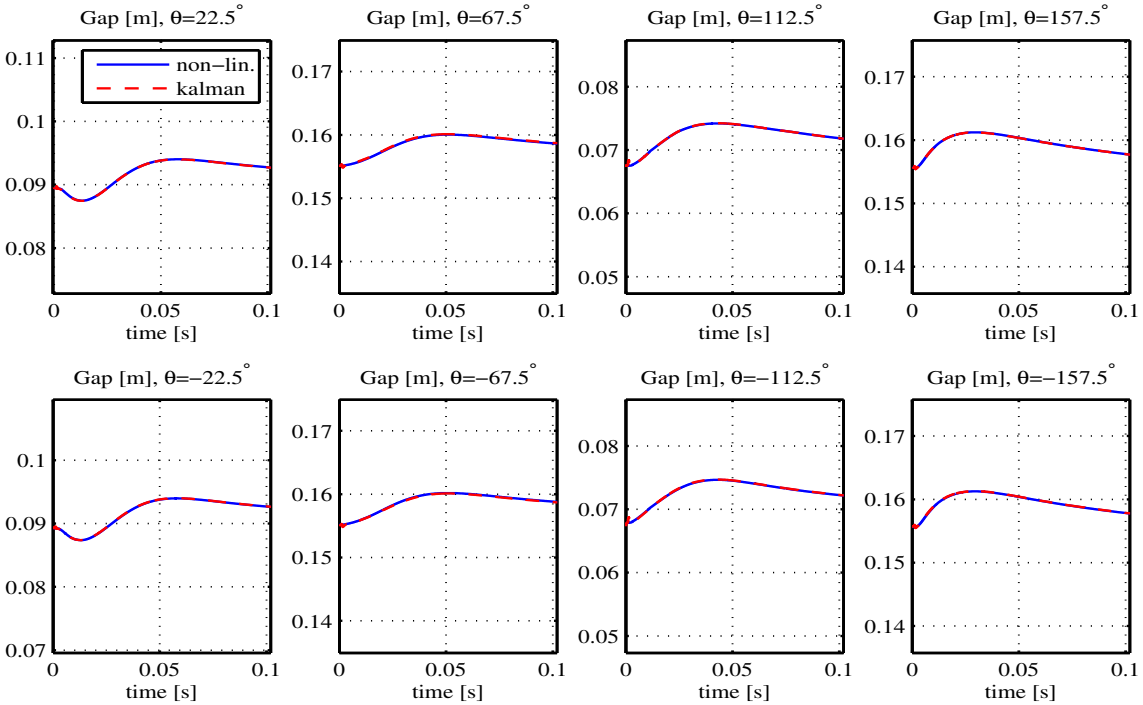

(b) Plasma-first wall gaps

Figure 6.13: Pert. #1, Maxfea simulation, and Kalman (reduced order) filtering

6.4 LQR controller design

LQR control is based on the definition of the following index, to be minimized on a infinite time horizon:

$$J_{LQR} = \int_0^\infty x(t)' M_x x(t) + u(t)' M_u u(t) dt; \tag{6.8}$$

the linear state-feedback controller minimizing 6.8 is found searching for the definite positive solution S of the continuous-time algebraic Riccati equation

$$A_L' S + S A_L - S B_L M_u^{-1} B_L' S + M_x = 0$$

leading to the definition of the feedback matrix

$$K = M_u^{-1} B_L' S.$$

A common rule to choose weights appearing in matrices M_x and M_u prescribes to use diagonal matrices, with the following positions ([18], p.537):

$$M_x(i,i) = \frac{1}{\text{max. acceptable value for } x_i^2}, \quad i = 1 \dots 26 \tag{6.9}$$

$$M_u(i,i) = \frac{1}{\text{max. acceptable value for } u_i^2}, \quad i = 1 \dots 8; \tag{6.10}$$

however, since state space variables do not have physical meaning in the reduced order model, we will adapt rule 6.9 choosing values for maximum variations in output quantities, e.g.

$$M_y(i,i) = \frac{1}{\text{max. acceptable value for } y_i^2}, \quad i = 1 \dots 23;$$

next, we will compute M_x considering the state-output relation existing in the linear model:

$$M_x = C_L' M_y C_L.$$

Table 6.3 resumes the choices for maximum acceptable values of input/output signals. The maximum values for $u_i = \Delta V_{PVAT,i}$ can be chosen to regulate LQR controller responsiveness; we choose to set these values as proportional (through the constant r) to coefficients approximating equilibrium resistive compensation voltages, to avoid problems due to lower saturation limits: in fact, applicable PVAT voltage variations are

$$\Delta V_{PVAT,i} \in \left[-V_{COMP,i},\ 1350 - V_{COMP,i} \right],$$

Measure	Max. exp. variation
$\Delta V_{PVAT,1}\ [V]$	$r \cdot 100$
$\Delta V_{PVAT,2}\ [V]$	$r \cdot 200$
$\Delta V_{PVAT,3}\ [V]$	$r \cdot 130$
$\Delta V_{PVAT,4}\ [V]$	$r \cdot 30$
$\Delta V_{PVAT,5}\ [V]$	$r \cdot 110$
$\Delta V_{PVAT,6}\ [V]$	$r \cdot 80$
$\Delta V_{PVAT,7}\ [V]$	$r \cdot 130$
$\Delta V_{PVAT,8}\ [V]$	$r \cdot 30$
$R_j,\ Z_j\ [mm]$	3
gap $[mm]$	2
$I_F\ [A]$	600
$I_{SC}\ [A]$	400

Table 6.3: LQR weights: max. expected variations for input/output variables

where $V_{COMP,i}$ are as in table 5.7. The values appearing in table 6.3 are actually tuned to obtain a more balanced control action. The chosen value for r and the resulting dominant time constant τ_R in the closed-loop system with this allocation is

$$r = 2.5, \quad \tau_R = 37.3\ ms.$$

Different allocations are possible; however, designing the LQR controller it has emerged that the dominant pole cannot be allocated at values much lower than $\tau_R = 25\ ms$, and with faster allocations, undesired oscillating behavior would emerge.

As has been done in previous sections, the LQG regulator (Kalman filter+LQR controller) has been firstly tested using voltage perturbations. It can be seen that gap control is effective (fig. 6.14, 6.15), since the variation in gap measures is much lower than in previous simulations (compare with fig. 6.7, 6.8). In figure 6.16 is reported the $PVAT$ voltage applied by the regulator. With voltage perturbations, the nonlinear model and linear full state model can still be compared considering closed-loop performance when applying the reduced order controller. On both models, the effect of $PVAT$ voltage saturations is taken into account; the agreement of the two closed loop responses is very good. In the following section, we will apply some perturbations to plasma parametrization, thus it will not be possible to compare the linear and nonlinear models. The perturbations that will be proposed provide a more realistic benchmark for controller performance.

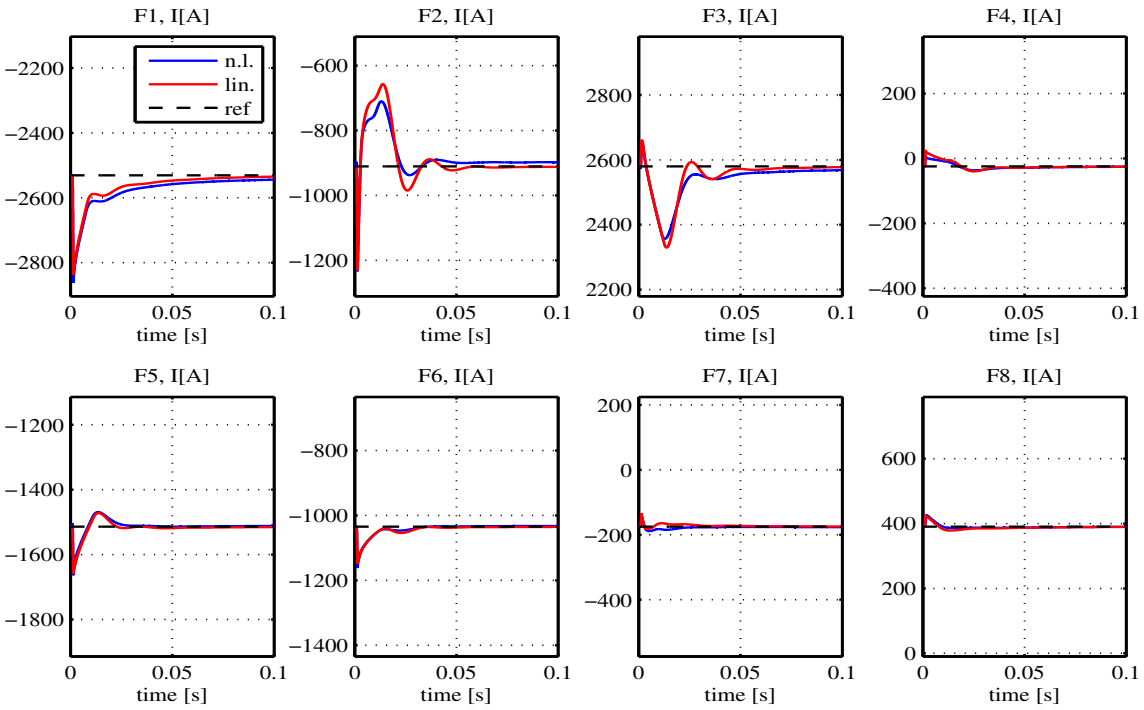

(a) F coils current

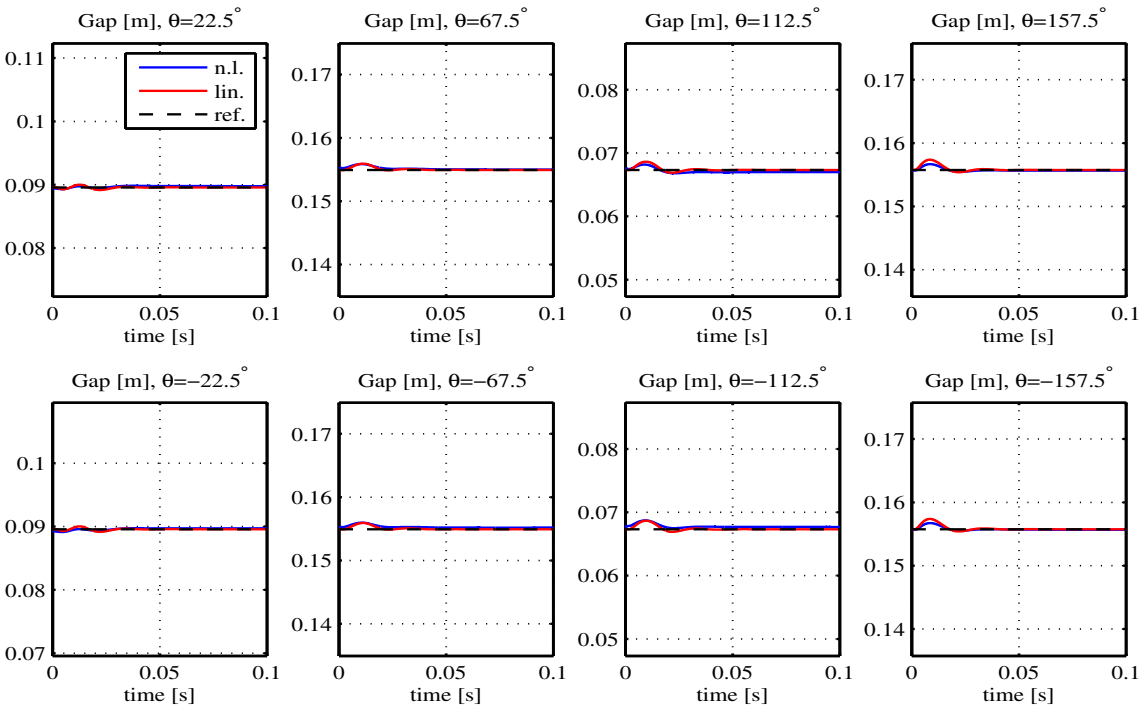

(b) Plasma-first wall gaps

Figure 6.14: Voltage pert. #1, LQG control. F coils current, and gaps

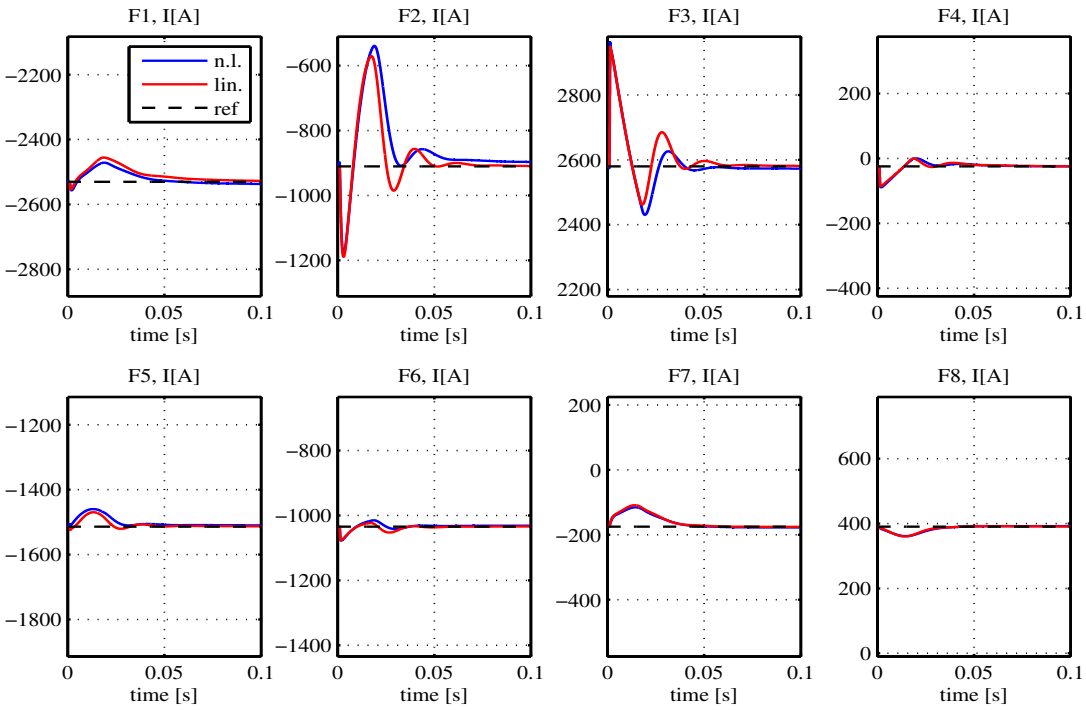

(a) F coils current

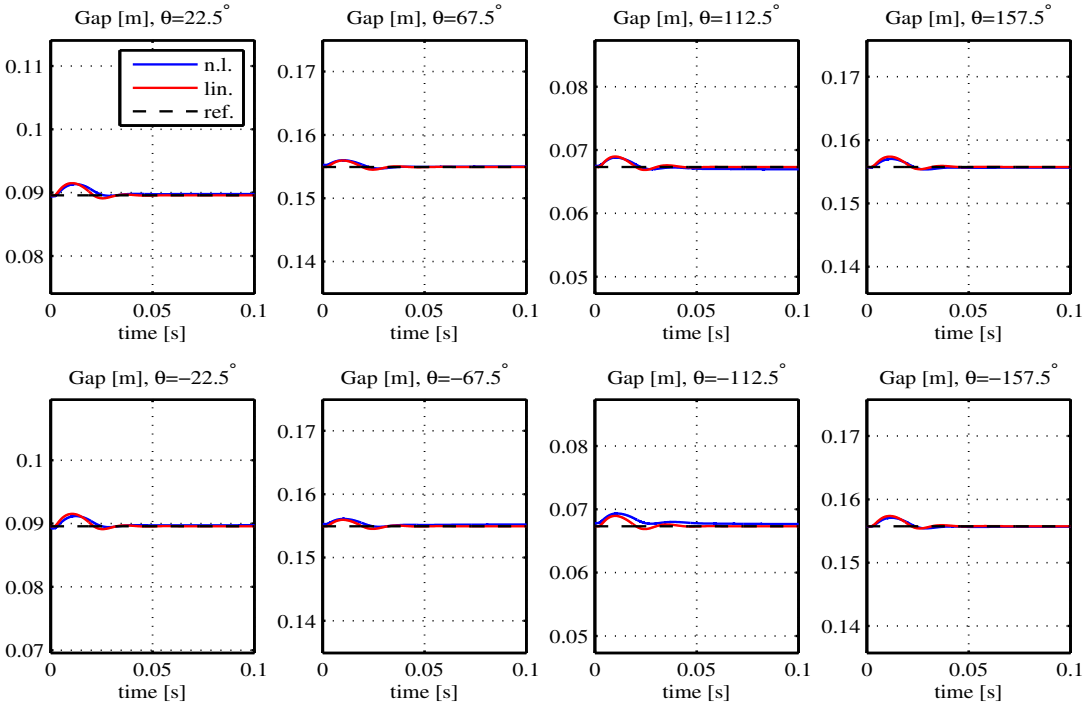

(b) Plasma-first wall gaps

Figure 6.15: Voltage pert. #2, LQG control. F coils current, and gaps

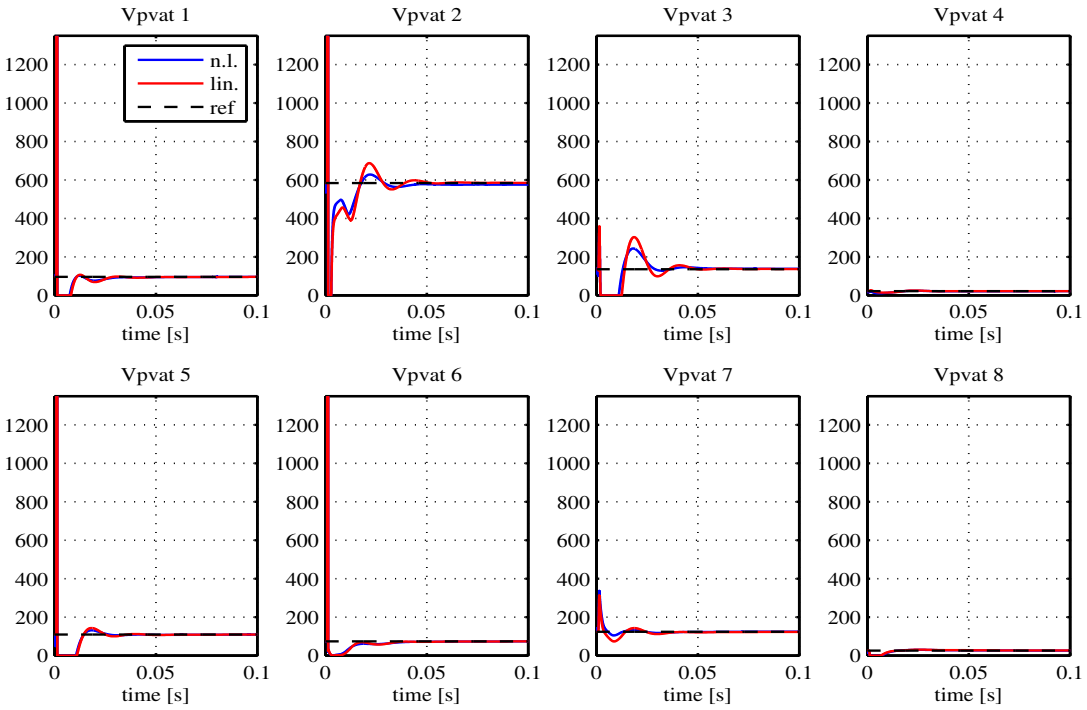

(a) Voltage pert. #1

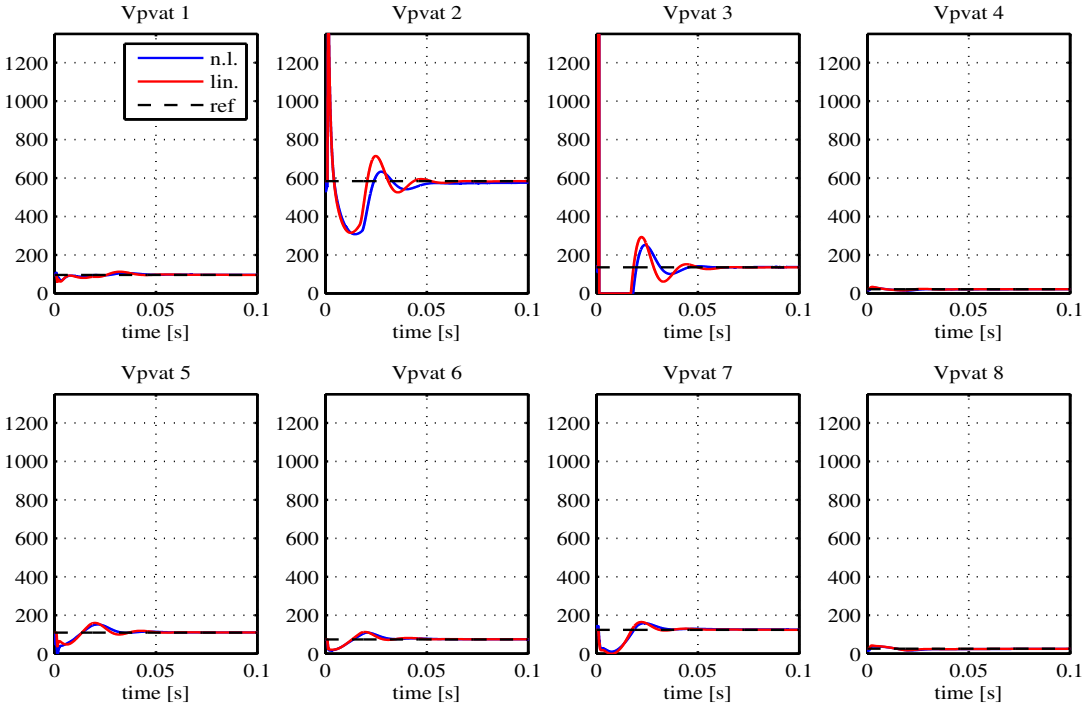

(b) Voltage pert. #2

Figure 6.16: *PV AT* applied voltage to compensate perturbations

6.5 Regulator benchmark: Tokamak perturbations

Since the LQG regulator has been implemented in Maxfea, it is interesting to test different kinds of perturbations, that can be simulated only on the nonlinear model. We will consider *minor disruption* perturbations, which are the worst-case perturbations that can be controlled to avoid the termination of the discharge. These perturbations can be modeled as variations in plasma parametrization, involving changes in α and β parameters in Maxfea.

Perturbations with recovery Firstly, we will consider perturbations of plasma parameters with recovery: we will apply a step variation in parameters, that will decay with exponential law to the original value. The perturbations are applied at $t_0 = 5\,ms$, and the transition law is

$$\alpha(t) = \alpha_0 + (\alpha_1 - \alpha_0) \cdot 1(t - t_0) \cdot e^{-\frac{t-t_0}{\tau_\alpha}} \tag{6.11}$$

$$\beta(t) = \beta_0 + (\beta_1 - \beta_0) \cdot 1(t - t_0) \cdot e^{-\frac{t-t_0}{\tau_\beta}}. \tag{6.12}$$

Table 6.4 resumes the applied perturbations; the resulting variations in l_i and β_θ are visible in graphs of figure 6.17.

Pert.#	$\frac{\alpha_1}{\alpha_0}$	$\frac{\beta_1}{\beta_0}$	$\frac{l_{i,1}}{l_{i,0}}$	$\frac{\beta_{\theta,1}}{\beta_{\theta,0}}$	$\tau_\alpha\ [s]$	$\tau_\beta\ [s]$
1	4	1.05	66.8%	~ 1	0.040	0.040
2	1	3/5	~ 1	59.8%	-	0.060
3	3	4/5	72.5%	77.0%	0.040	0.060

Table 6.4: Tokamak perturbations with recovery
Initial plasma parameters: $l_{i,0} = 0.95$, $\beta_{\theta,0} = 0.29$.

Perturbation $\#1$ is meant to be a perturbation with recovery on l_i only; the β parameter is slightly variated to maintain the resulting β_θ (that mostly depends from β, but also shows a slight dependence from α) as constant as possible. Perturbation $\#2$ is a perturbation with recovery on β_θ only and $\#3$ a perturbation with recovery on both β_θ and l_i; in the latter case, since we are altering both parameters, the variations on the single parameter are slightly reduced to allow numerical convergence.

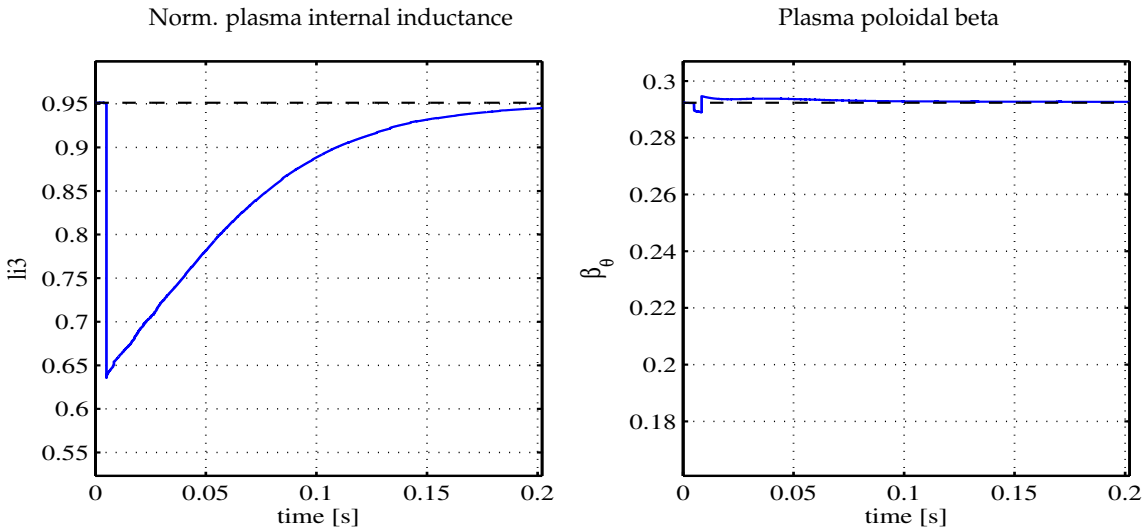

(a) Pert. #1 with recovery

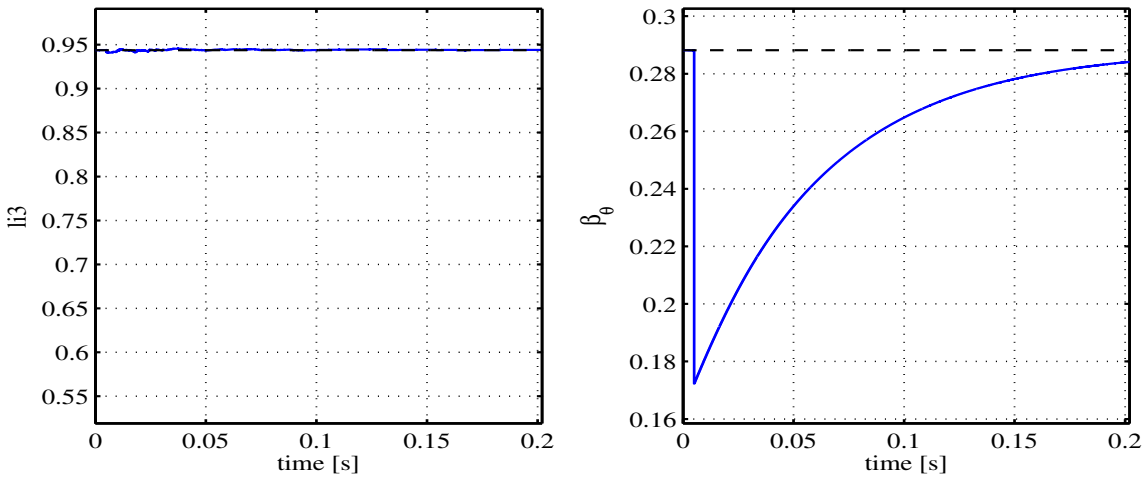

(b) Pert. #2 with recovery

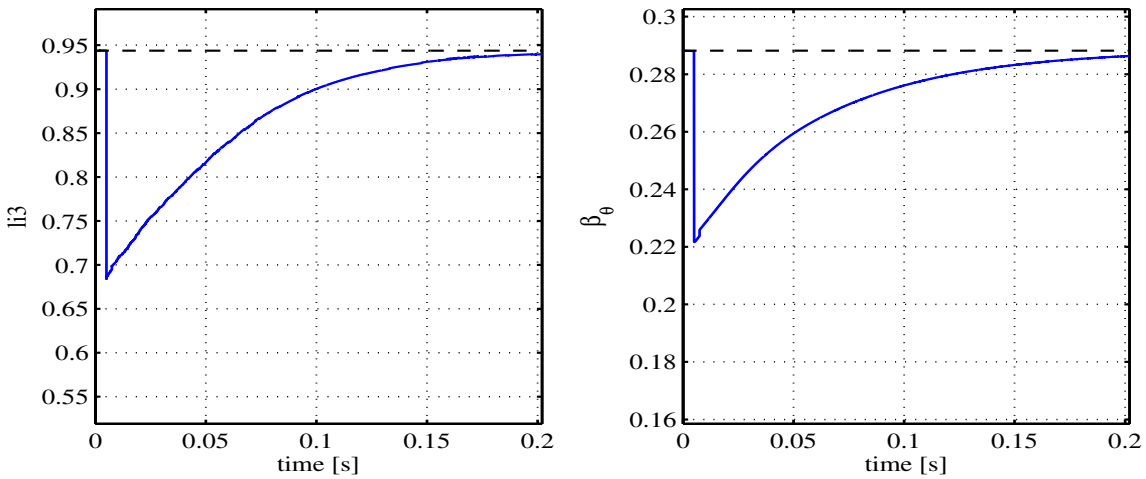

(c) Pert. #3 with recovery

Figure 6.17: Tokamak perturbations with recovery

Figures 6.18, 6.20 and 6.22 show the comparison between the perturbation effect on gaps without LQG control, and the perturbation effect with LQG control. Applied $PVAT$ voltage to compensate perturbations and variations on F coils current is also reported in figures 6.19, 6.21 and 6.23 respectively. The macroscopic effect of these perturbations on horizontal equilibrium (variation of the Λ parameter) is compensated by the fast stabilizing loop of plasma current centroid position. Enabling the LQG controller, gap errors are restored in all the cases; this did not happen without shape control in the case of perturbation #2 with recovery (variation of β parameter). Restoring of gap measures is also confirmed by the graph related to instantaneous quadratic error on gaps: the component related to gaps only in the argument of integral (6.8) is reported in figures 6.18.c etc.

Another critical parameter of plasma geometry is plasma-first wall distance on the horizontal plane at $\theta = 0°$, since this is the point where undesired plasma boundary contact with the first wall is most likely to happen. As figures 6.18.b etc. show, this measure is indirectly kept under control when the LQG controller is enabled, and a clearance of at least approx. $3\ cm$ from the first wall is assured.

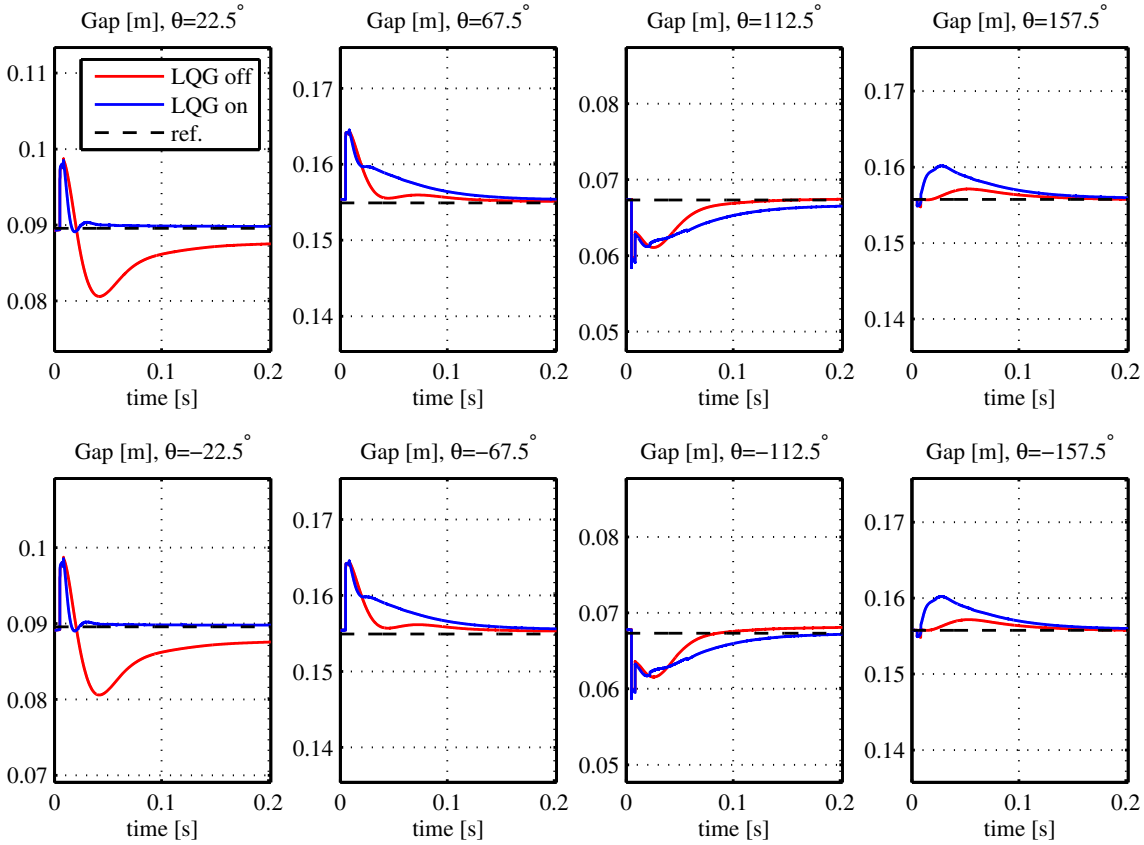

(a) Plasma-first wall gaps

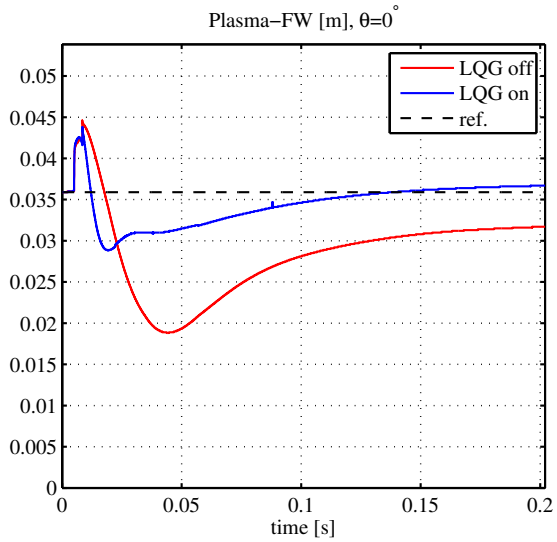

(b) Distance from limiter point

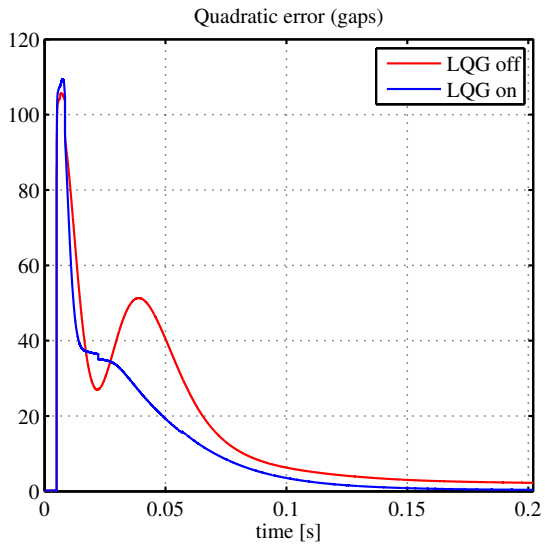

(c) Quadratic error (gaps)

Figure 6.18: Pert. #1 with recovery

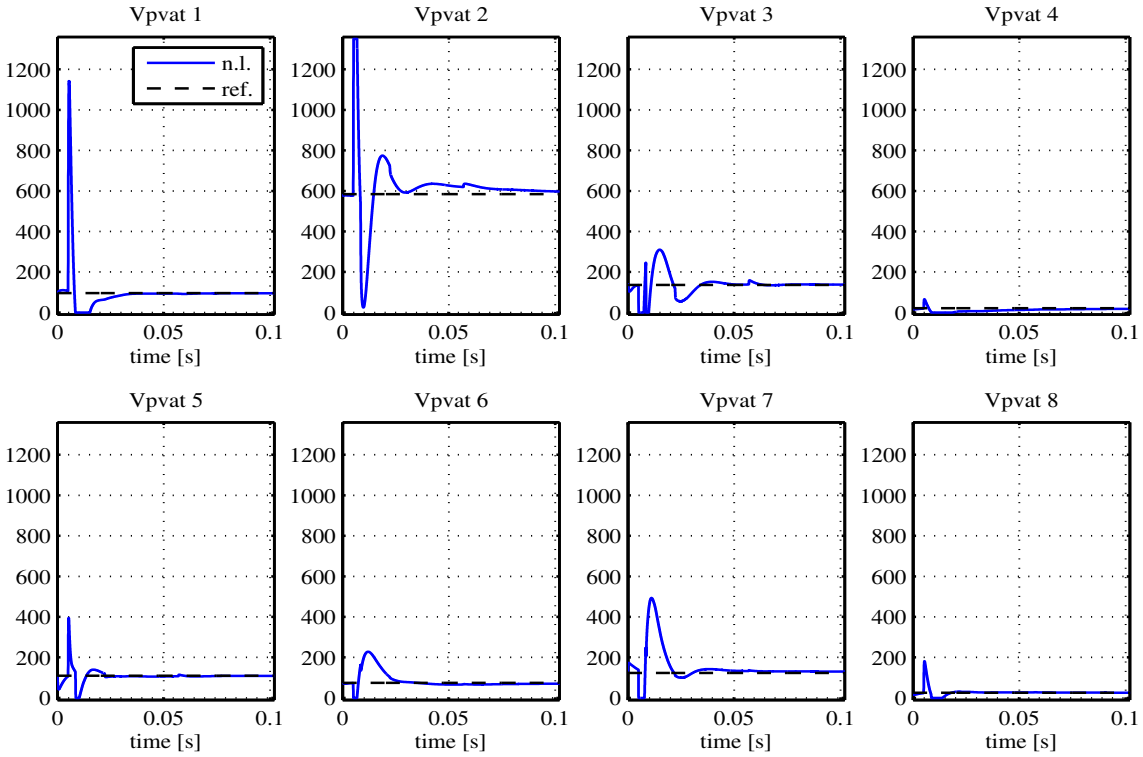

(a) PVAT applied voltage

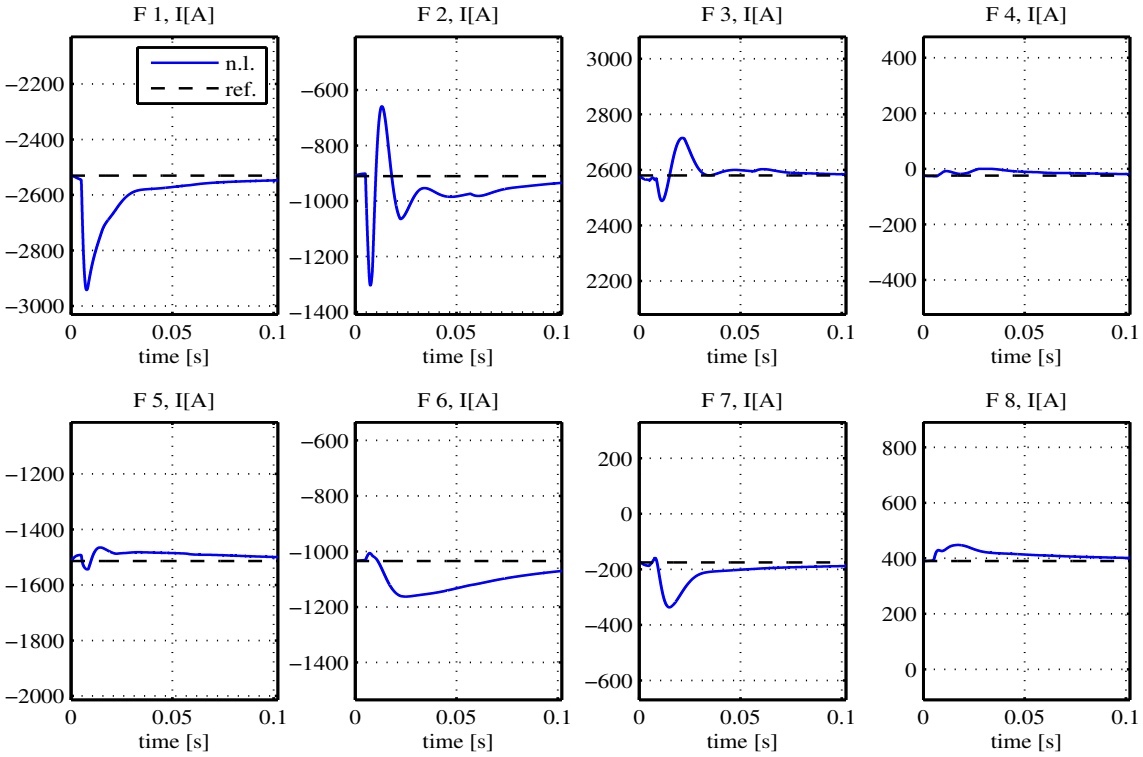

(b) F coils current

Figure 6.19: Pert. #1 with recovery, LQG control

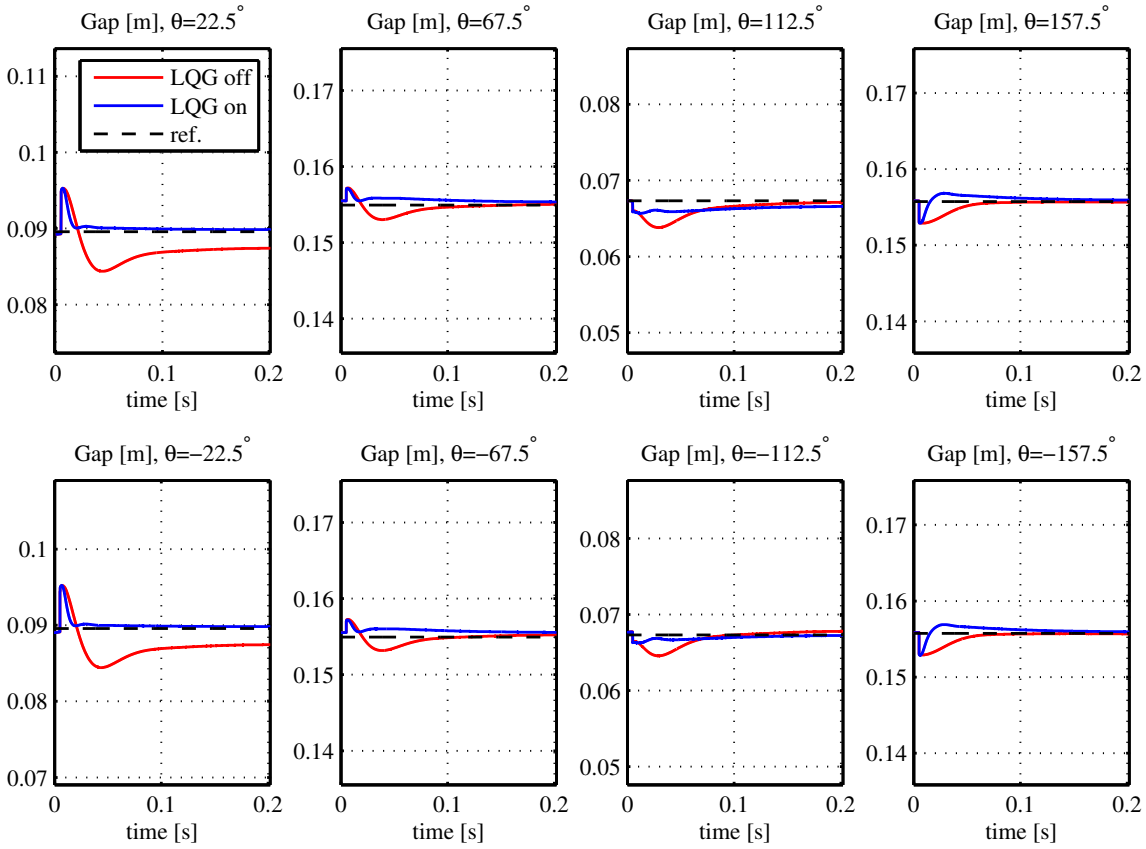

(a) Plasma-first wall gaps

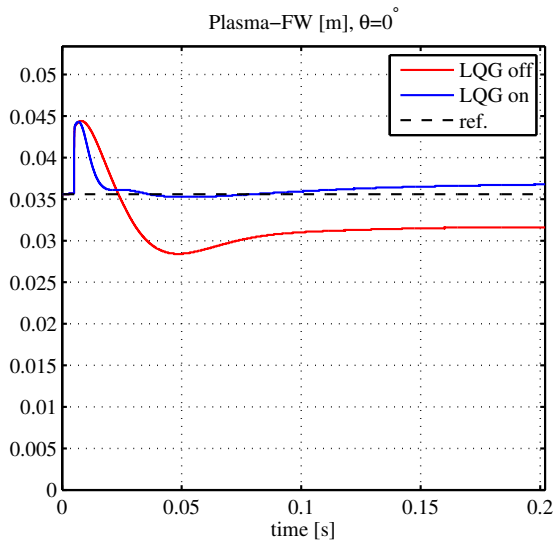

(b) Distance from limiter point

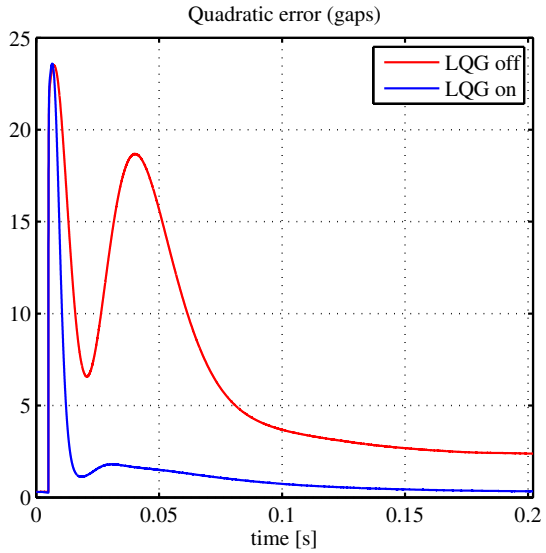

(c) Quadratic error (gaps)

Figure 6.20: Pert. #2 with recovery

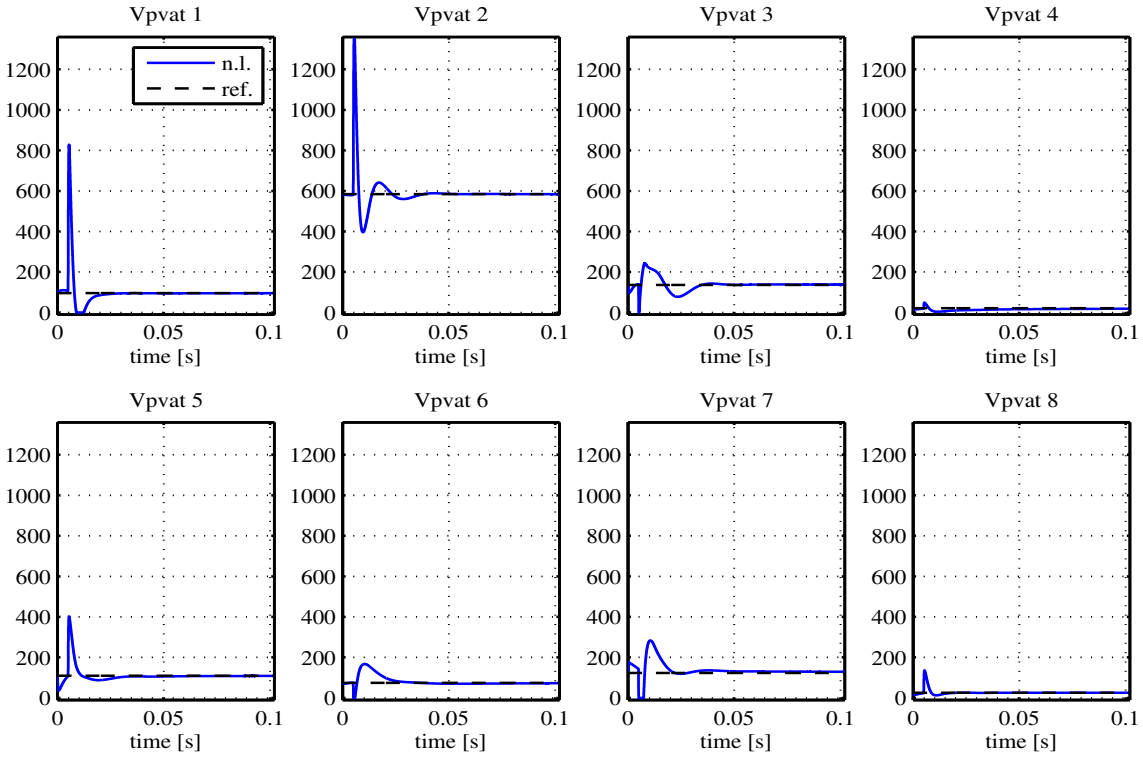

(a) PVAT applied voltage

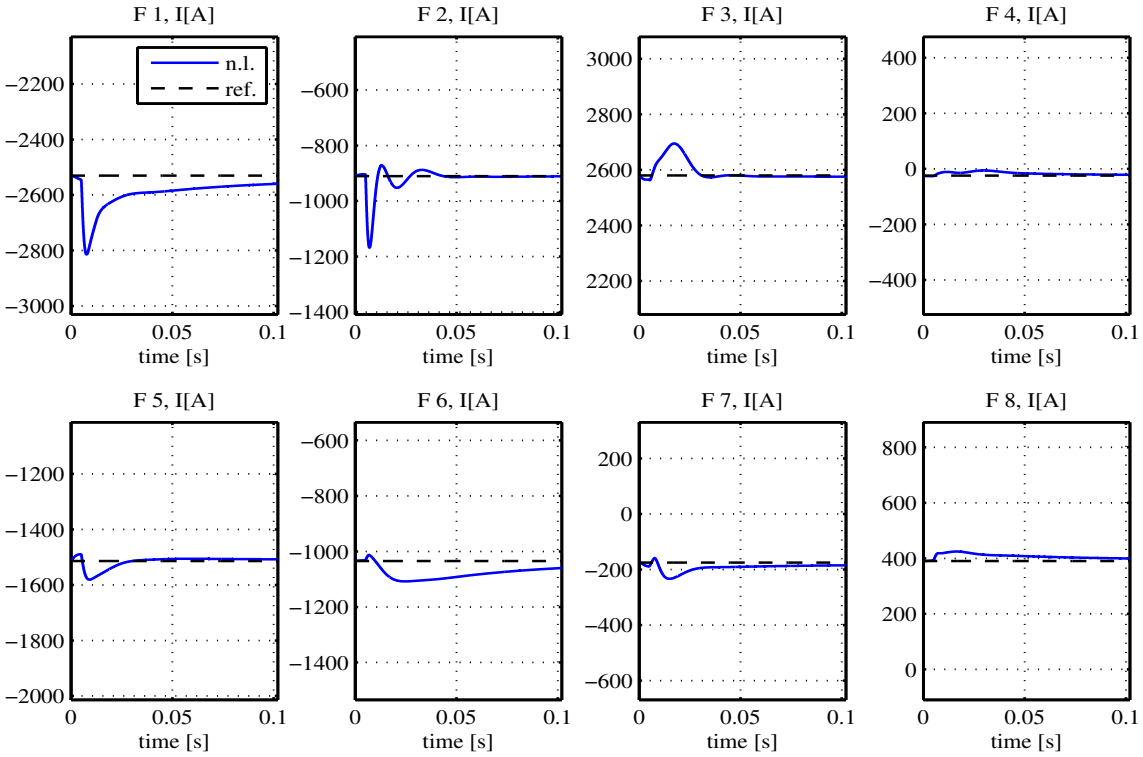

(b) F coils current

Figure 6.21: Pert. #2 with recovery, LQG control

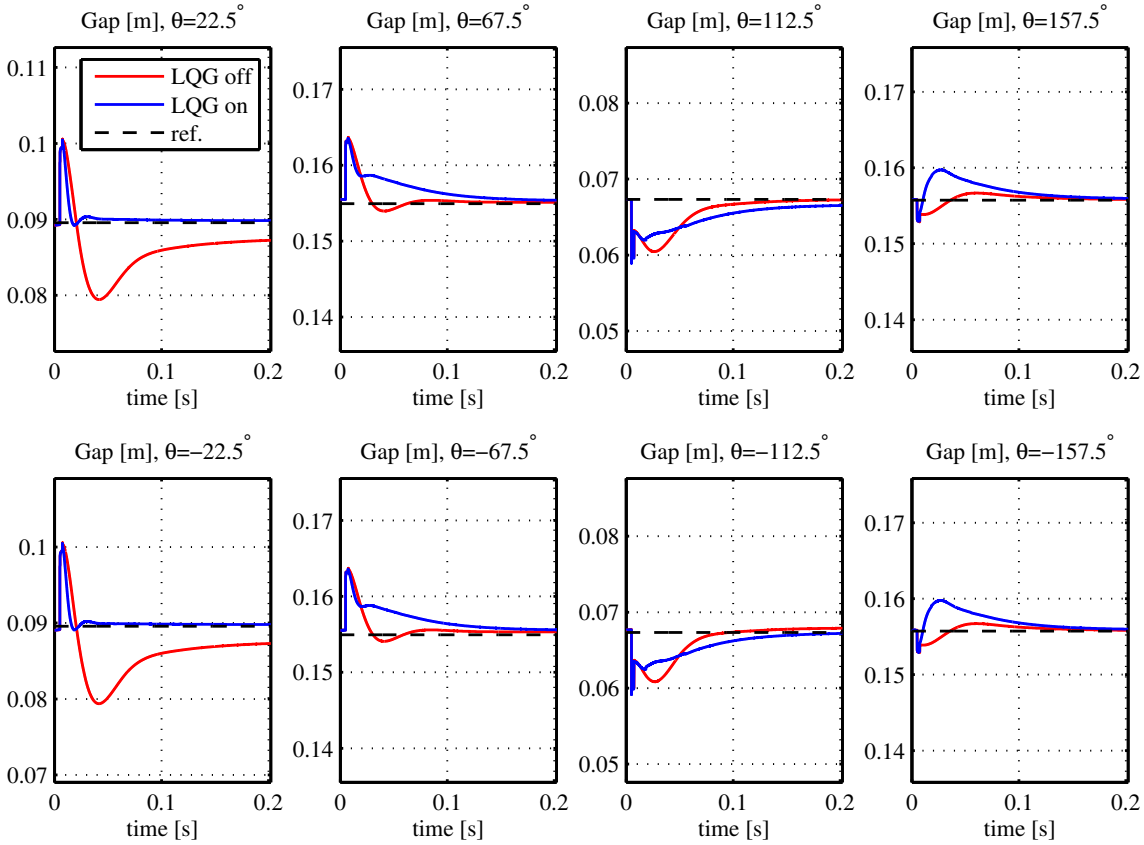

(a) Plasma-first wall gaps

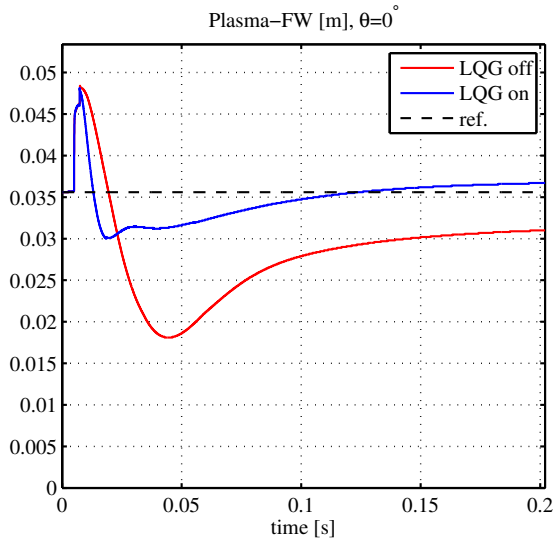

(b) Distance from limiter point

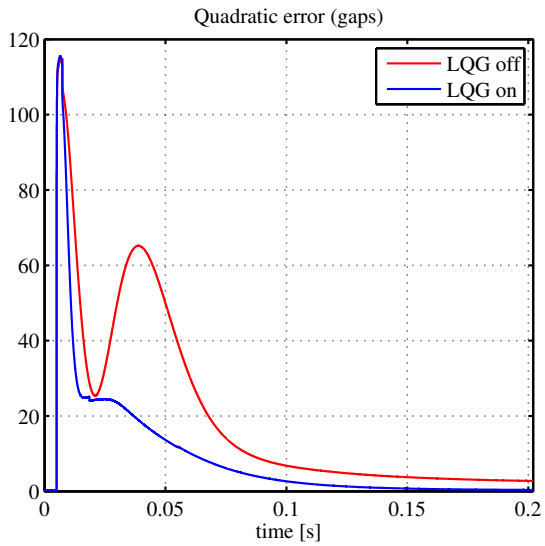

(c) Quadratic error (gaps)

Figure 6.22: Pert. #3 with recovery

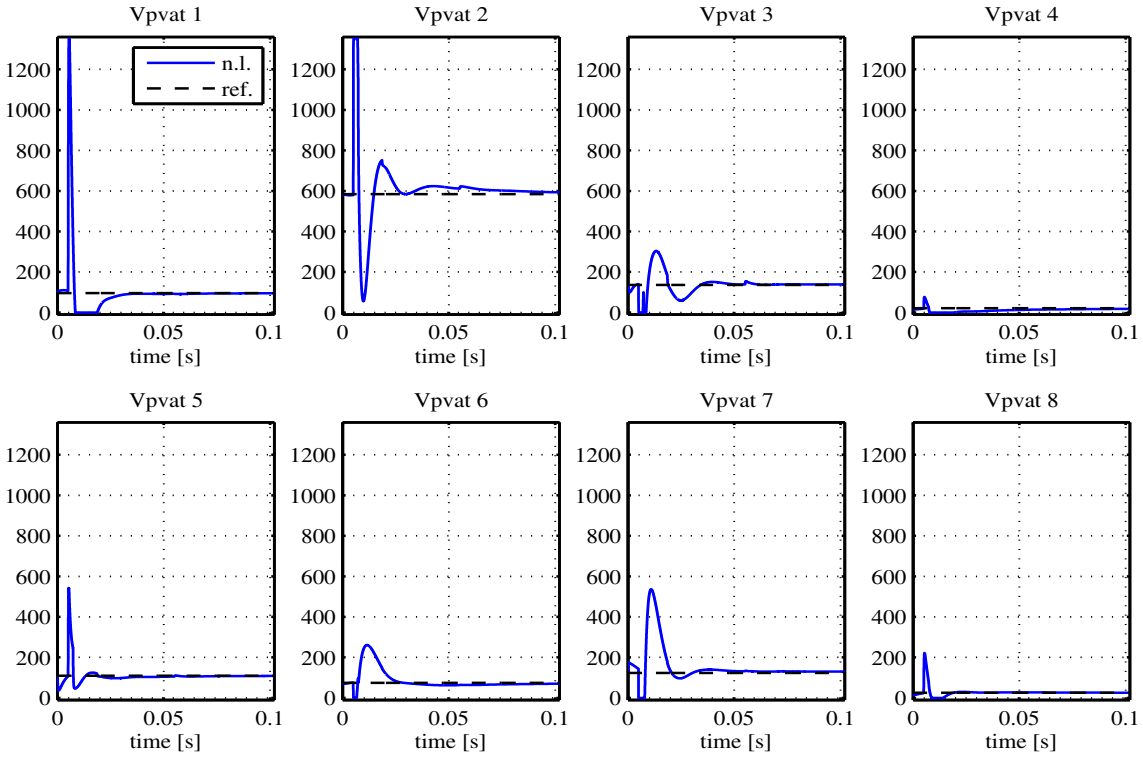

(a) PVAT applied voltage

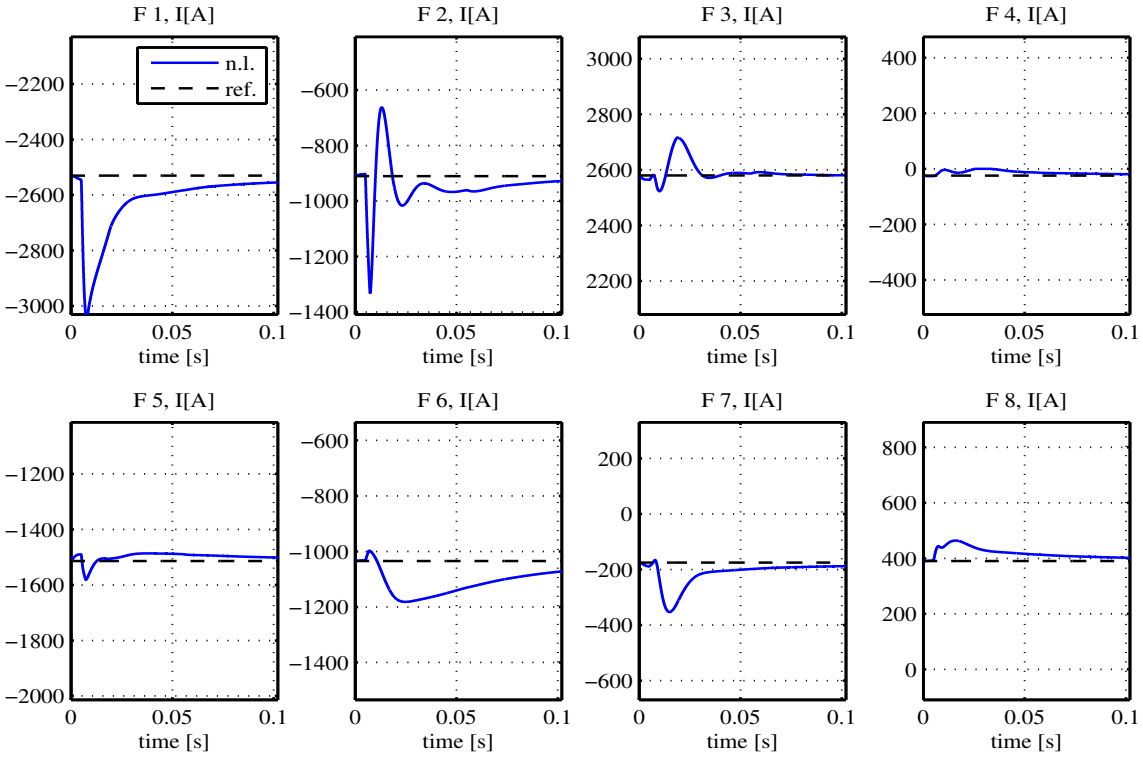

(b) F coils current

Figure 6.23: Pert. #3 with recovery, LQG control

Perturbations without recovery We will now consider the application of tokamak perturbations without recovery, complying to eq. (6.11), (6.12) if one assumes $\tau_\alpha \to +\infty$ and $\tau_\beta \to +\infty$. Since an integral control law is not implemented, this kind of perturbations will be useful to check whether static gain of the controller is sufficient to assure that critical geometric parameters are kept within a safe range of values. The controller will prove to be adequate in this sense, but some additional considerations will emerge.

For the purpose of these tests, perturbations #1 and #2 have the same step variations as in the case with recovery, while perturbation #3 is slightly different. Instead of modeling a decay of both α and β, that would model a loss in plasma internal inductance and plasma pressure, we model a variation that implies a loss in plasma internal inductance together with an increase in plasma average pressure. This kind of perturbations is less likely to be physically realistic, but it is advantageous as it keeps the Λ parameter (eq. 3.3) constant. This means that the vertical field required to maintain the plasma in equilibrium is, with some approximation, unchanged. The position stabilizing controller does not react to the perturbation in this case, which leads to more interesting conclusions in the case of parameter perturbations without recovery.

Table 6.5 resumes the applied perturbations, while the resulting variations in l_i and β_θ are reported in graphs of figure 6.24.

Pert.#	$\frac{\alpha_1}{\alpha_0}$	$\frac{\beta_1}{\beta_0}$	$\frac{l_{i,1}}{l_{i,0}}$	$\frac{\beta_{\theta,1}}{\beta_{\theta,0}}$
1	3	1.03	72.7%	~ 1
2	1	3/5	~ 1	59.8%
3	3	1.466	72.7%	142.7%

Table 6.5: Tokamak perturbations without recovery
Initial plasma parameters: $l_{i,0} = 0.95$, $\beta_{\theta,0} = 0.29$.

In all of these cases a steady state error on gaps remains (figures 6.25, 6.27 and 6.29), while a static control action altering the equilibrium currents configuration is visible in figures 6.26, 6.28 and 6.30: this is consistent with the fact that the plasma nonlinear model changes, due to the permanent change of the internal parameters. The linear model, derived for the initial value of the parameters, is less matched to the nonlinear model in these conditions, and the absence of integral tracking on gap measures explains why the steady state error emerges.

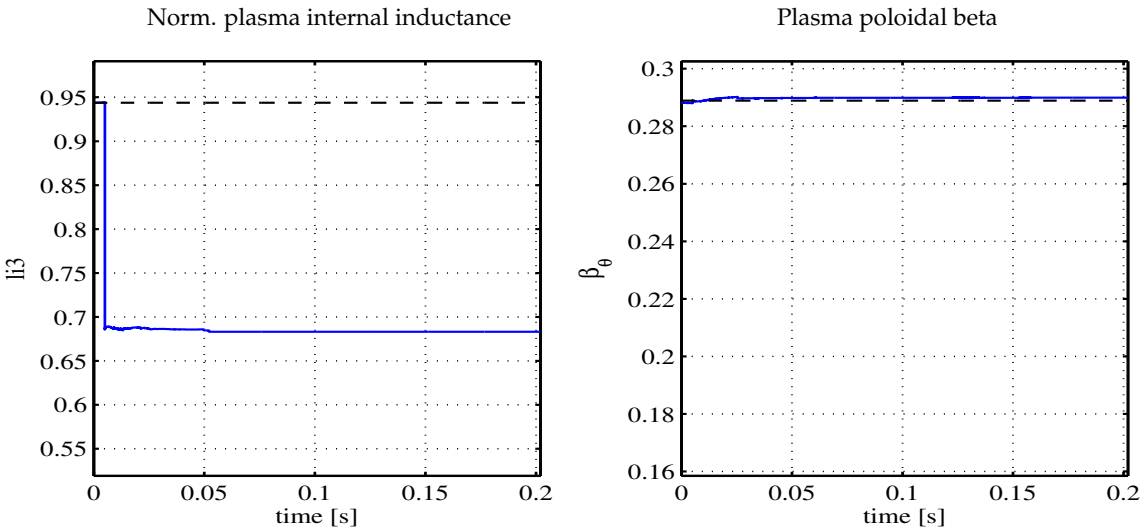

(a) Pert. #1 without recovery

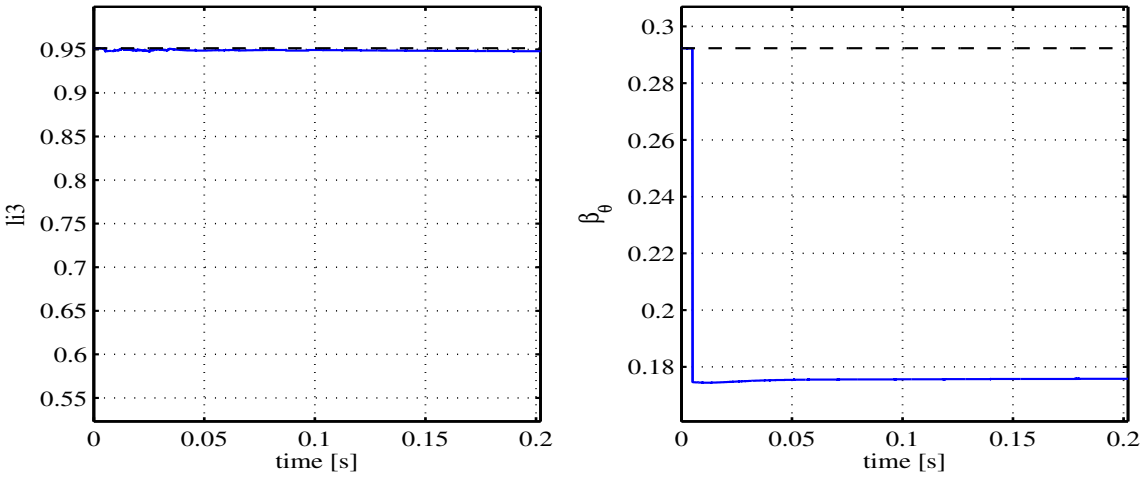

(b) Pert. #2 without recovery

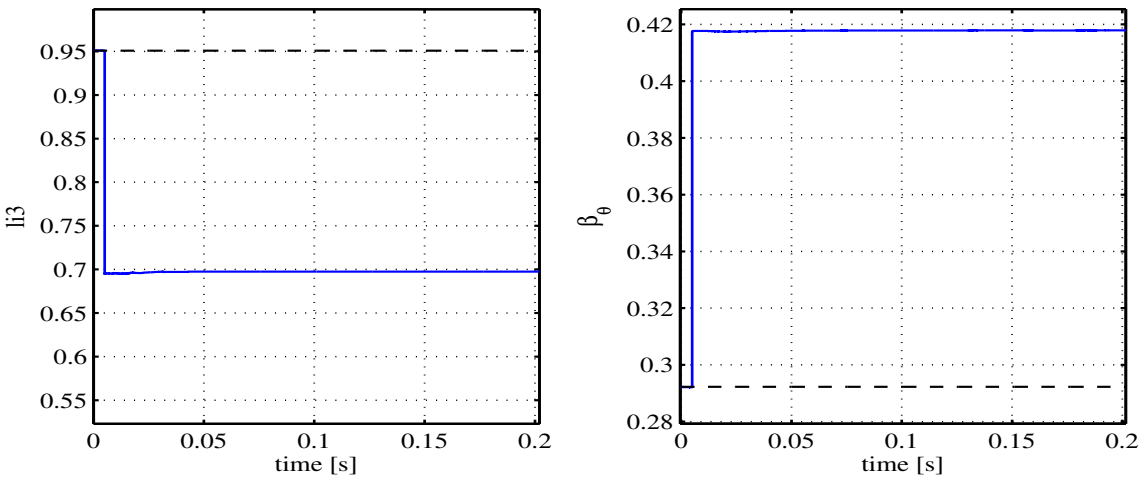

(c) Pert. #3 without recovery

Figure 6.24: Tokamak perturbations without recovery

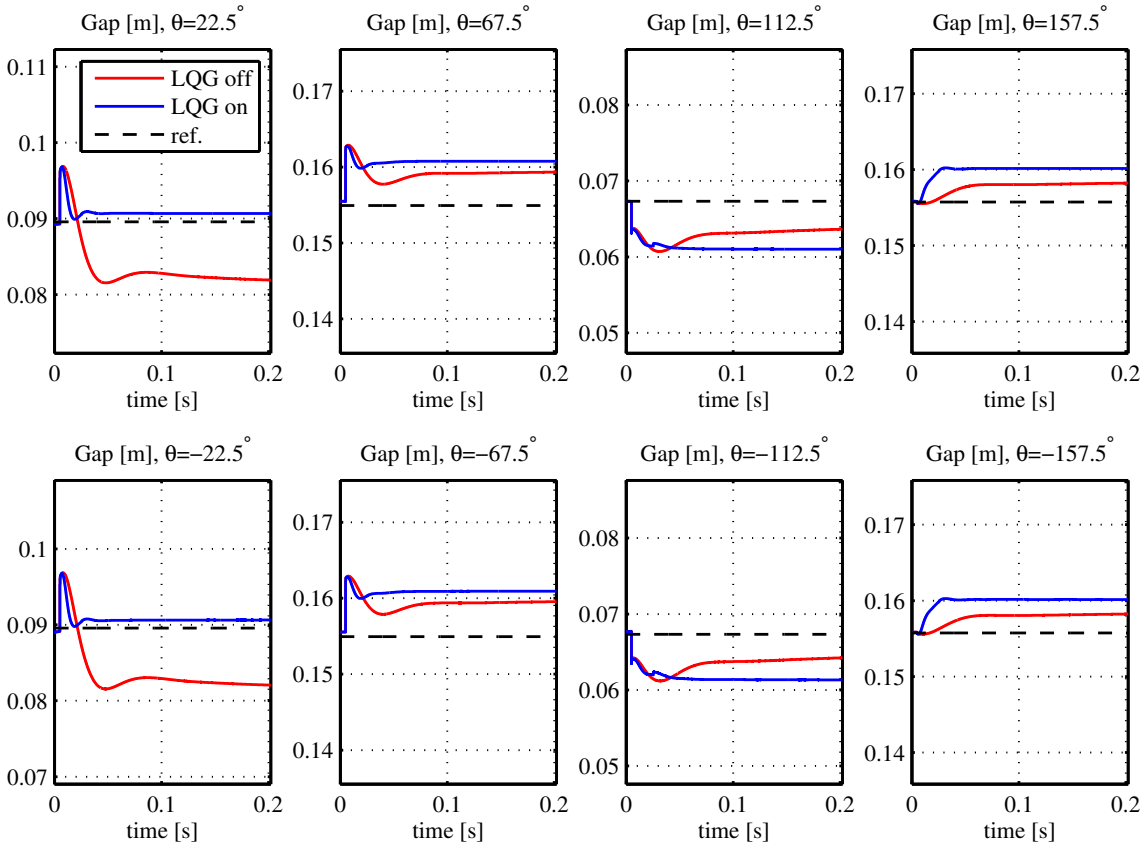

(a) Plasma-first wall gaps

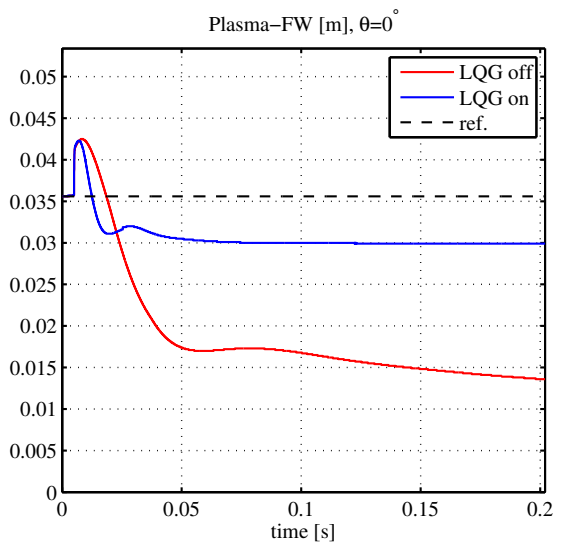

(b) Distance from limiter point

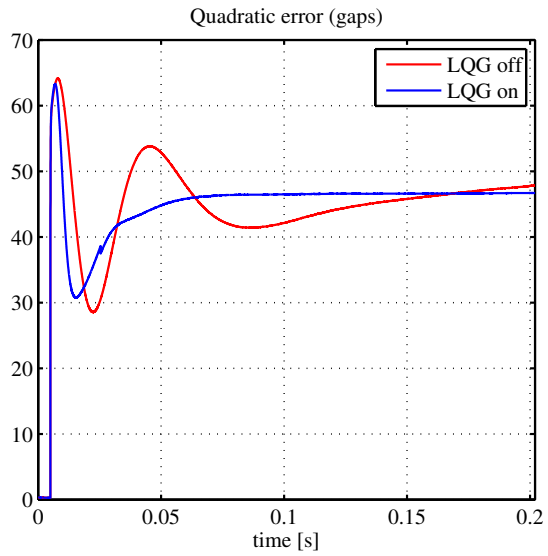

(c) Quadratic error (gaps)

Figure 6.25: Pert. #1 without recovery

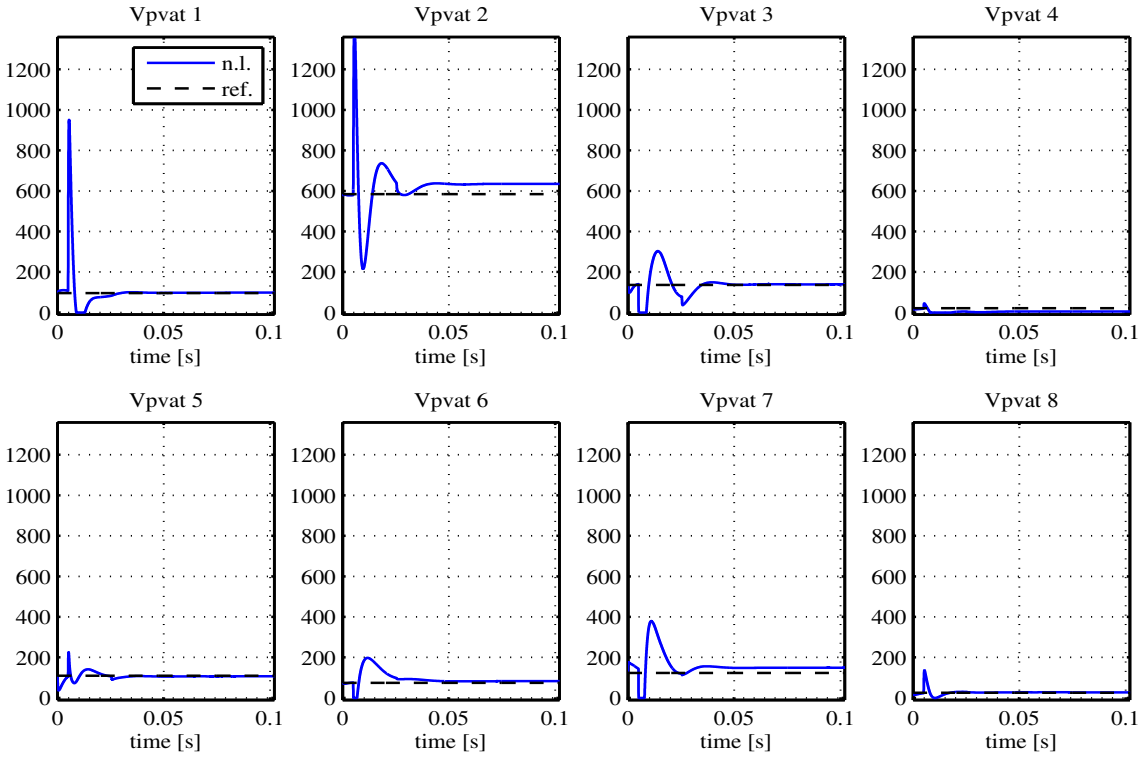

(a) PVAT applied voltage

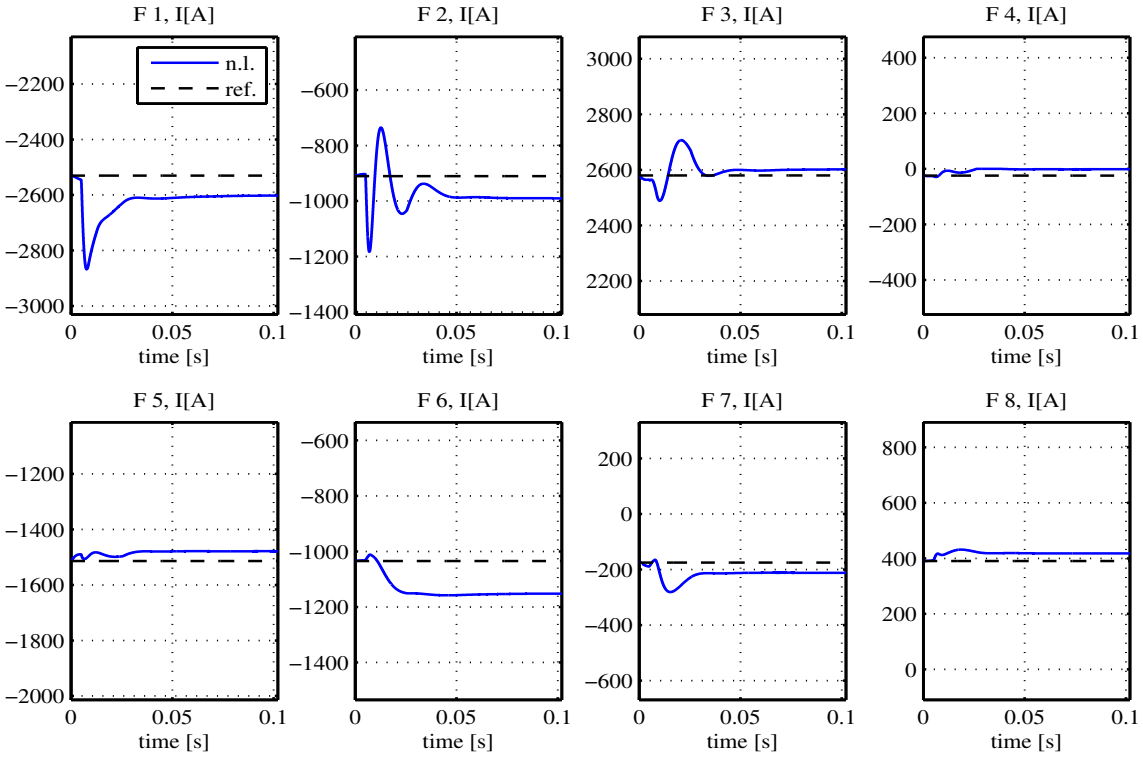

(b) F coils current

Figure 6.26: Pert. #1 without recovery, LQG control

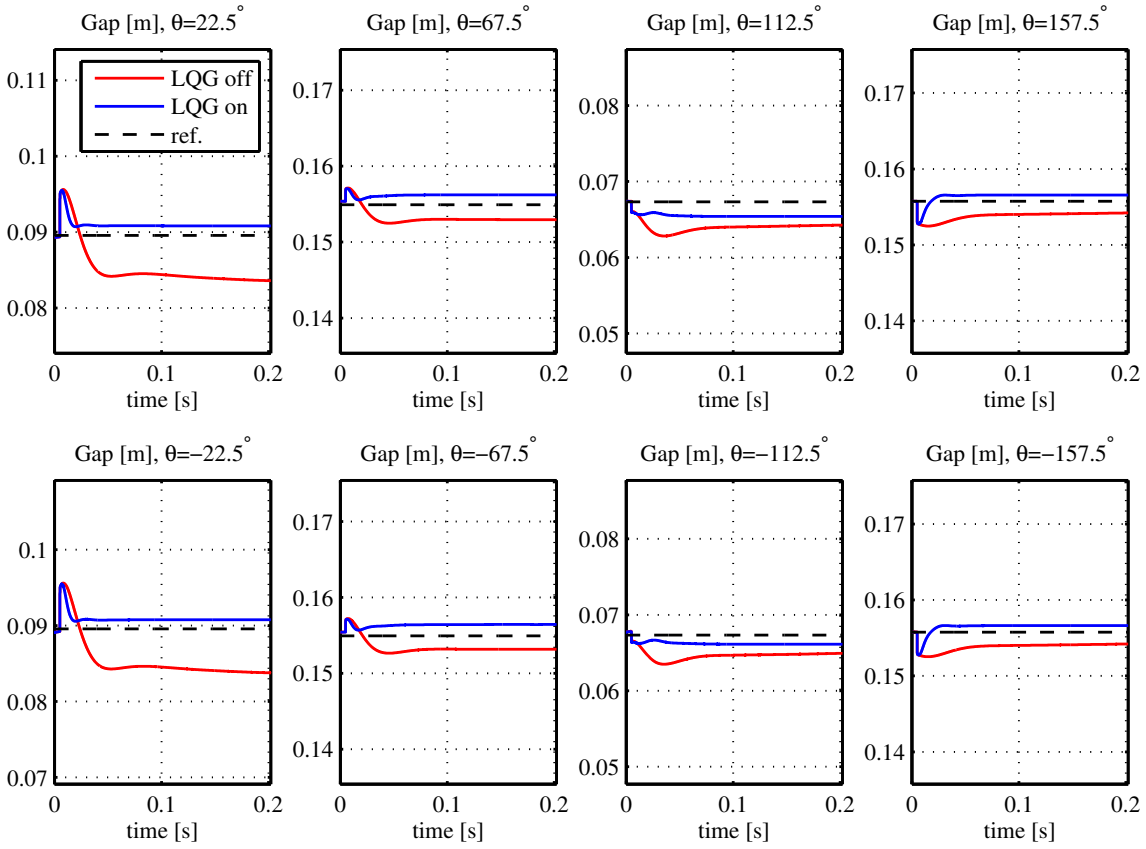

(a) Plasma-first wall gaps

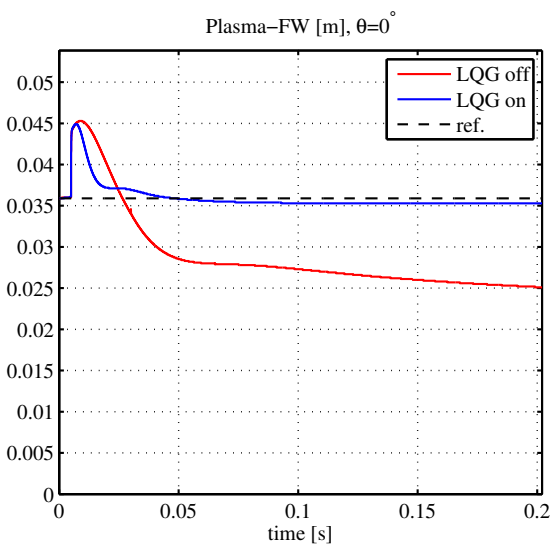

(b) Distance from limiter point

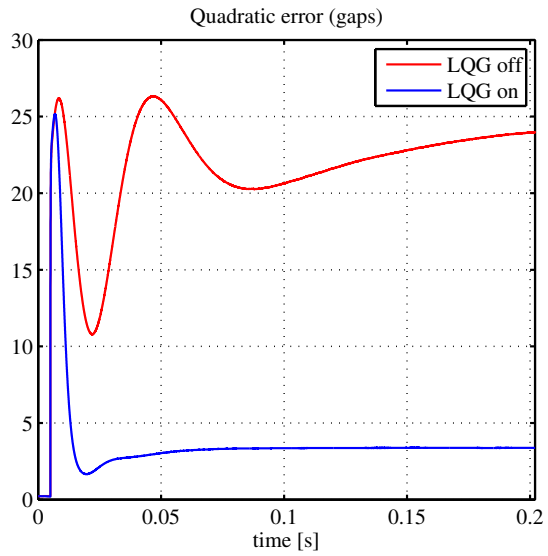

(c) Quadratic error (gaps)

Figure 6.27: Pert. #2 without recovery

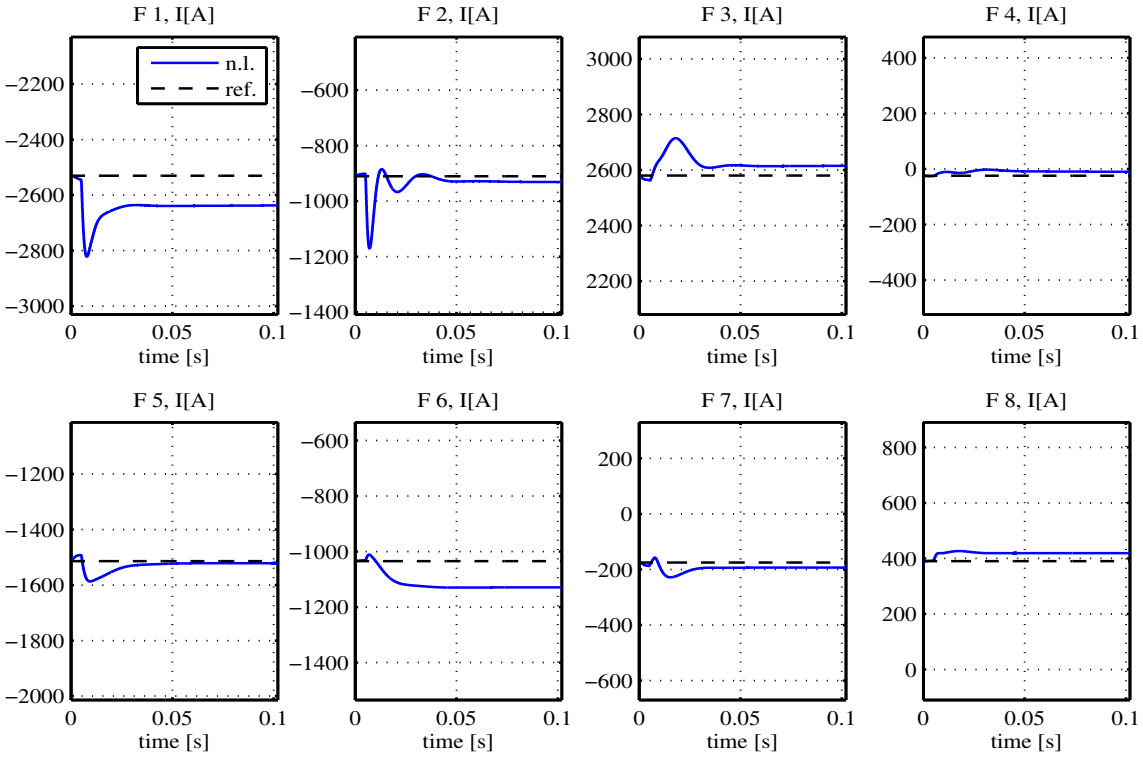

(a) PVAT applied voltage

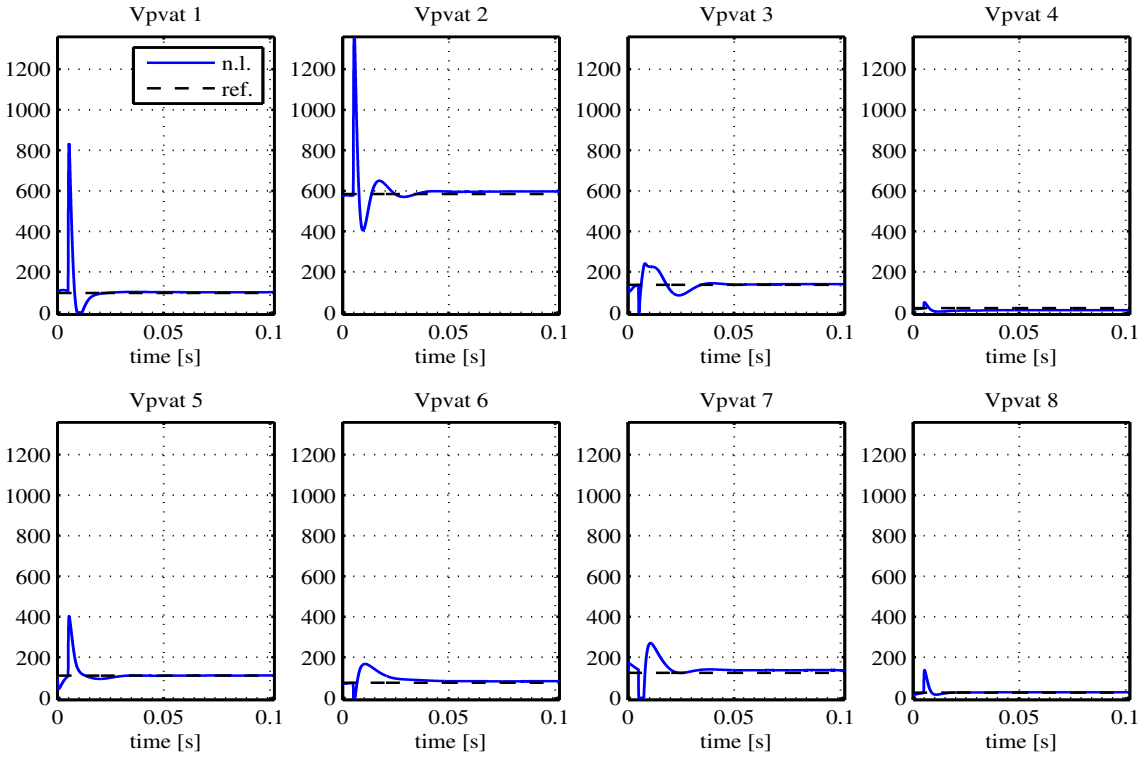

(b) F coils current

Figure 6.28: Pert. #2 without recovery, LQG control

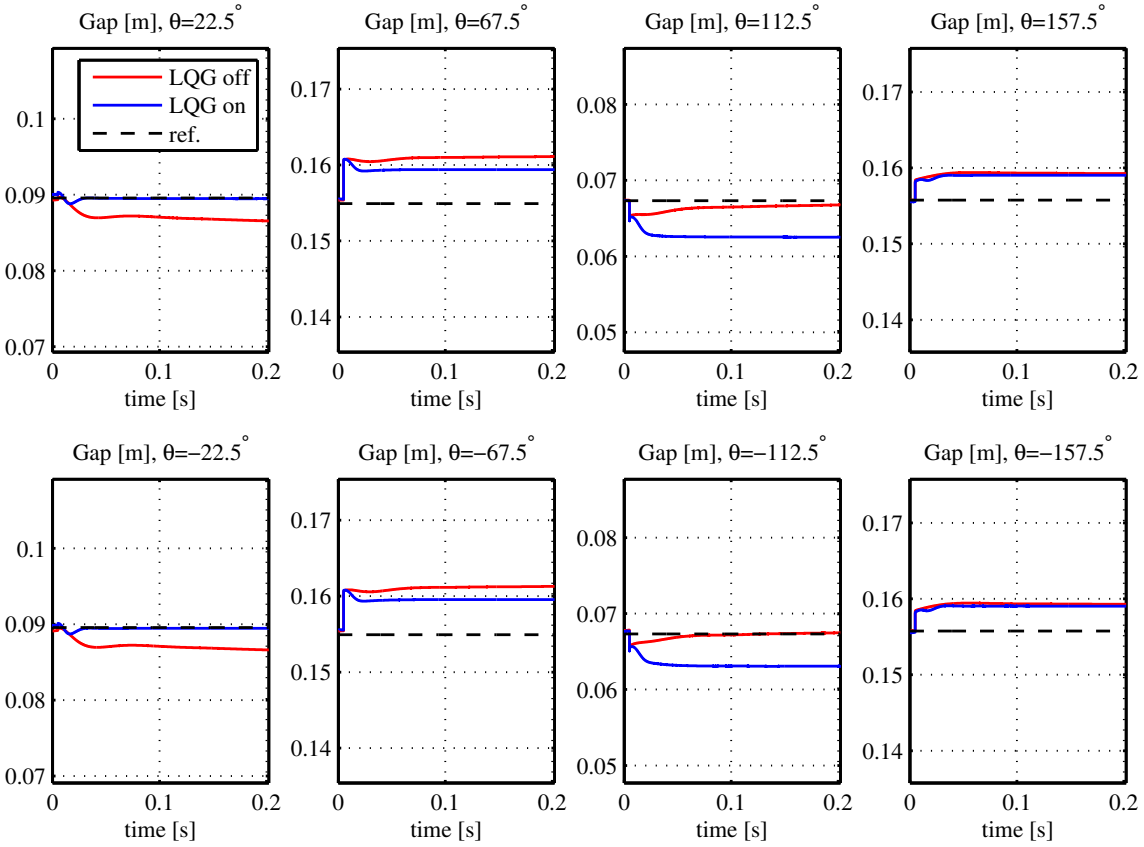

(a) Plasma-first wall gaps

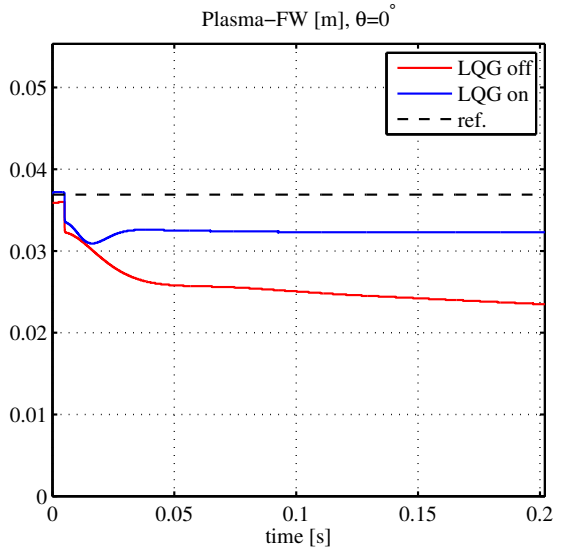

(b) Distance from limiter point

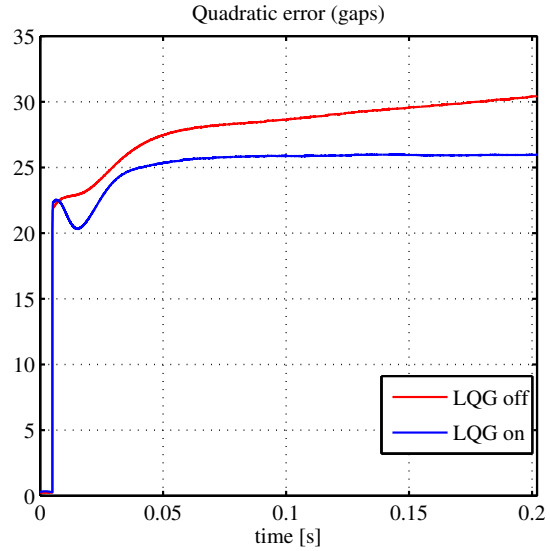

(c) Quadratic error (gaps)

Figure 6.29: Pert. #3 without recovery

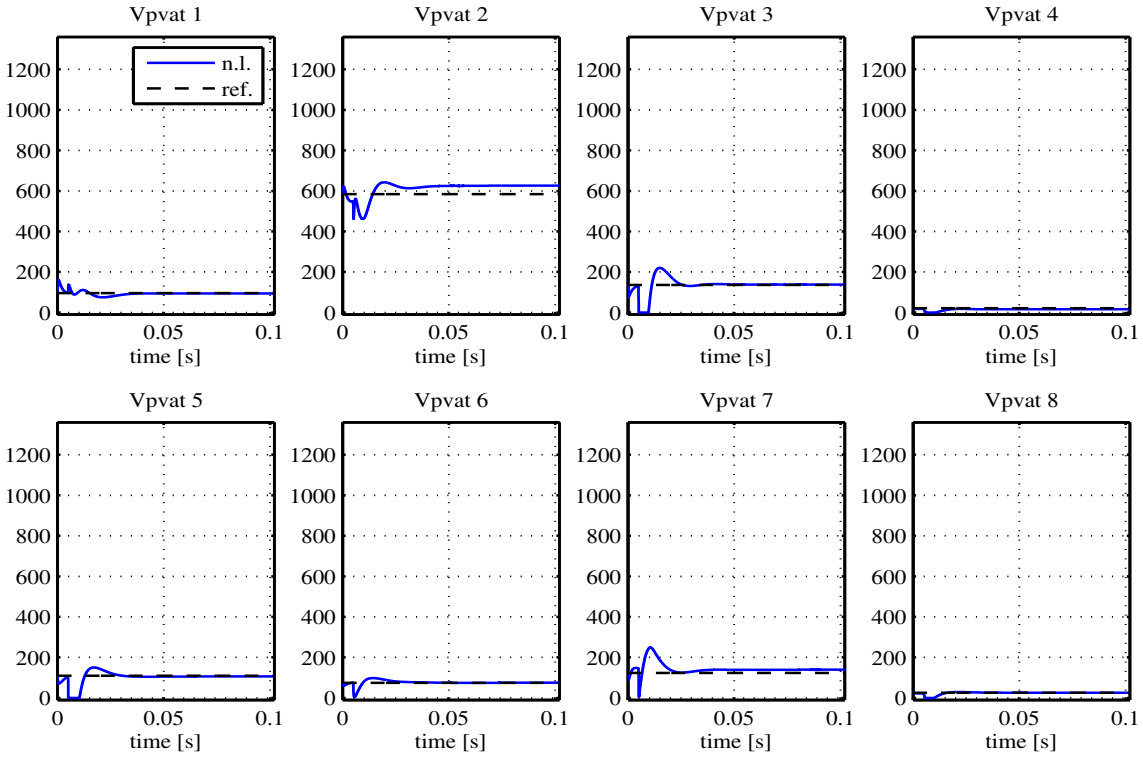

(a) PVAT applied voltage

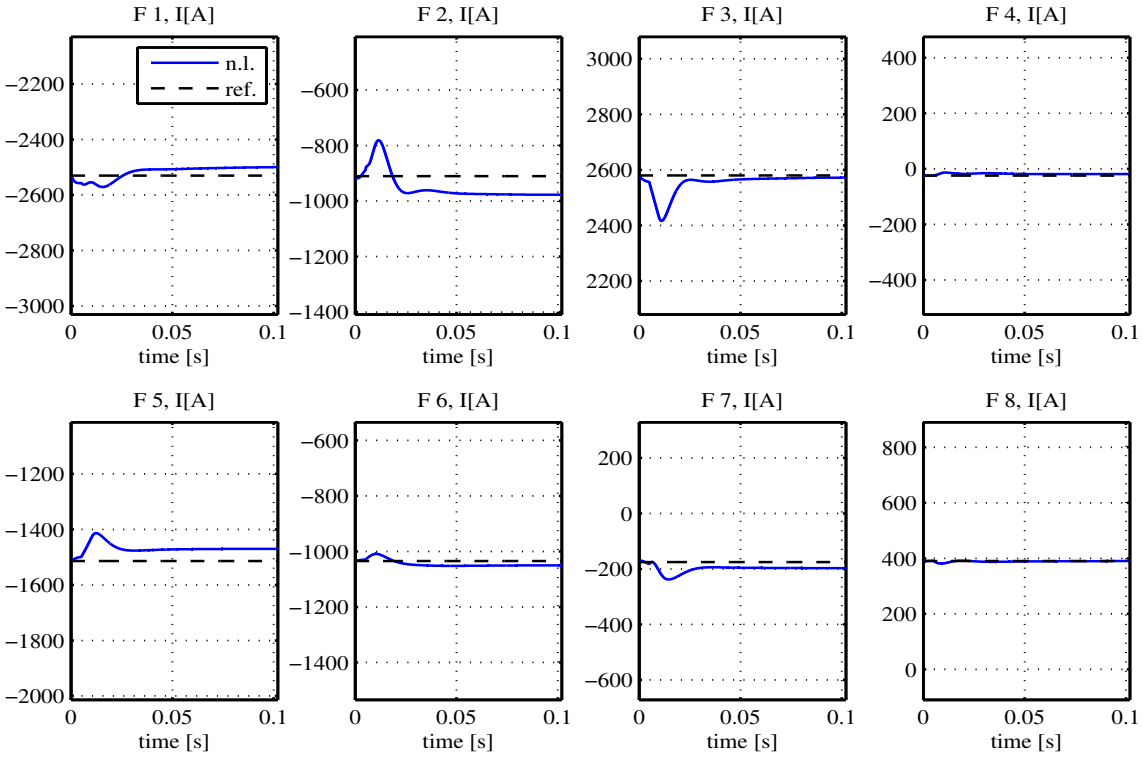

(b) F coils current

Figure 6.30: Pert. #3 without recovery, LQG control

Even if a steady state error exists, it is nevertheless better to enable the LQG controller, since plasma-first wall distance at $\theta = 0^\circ$ is kept under control (figures 6.25.b, etc.) and is asymptotically stabilized to a constant value. Without shape control, plasma-first wall clearance on the horizontal plane varies with longer time constants, and reaches lower, less safe values.

Perturbations #1 and #2 cause a non recovered excess of vertical field and an oscillation of the horizontal position of the plasma ring due to the interaction with the position stabilizing controller when the LQG controller is disabled, or with both the control loops when the LQG controller is enabled. The shape controller assures better control of plasma displacement, preventing the double-null configuration from degrading to a limiter configuration, since a clearance of at least $3\ cm$ is always assured in these cases. This should increase the quality of experimental discharges, avoiding the condition reconstructed in figure 4.7.

Perturbation #3 without recovery is interesting because, as will be proved in the next section (figure 6.32.f), the position stabilizing controller does not exert almost any control action in this case, yet the steady state error on gap measures emerges, confirming that this is caused by the increased difference between the perturbed nonlinear model and the nominal linear model, and is not due to the interaction between the position stabilizing controller and the shape controller. In this case, too, clearance from the first wall on the horizontal plane is better controlled enabling the LQG regulator.

Finally, considering total quadratic error on gaps measures, it can be observed that the controller seems to be more sensitive to permanent variations of the l_i parameter (figure 6.25.c) than to variations on the β_θ parameter (figure 6.27.b), since only in the latter case the controller is able to significantly reduce total quadratic error on gaps. The controller is designed on the basis of the linear model, whose dynamics are those of a network inductively coupled, and it is reasonable that a macroscopic variation on plasma internal inductance has a relevant effect on the modified inductance matrix, and in network dynamics as well.

In the following section, some considerations about power consumption are proposed.

6.6 LQG regulation: power consumption

The graphs on the left column of figures 6.31 and 6.32 report power consumption requirements of the poloidal field circuit, defined as the total power consumption of $PVAT$ converters, in the cases where plasma parameters perturbations are applied. The dashed line represents static power consumption required to compensate for resistive losses and maintain the equilibrium configuration without perturbations, and is the power consumption of the converters when the LQG controller is disabled. The solid line represents actual consumption when the LQG controller is enabled. Peak power consumption is not excessive, considering the rating of $PVAT$ converters; the derivative of total power consumption over time is however very high when perturbations are applied. We are considering a limit case design for the LQG controller, to evaluate its performance in restoring perturbations on gaps. However, it is possible to lessen peak power consumption by choosing a less demanding allocation (e.g. $r = 1$ instead of $r = 2.5$, table 6.3) that could be more suited to experimental conditions.

The right column of the same figures features power consumption of the position stabilizing controller before and after the introduction of the shape controller. Enabling the shape controller lessens peak power consumption of the saddle coils circuits, suggesting that the shape controller actually helps in maintaining the horizontal stability of the configuration. However, an increase in static power consumption of saddle coils circuits when the LQG controller is enabled suggests that the two control loops are partly interacting. An interaction between the two control loops could only exist with regard to the control of horizontal displacement, since vertical stabilization is completely decoupled from shape control action given that F coils cannot generate net radial field on the equatorial plane. In the cases of tokamak perturbations without recovery (figure 6.32), the interaction between the two control loops is more evident because a certain static power consumption of the position stabilizing controller appears.

Possibly, the position stabilizing controller could be designed giving more emphasis to frequency separation from the shape controller, e.g. using a proportional-derivative controller with a less dominant proportional component. Since the shape controller has been designed ad-hoc for the stabilized system, it is not the case to apply modifications to the stabilizing controller at this point. However, two considerations suggests that the examined configuration is acceptable.

Firstly, power consumption of the position stabilizing controller is degrees of magnitude lower than that of the shape controller (graphs are scaled in kW and MW respec-

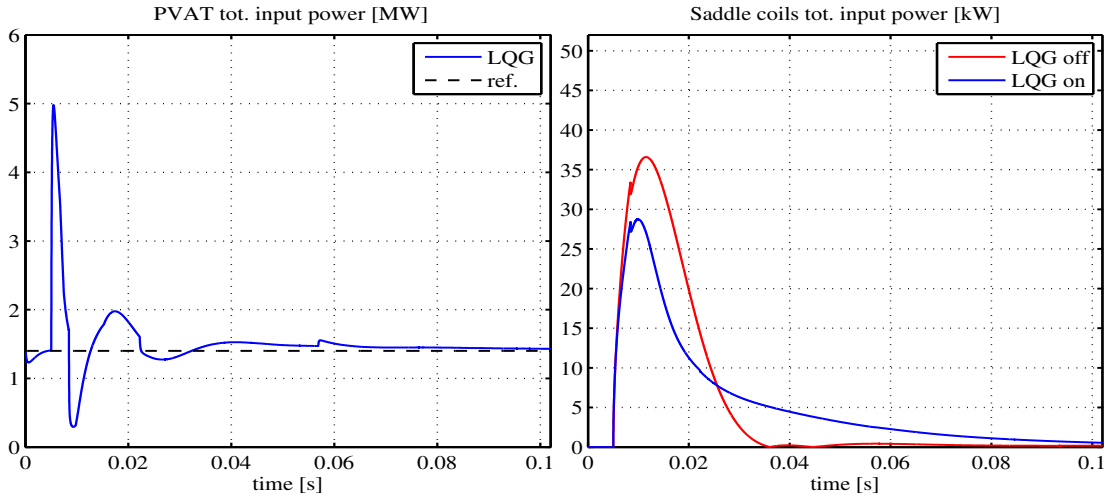

(a) Pert. #1 with recovery, $PVAT$ with LQG on

(b) Pert. #1 with recovery, saddle coils

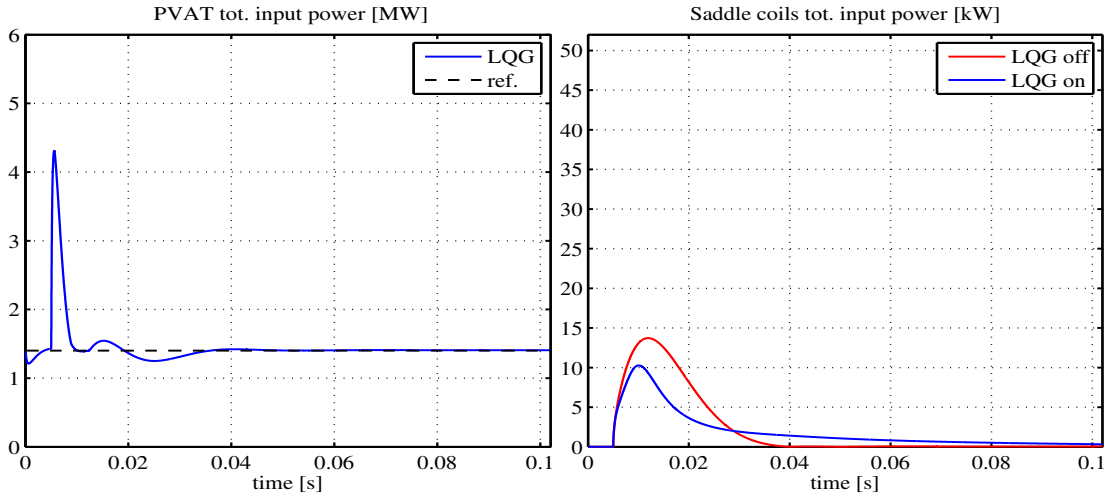

(c) Pert. #2 with recovery, $PVAT$ with LQG on

(d) Pert. #2 with recovery, saddle coils

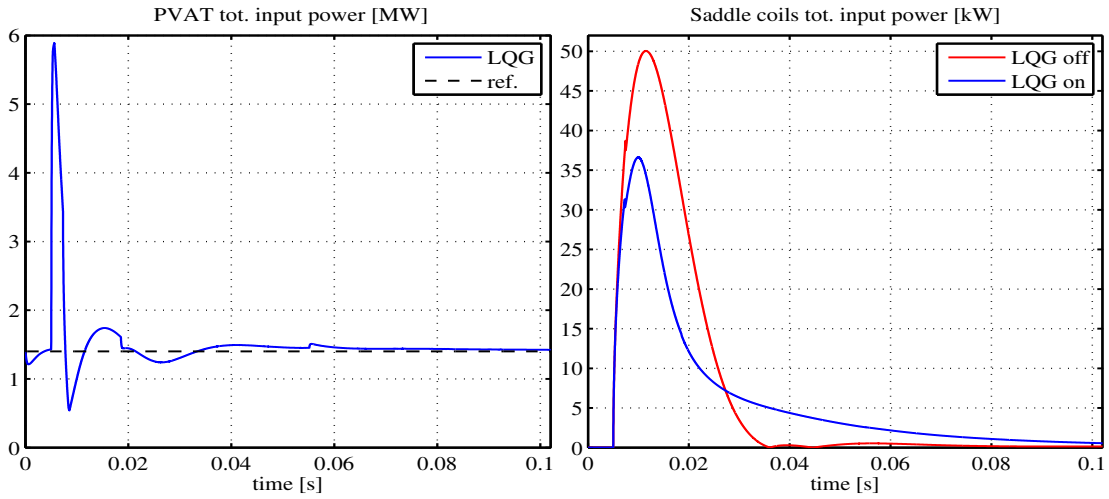

(e) Pert. #3 with recovery, $PVAT$ with LQG on

(f) Pert. #3 with recovery, saddle coils

Figure 6.31: Power consumption, perturbations with recovery

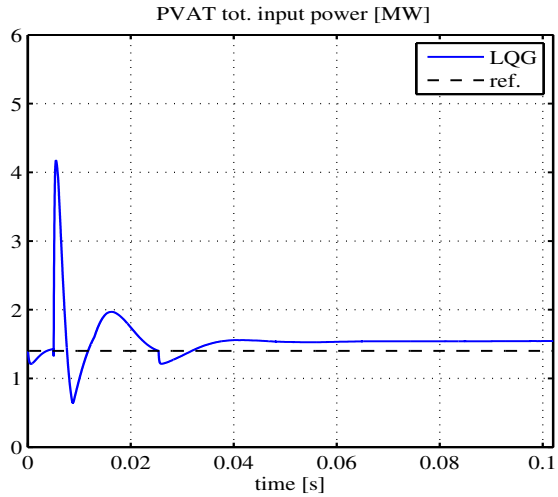

(a) Pert. #1 without recovery, $PVAT$ with LQG on

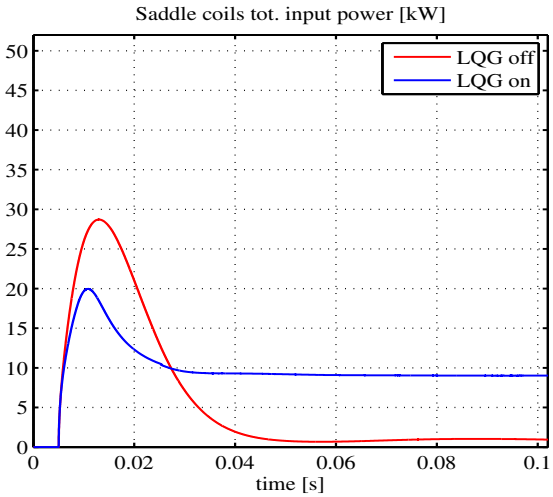

(b) Pert. #1 without recovery, saddle coils

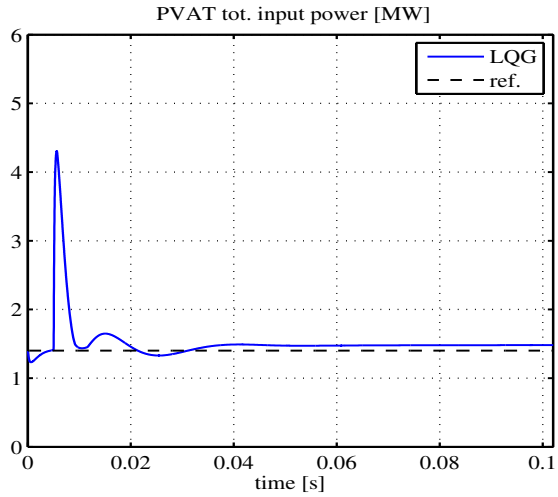

(c) Pert. #2 without recovery, $PVAT$ with LQG on

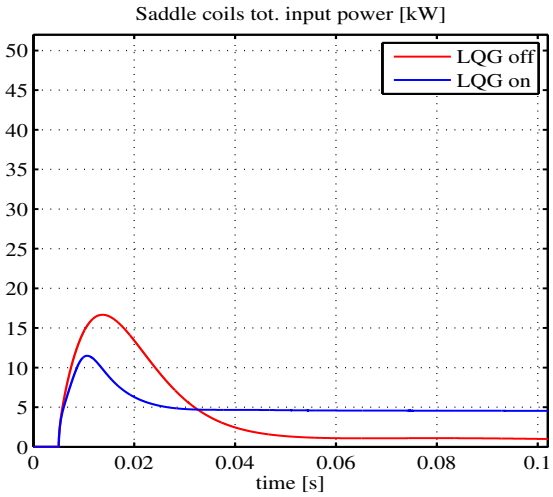

(d) Pert. #2 without recovery, saddle coils

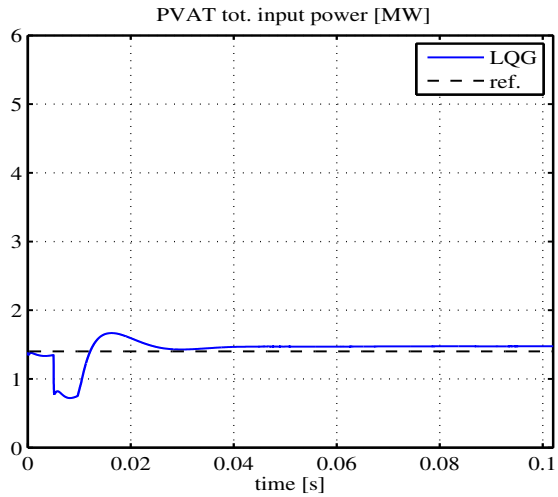

(e) Pert. #3 without recovery, $PVAT$ with LQG on

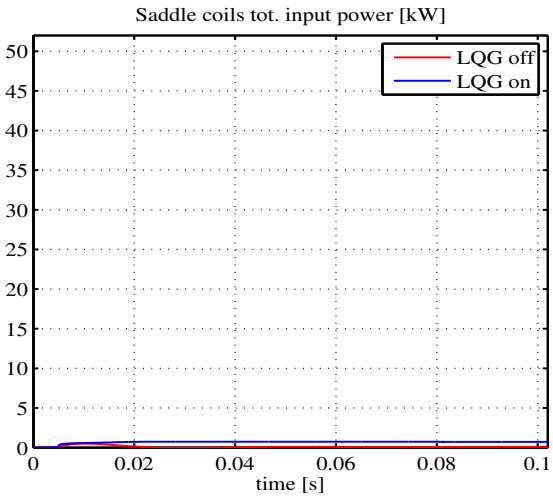

(f) Pert. #3 without recovery, saddle coils

Figure 6.32: Power consumption, perturbations without recovery

tively), so a worst-case static power consumption of $10\ kW$ by the position stabilizing controller when the plasma parametrization changes (figure 6.32.b) is negligible.

Secondly, the presence of a static error on gaps measures when plasma parametrization is not restored to initial values is not caused by the interaction between the two control loops, since, as can be seen in figure 6.32.f, it is possible to model a perturbation that does not lead to the activation of the plasma position stabilizing controller. In this case, there is surely no interaction between the two control loops, and, as it was shown in the previous section, static error on gaps is still present (figure 6.29).

A concluding test that evaluates the performance of the shape controller in tracking a ramp-up variation of gap references, leading to the transition from a circular plasma configuration to a double null plasma configuration, is reported in the following section.

6.7 Circular-DN transition with LQG control

The LQG controller will now be tested simulating the time-domain evolution of an experimental double-null discharge. As a matter of fact, the experimental discharge in RFX-mod starts with a circular plasma where F coils 3 and 8 are kept at zero current, and then evolves to double-null configuration increasing a positive current in those coils. The transition between circular and double null configuration has already been reproduced on the simulator imposing the experimental value of current in active coils (figure 4.2.b). However, we will now consider the evolution from circular plasma using the LQG controller to track a predefined reference for gap measures over time. In the time scale of the simulation, the transition begins at $t = 0.050\ s$ and ends at $t = 0.100\ s$, and a linear transition is imposed both for F coils currents and gap measures. The LQG controller is activated at the beginning of the transition, at $t = 0.050\ s$, when the plasma is still in a circular configuration. The initial configuration is very different from the DN configuration used to derive the linear model; nevertheless, tracking of gap reference for the whole duration of the transition is good (fig. 6.33).

Since the LQG controller was designed with an emphasis on gap control, this task has a priority over active coils current control, and the tracking of F coils current reference is less precise, since a larger error is allowed on these quantities to favour control action; this is a consequence of the maximum allowed variations that define LQ index weights, chosen in table 6.3. Since plasma boundary dynamics are strongly nonlinear, a linear transition on F coils current does not assure a linear transition on gaps measures. As a consequence, the current on some of the F coils (fig. 6.34), $F2$ and $F3$ in particu-

lar, undergoes strong variations during the transition. This could be unacceptable in an experimental context; however, it is possible to use a controller that focuses on F coils current control during the transition, allowing a degree of freedom on gap measures. Finally, the LQG controller can be enabled at the end of the transition. This could be achieved designing another version of the LQG controller to be used during the transition, simply arranging different weights in tab. 6.3 (e.g. more gap variation allowed, less F coils current variation allowed), and then switching to the original version of the LQG controller considered hereby at the end of the transition. The two versions of the controller would differ only by the state-feedback matrix used to compute $PVAT$ applied voltage. Results of this simulations are however very encouraging in suggesting that the LQG controller could actually be a valuable tool to increase transition control and overall discharge quality in the experimental framework of RFX-mod.

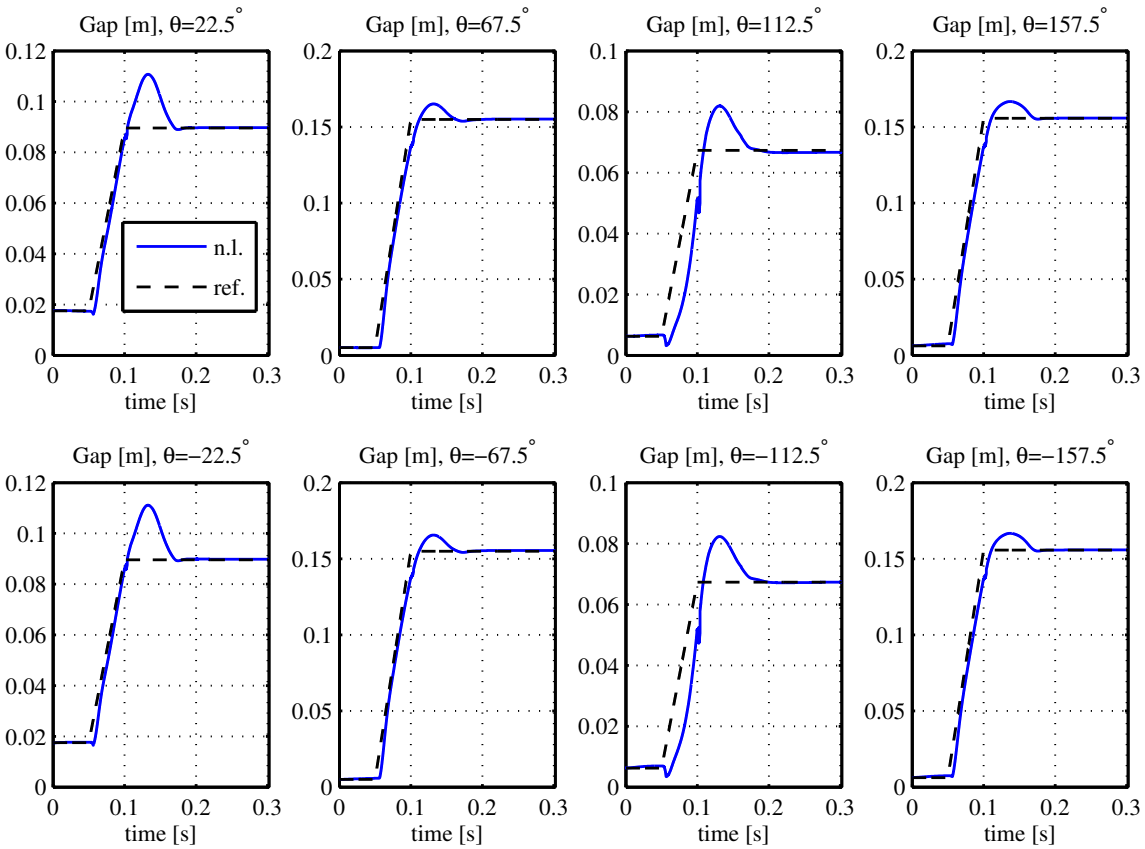

Figure 6.33: Circular-DN transition with LQG control, gaps

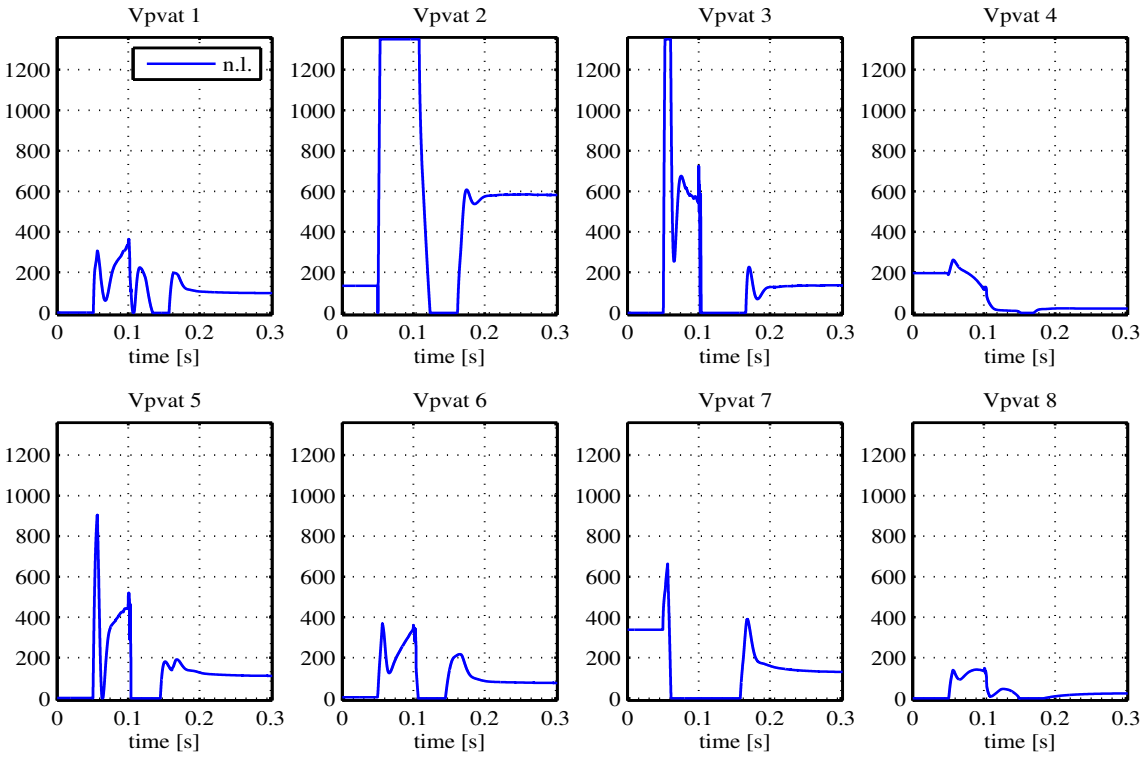

(a) PVAT applied voltage

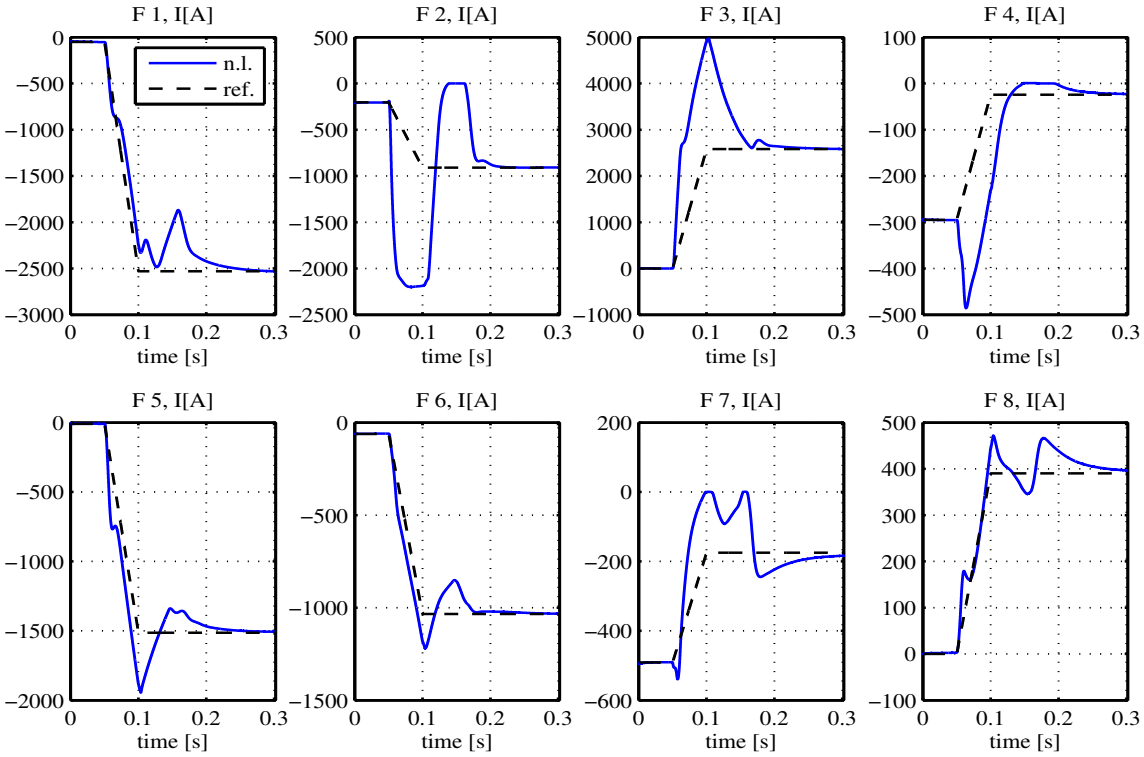

(b) F coils current

Figure 6.34: Circular-DN transition with LQG control, actuators

Conclusions

Several aspects of plasma discharge diagnosis and control have been considered in this work. Firstly, it has emerged how plasma shape reconstruction routines are critical when the design of a shape controller is prospected, since the ability to correctly reconstruct the controlled variables (plasma clearance from the first wall at gaps) directly impacts the precision of the control action. The plasma double-null configuration considered in this work has emphasized some critical aspects of reconstruction routines that were adopted for circular plasma configurations. Nevertheless, it was shown how the inclusion of information related to the effect of active coils current could extend existing routines, leading to more reliable reconstruction of plasma geometry. A routine that actually reconstructs the complete boundary line of the plasma was set up, and provided interesting results for what concerns the adaptation of existing integral plasma shape reconstruction methods applied to other experiments to the configuration of RFX-mod.

Further work could be developed in testing different reconstruction schemes to merge information provided by magnetic flux measurements and magnetic field measurements. In particular, the least square problem that originates the thin plate spline could be defined in terms of interpolation of flux and field measures instead of flux measures at different radii. The hypothesis needed to extrapolate the flux inside the plasma region could be removed in this case, and the reconstruction routine would adopt an approach more similar to the one used in early versions of XLOC. Also, different sets of basis functions for the interpolating surface could be tested, and the performance of the different sets could be assessed comparing the reconstruction with the boundary line provided by the simulator. The results proposed in this work are encouraging in suggesting that an accurate reconstruction of plasma shape for complex configurations is possible in RFX-mod, and the proposed method is worth to be further analyzed and extended for what concerns compliance to real time constraints and efficient implementation.

A shape controller has been designed and tested assuming that ideal gaps measures

were available. The possibility that the controlled variables are affected by measurement noise has accurately been taken into account, but further validation tests could be performed once a reliable plasma shape reconstruction routine has been implemented in the nonlinear simulator. The complete implementation of the reconstruction routine in the simulator could provide a very realistic benchmark for the shape controller, that at this point would be ready to be implemented in the experimental framework.

Other possible extensions of this work include position control of the two null points of the configuration, since the reconstruction of the complete flux map produces an estimate for their displacement; different sets of gaps could be tested, and it should also be possible to set up a control law to make the complete reconstructed flux map converge to a desired configuration. Actually, it should be possible to set up a LQG control scheme to directly regulate the coefficients of the interpolating surface. As it is easy to understand, the shape reconstruction problem and the shape control problem are intimately linked, and several aspects could be further developed when considering the similarities between the two problems.

For what concerns the shape control problem itself, a standard LQG control technique for linear systems has been used. The linear model that has been derived has proven to be reliable as long as the plasma parametrization is set to nominal values, but a certain sensitivity to variations in plasma parameters has emerged, in particular for what concerns plasma internal inductance. This could be one of the limiting factors when testing the controller in an experimental context, since plasma characteristics could be subject to strong variations in a real discharge.

Another limiting factor of the LQG control technique resides in the fact that it is impossible to adapt the controller to the asymmetric saturation limits that characterize the actuators in RFX-mod. In this work, it has been shown that an accurate choice of LQR weights allows the design of a controller with acceptable performance. In particular, weights were chosen as if saturation limits were symmetric. Different approaches could possibly better exploit the full range of the actuators.

In conclusion, the implementation of the complete shape controller in the experiment is mandatory to actually assess whether the considerations and the hypothesis that led the development of this work were thoughtful and the results reliable. The attention that has been posed on theoretical aspects and the extensive use of the simulator support this work, and the experiment, seen as the starting point and the final goal of this study, could provide a more accurate review of the critical aspects of the models that have been used.

Appendix A

Linear model and LQG control: Simulink scheme

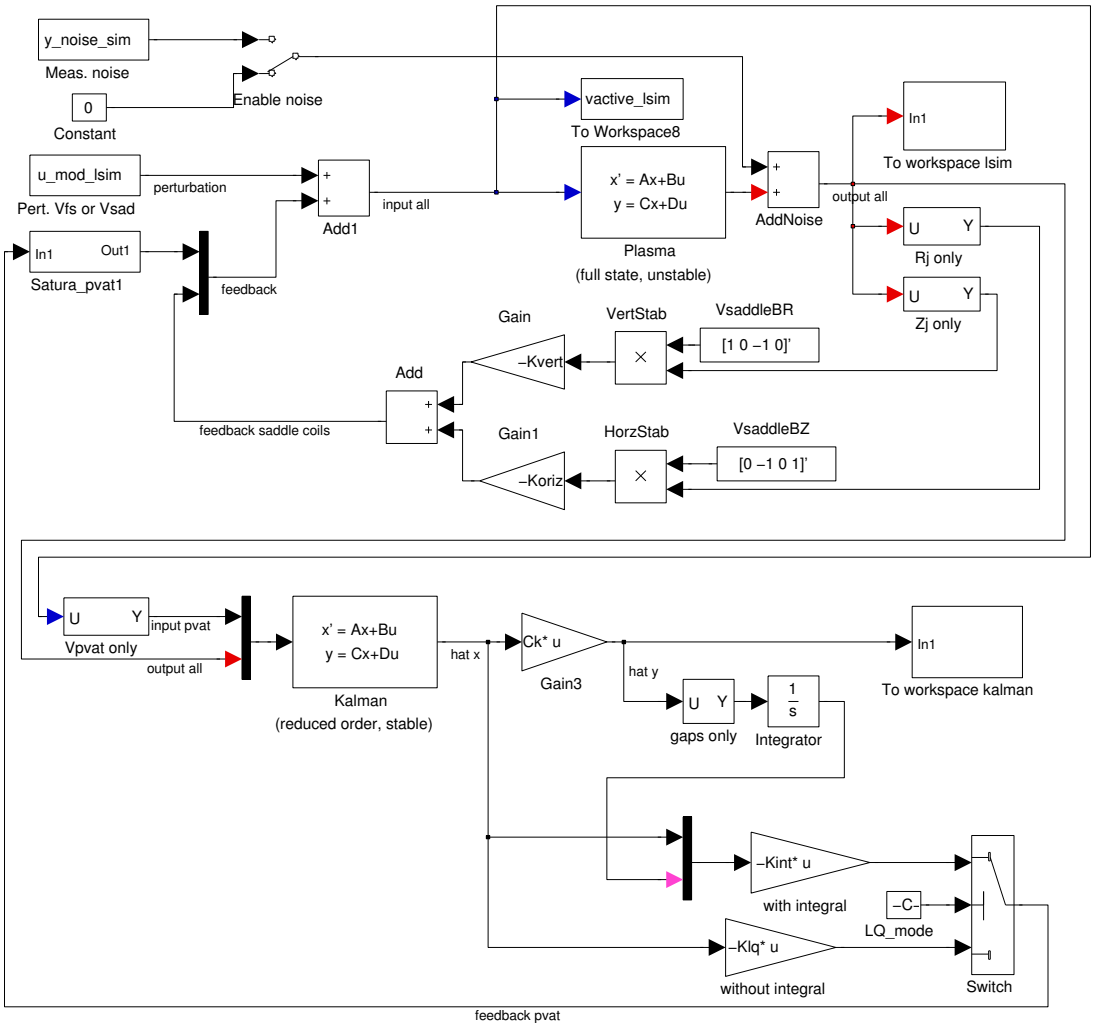

Figure A.1: Simulink scheme for LQG control

Figure A.1 reports the Simulink scheme used to perform linear simulations with the full-state model derived in chapter 5, and to test the LQG regulator designed in chapter 6. The stabilizing loop with feedback on saddle coils circuits is visible, while in the lower part of the scheme there are the Kalman filter and the LQ regulator based on the reduced order stabilized model. The scheme accurately models actuator saturation and allows the application of voltage perturbations or emulated measurement noise to the simulation.

Appendix B

Plasma boundary reconstruction: Matlab code

This section features the complete Matlab code used to obtain a reconstruction of the plasma boundary contour, as described in sect. 4.2. The code applies a subtraction of the effect of active coils currents on flux and field measures under the hypothesis that the linear superposition principle is valid. A Matlab implementation of the *eqflu* routine (`NewComputeDelta()`) is applied to the data obtained this way, to reconstruct magnetic flux in a more populated set of points. The Matlab `tpaps()` routine is used to obtain an interpolant of the flux function, and finally a set of flux maps computed by Maxfea is used to add back the effect of active coils to the thin-plate spline surface. The flux function is computed on a grid of 100×100 points, and the value is computed by interpolation on a finer grid using the `interp2()` routine when the gradient of the flux map needs to be computed to search for null points. The function `GapFromContour()` is used to post-process the contour line representing the plasma boundary to compute gaps measures.

The calculation of the flux function on a 100×100 grid spanning the whole device cross section, and the application of contour routines to compute the whole boundary line, make the program somewhat resource intensive; this has been done to produce a graphical reproduction of the complete flux map and of the plasma boundary line, but the code can easily be adapted to be more suited to real-time use when one is interested in computing gap measures only. Actually, in this case the flux function could be reconstructed only along the first-wall to estimate flux at the boundary in limiter configuration; in expected null points regions ($\mathcal{O}$ regions in figure 4.4) to estimate flux at the boundary in double null configuration, and finally along gap lines to estimate plasma-first wall distance at selected points.

```
clear all; close all

shot=29746

% Carico mappa del fusso dovuta a bobine F a 1000A
load ../fs_coil_field_effect/FxFsAll.mat

fps=3;
figuresize=[320 100 600 600];
figure('Position',figuresize);

eval(['mkdir ../../',int2str(shot),'/movie']);

if ~exist(['../dati_exp/' int2str(shot) 'ExpData.mat']);
    run ../ReadRFXExpDataRid
else
    eval(['load ../dati_exp/' int2str(shot) 'ExpData.mat;']);
end;


% Range temporale e intervallo frame
t_frame=[0.430:0.0001:0.450]; % per stima varianza

% Soglia per la determinazione del nullo, intesa come modulo quadro del
% gradiente di psi
nulSoglia=1.e-9;

% Correz. offset pickup toroidale con angoli Marrelli, facoltativo
corr_ang(1,:) = [0.30926064,0.41350806,-0.57013333,0.32118616,...
                 0.54592735,0.54205042,0.19339834,0.92131144];
corr_ang(2,:) = [-0.03268613,0.41480544,0.20469719,0.29319888,...
                 -0.36630881,0.33808011,0.22543849,0.59009963];
corr_ang(3,:) = [-0.24400695,0.31199950,0.65649521,0.42315990,...
                 -0.24534804,0.83835816,0.44737989,0.45641872];
corr_ang(4,:) = [0.99812609,0.14813846,-0.00616650,0.20182538,...
                 -0.19860078,0.27610695,0.35572317,0.76711601];
corr_ang(:,:) = corr_ang(:,:).*(pi/180);
for i=1:4
    for j=1:8
        Bp_fitti(i,j,:) = -Bt_fitti(i,j,:)*sin(corr_ang(i,j)) + ...
                          Bp_fitti(i,j,:)*cos(corr_ang(i,j));
    end
end;
```

```
% Medio considerando la sonda guasta
for j=1:2;Bp_fitti_ave(:,j)=mean(Bp_fitti(:,j,:),3);end;
% la terza sonda del quarto set toroidale e' rotta
j=3; Bp_fitti_ave(:,j)=(Bp_fitti(:,j,1)+Bp_fitti(:,j,2)+Bp_fitti(:,j,3))/3;
for j=4:8;Bp_fitti_ave(:,j)=mean(Bp_fitti(:,j,:),3);end;

%% Range per stima di un offset per pickup Btor costante
removeoffset=1;
tstimaoffset=[-0.05,0];
tstimofffp=[-2 -0.5];
if removeoffset
    indst1=find(t_dequ>=tstimaoffset(1),1,'first');
    indst2=find(t_dequ>=tstimaoffset(2),1,'first');
    offsetB=mean(Bp_fitti_ave(indst1:indst2,:));
    Bp_fitti_ave=Bp_fitti_ave-ones(numel(t_dequ),1)*offsetB;
    indfp1=find(t_dequ>tstimofffp(1),1,'first');
    indfp2=find(t_dequ>tstimofffp(2),1,'first');
    offsetFp=mean(d_fp(indfp1:indfp2,:));
    d_fp=d_fp-ones(numel(t_dequ),1)*offsetFp;
end

%% Switch vari
% per sovraimporre gap stimati da computedelta
gapstima=1;

% per generare un file avi in movie/mov_<shot>_exp.avi
avioutput=0;

% per sfruttare informazione su correnti bobine F
% ######## 1 2 3 4 5 6 7 8
usefscurr=[1 1 1 1 1 1 1 1]; % Quali correnti fs usare

%% Dati generali
ra=0.457; % raggio interno grafite
rfl=0.506; % raggio sonde fluxloops
rinterno1=0.75*rfl;
rinterno2=0.5*rfl;
rlin=0.49; % raggio medio vessel
R0=1.995; % asse macchina
rpb = 0.5085; % raggio sonde BpINT
th_Bp=[27 72 117 162 207 252 297 342]';
th_Fp=[22.5 67.5 112.5 157.5 202.5 247.5 292.5 337.5]';
```

```
th_Bp_rad=pi/180*th_Bp;
th_Fp_rad=pi/180*th_Fp;

thetafl=th_Fp_rad;
Rliner=1.17e-3;
mu0 = 4*pi*1.e-7;

xfl=R0+rfl*cos(thetafl);
yfl=rfl*sin(thetafl);
xinterno1=R0+rinterno1*cos(thetafl);
yinterno1=rinterno1*sin(thetafl);
xinterno2=R0+rinterno2*cos(thetafl);
yinterno2=rinterno2*sin(thetafl);
xy=[[xfl; xinterno1; xinterno2] [yfl; yinterno1; yinterno2]]';

% Per plot circonferenza vessel
N=360;
theta=(0:2*pi/N:2*pi);
r_fw=0.459;
r_vv_i=ra;
r_vv_o=0.505;
xvi=R0+r_vv_i*cos(theta);
yvi=r_vv_i*sin(theta);
xvo=R0+r_vv_o*cos(theta);
yvo=r_vv_o*sin(theta);
xfw=R0+r_fw*cos(theta);
yfw=r_fw*sin(theta);

% Preparazione grid per produzione grafici
points=100;
xmin=1.4; xmax=2.6; ymin=-0.6; ymax=0.6;
X=[xmin:(xmax-xmin)/(points-1):xmax];
Y=[ymin:(ymax-ymin)/(points-1):ymax];
XCrow=zeros(1,points^2);
YCrow=zeros(1,points^2);
for i=1:points
    for j=1:points
        XCrow(i+(j-1)*points)=X(j);
        YCrow(i+(j-1)*points)=Y(i);
    end
end

% Punti per la grid infittita per determinare il gradiente di psi e la
```

```
% presenza del nullo superiore (indicato dall'1 finale)
pointsnull=200;
xminu=1.6;
xmanu=2;
yminu1=0.1;
ymanu1=0.46;
Xnu1=[xminu:(xmanu-xminu)/(pointsnull-1):xmanu];
Ynu1=[yminu1:(ymanu1-yminu1)/(pointsnull-1):ymanu1];
XCnu1=zeros(1,pointsnull^2);
YCnu1=zeros(1,pointsnull^2);
for i=1:pointsnull
    for j=1:pointsnull
        XCnu1(i+(j-1)*pointsnull)=Xnu1(j);
        YCnu1(i+(j-1)*pointsnull)=Ynu1(i);
    end
end

% Punti per la grid infittita per determinare il gradiente di psi e la
% presenza del nullo inferiore (indicato dal 2 finale)
yminu2=-ymanu1;
ymanu2=-yminu1;
Xnu2=[xminu:(xmanu-xminu)/(pointsnull-1):xmanu];
Ynu2=[yminu2:(ymanu2-yminu2)/(pointsnull-1):ymanu2];
XCnu2=zeros(1,pointsnull^2);
YCnu2=zeros(1,pointsnull^2);
for i=1:pointsnull
    for j=1:pointsnull
        XCnu2(i+(j-1)*pointsnull)=Xnu2(j);
        YCnu2(i+(j-1)*pointsnull)=Ynu2(i);
    end
end

% Punti per la stima di psib sulla circonferenza, caso limiter
numtpsib=360;
theta0=2*pi/6; % per dividere stima psib in 3 settori
thetapsib=(theta0+2*pi/numtpsib:2*pi/numtpsib:theta0+2*pi)';
sector1=1:numtpsib/3;
sector2=numtpsib/3:2*numtpsib/3;
sector3=2*numtpsib/3:numtpsib;
xcircpsib=R0+ra*cos(thetapsib);
ycircpsib=ra*sin(thetapsib);
% Calcolo effetto delle bobime FS sui punti usati per la stima di psib.
% Ogni colonna corrisponde a una bobina.
```

```
fsfxoncirc=zeros(numtpsib,8);
for i=1:8
    fsfxoncirc(:,i)=interp2(X,Y,FluxFs(:,:,i),xcircpsib,ycircpsib);
end

% Interpolo i dati exp su una scala temporale meno fitta
[t_du,m_du]=unique(t_dequ);
[t_pu,m_pu]=unique(t_p);
[t_au,m_au]=unique(t_a);
Bp_frame=interp1(t_du,Bp_fitti_ave(m_du,:),t_frame,'linear');
fp_frame_ugly=interp1(t_du,fp(m_du,:),t_frame,'linear');
dfp_frame=interp1(t_du,d_fp(m_du,:),t_frame,'linear');
vt_frame=interp1(t_du,vt(m_du,:),t_frame,'linear');
ifs_frame=interp1(t_pu,ifs(m_pu,:),t_frame,'linear');
ifs_read=ifs_frame;
ipla_frame=interp1(t_au,i_pla(m_au,:),t_frame,'linear');

% Come flusso uso il 6 di fp e gli altri li ricostruisco dalle differenze
% di flusso per avere meno rumore
fp_frame=fp_frame_ugly(:,6)*ones(1,8)+dfp_frame;

if avioutput
    figure('Paperunit','inches');
    avijob=avifile(['../../',int2str(shot),'/movie/mov_exp.avi'],'fps',fps);
end

Contour=cell(numel(t_frame),1);
Time=zeros(numel(t_frame),1);

rpla_time=zeros(numel(t_frame),1);
rpla_tpaps=zeros(numel(t_frame),8);

addpath ../

%%%%% MAIN 'FOR' LOOP
for campione=1:numel(t_frame)

    tsim=campione;

    Psifl=fp_frame(campione,:)';
    Bpcurr=Bp_frame(campione,:)';
    Vtcurr=vt_frame(campione,:)';
```

```
if gapstima
    % Stima eqflu dei gap, passo a computedelta i dati 'veri'
    [dh,dv,rpladelta]=NewComputeDelta(1,Bpcurr',Psifl',Vtcurr');
    xrstim=R0+rpladelta'.*cos(th_Fp_rad);
    yrstim=rpladelta'.*sin(th_Fp_rad);
end

% Deupuro i dati dall'effetto delle bobine field shaping
for bob=1:8
    if usefscurr(bob)
        Bpcurr=Bpcurr-(ifs_read(tsim,bob)/1000)*bp_fs(:,bob);
        Psifl=Psifl-(ifs_read(tsim,bob)/1000)*fl_fs(:,bob);
    end
end

% Uso 'eqflu' per ricostruire il flusso ai raggi interni
[trashh,trashv,trashr,Psiri1] = ...
            NewComputeDelta(1,Bpcurr',Psifl',Vtcurr',rinterno1);
[trashh,trashv,trashr,Psiri2] = ...
            NewComputeDelta(1,Bpcurr',Psifl',Vtcurr',rinterno2);

%% TPAPS interpolation
vals=[Psifl' Psiri1 Psiri2];

tic
st = tpaps(xy,vals,0.96); % ultimo parametro 1 significa interpola
% valori piu' bassi regolarizzano la mappa
% le prestazioni migliori con un po' di regolarizzaz. es p=0.96
toc
% Valuto la thin plate spline nella grid 100X100, per plot
avals=fnval(st,xy);
Fvals=fnval(st,[XCrow;YCrow]);
Fvals=reshape(Fvals,100,100);

for bob=1:8
    if usefscurr(bob) % Sommo mappa di flusso dovuta alle FS
        Fvals=Fvals+(ifs_read(tsim,bob)/1000)*FluxFs(:,:,bob);
    end
end

% Valuto la presenza del nullo di B sulla parte superiore
FvalsNull1=interp2(X,Y,Fvals,XCnu1,YCnu1,'cubic');
FvalsNull1=reshape(FvalsNull1,pointsnull,pointsnull);
```

```
[FvGx1 FvGy1]=gradient(FvalsNull1);
FvGrad1=FvGx1.^2+FvGy1.^2;
nulVal1=1; % big number
imin1=1;
jmin1=1;
% Attenzione che matlab ordina le variabili come F(Y,X)
% e si aspetta contour(X,Y,F)
for iii=1:numel(Xnu1)
    for jjj=1:numel(Ynu1)
        if FvGrad1(jjj,iii)<nulVal1
            nulVal1=FvGrad1(jjj,iii);
            imin1=iii;
            jmin1=jjj;
        end
    end
end
nulRaggio1=sqrt((Xnu1(imin1)-R0)^2+(Ynu1(jmin1))^2);
disp(['nulRaggio1: ',num2str(nulRaggio1)]);
psib_nul1=-100; % - big number
nul1=0;
if (nulVal1<nulSoglia && nulRaggio1<ra)
    % caso nullo sulla meta' superiore
    nul1=1;
    xnul1=Xnu1(imin1);
    ynul1=Ynu1(jmin1);
    psib_nul1=FvalsNull1(jmin1,imin1);
    disp('Individuato nullo SUP');
end

% Idem per cercare il nullo inferiore
FvalsNull2=interp2(X,Y,Fvals,XCnu2,YCnu2,'cubic');
FvalsNull2=reshape(FvalsNull2,pointsnull,pointsnull);
[FvGx2 FvGy2]=gradient(FvalsNull2);
FvGrad2=FvGx2.^2+FvGy2.^2;
nulVal2=1; % big number
imin2=1;
jmin2=1;
for iii=1:numel(Xnu2)
    for jjj=1:numel(Ynu2)
        if FvGrad2(jjj,iii)<nulVal2
            nulVal2=FvGrad2(jjj,iii);
            imin2=iii;
            jmin2=jjj;
```

```
        end
    end
end
nulRaggio2=sqrt((Xnu2(imin2)-R0)^2+(Ynu2(jmin2))^2);
psib_nul2=-100; % - big number
nul2=0;
if (nulVal2<nulSoglia && nulRaggio2<ra)
    % caso nullo sulla meta' inferiore
    nul2=1;
    xnul2=Xnu2(imin2);
    ynul2=Ynu2(jmin2);
    psib_nul2=FvalsNull2(jmin2,imin2);
    disp('Individuato nullo INF');
end

disp(['nulVal1: ',num2str(nulVal1),'  nulVal2: ',num2str(nulVal2)]);
disp(['nulRag1: ',num2str(nulRaggio1),'   nulRag2: ',num2str(nulRaggio2)]);
% caso limiter: va calcolato sempre nel caso in cui ci sia il nullo ma
% il plasma tocchi la parete esterna dal lato dove il nullo non c'e, e
% confrontato il valore limiter col valore nullo

% stimo psib valutando il massimo su valori infittiti sulla
% circonferenza
FvalsCirc=fnval(st,[xcircpsib';ycircpsib']);
for bob=1:8
    if usefscurr(bob)
        FvalsCirc=FvalsCirc+(ifs_read(tsim,bob)/1000)*fsfxoncirc(:,bob)';
    end
end

% Divido la stima in 3 settori: I primi 2 sono nei
% pressi delle zone di nullo. Il terzo e' la parte piu' esterna,
% dove il plasma se interagisce e' sempre in limiter.

psib_limiter_1=max(FvalsCirc(sector1));
psib_limiter_2=max(FvalsCirc(sector2));
psib_limiter_3=max(FvalsCirc(sector3));

% Vedo se il boundary e' al nullo o al limiter in ciascuno dei 3
% settori

if nul1
    psib_stim_1=psib_nul1;
```

```
else
    psib_stim_1=psib_limiter_1;
end

if nul2
    psib_stim_2=psib_nul2;
else
    psib_stim_2=psib_limiter_2;
end

psib_stim_3=psib_limiter_3;

psib_stim=max([psib_stim_1;psib_stim_2;psib_stim_3]);


% Produzione grafici
disp(' ---- Ora plotto i grafici ---- ');
figure(1);
plot(xvi,yvi,'k','LineWidth',1);hold on;
axis equal;grid on;
plot(xvo,yvo,'k','LineWidth',1);
plot(xfw,yfw,'k');
if gapstima
  plot(xrstim,yrstim,'k+ ','LineWidth',2,'MarkerSize',10)
end
if nul1
  plot(xnul1,ynul1,'r+ ','LineWidth',3,'MarkerSize',12)
end
if nul2
  plot(xnul2,ynul2,'r+ ','LineWidth',3,'MarkerSize',12)
end
plot(xy(1,:),xy(2,:),'m+ ','LineWidth',2,'MarkerSize',8);
% contour(X,Y,Flux,50);
contour(X,Y,Fvals,30);
title(['Est. flux, real data, shot = ',num2str(shot),'; time = ',...
num2str(t_frame(campione),'%4.3f'),' s; ipla = ',...
num2str(ipla_frame(campione),'%8.0f'),' A']);
colorbar;
[C,h]=...
contour(X,Y,Fvals,[psib_stim psib_stim],'LineColor','r','LineWidth',2);
Contour{campione}=C;
Time(campione)=t_frame(campione);
set(gca,'nextplot','replacechildren');
```

```
    mov_exp(campione)=getframe(gcf);
    if avioutput
        avijob=addframe(avijob,gca);
    end
    %% Calcolo gap ricostruiti
    rpla_time(campione)=t_frame(campione);
    rpla_tpaps(campione,:)=GapFromContour(C,th_Fp_rad);

end

if avioutput, avijob=close(avijob); end
eval(['save ../../',int2str(shot),'/movie/mov_exp.mat mov_exp']);
eval(['save ../../',int2str(shot),'/rpla_tpaps_exp.mat rpla_time rpla_tpaps']);

disp('Varianza stime gap:');
disp(num2str(var((rpla_tpaps+fliplr(rpla_tpaps))/2)));

%%%%%%%%%%%%%%%%%%%%%%%%%%%%%%%%%%%%%%%%%%%%%%%%%%%%%%%%%%%%%%%%%%%%%%%%%%%%%%

function rplasma=GapFromContour(C,ang)
% Riceve in input un contour matlab [C], relativo alla superficie di flusso del
% boundary, e calcola le intersezioni coi raggi passanti per il centro
% macchina (R0,0) agli angoli [ang].

R0=1.995;
ra=0.459;

nang=numel(ang);
rplasma=ra*ones(1,nang);

% Trovo punti che stanno dentro alla camera da vuoto (matlab dà un valore
% fuori range per il primo punto)
gp=find((C(1,:)-R0).^2+C(2,:).^2 <= (ra)^2); % good points: punti buoni
gploop=[gp gp(1)]; % Richiudo primo e ultimo punto

xc=C(1,gploop)'-R0;
yc=C(2,gploop)';

prevha=zeros(1,nang); % precedente altezza rispetto a ogni angolo
prevpr=zeros(1,nang); % precedente proiezione rispetto a ogni angolo

for cc=1:numel(gploop)
    for aa=1:nang
```

```
        rtemp=ra;
        % Ruoto sistema di riferimento
        pr=xc(cc)*cos(ang(aa))+yc(cc)*sin(ang(aa)); % proiezione sul raggio
        ha=-xc(cc)*sin(ang(aa))+yc(cc)*cos(ang(aa)); % altezza risp. raggio
        if pr>0 % devo restringermi a raggio positivo
        % Caso: coppia di punti a cavallo del raggio e abbastanza vicini
        % Calcolo intersezione della congiungente i 2 punti col raggio e aggiorno rplasma
            if (prevha(aa)*ha<0)&&(abs(prevpr(aa)-pr)<0.1*ra)
                df=abs(prevha(aa));
                dl=abs(ha);
                pf=prevpr(aa);
                pl=pr;
                rtemp=(pl*df+pf*dl)/(df+dl);
            end
            if ha==0 % caso degenere: punto di contour esattamente sul raggio
                rtemp=pr;
            end
            if rtemp<rplasma(aa)
                rplasma(aa)=rtemp;
            end
        end
        prevha(aa)=ha;
        prevpr(aa)=pr;
    end
end
```

Appendix C

Controller implementation: FORTRAN77 code

The code implemented in the user-defined control routine of Maxfea is presented in this section. It provides the implementation of poloidal circuit equations, modeling the reconnection of M and F coils, since in the simulator these are represented as independent circuits. Inductive coupling is computed according to their position and shape, and the simulator would evolve currents in these circuits without complying to the condition expressed by eq. 5.9. To actually force this condition, and to correctly model resistive coupling between coils composing a sector of the circuit, a condition similar to that of figure 5.3.b is modeled, but a resistance `R_gr` of value $10\ \Omega$ is connected in parallel to the circuit. This element applies a feedback voltage whenever total sector current is not null, forcing the desired condition. This is actually a simplification of the original code [6] modeling the complete poloidal circuit as in figure 2.6, that used to include $PCAT$ converters and R_T elements. Here, the 4 sectors of the circuit are modeled as independent and no loop voltage can be applied, consistently with the hypothesis of the linear model. We consider a simplified implementation that still guarantees consistence between the linear and nonlinear model, and produces comparable simulation outputs.

Next, the code provides the implementation of the position stabilizing controller and of the shape controller using ideal Maxfea measures as controlled variables; the function that computes the gap along the radius (`gap_along_r()`) is an adaptation of the original algorithm that by default computes geometric distances in Maxfea. The implementation of diagnostic routines in the nonlinear model to estimate output variables from magnetic data and to evaluate their impact in closed loop performance is a possible extension of this work.

```
*** Definizione variabili, riferimenti, caricamento matrici controllore ***
[...]

*** Codice eseguito a ogni step di simulazione ***

* Perturbazione alfa/beta
      if((perturb_alfa).and.(ztime.ge.(tstartdisrpt-zepsi))) then
        alfap=alfap0+d_alfap*exp(-(ztime-tstartdisrpt)/tau_alfa)
      endif

      if((perturb_beta).and.(ztime.ge.(tstartdisrpt-zepsi))) then
        betap=betap0+d_betap*exp(-(ztime-tstartdisrpt)/tau_beta)
      endif

* Calcolo gap lungo il raggio
      call gap_along_r(R0,ra,th_flux,8,rpla_proj)
      do i=1,8
        gap_proj(i)=ra-rpla_proj(i)
      enddo

* Azzerramento tensioni applicate ai circuiti
      do i=1,17
        plcivu(i)=0
      enddo

* Azzerramento tensioni PVAT
      do i=1,8
        vpvat(i)=0
      enddo

* Riferimento posizione controllori: centroide di corrente
      R_meas=datplasma(4)
      Z_meas=datplasma(5)

* Controllo posizione su bobine sella
      if (pos_contr) then
        errR=R_meas-R_ref
        errZ=Z_meas-Z_ref
* Radiale: BcampoZ=[0 -1 0 1] ma segno - dovuto al feedback
        plcivu(13+2)=plcivu(13+2)+kpR*errR
        plcivu(13+4)=plcivu(13+4)-kpR*errR
* Verticale: BcampoR=[1 0 -1 0] ma segno - dovuto al feedback
```

```
          plcivu(13+1)=plcivu(13+1)-kpZ*errZ
          plcivu(13+3)=plcivu(13+3)+kpZ*errZ
        endif

* Preparazione per elaborazioni di settore e per scrittura correnti
* nei file di output
        do i=1,10
          pol_current(i)=plcico(i)
        enddo
        pol_current(11)=(plcico(11)+plcico(12))/2
        pol_current(12)=plcico(13)

* u KF per aggiornamento stima. Uso la vpvat al passo precedente.
* Adatto le convenzioni di segno
        do i=1,8
          ukf(i)=sign_pvat(i)*(vpvat_old(i)-vcomp_pvat(i))
        enddo

* y0 KF per aggiornamento stima
        y0kf(1)=xipla-ipla_ref
        y0kf(2)=R_meas-R_ref
        y0kf(3)=Z_meas-Z_ref
        do i=1,8 ! gap
          y0kf(3+i)=gap_proj(i)-gap_ref(i)
        enddo
        do i=1,8 ! correnti bobine FS
          y0kf(11+i)=pol_current(4+i)-ifs_ref(i)
        enddo
        do i=1,4 ! correnti bobine a sella
          y0kf(19+i)=plcico(13+i)
        enddo
        write(1105,*) ztime,(y0kf(i),i=1,ymr)

* azzerro variazione stato
        do i=1,dmr
          dxkf(i)=0
        enddo

* evoluzione libera KF
        do i=1,dmr
          do k=1,dmr
            dxkf(i)=dxkf(i)+Akf(i,k)*xkf(k)*dtimep
          enddo
```

```
        enddo

* correzione dovuta all'ingresso
        do i=1,dmr
          do k=1,umr
            dxkf(i)=dxkf(i)+Bmr(i,k)*ukf(k)*dtimep
          enddo
        enddo

* correzione dovuta all'uscita
        do i=1,dmr
          do k=1,ymr
            dxkf(i)=dxkf(i)+Lmr(i,k)*y0kf(k)*dtimep
          enddo
        enddo

* aggiorno stato KF
        do i=1,dmr
          xkf(i)=xkf(i)+dxkf(i)
        enddo
        write(1100,*) ztime,(xkf(i),i=1,dmr)

* Calcolo uscita stimata (usata in scrittura e per integrale errore ai gap)
        do i=1,ymr
          ystimkf(i)=0
          do k=1,dmr
            ystimkf(i)=ystimkf(i)+Cmr(i,k)*xkf(k)
          enddo
        enddo
        write(1110,*) ztime,(ystimkf(i),i=1,ymr)

* Calcolo integrale variazione ai gap usando la stima del KF
        do i=1,8
          gapint(i)=gapint(i)+ystimkf(3+i)*dtimep
        enddo

* Calcolo ingresso controllore lqr
        do i=1,umr
          ulq(i)=0
          if (.not.intgr_contr) then !uso Kmr
            do k=1,dmr
              ulq(i)=ulq(i)+Kmr(i,k)*xkf(k)
            enddo
```

```
          else !uso Kint
            do k=1,dmr
              ulq(i)=ulq(i)+Kint(i,k)*xkf(k)
            enddo
            do k=1,8
              ulq(i)=ulq(i)+Kint(i,dmr+k)*gapint(k)
            enddo
          endif
        enddo
        write(1120,*) ztime,(ulq(i),i=1,umr)

* Applicazione vpvat per il controllo LQR con cambio convenzioni di segno
* !!! Segno meno davanti in quanto retroazione negativa A [-] BK !!!
        if (shape_contr) then
          do i=1,8
            vpvat(i)=vpvat(i)-ulq(i)*sign_pvat(i)
          enddo
        endif

* Compensazione resistiva (costante)
        if (comp_res) then
          do i=1,8
            vpvat(i)=vpvat(i)+vcomp_pvat(i)
          enddo
        endif

* Saturazione tensioni pvat
        if (satura_pvat) then
          do i=1,8
            if (vpvat(i).gt.max_pvat) then
              vpvat(i)=max_pvat
            endif
            if (vpvat(i).lt.min_pvat) then
              vpvat(i)=min_pvat
            endif
          enddo
        endif

* Applicazione perturbazione PVAT e bobine sella
* (esclusa dalla saturazione)
        write(*,*) ztime
        if(ztime.ge.tstartstep-zepsi .and. ztime.le.tstopstep+zepsi) then
          do i=1,8
```

```
            vpvat(i)=vpvat(i)+voltamp*disturbapvat(i)
          enddo
          do i=1,4
            plcivu(13+i)=plcivu(13+i)+voltamp*bobinesella(i)
          enddo
        endif

* Memorizzo tensione pvat
        vpvat_old=vpvat

* Sulla base delle tensioni VPVAT appena calcolate, calcolo tensioni
* plcivu (1...13) applicate ai circuiti dovute alle equazioni di settore.
* Ogni settore del circuito poloidale e' considerato come il parallelo
* di 4 elementi: es. M1 // F2 // F7 // R_gr.
* La resistenza di ground e' necessaria per introdurre un feedback
* nella simulazione: A ogni step infatti es. Im1, If2, If7 evolvono
* in modo che la loro somma non sia piu' nulla. Con R_gr "grande",
* se c'e' sbilanciamento si crea tensione di settore
* grande che tende a ribilanciare le correnti.

* calcolo le correnti del settore poloidale (M+FS)
* numerate come il corrispontente circuito M
        i_s(1)=pol_current(1)+pol_current(6)+pol_current(11)
        i_s(2)=pol_current(2)+pol_current(5)+pol_current(12)
        i_s(3)=pol_current(3)+pol_current(8)+pol_current(9)
        i_s(4)=pol_current(4)+pol_current(7)+pol_current(10)

* Calcolo le tensioni applicate al settore supponendolo in serie con R_gr

         v_s(1)=-i_s(1)*R_gr
         v_s(2)=-i_s(2)*R_gr
         v_s(3)=-i_s(3)*R_gr
         v_s(4)=-i_s(4)*R_gr

* Eventuale saturazione correnti con vdiode

         do j=1,8
           vdiode(j)=0
         enddo

        if (satura_pvat) then
         if (pol_current(4+1).gt.0) vdiode(1)=100*pol_current(1+4)
         if (pol_current(4+2).gt.0) vdiode(2)=100*pol_current(2+4)
```

```
          if (pol_current(4+3).lt.0) vdiode(3)=100*abs(pol_current(3+4))
          if (pol_current(4+4).gt.0) vdiode(4)=100*pol_current(4+4)
          if (pol_current(4+5).gt.0) vdiode(5)=100*pol_current(5+4)
          if (pol_current(4+6).gt.0) vdiode(6)=100*pol_current(6+4)
          if (pol_current(4+7).gt.0) vdiode(7)=100*pol_current(7+4)
          if (pol_current(4+8).lt.0) vdiode(8)=100*abs(pol_current(8+4))
        endif

* Applicazione tensione alle bobine: suppongo che la loro resistenza
* sia intrinseca nel circuito maxfea, vanno definite come resistenze
* esterne nel file .pla

        plcivu(1)=v_s(1)
        plcivu(2)=v_s(2)
        plcivu(3)=v_s(3)
        plcivu(4)=v_s(4)

        plcivu(5)=v_s(2)-vpvat(1)-vdiode(1)
        plcivu(6)=v_s(1)-vpvat(2)-vdiode(2)
        plcivu(7)=v_s(4)+vpvat(3)+vdiode(3)
        plcivu(8)=v_s(3)-vpvat(4)-vdiode(4)
        plcivu(9)=v_s(3)-vpvat(5)-vdiode(5)
        plcivu(10)=v_s(4)-vpvat(6)-vdiode(6)
        plcivu(11)=(v_s(1)-vpvat(7)-vdiode(7))/2
        plcivu(12)=(v_s(1)-vpvat(7)-vdiode(7))/2
        plcivu(13)=v_s(2)+vpvat(8)+vdiode(8)

*** Scrittura dati nei file di output ***
[...]

*** Subroutine per calcolo dei gap lungo il raggio ***

subroutine gap_along_r(R0,ra,th_flux,totang,rplasma)

* Calcolo la distanza separatrice-bordo grafite lungo il raggio, anziche'
* in termini di distanza geometrica come viene fatto in mx2slp2,
* righe 1100->1300.

* R0: centro geometrico macchina; ra: raggio bordo plasma
* th_flux: angoli rispetto ai quali si vuole calcolare il gap
* totang: numero totale angoli in th_flux
* rplasma: raggio stimato rispetto a (R0,0)
```

```
      INCLUDE 'vectors.f'
      logical debug_on
      integer nplasmael,ii(3),nmat,ang,totang
      real*4 R0 ra ztime psib,u(3),vl
      real*4 xxx(3),yyy(3),zmin,zmax,ttt1,ttt2,ttt3
      real*4 rplasma(totang),th_flux(totang)
      real*4 pf,pl,df,dl,rtemp

* definizione variabili e parametri

      debug_on=.false.
      nmat=50!plasma material
      ztime=datplasma(2)
      psib=datplasma(51)
      vl=psib/(2*pigrec)

      do ang=1,totang
        rplasma(ang)=ra
      enddo

      if (debug_on) write(679,*)'time=',ztime,'psi/2pi=',vl

* Copio da mx2slp2 la procedura per ricavare xl,xf: per ogni triangolo
* della mesh appartenente al plasma, sono i due punti di intersezione della
* linea del boundary con i lati del triangolo

      DO 300 i = 1 , ntr
        IF ( tr2(i,7).NE.nmat ) GO TO 300

            ii(1) = 1
            ii(2) = 2
            ii(3) = 3

          zmin = 1.E30

          DO 120 k = 1 , 3
            u(k) = pnode(tr2(i,ii(k)))
            xxx(k) = wnode(tr2(i,ii(k)),1)
            yyy(k) = wnode(tr2(i,ii(k)),2)
            IF ( u(k).LT.zmin ) THEN
              n = k
              zmin = u(k)
            END IF
```

```
120          CONTINUE

             IF ( u(1).EQ.u(2) .AND. u(1).EQ.u(3) ) GO TO 300

             zmax = max(u(1),u(2),u(3))
             zmin = min(u(1),u(2),u(3))
             IF ( ((zmin-vl)*(zmax-vl)).GT.0. ) GO TO 300


             ttt1 = u(n)
             ttt2 = xxx(n)
             ttt3 = yyy(n)
             u(n) = u(1)
             xxx(n) = xxx(1)
             yyy(n) = yyy(1)
             u(1) = ttt1
             xxx(1) = ttt2
             yyy(1) = ttt3
             IF ( u(2).GT.u(3) ) THEN
                ttt1 = u(3)
                ttt2 = xxx(3)
                ttt3 = yyy(3)
                u(3) = u(2)
                xxx(3) = xxx(2)
                yyy(3) = yyy(2)
                u(2) = ttt1
                xxx(2) = ttt2
                yyy(2) = ttt3
             END IF

             la = 0

             IF ( (vl.LT.max(u(1),u(2))) .AND. (vl.GT.min(u(1),u(2))) )
            &       THEN
                xf = xxx(1) + (vl-u(1))*(xxx(2)-xxx(1))/(u(2)-u(1))
                yf = yyy(1) + (vl-u(1))*(yyy(2)-yyy(1))/(u(2)-u(1))
                la = 12
                GO TO 140
             END IF

             IF ( (vl.LT.max(u(3),u(2))) .AND. (vl.GT.min(u(3),u(2))) )
            &       THEN
                xf = xxx(2) + (vl-u(2))*(xxx(3)-xxx(2))/(u(3)-u(2))
```

```
                yf = yyy(2) + (vl-u(2))*(yyy(3)-yyy(2))/(u(3)-u(2))
                la = 23
                GO TO 140
              END IF

              xf = xxx(1) + (vl-u(1))*(xxx(3)-xxx(1))/(u(3)-u(1))
              yf = yyy(1) + (vl-u(1))*(yyy(3)-yyy(1))/(u(3)-u(1))
              la = 13

140           IF ( vl.LT.max(u(2),u(3)) .AND. vl.GT.min(u(2),u(3)) .AND.
     &               la.NE.23 ) THEN
                xl = xxx(2) + (vl-u(2))*(xxx(3)-xxx(2))/(u(3)-u(2))
                yl = yyy(2) + (vl-u(2))*(yyy(3)-yyy(2))/(u(3)-u(2))
                GO TO 160
              END IF

              xl = xxx(1) + (vl-u(1))*(xxx(3)-xxx(1))/(u(3)-u(1))
              yl = yyy(1) + (vl-u(1))*(yyy(3)-yyy(1))/(u(3)-u(1))
              if (debug_on) write(679,*) 'triang=',i,xl,yl,xf,yf

* A questo punto ho calcolato correttamente (xl,yl) e (xf,yf)
* Traslo nel sistema di riferimento centrato in (R0,0)

              xl=xl-R0
              xf=xf-R0

* Calcolo le proiezioni dei due punti sugli otto raggi: ruoto
* il sistema di riferimento in modo che sia quello del raggio corrente

160           do ang=1,totang

* pf e pl sono le proiezioni di (xf,yf) e (xl,yl) sul raggio
* df e dl sono le altezze degli stessi punti rispetto al raggio

              pf=xf*cos(th_flux(ang))+yf*sin(th_flux(ang))
              df=(-xf*sin(th_flux(ang))+yf*cos(th_flux(ang)))
              pl=xl*cos(th_flux(ang))+yl*sin(th_flux(ang))
              dl=(-xl*sin(th_flux(ang))+yl*cos(th_flux(ang)))
              if (debug_on) write(679,*) 'angle=',ang,pf,df,pl,dl
              rtemp=ra

* vedo se sono opposte: df*dl minore di 1. In tal caso il raggio
* passa per il triangolo
```

```
          if ((df*dl).lt.0) then

* considero i moduli per usare le altezze nella proporzione

            df=abs(df)
            dl=abs(dl)

* calcolo intersezione con proporzione

            rtemp=(pl*df+pf*dl)/(df+dl)
            if (debug_on) write(679,*) 'rtemp= ',rtemp
            endif

* gestisco i casi degeneri

          if (df.eq.0) then
            rtemp=pf
          endif
          if (dl.eq.0) then
            rtemp=pl
          endif

* aggiorno rplasma

          if ((rtemp.lt.rplasma(ang)).and.(rtemp.ge.0)) then
            rplasma(ang)=rtemp
          endif
         enddo
300     CONTINUE
      return
      end
```

List of Tables

2.1 RFX-mod specifications 19
2.2 Radius of assembly layers 20
2.3 RFX-mod inner magnetic probes ($k, l \in \mathbb{Z}$) 24
2.4 RFX-mod PF circuit sectors with M coils interconnection 24

3.1 *dnfat38* double-null configuration, field shaping coils current 40
3.2 Estimates of vertical instability growth rate 40

5.1 Plasma parameters in shot #29746, $t \approx 0.4s$ 63
5.2 Coil currents in shot #29746, $t \approx 0.4\ s$ 64
5.3 Intrinsic M and F coil resistance 67
5.4 Total resistance for toroidal structures 68
5.5 Sector currents in shot #29746, $t \approx 0.4s$ 72
5.6 Rescaled coil currents, complying with $I_{S,i} = 0,\ i = 1 \dots 4$ 72
5.7 PVAT voltages for resistive compensation 75
5.8 Voltage perturbations for linear model validation 80

6.1 Input/output variables for LQG control 100
6.2 Output variances from experimental data 103
6.3 LQR weights: max. expected variations for input/output variables 107
6.4 Tokamak perturbations with recovery 111
6.5 Tokamak perturbations without recovery 120

List of Figures

1.1 Binding energy per nucleon 10
1.2 The Lawson criterion 12
1.3 Toroidal and cylindrical coordinates 15
1.4 Radial profiles for equilibrium configurations 17
1.5 F-Θ graph: Taylor equilibrium states 18

2.1 Sectional view of RFX-mod toroidal assembly 21
2.2 RFX-mod shell and structure, exploded view 21
2.3 RFX-mod section 22
2.4 Machine room of RFX-mod 23
2.5 Top view of RFX-mod main diagnostics 23
2.6 RFX poloidal field circuit 25
2.7 RFX toroidal field circuit 26
2.8 A subset of 12 saddle coils 27

3.1 Limiter and diverted configuration for a generic Tokamak 31
3.2 Shot #29648, plasma current 34
3.3 Shot #29648, Λ estimates from magnetic data 36
3.4 Shot #29648, experimental and simulated magnetic data 37
3.5 Shot #29746, Λ estimates from magnetic data 38
3.6 Shot #29746, experimental and simulated magnetic data 39
3.7 Exponential fit of plasma vertical displacement 41

4.1 Definition of plasma geometric measures 44
4.2 Application of gap estimation methods to Maxfea virtual measures 47
4.3 XLOC approach to plasma boundary reconstruction 49
4.4 Regions for the calculation of ψ_b 53
4.5 Application of thin-plate spline reconstruction to Maxfea virtual measures 55

4.6 Thin-plate spline flux map reconstruction, experimental data 56
4.7 Reconstructed evolution of the experimental discharge 57
4.8 Shot #29746, current centroid reconstruction, simulated data 61
4.9 Shot #29746, current centroid reconstruction, higher probe resolution . . . 62
4.10 Shot #29746, application to experimental data 62

5.1 Discretized mesh used to derive the linear model 65
5.2 Side currents and mesh currents representations 69
5.3 Poloidal circuit sector representations in the linear model 73
5.4 Components of unstable eigenvectors (vessel), and resulting field 75
5.5 Decay index of the field generated by external coils 76
5.6 Mesh modifications to include saddle coils circuits, detail 77
5.7 Unstable eigenvectors after introduction of saddle coils circuits 79
5.8 Perturbations #1 and #2, open loop. Current centroid 81
5.9 Perturbation #1, open loop. F coils currents and gaps 82
5.10 Perturbation #2, open loop. Currents and gaps 83
5.11 Definition of plasma-first wall distance measures 84
5.12 Perturbation #1, different plasma-first wall distance measures 85

6.1 Bode diagrams for horizontal position stabilization 89
6.2 Bode diagrams for vertical position stabilization 89
6.3 Root locus of reduced order (PEM) transfer functions, detail 90
6.4 Volt. perturbation #3, radial position controller test 92
6.5 Volt. perturbation #4, vertical position controller test 93
6.6 Volt. perturbations #1, #2, closed loop on R_j and Z_j. Controlled variables 94
6.7 Volt. perturbation #1, closed loop on R_j and Z_j. F coils current, and gaps 95
6.8 Volt. perturbation #2, closed loop on R_j and Z_j. F coils current, and gaps 96
6.9 Singular values (*log*) plot, system $\mathcal{S}_0$ 98
6.10 Bode plot, transfer function singular values 98
6.11 Gaps response to voltage perturbations, reduced order models 99
6.12 Pert. #1, linear sim. + meas. noise, and Kalman (reduced order) filtering . 104
6.13 Pert. #1, Maxfea simulation, and Kalman (reduced order) filtering 105
6.14 Voltage pert. #1, LQG control. F coils current, and gaps 108
6.15 Voltage pert. #2, LQG control. F coils current, and gaps 109
6.16 $PVAT$ applied voltage to compensate perturbations 110

6.17 Tokamak perturbations with recovery 112
6.18 Pert. #1 with recovery 114
6.19 Pert. #1 with recovery, LQG control 115
6.20 Pert. #2 with recovery 116
6.21 Pert. #2 with recovery, LQG control 117
6.22 Pert. #3 with recovery 118
6.23 Pert. #3 with recovery, LQG control 119
6.24 Tokamak perturbations without recovery 121
6.25 Pert. #1 without recovery 122
6.26 Pert. #1 without recovery, LQG control 123
6.27 Pert. #2 without recovery 124
6.28 Pert. #2 without recovery, LQG control 125
6.29 Pert. #3 without recovery 126
6.30 Pert. #3 without recovery, LQG control 127
6.31 Power consumption, perturbations with recovery 130
6.32 Power consumption, perturbations without recovery 131
6.33 Circular-DN transition with LQG control, gaps 133
6.34 Circular-DN transition with LQG control, actuators 134

A.1 Simulink scheme for LQG control 137

Bibliography

[1] A. Buffa, L. Giudicotti, Dispense del corso di Fisica dei Plasmi, *University of Padua*, 2008

[2] J. Wesson, Tokamaks - 3^{rd} ed., *Oxford University Press*, 2004

[3] G. Rostagni, RFX: an expected step in RFP research, *Fusion Engineering and Design*, **25**, 1995

[4] J. B. Taylor, Relaxation of Toroidal Plasma and Generation of Reverse Magnetic Fields, *Physical Review Letters*, **33**, 1974

[5] P. Sonato *et al.*, Machine modification for active MHD control in RFX, *Fusion Engineering and Design*, **66-68**, 2003

[6] M. Cavinato, G. Marchiori, Design of the new RFX equilibrium active control system, *Fusion Engineering and Design*, **74**, 2005

[7] V. Toigo *et al.*, Components and system tests on the RFX toroidal power supply, *Fusion Engineering and Design*, **75-79**, 2005

[8] A. Pironti, M. Walker, Fusion, Tokamaks and Plasma Control: an introduction and tutorial. *IEEE Control System Magazine*, special issue, 2005

[9] A. Beghi, M. Cavinato, A. Cenedese, Nonlinear dynamic modelling for control of fusion devices, *47th IEEE Conference on Decision and Control*, 2008

[10] P. Zanca, O. Barana, M. Cavinato, Determinazione della superficie assisimmetrica di plasma nel nuovo RFX, internal technical note, *IGI-RFX consortium*, 2004

[11] P. Zanca, Modifiche al programma *eqflu-dequ* per la determinazione della superficie assisimetrica del plasma, internal technical note, *IGI-RFX consortium*, 2011

[12] D.P. O'Brien, J.J. Ellis and J. Lingertat, Local expansion method for fast plasma boundary identification in JET, *Nuclear Fusion*, **33**, 1993

[13] F. Sartori, A. Cenedese, F. Milani, JET real-time object-oriented code for plasma boundary reconstruction, *Fusion Engineering and Design*, **66-68**, 2003

[14] F. L. Bookstein, Principal warps: Thin-plate splines and the decomposition of deformations, *IEEE transactions on pattern analysis and machine intelligence*, **11**, 1989

[15] P. Bettini, M. Cavinato, A. Portone, Derivation of free-boundary equilibrium linear models by a flux perturbation method, *Nuclear Fusion*, **49**, 2009

[16] V.S. Mukhovatov, V.D. Shafranov, Plasma equilibrium in a Tokamak, *Nuclear Fusion*, **11**, 1971

[17] M. G. Safonov *et al.*, Optimal Hankel model reduction for Nonminimal Systems, *IEEE Transactions on automatic control*, **35**, 1990

[18] G. Franklin, J.D. Powell, A. Emami-Naeini, Feedback Control of Dynamic Systems - 4^{th} ed., *Prentice Hall*, 2002

[19] B. M. Torri, Controllo di forma del plasma nell'esperimento RFX-mod, Degree thesis, *University of Padua*, 2009

[20] G. Conte, Controllo Lineare Quadratico Gaussiano della forma del plasma nell'esperimento ITER tramite spline, Degree thesis, *University of Padua*, 2004